Development of Polydopamine Nanotubes into a Multi-Functional Drug Delivery System

by

Yuzhe Sun

A dissertation submitted to the Graduate Faculty of
Auburn University
in partial fulfillment of the
requirements for the Degree of
Doctor of Philosophy

Auburn, Alabama
August 7, 2021

Keywords: polydopamine, nanoparticle, controlled release, drug delivery

Approved by

Edward Davis, Chair, Associate Professor of Mechanical Engineering
Bart Prorok, Professor of Mechanical Engineering
Pengyu Chen, Associate Professor of Mechanical Engineering
Robert D. "Rusty" Arnold, Professor of Pharmacy
Guanqun Cao, Associate Professor of Statistics

Abstract

In this study, a template-assisted method for the synthesis of polydopamine nanotubes is developed. By altering the amount ratio between dopamine and template, a robust tubular structure is obtained. This unique process allows modification of the outer and inner layers of the nanotube in separate steps. The outer layer of the nanotubes is coated with polyethylene glycol to enhance its biocompatibility. Then the inner layer is modified with thermo-sensitive poly(N-isopropylacrylamide) to increase the nanostructure's thermal responsiveness. The modified nanotubes show better stability in an aqueous solution than the pristine nanotubes. Moreover, the photothermal effect of polydopamine allows the remote control of poly(N-isopropylacrylamide), which presents a hydrated or dehydrated state under different temperatures. Furthermore, the abundant catechol groups present as the reductive sites to immobilize the Fe_3O_4 magnetic nanoparticles, which endows magnetic response to the nanotubes. To investigate the controlled release of nanotubes' capability to payloads, doxorubicin, a cationic small molecular drug, is used as a payload model. The release rate in different pH, magnetic field, and a near-infrared laser is tested. As a result, a multi-linear regression model is established to describe the impacts of various stimuli on the doxorubicin release rate from the nanotube.

Besides the nanotube, synthesis of hollow polydopamine bowl-shaped nanocapsules (nanobowls), as small as 80 nm in diameter, via a one-pot template-free rapid method is developed in this study. The addition of dopamine to a solution of 0.606 mg/ml Tris(hydroxymethyl) aminomethane in an ethanol/water mixed solvent results in hollow spherical formation nanocapsules within two hours. At longer reaction times, the formation of conventional solid

nanospheres dominates the reaction. The nanocapsules' wall thickness was increased as the dopamine concentration in the reaction medium increased and sufficient oxygen supported. Under dehydrated status, the nanocapsules with thin wall thickness and prepared with deficient oxygen were prone to collapse. Moreover, the degree of collapse of individual nanoparticles changes from complete to partial to no collapse as the wall thickness increased. Varying the ethanol content affects the nanocapsules' cavity size and overall dimension but does not result in a noticeable change in their wall thickness. The largest cavity and dimension appear with 20 vol.% ethanol contained in the reaction medium. The formation mechanism of the hollow nanocapsule structure related to the lower solubility of dopamine in alcohol solvent is then provided.

Acknowledgments

I would like firstly to express my sincere gratitude to Dr. Edward Davis for supporting, guiding, and inspiring me during my whole Ph.D. time. His optimistic spirit and critical perspective are invaluable for me to overcome difficulties in my research. I cannot imagine the dissertation being possible without his encouragement and persistent help.

I would also like to acknowledge the time and effort from my committee members, Dr. Bart Prorok, Dr. Pengyu Chen, Dr. Robert D. "Rusty" Arnold, and university reader, Dr. Guanqun Cao. I genuinely appreciate your valuable suggestions and comments on my dissertation.

I would like to thank Dr. Bart Prorok and Dr. Michael E. Miller for the approach to electron microscopes. I want to thank Dr. Cheryl Colquhoun for the training and access to infrared spectroscopy. I would also like to thank Dr. Allan E. David for supporting the characterization of nanomaterials. And I would like to extend my thanks to Dr. Zhongyang Cheng for supporting the thermal analysis instrument.

I would like to show my gratitude to the staff in Materials Engineering. Thanks to Mr. Steven Moore for equipment training and problem troubleshooting. Appreciate Ms. Cheryl Rhodes, who is so patient, kind, and always ready to help.

I will always treasure my Auburn-made friendship. Thanks to my seniors, Dr. Anqi Zhang, Dr. Songtao Du, Dr. Lang Zhou, Dr. Yuzhe Liu, Dr. Liangxi Li, Dr. Hossein Talebinezhad, Dr. Yang Tong, Dr. Yuanyuan Zhang, and Dr. Xingxing Zhang. They help me a lot in my early years in Auburn. And appreciate my colleagues Dr. Pu Deng, Dr. Xin Sha, Jun Chen, Dr. Jianguo Xi,

Haotian Wu, Wen Yang, Jiacheng He, Jiachen Liu, Jindong Wei. Thanks for your help and companions on the journey.

Finally, I would like to show a special thanks to my parents, Shaoyin Sun and Runfeng Zhang. Your unconditional love and support give me the courage to go through all the difficulties.

Table of Contents

List of Figures

List of Tables

List of Abbreviations

AMF	Alternating Magnetic Field
AR	Aspect Ratio
BIBB	2-Bromoisobutyryl Bromide
BTZ	Bortezomib
CMC	Critical Micelle Concentration
DA	Dopamine
DDS	Drug Delivery System
DI	Deionized
DLS	Dynamic Light Scattering
DOPE	1,2-Dioleoyl-Sn-Glycero-3-Phosphoethanolamine
ECM	Extracellular Matrix
EPR	Enhanced Permeability And Retention
FON	Fluorescent Nanoparticles
FTIR	Fourier Transform Infrared Spectroscopy
GSH	Glutathione
H_3BTC	Benzene-1,3,5-Tricarboxylic Acid
HA	Hyaluronic Acid
HCl	Hydrochloride Acid
HF	Hydrofluoric Acid
HNT	Halloysite Nanotubes
IFP	Interstitial Fluid Pressure
IR	Infrared Ray
LD_{50}	Median Lethal Dose
LSPR	Localized Surface Plasmon Resonance
MOF	Metal-Organic Frameworks
mPEG	Polyethylene glycol methyl ether
MPS	Mononuclear Phagocyte System
MRI	Magnetic Resonance Imaging
MSN	Mesoporous Silica Nanoparticles
MTT	(3-(4,5-Dimethylthiazol-2-Yl)-2,5-Diphenyltetrazolium Bromide
M_w	Molecular Weight
NIR	Near-Infrared
OEGMEMA	Oligo Ethylene Glycol Methyl Ether Methacrylate
PAI	Photoacoustic Imaging
PCL	Polycarprolactone

PDA	Polydopamine
PDA-HNT	Polydopamine Coated Halloysite Nanotube
PDA-NS	Polydopamine Nanosphere
PDA-NT	Polydopamine Nanotube
PDT	Photodynamic Therapy
PEG	Polyethylene Glycol
PEG-NH_2	Amine-Terminated Methoxy-Poly(Ethylene Glycol)
PEG-PDA-HNT	Pegylated Polydopamine Coated Halloysite Nanotube
PEG-PDA-NS	Pegylated Polydopamine Nanosphere
PEG-PDA-NT	Pegylated Polydopamine Nanotube
PEI	Polyethyleneimine
PET	Positron Emission Tomography
PLGA	Poly(Lactic-Co-Glycolic Acid)
PNIPAM	Poly(N-Isopropylacrylamide)
PS	Polystyrene
PTFE	Polycarbonate
rGO	Reduced Graphene Oxide
ROS	Reactive Oxygen Species
SD	Standard Deviation
SI-ATRP	Surface-Initiated Atom Transfer Radical Polymerization
T_1	Longitudinal Relaxation
T_2	Transversal Relaxation
TEM	Transmission Electron Microscopy
TEOS	Tetraethyl Orthosilicate
TGA	Thermogravimetric Analysis
T_m	Melting Point
Tris	Tris(Hydroxymethyl)
US	Ultrasound

Chapter 1

Introduction and Literature Review

Cancer is the second leading cause of death in the United States. In 2017, 24% of deaths were due to cancer. However, people have achieved remarkable progress in the battle with cancers. The concealment of cancer makes the early diagnosis challenging. Furthermore, effective therapies for medium- and terminal-stage patients are still limited.

The difficulties lie in many aspects. The application of conventional anticancer medicines is usually bothered by problems like low water solubility, degradation in the physiological environment, severe adverse effects. Due to the high specificity, bioactivity, sophisticated functions, macromolecule therapeutics have attracted significant attention. However, the vulnerability in structure and activity, high personalization cost, and the larger dimension than small molecular medicines put forward rigor requirements in manufacturing and administration. After the drug is administrated, there are several biological barriers before active ingredients are delivered to the ultimate target. Combined with the reticular network in the liver and spleen, the mononuclear phagocyte system (MPS) can efficiently capture and clear foreign substances. The heterogenicity of the Enhanced permeability and retention (EPR) effect may diminish the medicine delivery to tumors. The increased interstitial fluid pressure and the dense physical barrier composed of collagen and cancer cells also prevent drug delivery in solid tumors' deep core region. Even after the medicine is delivered in cancer cells, the altered intracellular environment, and the antineoplastic resistance may impair its therapeutic activity.

The smart drug delivery nanosystem is a strategy to enhance the delivery efficiency of anticancer medicines. Extensive studies have been conducted to develop such systems, including but not limited to micelles, liposomes, polymeric nanoparticles, mesoporous silica nanoparticles, metal-organic frameworks. Nevertheless, there is still a great distance from clinical application. A nanomaterial with good biocompatibility, facile functionalization approach, responsiveness to stimuli, and accessible excretion or degradation route is still highly desirable. Polydopamine (PDA) is a promising material that can fulfill these requirements. The melanin-like material shows excellent biocompatible properties. The abundant catechol and amino residual groups on the surface make it possible to efficiently attach the chemical groups and magnetic nanoparticles. The material also has an apparent photothermal effect. Furthermore, it has been reported that the PDA could be degraded by reactive oxygen species (ROS), which can be produced during metabolism.

This work focuses on using PDA to fabricate nanoparticles for drug delivery. Three projects are included and stated in chapter 2, 3, and 4. In chapter 2, a template-assisted method to fabricate PDA nanotubes is established. The thickness of the nanotube plays a critical role in the final morphology of the structure. The morphology, chemical composition, and photothermal efficiency of the tubular structure, along with its doxorubicin loading and release performance, are characterized and compared with the conventional polydopamine nanospheres. Next, in chapter 3, given the crucial role of the dopamine concentration in PDA formation, a fabrication method for bowl-like PDA nanocapsules is developed in water/alcohol solution. The prior precipitation of PDA forms the nanocapsules at the interface between alcohol and water. Furthermore, the morphology of the nanocapsules can be changed by varying reaction parameters, including the ratio between alcohol and water, the type of alcohol, and oxygen support. Finally, in chapter 4, further modification of PDA nanotubes was conducted to make it a multifunctional drug delivery

system. During the template-assisted fabrication of nanotubes, the outer layer and inner layer of PDA nanotubes are exposed in different steps, making the separate modification of both layers possible. Therefore, PEGylation and in situ polymerization of thermo-sensitive poly(N-isopropylacrylamide) (PNIPAM) were performed on the outer and inner layers. The Fe_3O_4 nanoparticles were then in situ synthesized to endow magnetic responsiveness to the nanotubes. The nanotubes' loading and release performance to a model agent, methylene blue, was then tested in different conditions, i.e., the different pH, various near-infrared laser power, and the presence of a magnetic field. A multi-linear regression model is then established to predict the release rate.

1.1. Drug Delivery Nanoplatforms

Drug delivery systems can carry therapeutic agents as 1) encapsulated payloads physically confined in a nanocapsule, 2) bound constituents covalently conjugated on nanocarriers, and 3) absorbed molecules stabilized via noncovalent interactions. It is important to note that these classifications are not exclusive; for example, drugs can be present as absorbed species in an encapsulating nanocarrier. For nanocapsules, release occurs via breakage of the membrane or more slowly via diffusion. For conjugated systems, cleavage of the covalent bond releases the active agents. In contrast, desorption, followed by diffusion, is the primary release mechanism for compounds loaded via noncovalent interactions. In this section, we discuss the major classes of materials, the general synthesis and drug loading strategies for each, the material properties that can be leveraged to imbue stimuli-responsive release, along with the advantages and disadvantages for each.

1.1.1. Major Drug Delivery Nanoparticles

1.1.1.1. Polymeric Micelles

Micelles, Figure 1.1, are self-assembled structures formed when the amphiphilic molecules' concentration exceeds the critical micelle concentration (CMC). [10] The core-shell structure of micelles is maintained by a thermodynamic equilibrium resulting from hydrophobic and hydrophilic interactions. Micelles are small in size; hydrodynamic diameters are typically 5 – 100 nm. [11] Due to the mild conditions required, the payload can be encapsulated during micelle synthesis. [12-13] However, stability in physiological environments remains a concern. When the concentration of the amphiphilic molecules that comprise the micelle is lower than the CMC, the micelles will dissociate. When injected into the body, the significant dilution of the micellar system coupled with an increase in the CMC due to changes in temperature, pH, and salinity and other amphiphilic molecules such as plasma proteins can destabilize the micelles and induce the release of the payload. Methods used to stabilize micelles include increasing the length of hydrophobic blocks and reducing the length of hydrophilic blocks.[14-16] These methods can lead to increased micelle size, which is unfavorable for extending the half-life and EPR effect. Unstable micelles are formed if the hydrophilic block is too short.[17] More common methods for stable micelles incorporate covalent crosslinking and enhancing intermolecular interaction (such as optimized topology, $\pi - \pi$ interaction, and host-guest complexation) in the core or shell of micelles.[18-25] When pH,[26-28] redox,[29-32] enzyme,[33] or photo[34] sensitive bonds are used to stabilize the micelle, the corresponding stimuli can cause micelle swelling or dissociation and release of the payload, Figure 1.1 (a-c). Alternatively, processes such as protonation or temperature-induced hydrophobicity changes can weaken intermolecular interactions and destabilize the systems,

Figure 1.1 (d-f). [35-40] Micellar stability can also be impacted by exogenous stimuli such as ultrasound (US), Figure 1.1 (g). [32, 41-47] Drugs can also be conjugated to the amphiphile, usually to the hydrophobic block, via stimuli-responsive bonds, Figure 1.1 (h). [48]

In addition to amphiphilic polymer fabricated micelles, micelles have also been formed from supramolecules. In a supramolecule, noncovalent interactions are used to produce amphiphilic structures. [49-50] In these materials, the hydrophilic and hydrophobic chains

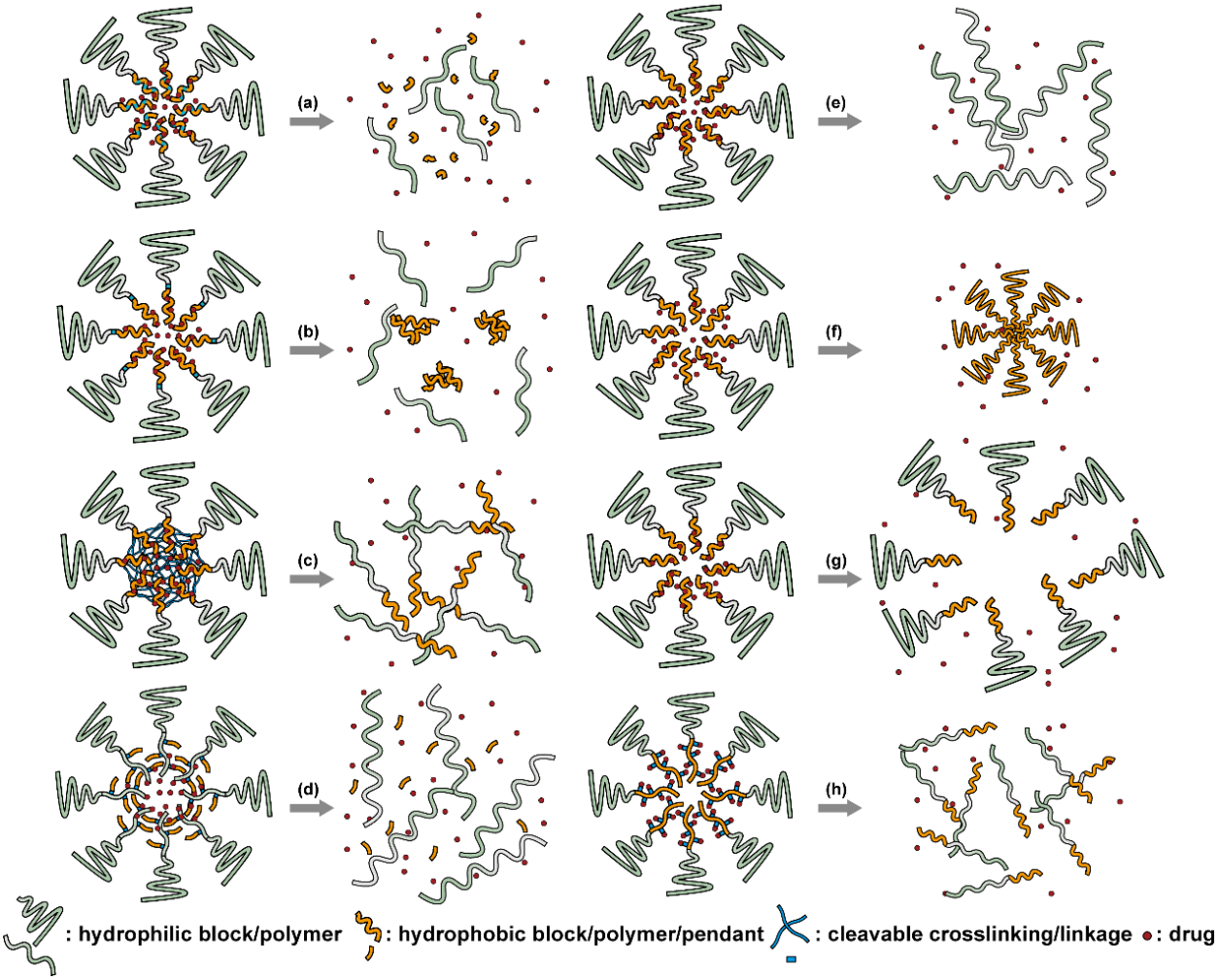

Figure 1.1 Stimuli-responsive strategies for micelle-based DDSs. Cleavable bonds can be used (a) on the hydrophobic backbone, (b) as the hydrophilic-hydrophobic connection, and (c) as crosslinks between amphiphilic molecules. Breaking these bonds results in the breakup of the micelle. Altering the amphiphilic nature of the materials (d) by breaking bonds that connect hydrophobic pendants to moderately hydrophobic blocks, or via stimuli-responsive (e) hydrophobic or (f) hydrophilic blocks results in micelle break up or collapse. (g) Micelles can be disrupted mechanically. (h) Payloads can be covalently bonded to the amphiphilic molecules. Breaking these bonds results in payload release and micellar breakup.

terminate in groups that form strong noncovalent interactions, such as host-guest interactions and electrostatic attraction between ionizable substituents. The amphiphilic structure arises due to conjugation between these groups. [51] Drug loading can be facilely conducted through self-assembly as the micelles are formed. All of the previously mentioned techniques to stabilize micelles and stimulate drug release can be applied to supramolecular micellar structures. [52-55] Specifically, the noncovalent conjugation could be disrupted by temperature elevation, pH-reduction induced protonation, competitive binding, and metal ion chelating in supramolecular-based systems. [56-57] As a result, the drug release is enhanced. As these are relatively new materials, the investigation of toxicity, biodegradability, and pharmacokinetics is limited. The stability of the noncovalent joints also remains a concern, especially in the complicated physiological environment.

1.1.1.2. Liposomes

Liposomes, Figure 1.2, are self-assembled vesicles with bilayer membranes composed of lipids serving as vessel walls. Because they are composed primarily of phospholipids, liposomes tend to be biodegradable and biocompatible. They initiate little to no immunogenic response. The similarity between this structure and that of cell membranes suggests their use in DDSs. Liposome-based DDSs are primarily produced by two methods; hydration of a lipid film and reverse-phase evaporation. In the first method, a lipid-containing solution is dried to form a film, which is then hydrated while being agitated to assemble liposomes.[58-59] In the second process, a lipid solution in an organic solvent is mixed with an aqueous solution to form a lipid-stabilized water-in-oil emulsion. As the organic solvent is evaporated from the system, it transforms into lipid bilayer

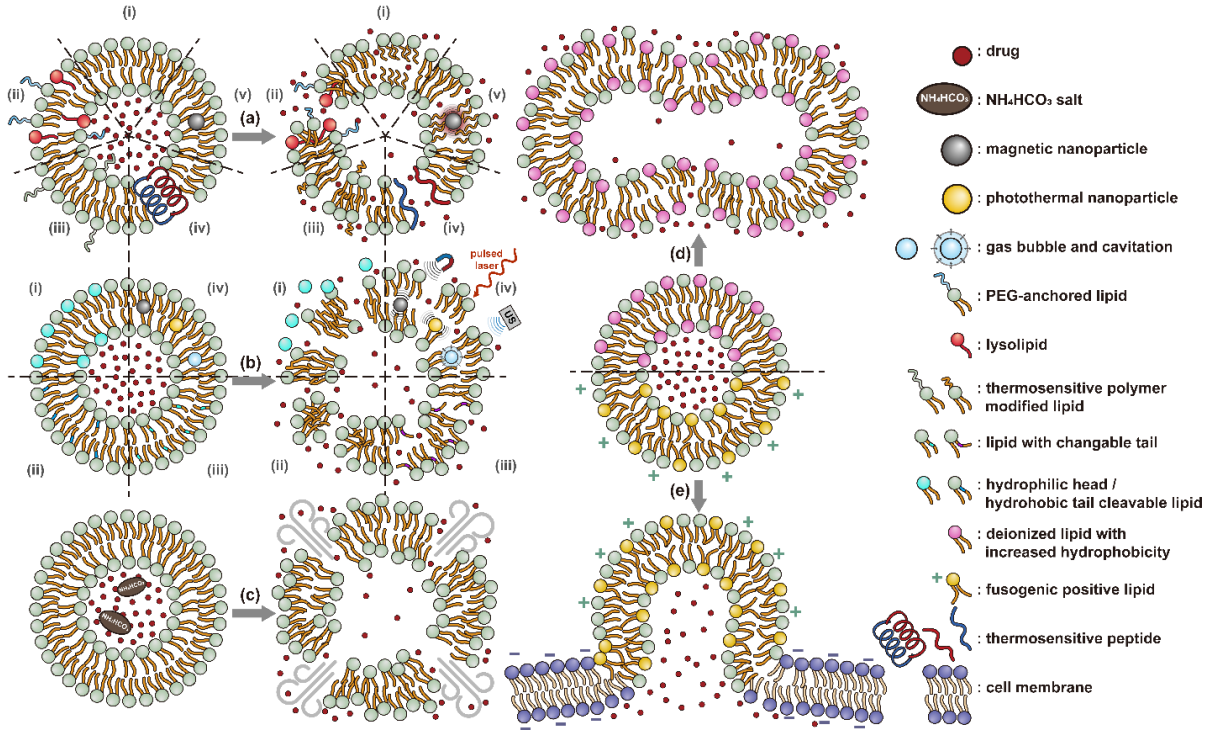

Figure 1.2 Stimuli-responsive strategies of liposomes. (a) Thermally-induced effects such as (i) gel-fluid transitions (melting) in the bilayer, (ii) pore formation, induced and stabilized by lysolipids and PEG-conjugated lipids, (iii) insertion of dehydrated thermoresponsive polymers, (iv) pore formation due to conformational changes of peptides in the lipid membrane, and (v) melting of the bilayer promoted by the heat released from embedded magnetic nanoparticles in an applied AMF all serve to increase the bilayer permeability and initiate release. (b) Destabilization of the lipid packing via (i) cleavage of the connection between the lipophilic tails and hydrophilic head groups, (ii) cleavage of one of the lipophilic tails, (iii) isomerization or oxidation of the lipophilic tail, and (iv) cavitation induced by external agitation (vibration of magnetic nanoparticles in AMF, the photoacoustic effect, and ultrasound-generated cavitation) also initiates release. The release can also be initiated (c) by the disruption caused by gas generated within the liposome and during fusion with other liposomes (d) or cell membranes (e).

vesicles.[60] In either case, the payload can be incorporated into the DDS by dissolving it in the aqueous phase used during liposome production.[61] Drugs can also be loaded after the liposome is formed as long as a suitable chemical potential gradient is established across the lipid bilayer.[62-67] As the payloads diffuse into the liposome core, they react with “trapping” agents already present in the liposome preventing their counter diffusion and leading to their accumulation.[68-70] This technique, known as remote loading, can increase the loading capacity and reduce leakage issues.[71-72] Compared with other DDSs, a unique advantage of liposomes

is the capability to deliver both hydrophilic compounds loaded in the core and hydrophobic compounds loaded in the bilayer. This feature enables the co-delivery of combinational formulations to achieve a synergic effect.[73] However, liposomes' utility for delivering lipophilic or amphiphilic drugs is more limited as they tend to diffuse across the lipid bilayer.[74]

Like micelles, stability is a concern in liposome-based DDSs. Many lipids have a relatively low melting point (T_m), and body temperature increases the membrane's fluidity, enhancing payload leakage.[75] Liposomes also have a relatively short shelf-life due to fusion, aggregation, and drug leakage during storage.[73] Lyophilization can enhance liposome shelf stability and simplifies preparation when administered.[76] However, unsaturated phospholipids are vulnerable to oxidation *in vivo*, leading to the disruption of lipid bilayers.[73] Increasing the amount of saturated phospholipid in the system can mitigate this issue.[73, 77-78] The addition of cholesterol has been found to enhance drug retention and stability and to reduce the rate of opsonization in physiological environments.[79-82] However, too much cholesterol may impair stimuli-responsive behavior. In Gaber et al.'s work, the thermo-responsive behavior was almost eliminated when 30 mol% cholesterol was used.[83] A reduction in liposome aggregation and fusion can be achieved by decorating the outer surface with a protective component such as poly(ethylene glycol) PEG.[84-85] Modification is typically accomplished via incorporating a lipid conjugated with the appropriate protective group during the liposome formation or by modifying the lipids in the outer layer of the bilayer after liposome formation.[86-88] However, in the first technique, some protective lipids may be inserted into the inner bilayer, where it does not reduce liposome aggregation but reduce the payload capacity. The membrane fluidity is also impacted by the incorporation of protective lipids in both techniques. Protective lipid micelles and unprotected liposomes are incubated together at a temperature close to the lipid melting point. Under these

conditions, the protective lipid can spontaneously transfer from the micelle to the outer lipid layer.[89] This method efficiently inserts protective lipids on only the outer layer of the lipid membrane, preserving the membrane fluidity and limiting issues with residual reactive groups associated with chemical modification of the lipids.[86, 90] This technique can also be applied to achieve a wide range of other functional modifications.[88-89, 91]

The instability of liposomes suggests three primary mechanisms for initiating drug release: 1) the creation of pores or cracks in the bilayer to enhance permeability, Figure 1.2 (a), 2) destabilizing the liposome by mechanical disturbance, via chemical degradation, or gas disruption, Figure 1.2 (b and c), and 3) initiating the fusion of the liposome with other liposomes or biological membranes, Figure 1.2 (d and e). When low melt point lipids are used in the formulation, body temperature or local hyperthermia can be sufficient to melt the bilayer.[92-94] As the bilayer transitions from a gel to melt, pores form, significantly increasing the diffusion rates across it. Pore formation can be enhanced by incorporating lysolipids, lipids with thermally responsive polymer groups attached, and the inclusion of peptides in the bilayer. US and alternating magnetic fields (AMF) are commonly used strategies to disrupt liposomes via mechanical agitation.[95-100] When AMF is used, appropriate sensitizers such as iron nanoparticles need to be incorporated into the liposomes. Perfluoropentane emulsions can be encapsulated in liposomes to generate gas under US disrupting the structure.[101-103] Incorporation of lipids that degrade under appropriate pH, redox, enzymatic, or other conditions can also be used to destabilize the bilayer under those conditions.[96, 98, 100, 104-107]

The payload can also be released when liposomes fuse with each other or with biological membranes, Figure 1.2 (d and e).[108-112] Compared with the endocytosis pathway, liposome fusion with the cell wall bypasses the extracellular excretion and endo-lysosomal escape issues

and releases payloads directly into the cytoplasm.[113-115] This process avoids endosomal degradation of the payload, which can be significant for macromolecular biologics.[116-117] A widely accepted mechanism for this behavior, the "flip-flop" of lipids, has been proposed by Szoka's group.[118-119] Several strategies have been demonstrated to improve the fusion efficiency, such as using cationic lipids,[118, 120] utilizing lipids that can adopt non-bilayer phases (like 1,2-dioleoyl-sn-glycero-3-phosphoethanolamine (DOPE)[121]), decorating the cell-penetrating peptides on the surface (like KALA[113] and TAT[122]), including phage fusion proteins,[123] and incorporating aromatic compounds[124] in lipid bilayers. Reshtnyak et al. utilized a fusogenic peptide to enhance liposomes and cell fusion. At low pH, the conformational change of the peptide enhances fusion between liposomes and cells.[125-129] Alternatively, the fusogenic compounds can be deactivated via covalent bonding and reactivated via stimuli-induced cleavage of the bond.[108-112]

1.1.1.3. Polymeric Nanoparticles

Nanoparticles formed from high molecular weight (M_w) polymer can encapsulate therapeutic agents, Figure 1.3. They are typically produced during a polymerization process or via precipitation from polymer solutions.[130] Emulsion or microemulsion polymerization can be used to create solid polymer nanoparticles. However, residual initiator, stabilizer, and catalyst can remain and poses safety concerns. Therefore, precipitation and coacervation techniques are more widely used for biomedical applications. In these processes, the dissolved polymer undergoes precipitation to form solid polymeric nanoparticles, typically adding neutralizing electrolytes or nonsolvent.[131] Polymeric nanoparticles are generally more stable than micelles and liposomes, particularly those based on covalently bonded networks. However, they are usually susceptible to

the rapid formation of a protein corona on their surface that enhances clearance by the immune system.[132] PEGylation of the surface can reduce this issue.

In addition to solid polymeric nanoparticles, hydrogel nanoparticles, also called nanogels, have also been investigated as a nanoparticle-based DDS. Nanogels are composed of networked hydrophilic polymers and can be prepared using similar methods for traditional solid polymer nanoparticles.[133-134] In emulsion-based synthesis, a multifunctional monomer is included to allow the formation of a covalently crosslinked structure. In contrast, for precipitation and coacervation techniques, precursors with functional groups capable of forming physical crosslinks are used. Typically hydrophobic-hydrophobic interactions and electrostatic interactions allow for self-assembly of the hydrogel nanoparticle via precipitation techniques.[133] Generally, the

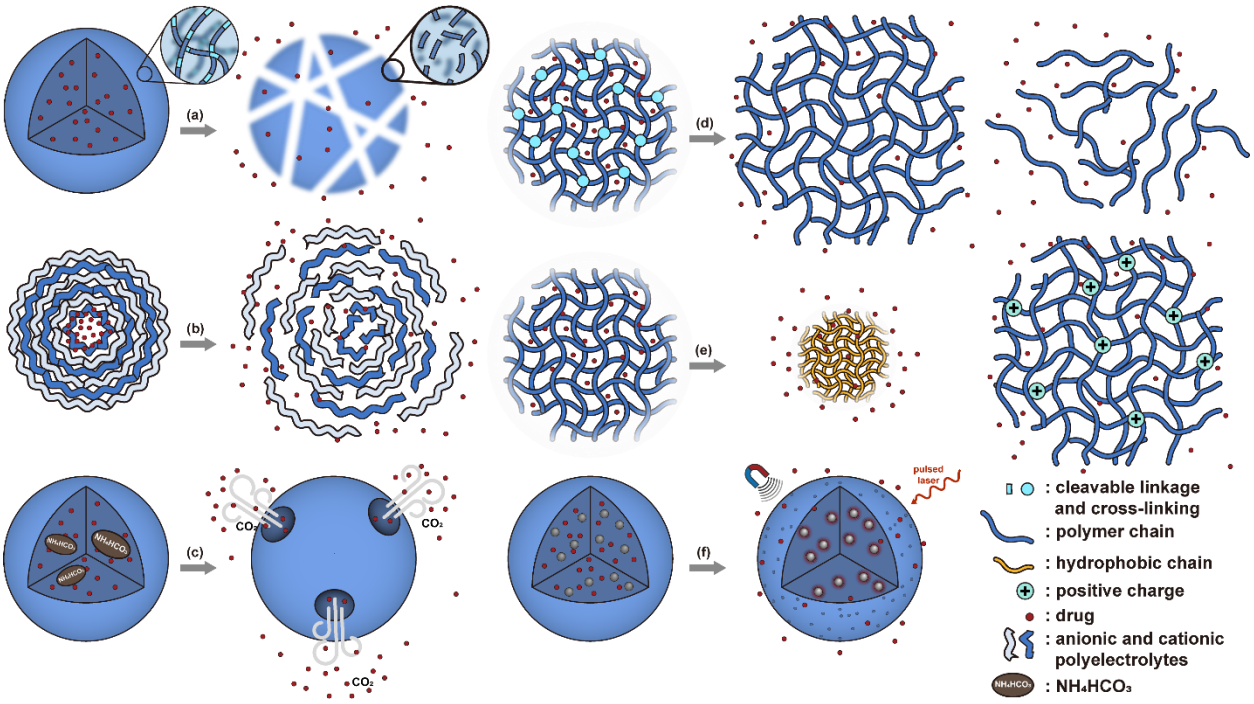

Figure 1.3 Stimuli-responsive strategies for solid polymeric nanoparticles and nanogels. (a) Cleavage of bonds in the polymer chain results in degradation and dissolution. (b) Protonation reduces polyelectrolyte interactions weakening the structure of particles produced via LbL techniques. (c) The decomposition of NH_4HCO_3 produces CO_2 gas rupturing the particle. (d) Cleavage of crosslinkers in nanogel networks results in swelling or dissociation. (e) Temperature elevation results in increased hydrophobicity and shrinkage of a nanogel, while protonation increases hydrophilicity and results in increased swelling. (f) AMF or NIR irradiation can be used to heat and agitate the system increasing payload release.

networks formed via physical crosslinking are not as stable as those formed via covalent crosslinking.

Therapeutics can be loaded into solid polymeric nanoparticles and nanogels via two approaches, incorporation during nanoparticle production and adsorption.[135-137] One advantage over micelles and liposomes is that moisture-sensitive payloads can be loaded from nonaqueous phases during the synthesis of polymeric nanoparticles, protecting them from degradation during DDS preparation and transport within the body. Further discussion of the principles, preparation and biomedical applications of polymeric nanoparticles and nanogels can be found in several excellent reviews.[138-141]

Conventionally, polymeric nanoparticles have been used for sustained release applications.[142] When biodegradable polymers are used, the release can last for over a month as the polymer hydrolyzes or is enzymatically degraded. [137] When stimuli-responsive groups are used, payload release can be significantly faster. Similar to micelles, breaking cleavable bonds can be used to initiate the disintegration of polymeric nanoparticles and nanogels, Figure 1.3 (a and d). Various stimuli, including pH, [143-144] enzymes, [145-151] redox agents [152-157] and photoirradiation, [158-161] have been used to cleave bonds located on the polymer backbone or crosslinking site. When polyelectrolytes are used, protonation under acidic conditions weakens ionic bonding resulting in the dissolution of nanoparticles and drug release, Figure 1.3 (b).[145, 162-164] For nanogels, protonation- or dehydration-induced osmotic pressure [165-166] and hydrophilicity changes [167-168] can lead to their swelling or collapse and promote drug release, Figure 1.3 (e). Recently, Liu et al. incorporated NH_4HCO_3 in poly(lactic-co-glycolic acid) (PLGA) nanoparticles, Figure 1.3 (c). [169] CO_2 gas was generated with sufficient pressure to rupture the nanoparticle and release the payload under acidic conditions. Finally, remote heating via AMF or

near-infrared (NIR) irradiation can increase the diffusion rates of payload from these systems, Figure 1.3 (f).

1.1.1.4. Inorganic Porous Nanocarriers

Mesoporous silica nanoparticles (MSN)[170] and metal-organic frameworks (MOF), [171] Figure 1.4, are the most studied porous inorganic nanostructures. MSNs are synthesized via the condensation of tetraethyl orthosilicate (TEOS) in the presence of surfactant as templates. [172-173] These nanoparticles have a large surface area and tunable pore size. Issues with biodegradability hinder the development and application of MSN systems. [74] Degradation typically takes several weeks, [174] and nanoparticles can accumulate in organs like the liver and spleen.[175] MSN accumulation due to repeated administration may lead to liver injury. [176] Several strategies have been explored to enhance biodegradability. Shen et al. synthesized large-pore, thin-wall MSNs with a high Q^3/Q^4 silicon ratio (the ratio of silicon in $(HO)Si(OSi)_3$ versus in $Si(OSi)_4$).[177] These materials exhibited higher proton mobility in mesopore channels and can be degraded entirely in 24 hours in simulated body fluid.[178] MSN degradation can also be accelerated by incorporating biodegradable[179-188] or water-soluble components.[189] Pores can be blocked by gatekeepers to minimize premature release. Three gatekeeper strategies have been developed: 1) nanoparticles attached to the pore openings via covalent bonds,[190-192] 2) organic molecules, usually having a large dimension like β-cyclodextrin and pillararene, anchored at pores via covalent bonding or noncovalent interactions,[172, 193-199] and 3) membranes surrounding the MSN.[200-202] Systems that use temperature changes,[194] magnetic fields,[203] ultrasound,[204] photoirradiation,[201] pH changes,[192, 196] redox agents,[190-191, 197, 200] and enzymes[195, 198, 202] to break the bonds attaching the gatekeeper or to disrupt the

membrane have been developed, Figure 1.4 (a-c). Silica shells can also be degraded or mechanically disrupted to release payload encapsulated Figure 1.4 (d).[188, 203]

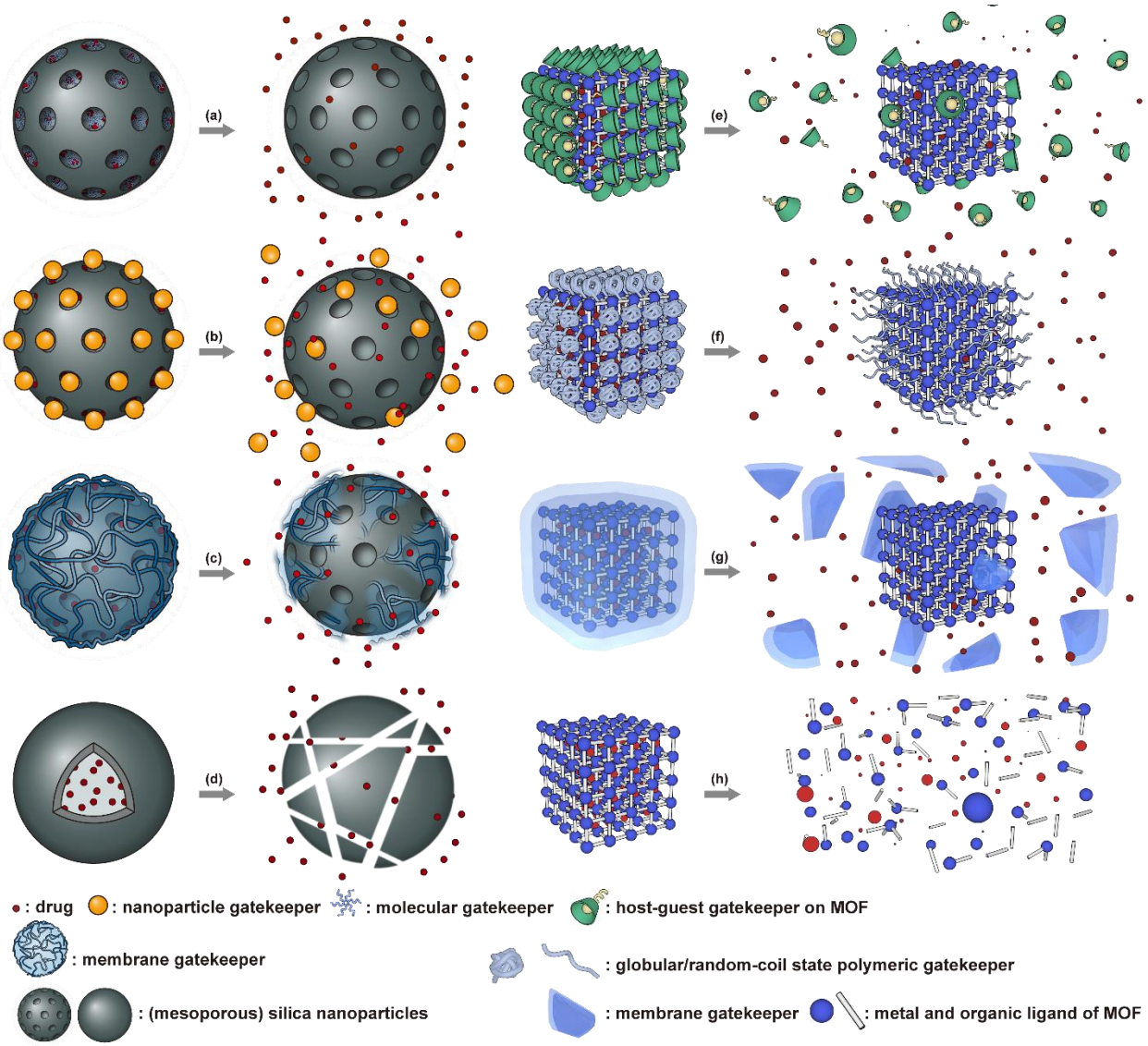

Figure 1.4 Stimuli-responsive strategies for inorganic nanoparticles. Molecular (a) or nanoparticle (b) based gatekeepers can be used to block the pores in MSN based DDSs. Gatekeepers based on supramolecular host-guest interactions (e) and polymers with a collapsed morphology are used on MOF based DDSs. Polymer shells can serve as a gatekeeper for both systems (c) and (g). Removal or disruption of the gatekeepers enabling the diffusion of the payload from the pores. The MSN (d) or MOF (h) structure can also be disrupted, releasing the payload.

MOF is an emerging hybrid nanostructure synthesized by the coordination of metal ions and organic ligands.[171] These systems have a highly ordered and tunable porous structure endowing them with a large surface area for drug adsorption.[205-206] Drugs can be incorporated

during[207] or after synthesis.[208-209] Payload release can be controlled via gatekeepers similarly to the approaches used for MSNs, Figure 1.4 (e and f). Stimuli such as pH,[57, 170-171] glutathione (GSH),[170] salinity,[56-57, 210] temperature changes,[57, 210] photoirradiation,[211] and AMF[212] have all been studied to trigger the detachment of gatekeepers from MOFs. Membrane gatekeepers have also been explored for MOF systems, Figure 1.4 (g). Payload release can also be stimulated by disrupting the MOF structure through weakening the metal ion-ligand interactions that hold the system together, Figure 1.4 (h). Techniques that use pH labile bonds, [213-216] redox-cleavable ligands, [217-219] and azobenzene-bearing organic ligands [220] have been explored. This approach has been extended to the systems that use drug, [221] prodrug, [222-223] or another therapeutic agent (photothermal, [224] photodynamic, [225] or imaging [226]) as the organic ligands in the MOF structure. They eliminate the need for a gatekeeper, and any stimulus that disrupts the ligand metal coordination acts to release the drug from the MOF.

1.1.1.5. Systems not based on encapsulation

In some systems, the drug is not encapsulated but is adsorbed to the nanoparticles, typically to the surface, via noncovalent interactions or covalent linkages, Figure 1.5. The payload is released as the adsorption equilibrium is shifted by stimuli such as protonation[227] or temperature elevation,[3] Figure 1.5 (a). Mechanical disruption has also been used to drive desorption, Figure 1.5 (b).[212] Payloads attached by covalent links are released with the bonds are broken by stimuli such as pH,[12, 228] redox reactions,[48, 229-230] enzymatic attack,[231-232] and photoirradiation,[233] Figure 1.5 (c). Systems based on covalent bonding can avoid premature release and achieve high-fraction release at the target site.[48, 155, 234-235] However, the design

of DDSs based on covalent bonding introduces the additional requirement that complementary conjugatable groups be present on the payload and the DDS.[74]

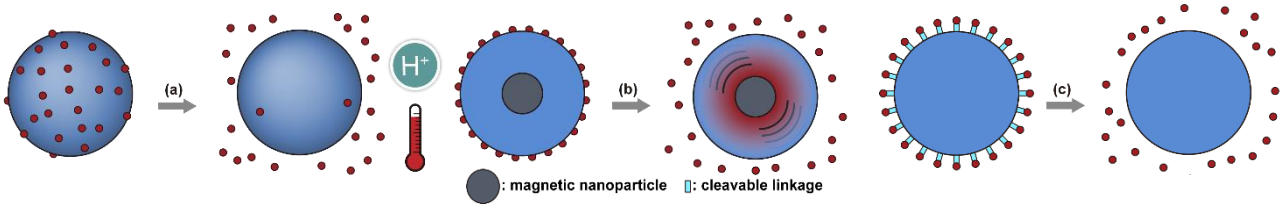

Figure 1.5 Stimuli-responsive strategies for other particles. (a) Payload adsorbed to the surface of DDSs can be released when adsorption equilibrium shifts due to increased temperature or pH changes. (b) The release can also be stimulated by mechanical agitation via AMF. (c) For systems utilizing covalent bonding, release occurs after bond cleavage, for example, hydrolysis, enzymatic cleavage, and redox reactions.

Therapeutic agents have been loaded onto inorganic nanoparticles via noncovalent interactions, such as noble metals, [236-239] carbon-based nanomaterials, [240] black phosphorus [227, 241] and boron nanosheets. [242] The adsorption approach has been evaluated for organic systems as well, like dendrimers[240-242] and polydopamine nanoparticles. [3, 243-244] One major issue with DDSs based on adsorption is that adsorbing the drug via noncovalent interactions leaves the drug exposed to the physiological environment and susceptible to degradation or premature release, particularly in the case of solid nanoparticles where loading only occurs on the outer surface.

Covalently bonding reduces premature release and has been used to attach payloads to the surface of organic nanoparticles such as dendrimers [240, 245-247] and polymeric nanoparticles. [248-249] Covalent bonding has also been used to prepare prodrug conjugates bonding therapeutic agents to free polymer or proteins. [233, 250-253] The small size of these prodrugs, typically less than 10 nm in diameter, endows them with long circulation half-life and enhances their extravasation via the EPR effect. [74] However, the drug remains exposed to the physiological environment where it is subject to degradation. Conjugating the payload to polymer chains in a

nanogel [155, 235, 254-255] or micelles [48, 229-230, 256-258] reduces premature release and protects the payloads from physiological environments.

Table 1.1 Summary of advantages and limitations of the various DDS platforms

DDS	Advantages	Limitations
Polymeric micelles	• Simple synthesis and loading approach • Small size (10-100 nm)	• Stability when diluted and interacting with the complicated physiological environment
Liposomes	• Both hydrophilic and hydrophobic payloads • Capable of fusing with membranes enabling endosomal escape	• Stability a concern due to the self-aggregation phenomenon
Polymeric nanoparticles	• Better stability than colloidal structures. • Simple routes to non-spherical shapes • Suitable for moisture-sensitive payloads	• Requires surface modification to avoid clearance (solid nanoparticles) • Relatively high rigidity (solid nanoparticles) • Drug leakage (nanogels)
Inorganic nanoparticles	• Good stability • Good control of drug release with gatekeepers • Facile control of particle dimensions and pore size • Large surface area	• High rigidity • Poor biodegradability (especially for MSN) • Degradation products raise safety concerns • Stability (acid-sensitive MOF)
Non-encapsulated systems	• Low drug leakage (drug conjugates) • Small size (drug conjugates)	• Payloads exposed to the physiological environment • Premature release (adsorption system) • Requirement of a specific group (drug conjugates)

1.1.2. Targeting Drug Delivery

1.1.2.1. Passive Targeting

Tumor tissue is substantially different from normal tissues, Figure 1.6, where the endothelial cells are orderly and compactly arranged. In contrast, the microvasculature in tumor tissue contains enlarged endothelial gaps, and the membrane separating the vessels from the tumor is discontinuous.[259] This morphology results in numerous “openings” in the vessel walls of

tumors rendering them leaky. In typical vasculature, the gaps in the endothelial cells are 5 – 10 nm. Those in tumor vasculature are typically 100 – 780 nm, enabling more oxygen and nutrients to reach the tumor resulting in rapid growth.[74, 260] On the other hand, the dysfunction of the lymphatic drainage system reduces the clearance of therapeutics from the tumor tissue.[261] The combination of enhanced extravasation from the capillaries and reduced clearance via the lymphatic system is known as the enhanced permeability and retention (EPR) effect, which results in the accumulation of macromolecules and nanoparticles in tumors. [262-263] Passive targeting uses this effect by carefully controlling the dimension of the DDS. If it is too small, the DDS can be rapidly cleared through the kidney. If it is too large, it is difficult for the DDS to extravasate into the tumor tissue. It is generally accepted that 30-200 nm in diameter is the appropriate dimension for DDSs to exploit the EPR effect.[264] However, the heterogeneity of tumors means that the proper DDS size may vary significantly between patients and tumor types;[265-267] large differences are seen even within a single tumor.[268] Even a 10 nm difference from the optimal size can result in a distinct reduction of internalization efficiency.[269] Therefore, determining the size required to optimize therapeutic efficacy in an individual patient is critical and requires a trial-and-error approach. Another issue is whether the EPR effect exists and can be utilized on metastatic tumors.[270-272] Finally, it is essential to note that non-cancerous pathological sites such as those associated with inflammations can exhibit the EPR effect as well. The accumulation of DDSs carrying antineoplastic compounds in those tissues is undesired.[273-274]

While the EPR effect is enabled by the unique structure of vasculature in tumors, other characteristics of tumor tissue counteract this approach. The most significant is that many tumors have an increased interstitial fluid pressure (IFP), impeding mass transport deeper into the tumor.[275] The IFP in some tumors is sufficient to push cancer cells and growth factors out into

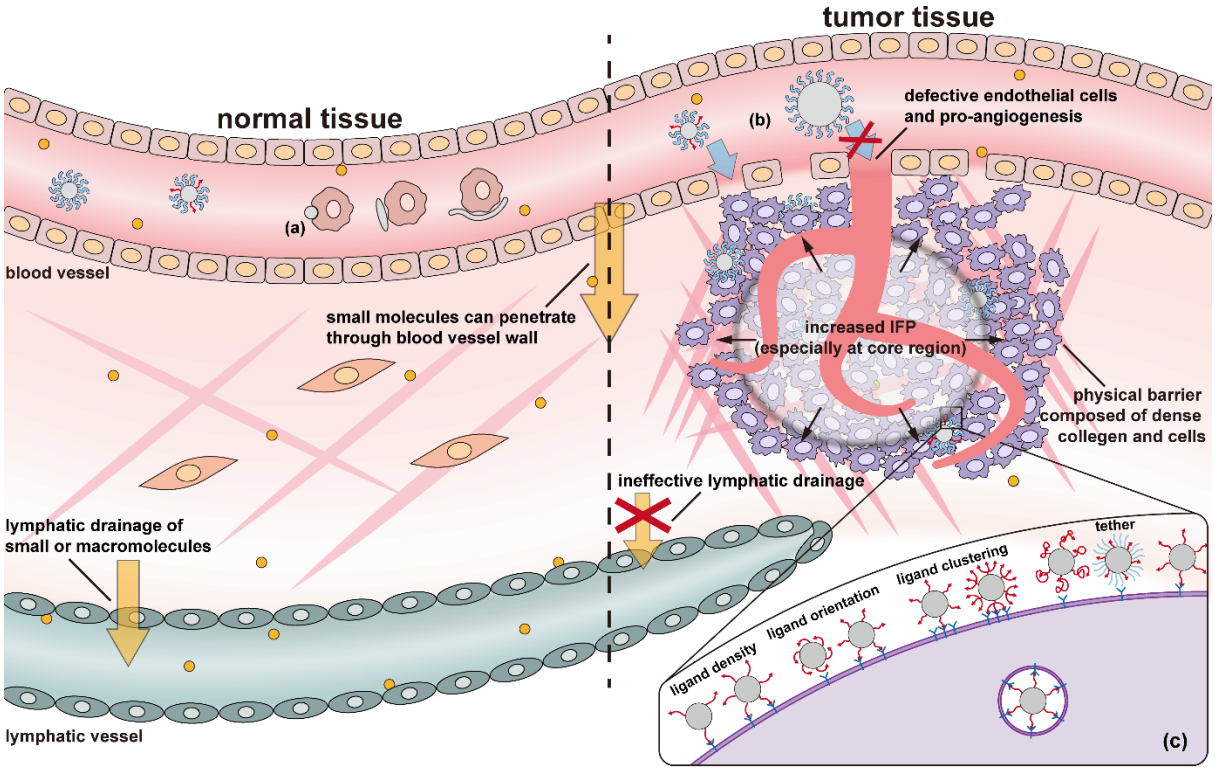

Figure 1.6 Schematic illustration for critical differences between normal and tumor tissues. Lymphatic drainage of small molecules is reduced in tumor tissues, tumor vasculature has different porosity due to defective endothelial cells and pro-angiogenesis, tumors typically have an increased interstitial fluid pressure, and the dense collagen and cellular network forms a physical barrier within the tumor. Physicochemical factors affecting targeting include size, shape, flexibility, and surface properties. (a) Nanoparticles without proper stealthy decoration may be rapidly recognized and cleared through phagocytosis, while anisotropic or flexible nanoparticles are more likely to avoid phagocytosis. (b) Nanoparticles that are too large cannot enter the tumor from the vasculature despite its enhanced permeability. (c) Ligand density, orientation, clustering, and tethers all affect ligand-mediated endocytosis.

surrounding tissue, facilitating tumor progression.[276] Similarly, IFP can reduce the amount of drug delivered to the target cells and increase systemic toxicity by pushing therapeutics into surrounding tissues.[277-278] Often, the pressure gradient rises as the tumor core is approached, making deep tumor penetration difficult. [264, 275] Other anatomical and physiological barriers, composed of several cell layers and a dense extracellular matrix (ECM), limit DDS's ability to reach cancer cells in the tumor.[276] Therapeutic agents can be included in the DDS formulation to alleviate these issues, such as nitric oxide, histamine, TNF-α, vascular endothelial permeability factor (VEGF). These agents can lower IFP, improve vascular permeability, and enhance

extravasation.[268, 270, 279-281] Also, tumor ECM can be degraded by hyaluronidase, enhancing the ability of DDSs to reach the cancer cells.[280] Finally, a combination of TGF-β inhibitor, ECM degradation enzymes, and the hormone relaxin can be used to reduce fibrosis and normalize ECM.[282-284] While a full discussion is beyond the scope of this review, Attia et al. and Narum et al. have prepared excellent reviews of these techniques.[285-286]

1.1.2.2. Active Targeting

Advances in molecular biology have revealed multiple ligands capable of binding to the receptors. These receptors are overexpressed on cancer cells or by the periphery endothelial cells bounding the tumor. [287-288] Examples of ligands include large mono antibodies,[233] small molecules such as folate and SV119,[197, 289] glycoproteins that can induce receptor-mediated endocytosis, [290] oligosaccharides, [164] peptides, [198] and nucleic acid aptamers.[291] Extensive targeting studies have revealed a myriad of targeting ligands to deliver therapeutics to heterogeneous tumor types. [264] The binding between these targeting ligands and the corresponding receptors is via noncovalent interactions, such as electrostatic forces, hydrogen bonds, and Van der Waals forces. Multiple studies have demonstrated the enhanced cellular uptake and tumor accumulation with target ligands decorated on a DDS surface. [38, 170, 202, 292-298] The strong affinity between ligands and receptors can promote the accumulation of nanocarriers in tumors, essentially enhancing the EPR effect.[19, 299-300] Furthermore, ligand-target binding can facilitate cellular internalization of DDS, which also benefits the delivery. [301-302] The technique can target angiogenic endothelial cells as well, which can destroy the tumor vasculature and deprive the tumor of oxygen and nutrients. Chase et al. presented an in-depth overview of this strategy.[303]

A few factors are critical in promoting cellular uptake via ligand binding, Figure 1.6 (c), e.g., the strength of the binding interactions, the density of the ligand coverage on the particle surface, and the orientation and distribution of the ligands on the DDS surface. A brief synopsis of the typical cellular internalization process is provided here to elucidate these effects. According to Nel et al., ligand-mediated uptake of nanoparticles initiates with the binding of ligands on nanoparticles that diffuse close to the cell surface with their corresponding receptors on the cell membrane.[304] Next, more receptors migrate to the connected region and bind with more ligands. The cell membrane then wraps the nanoparticle and internalizes it. During the process, specific ligand-receptor binding affinity, non-specific nanoparticle-cell membrane affinity, and the formation of a clathrin coat on the developing endosome promote nanoparticle wrapping. The entropic cost of receptor migration to the nanoparticle, cell membrane bending, and diffusion of the nanoparticle away from the cell downregulates endocytosis. Strong binding affinity minimizes the net energy costs of the process, increasing endocytosis. The choice in how the ligand is attached to the DDS also affects performance. According to Wang et al.'s simulation, the compression and stretching of ligand tethers lead to entropy loss, which increases the required energy for internalization.[305] The binding site of the ligand should be readily accessible, i.e., face outwards from the particle surface and not be sterically hindered by other surface groups.[291, 306-307] Ligand density is also critical; in general, higher density promotes endocytosis.[308-309] However, high density can result in multiple ligands competing for each binding site reducing overall binding strength.[310] Once a ligand has bound a receptor, ligands from other nanoparticles are prevented from binding the receptor. Thus, high ligand-density may over-recruit receptors, maximizing the endocytosis of one particle but overall diminishing the cellular internalization of the DDS.[310] When administrated *in vivo*, the clearance effect of ligand density should also be considered. The

high density of target ligands on a surface may diminish the density of a stealth component, like PEG, therefore increasing clearance by the mononuclear phagocyte system (MPS).[308] Finally, some receptors are expressed on cancer cells in clustered patterns, [311-314] and similarly clustered ligands enhance nanoparticle-cell binding.[315] Therefore, ideal ligand decoration should have a relatively high density, proper orientation and distribution, as well as tethers with appropriate length.

Although a tremendous amount of work has been conducted to optimize target ligands, the improvement of using targeting ligands is modest.[316-317] This strategy works best when the DDS is effectively transported to and accumulates in the tumor near the cancer cells. Nevertheless, the decoration of targeting ligands weakens their clearance by MPS inevitably. [316, 318] Thus, it is of interest to endow DDS switchable characteristics, which reduces its clearances by the MPS but enhances its uptake by cancer cells. And some studies have been conducted for this object. [319]

1.1.3. Effects of Nanoparticles' Physicochemical Properties

1.1.3.1. Size

Long circulation time enables individual DDS nanoparticles to have multiple chances to exit the vasculature at the tumor site. Thus, techniques to enhance circulation time can improve EPR based targeting. The clearance of foreign bodies from the bloodstream primarily occurs in the kidneys, the spleen, the liver, and the MPS. Filtering mechanisms in the kidneys, spleen, and liver primarily, but not exclusively, remove foreign bodies based on size. The normal renal function typically clears particles smaller than ~6 nm. For nanocarriers in the 6 – 8 nm range, Longmire et al. reported that clearance depends on size and surface charge.[320] Thus, to avoid clearance by

the kidney, nanocarriers should have a hydrodynamic diameter above 10 nm. However, the nanocarrier dimensions cannot be too large due to the significant physical filtration capacity of the spleen and liver. The tight reticular mesh in the spleen can trap nanocarriers larger than 200 nm, and the liver can effectively capture particles larger than 150 nm. [321-322] Nanoparticles trapped and degraded by hepatocytes are eliminated via biliary excretion. However, this process is slow compared to other clearance mechanisms, and the buildup of nanomaterials in the liver is a concern.[74] In addition to the clearance by the kidney, spleen, and liver, the mononuclear phagocyte system (MPS), which is broadly distributed in the circulatory system and highly concentrated in the liver and spleen, can effectively clear foreign nanoparticles as small as 10 nm.[320] While particles of 10 – 150 nm can avoid clearance by the kidney, spleen, and liver, additional strategies are needed to reduce recognition and clearance by the MPS.

Size can also significantly impact cellular uptake. Regardless of the binding mechanism, whether non-specific or ligand-mediated, the cytoplasmic membrane engulfs a nanoparticle via invagination. Then the particle is encapsulated in an endosome and transported to lysosomes for degradation.[323] After that, endo/lysosome escape strategies are required to deliver medicine to organelles or the nucleus. The readers can refer to several reviews for more detailed information on these issues.[324-325] It is important to understand that endocytosis is size-dependent. A threshold of particle size exists, ~ 5 nm, below which endocytosis does occur.[326] The optimal size for both inorganic and polymeric nanoparticles seems to be in the range of 40 to 60 nm.[327-332] When the size is larger than the optimal size, the endocytosis efficiency is reduced gradually.[333] These effects are related to the energy requirement for membrane bending and the free energy released by the particle adsorbing or binding to the surface. The enhanced cell membrane-nanocarriers affinity can increase the free energy released from adsorption, promote

endocytosis and reduce the threshold size. [333] Furthermore, it should be noted that nanoparticle aggregation may increase the effective size of nanoparticles. For particles smaller than the optimal size, clustering can promote cell uptake. While for particles larger than the optimal size, clustering may block cell uptake. [334]

1.1.3.2. Surface Properties

DDS surface properties, such as charge and hydrophobicity, also impact circulation time by mediating interactions with the MPS system. Generally, the cell membranes are negatively charged. Thus, a higher endocytosis efficiency is expected from positively charged nanoparticles, and one would expect that a negatively charged surface would enhance circulation time. However, while this trend is observed in carefully controlled experiments,[335-338] a noticeable impact is not observed during *in vivo* tests.[339] Because both positive and negatively charged particles attract proteins to the surface that activate the MPS. Hydrophobic surfaces can also enhance the formation of an MPS activating protein corona.[340-342] As a result, a neutral (or weakly negatively charged) hydrophilic surface is favorable for long-term circulation. PEGylation of outer surfaces is the most used mechanism to enhance circulation time. Knop et al. prepared a systematic review of the application of PEG to nanoparticles.[343] They concluded that a short polymer chain (1-5 kDa) and a high surface density effectively extend circulation time. However, a significant immune response can be initiated if a large dose of PEG-coated nanocarriers is used or after repeated dosing.[343] Other drawbacks of PEG decoration include poor degradability and toxic side-products during PEG synthesis and grafting.[343-346] Also, after nanocarriers enter tumors, the hydrophilic PEG-rich surface may block the cellular uptake by cancer cells. The release of payloads in the tumor extracellular matrix may reduce therapeutic efficacy and result in their return

to the blood capillaries via the increased IFP, potentially inducing systemic toxicity.[277] Though alternative synthetic polymers have been explored to replace PEG, most of them do not exhibit equivalent performance nor have in-depth biocompatibility or long-term safety studies of them been performed.[343] In contrast, bio-inspired natural materials, such as polysaccharides, albumin, and red blood cell membrane, can not only extend circulation life but also mediate selective cancer cell uptake of DDS.[347-350]

The effects of surface roughness on cellular internalization are not apparent. Schrade et al. attached 12 nm silica nanoparticles on polystyrene (PS)-based nanoparticles to fabricate rough nanoparticles and reported that uptake by HeLa cells was more significant for the smoother nanoparticles regardless of surface charge.[351] Piloni et al. reported greater uptake by murine macrophages, breast cancer cells, and fibroblasts of smooth nanoparticles than 150nm micelles with 20nm-radius protrusions.[352] In contrast, Niu et al. found that the attachment of 20nm silica particles on smooth 230nm silica nanoparticles enhanced their uptake by breast adenocarcinoma and squamous carcinoma cells regardless of hydrophilicity of particle surface. They attributed this to the enhanced protein aggregation in the void spaces between protrusions. Verma et al. explored this behavior by preparing "rough" surfaces on gold nanoparticles.[353] They report that nanoparticles with randomly distributed "pits" exhibited moderately enhanced uptake by mouse dendritic cells versus smooth nanoparticles. While nanoparticles with a striated surface, prepared with alternating regions of anionic and hydrophobic groups, exhibited the highest uptake rate. Overall, the effect of surface roughness on cellular uptake is still in dispute. Part of the reason may be the different experimental conditions, material compositions, and size ranges explored.

1.1.3.3. Shape

The shape also influences cellular uptake, circulation time, and EPR based accumulation in tumor sites. High aspect ratio (AR) particles exhibit different cellular uptake than isotropic particles. The results on cellular uptake seem contradictory: some studies indicate higher uptake for high AR nanoparticles, [234, 354-355] while others suggest a higher uptake for spherical particles. [356-357] Other nonspherical particles like nanodiscs and nanocubes have also been explored. Endocytosis simulations of these shapes show that the internalization efficiency was reduced as the energy required by the cytoplasmic membrane for nanoparticle wrapping increased.[358] Wrapping a nanodisk has the highest energy cost, followed by nanorods, nanocubes, and nanospheres. Some experimental observations agree with simulations and indicate that nonspherical shapes exhibited lower endocytosis rates.[328, 359-360] However, in other studies, nonspherical nanoparticles exhibit enhanced endocytosis.[361-362] Mitragotri et al. suggested that internalization initiation depends on the local dimension of the nanoparticle in contact with the cells.[363-364] Generally, the smaller the local dimension, the more likely the process is initiated. They evaluated several geometries and found significantly lower phagocytosis rates for wormlike nanoparticles of polystyrene than for nanospheres.[357] Both particles had the same volume, but the aspect ratio of the wormlike particles was greater than 20. Geng et al. found that wormlike micelles also exhibited a prolonged circulation time, up to 5 days.[365] They attributed these results to macrophage capture being overcome by the large hydrodynamic forces these particles experience. They also noted that this long circulation life was reduced when they added crosslinks, suggesting stiffness is a factor in the behavior. Several studies have reported lower internalization for high AR nanoparticles in tumors, where hydrodynamic forces are minimized compared to the circulatory system. [366-368] Interestingly, the opposite result has been reported for particles decorated with target ligands, for which high AR nanoparticles exhibit more

internalization than their spherical cousins.[355, 369-370] This contrast is attributed to more ligands available on high AR nanoparticles, allowing multivalent binding of nanoparticles to cells. The effect of AR on tumor site accumulation via the EPR effect seems clearer. Several *in vivo* studies have demonstrated higher accumulation in tumors and reduced liver capture for high AR nanoparticles.[356, 371-372] While high AR nanoparticles seem to accumulate in the lung and spleen more frequently.[234, 373] Overall, more work is still needed to address the effect of anisotropic DDS on cellular uptake, circulation and tumor accumulation.

1.1.3.4. Stiffness

As a flexible, "soft" nanoparticle interacts with a cell membrane, it can spread on the membrane enabling more binding at the interface. This effect suggests that low modulus nanoparticles may promote the initiation of endocytosis and reduce the threshold size for endocytosis. On the other hand, as the cell membrane wraps the nanoparticle, "soft" nanoparticles can deform into cone-like shapes with a relatively sharp tip and curved cap, followed by an ellipsoidal shape oriented perpendicular to the cell membrane. These deformations require additional energy and deformation of the cell membrane to wrap the nanoparticle and complete endocytosis. As a result, softer nanoparticles undergo slower endocytosis than stiffer ones. Both effects were observed in the simulations developed by Yi et al. [374-375] and Shen et al., [376] where the endocytosis of flexible nanoparticles initiated earlier but completed later than the process of more rigid particles. Shen et al.'s simulation also suggested that the smaller the nanoparticle and the lower the affinity between the nanoparticle and cell membrane, the more significant effect the stiffness exhibits during endocytosis. Experimental studies are somewhat contradictory, with some reporting faster endocytosis for softer nanoparticles.[377-379] In contrast,

others suggest stiffer particles are more readily internalized, [380] and Banquy et al. reported that the nanoparticles with an intermediate Young's modules exhibited the highest uptake efficiency.[381] It should be noted that the stiffness ranges tested in these studies are different, and there is evidence that other properties modify the effect of stiffness on cellular uptake. Banquy et al. suggest that stiffness and size are interrelated, i.e., the stiffness effect on larger particles is not as significant as on smaller particles. [381] The interaction effect between shape and stiffness on endocytosis for different cells was explored by Alexander et al. [362] They found cellular uptake to be highly dependent on flow conditions, shape, rigidity, and cell lines.They also demonstrated that clearance via the MPS was reduced for soft nanoparticles. Soft nanoparticles can also more easily penetrate capillary walls during circulation, [362, 382] suggesting that soft DDSs could better take advantage of the EPR effect. Enhanced tumor accumulation and reduced clearance by the MPS system of soft DDSs have also been demonstrated *in vivo*.[383-385]

1.2. Polydopamine as a Drug Delivery Material

Various biocompatible and degradable polymers have been explored for drug delivery to alleviate undesirable effects and improve the performance of chemotherapeutics. Polyesters, such as polylactic acid (PLA), poly (lactic-*co*-glycolic acid) (PLGA), polycaprolactones (PCL), are the earliest and most studied degradable polymers. Since then, lots of degradable polymers have been developed. In 2007, inspired by the adhesive versatility of protein (Mefp5) secreted by the mussel, Messersmith et al. used dopamine to synthesize a polymer termed polydopamine. Due to the richness of two crucial functional groups (catechol and amine groups) found in the protein, PDA also shows superior adhesive properties to nearly all kinds of materials.[386] Simply immersing substrates in a dopamine solution with a basic environment (2 mg of dopamine per 1 ml of 10 mM

tris buffer, pH 8.5), a PDA film could be spontaneously synthesized. Also, because of these two groups, functionality and modification could be easily accomplished based on PDA. Therefore, PDA has been a promising DDS material, for which the ample functional groups and facile synthesis approach are favored.[387]

1.2.1.1. Biocompatibility and Biodegradability

As a material to be injected into a human body, biocompatibility and biodegradability are the fundamental requirements. Dopamine is an important chemical, which involved in many biological processes. However, a high concentration of dopamine is hazardous. Superfluous H_2O_2 could be produced when there is too much dopamine. As a result, cytotoxicity can be generated from H_2O_2.[388] Nevertheless, the activity of dopamine is much weakened after polymerization. Furthermore, with a similar chemical construction as natural melanin distributed widely in the body, PDA is expected to show good biocompatibility and be biodegradable in the human body without inflammation or other side effects caused by foreign substances.

Many studies have investigated the cytotoxicity of PDA. Almar, et al. initially did the (3-(4,5-dimethylthiazol-2-yl)-2,5-diphenyltetrazolium bromide (MTT) assay on PDA capsules.[389] After incubation of LIM1215 cell (a colon carcinoma cell from the human colon) in PDA capsules, the presence of PDA was found to have negligible effects on cell proliferation. Then Ku, et al. tested the surface modified by PDA with mammalian cells.[390] The surface coated by a thin layer of PDA showed several folds increase in cell viability. Furthermore, these coated layers were observed to promote the general cell adhesion process substantially. Similarly, Luo's group also observed the promotion of cell adhesion and proliferation on PDA-coated surfaces.[391] Moreover,

Lu's group assessed the cytotoxicity of PDA via mouse 4T1 breast cancer cells. The results turned out that even the PDA dose is as high as 1.2 mg/ml, the cell viability remains around 90%.[2]

However, non-cytotoxicity cannot guarantee the reliability of application in vivo. Liu, et al. tested the biocompatibility of PDA nanospheres in vivo.[2] By injecting these nanospheres into mice intravenously, the long-term biocompatibility of PDA was evaluated using five hepatic indicators: alkaline phosphatase, alanine transaminase, aspartate transaminase, total protein, and albumin/globin ratio. The results turn out that after one month of injection, all indicators fell into normal ranges without sign of liver injury. In the same study, they tested the blood of mice injected with PDA nanospheres. The blood parameters were compared before and after one month of injection. However, no noticeable difference was presented. Furthermore, in the histological analysis of the mice's organs, no tissue damage was found, which indicated excellent biocompatibility of PDA.

As an indicator of toxicity, the median lethal dose (LD_{50}) of dopamine was measured. After polymerization, the LD_{50} of PDA is as high as 483.95 mg/kg, which is almost double that for aspirin and cola.[392] In addition, the preliminary studies found out that after PDA nanoparticle injection, the treated animals did not show abnormalities in their activities like breathing, drinking, eating, moving, urination, exploring, and neurological status.[387]

Other than acute toxicity, long-term influence and a metabolic pathway should also be considered. An ideal nanocarrier should be completely metabolized or degraded without releasing any toxic substance. Though there is no systemic evaluation of the biodegradability of PDA, there are studies about melanin, which has similar structures and properties as PDA. Melanin is a natural chemical widely distributed in animals, plants, and even microorganisms. It could be degraded through a normal metabolism pathway.[393-394] And the biodegradability of melanin implants

was proved by Langar's group. In 8 weeks, the implants were completely degraded in vivo.[395] Furthermore, degradation of PDA in the presence of hydrogen peroxide was observed in two studies.[2, 396] Given that the chemical could be generated by an oxidase widely distributed in phagocytes and organs, theoretically, PDA is biodegradable.[397]

1.2.1.2. Responsive Properties of PDA

Two PDA features make it an appropriate material for control release: high photothermal conversion efficiency (~40 %) and alteration of zeta potential as pH change. [2, 398] The photothermal effect could raise the temperature under NIR and trigger drug release via approaches introduced before. Additionally, the change of zeta potential can be used as a response to pH change in tumors.

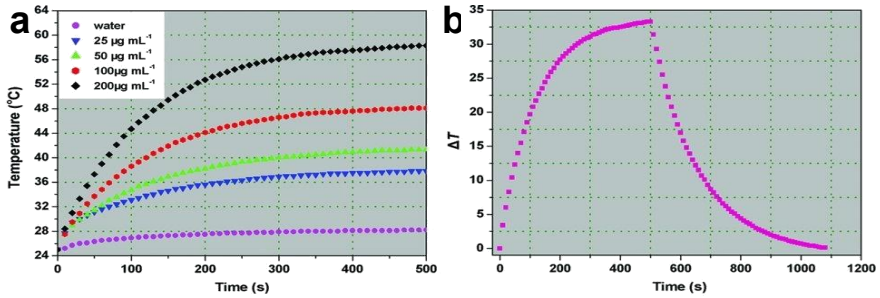

Figure 1.7 Photothermal performance of PDA-NS.(a) Temperature elevation of water and PDA nanoparticles aqueous solutions with different concentrations as a function of irradiation time. (b) The photothermal response of PDA nanoparticles aqueous solution (200 μg mL^{-1}) for 500 s with a NIR laser (808 nm, 2 W cm^{-2}), after which the laser was shut off. [2]

Liu's group firstly reported the novel photothermal effect of PDA. [2] (Figure 1.7) According to their study, PDA has a higher photothermal conversion efficiency (40%) than Au nanorods (22%). In addition, after IR irradiation, the PDA nanoparticle showed good stability with nearly no change on UV-vis absorption spectrum and under TEM. However, the UV-vis absorption spectrum was remarkably changed for Au nanorods, and their morphology was destroyed. Furthermore, Ding, et al. fabricated unique coiled PDA nanofibers via lipid nanotube as a template.

[399] Compared with the straight nanotubes they fabricated, this coiled nanofiber results in nearly double the temperature raised under infrared irradiation. Their study indicates that with a sophisticated designed structure, the photothermal effect of PDA could be further elevated. Furthermore, the stimulation of NIR can also accelerate drug release. Under the NIR laser, a burst release of drugs was observed in a series of studies. [1, 3-5, 243, 400] In addition, in Na's work, photosensitizer was immobilized on PDA nanoparticles via iron coordination of both chemicals. Such a modification endowed PDA nanoparticle photodynamic therapy (PDT) property, which means under laser

irradiation, reactive oxygen species (ROS) could be generated and coordinate with photo-thermal effect to enhance the therapeutic effect. [401]

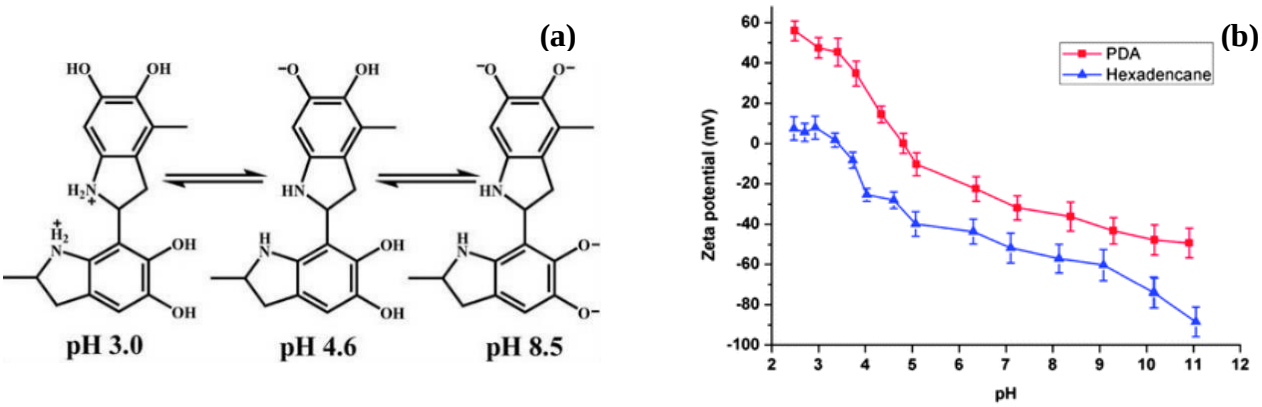

Figure 1.8 States of PDA in different pH conditions. (a) Structure of PDA in different pH [402] (b) Zeta potential of PDA particles and hexadecane oil droplets in water [403]

The other attractive property of PDA is the pH-responsive release of charged molecules. The pH value drops from around 7.4 to 5.5 as nanoparticles are delivered from blood to lysosomes of cancer cells. At the acidic condition, the protonation of amino and hydroxyl groups on catechol could raise the zeta-potential of PDA, Figure 1.8 (b). Zhou et al. prepared an electrochemical interface using this property to govern ion permeability. [404] By immersing the PDA membrane in different pH conditions, the ionization states of the amine groups and phenolic hydroxyl groups on PDA made the membrane present different charge states. As a result, the permeability of cations

and anions can be altered. Their further study manifested the PDA capability to selectively adsorb and release methyl orange (cationic in acid) and rhodamine 6G (anionic in base) in different pH conditions. [402]

By measuring the zeta potential value of PDA under different conditions, it was demonstrated that PDA charged from negatively to nearly neutrally from pH 7.4 to 5. [403, 405] In Wang et al.'s study, more DOX was released from PDA-modified Au nanoparticles in acidic condition (pH 5) than neutral condition (pH 7.4). [406] Then some other studies further demonstrate the possibility of directly using PDA for pH-responsive drug release. [3, 400] All these features make PDA a promising pH-responsive material.

1.2.1.3. Modification of PDA

1.2.1.3.1. Michael addition and Schiff base reaction for catechol and amino groups

Other than the superior properties as a biomedical material, the abundant catechol and amino groups on PDA make it possible to further modify the material. Functional groups and targeting ligand could be simply grafted on PDA via Michael addition or Schiff base reaction under alkaline conditions, Figure 1.9.

Unlike some reactions requiring harsh conditions, this modification can be easily conducted at room temperature in a mild aqueous condition (~pH 8.5). Messersmith's group did a comprehensive investigation on PDA coating synthesized by self-polymerization. [386] They coated PDA on a series of substrates, involving polymers (PTFE, polycarbonate, and nitrocellulose), metal oxides (SiO_2 and TiO_2), and metals (Cu and Au). Then these PDA coatings were modified with alkanethiol and amine- or thiol- terminated methoxy-poly(ethylene glycol) (mPEG-NH_2 or mPEG-SH) via immersing PDA coating in base solutions of such chemicals. The

following contact angle test indicates the alkanethiol modified surfaces all have a large contact angle, which means they have similar and strong hydrophobicity. While the mPEG-NH_2 or mPEG-SH modified surfaces all had a small contact angle, reflecting the hydrophilic property. For

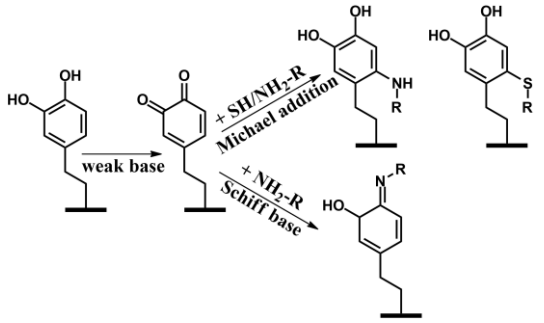

Figure 1.9 Michael addition and Schiff base reaction on PDA

biomedical application, cell adhesion of PDA coatings modified with mPEG-NH_2 and glycosaminoglycan hyaluronic acid (HA) were studied. The results suggest that through conjugation with functional groups, compared with bare substrates, mPEG-NH_2 modified surface has negligible cell adhesion, which is consistent with the stealth effect of PEG. [343, 407-408] While for HA modified surface, the cell adhesion was significantly enhanced. Their further study demonstrates that the method could immobilize biomolecules without influencing their activity. Furthermore, unlike EDC/NHS coupling, the reaction is unaffected by water. [409]

Such a facile method has been widely used in the modification of nanoparticles for drug delivery. For example, lots of researches use amine- or thiol-terminated mPEG to enhance the physiological stability of nanoparticles. [1, 3, 244, 399-400, 406] Besides improving biocompatibility, such a facile reaction can also be used to synthesize hydrogels. Cheng's group synthesized a PDA/PEG hydrogel by the Michael addition reaction between 4-arm-PEG-SH and PDA. [1] The hydrogels show good compatibility. Then during the in vivo assay, the chemo-photothermal treatment using the hydrogel showed the most efficient inhibitive effect on tumor growth compared with the control group.

This method can also be used to attach targeting ligand to nanoparticles. [410-411] After the nanoparticles were prepared, amino-end target ligand could be decorated to the surface of PDA. With drug loaded, the PDA nanoparticles showed remarkable cytotoxicity during in vitro tests. Furthermore, in vivo tests indicated that these nanoparticles have higher accumulation in tumors after injection.

1.2.1.3.2. Grafting via Nucleophile Acyl Substitution

Also, because of -OH and -NH2, chemicals with acyl groups could react with PDA to graft chemicals. Such a method is used to immobilize of initiator and further in situ polymerization, in Figure 2.28. Messersmith's group conducted an early study. [412] They started with modifying dopamine with an initiator, 2-bromopropionyl bromide. Then the modified dopamine molecules were then absorbed on a metal substrate. The atom transfer radical polymerization (SI-ATRP) of oligo ethylene glycol methyl ether methacrylate (OEGMEMA) was then initiated on the modified surface of metal substrates. Compared with the unmodified substrates, the modified metal substrates show a significant antifouling property. Further, a cell array with cell-adhesive and cell-resistant regions was fabricated using the photolithography technique.

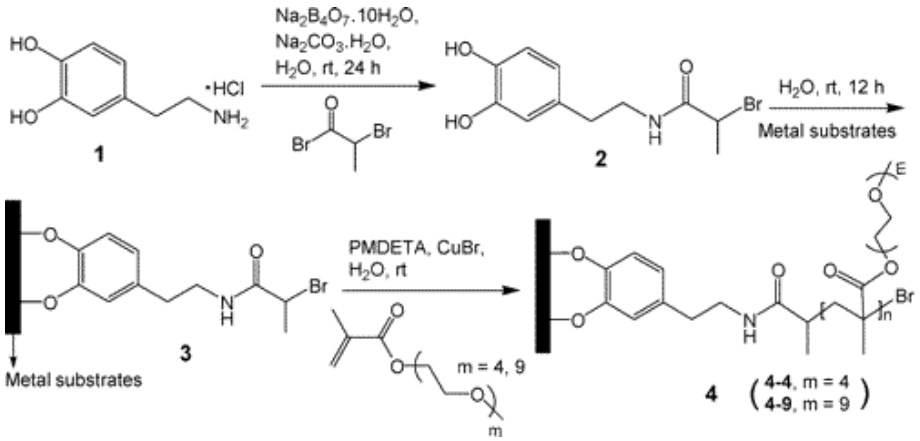

Figure 1.10 Synthesis and anchoring of the DOPA mimetic Initiator and the SI-ATRP [412]

Similar research was conducted by Li et al. [413] They used the catechol groups on PDA coating to react with carboxylic groups on 2-Bromoisobutyryl bromide (BIBB), which was later used to initiate the of acrylic acid on the PDA modified surface. This method produced a pH-responsive membrane which showed different permeability of aqueous solution due to different charge states of carboxyl groups in various pH. Furthermore, by replacing different substrates, initiators, and monomers, such a method made in situ polymerization on the surface of other materials possible.

1.2.1.3.3. Immobilization of Metal

Other than the organic functional group, metals are widely used in the functionalization of nanoparticles. The catechol groups on PDA provide reactive sites for metal immobilization. Metal ions from a solution can immobilize on PDA via two approaches: coordination with catechol groups and precipitation as metal nanoparticles via the reduction of catechol groups, Figure 1.11 (a) and (b).

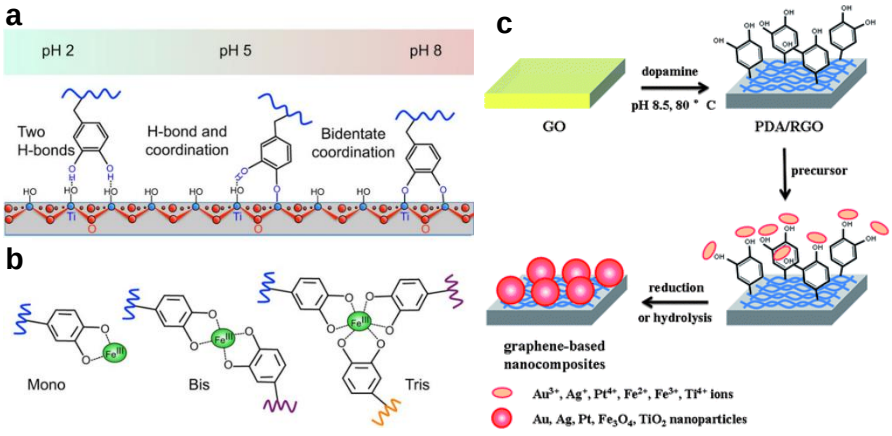

Figure 1.11 Interaction between PDA and metals. (a) Interfacial catechol bonding to metal oxide surfaces changes with pH. (b) Valency increases of metal-catechol coordination with pH [414] (c) Polymerization of dopamine on graphene oxide and in situ deposition of noble metals, metal oxide nanoparticles on its surface. [415]

By incorporating metal on PDA, Chen's group fabricated a multifunctional therapeutic platform. The labeled 64Cu was coordinated onto the PDA nanoparticles for positron emission tomography (PET) in this work. [5] The obtained nanoparticles showed high tumor-to-background contrast in PET imaging. The temperature elevation induced by the photothermal effect of PDA did not lead to copper leakage from the nanoparticle. In addition, magnetic resonance imaging (MRI) and photoacoustic imaging (PAI) were also demonstrated on the PDA nanoparticles by anchoring gadolinium (Gd) on PDA. In addition, there was no apparent cytotoxicity observed on the system.

Lu's group also used this technique to prepare an MRI contrast agent using the iron. [416] By repeatedly immersing PDA nanoparticles in $FeCl_3$ solution and benzene-1,3,5-tricarboxylic acid (H_3BTC) solution, a T_1/T_2 dual-mode contrast agent with chelated iron ions and iron carboxylate were prepared. The chelated iron ions could work as a longitudinal relaxation (T_1) contrast agent, giving high tissue resolution. Furthermore, the latter could serve as a transversal relaxations (T_2) contrast agent for MRI, which has a high capacity in lesion detection during imaging softer tissue. [417] By the same approach, other functional metal elements can also be immobilized on PDA. [418] In Liu et al.'s study, the acidic condition in the tumor could enhance MRI based on Fe-catechol coordination, which further improves the contrast of imaging. [419]

Besides the fabrication of nanostructure, the interaction between metals and PDA (specifically, the catechol on the surface) can also be used in drug delivery. As mentioned above, metal ions could be immobilized on catechol groups from PDA via coordination bonding. In addition, there is also coordination interaction between the metal ions and the oxygen atom on C=O and C-O bonds in drugs. Thus a "catechol-metal-drug" interaction is expected to be utilized for drug control release. Zheng et al. fabricated PDA-coated mesoporous silica nanoparticles with

Fe^{3+} or Zn^{2+} attached (MSN@PDA-M^{n+}). [420] Dox was used as model drug molecules to load and release on this nanoparticle. Compared with nanoparticles without metal ions coordinated (MSN@PDA), MSN@PDA-M^{n+} showed smaller release in neutral conditions. While the condition was weakly acidic, a fast and relatively complete release was observed in a short incubation time. Such a mechanism was also used for the release of bortezomib (BTZ) by Liu et al. [421]

The coordination of Fe^{3+} and catechol could be another route to fabricate a gel. In Xu et al.'s work, a copolymer, poly(styrene-co-DOPMAm), was synthesized with dopamine as pendants. [422] In the presence of Fe^{3+} in basic condition, such a copolymer formed a reversible gel very fast. When transferred to the acidic condition, the gel dissolved in 5 minutes. Then the coordination between Fe^{3+} and catechol was investigated by Lei's group in different pH. [423] In the pH range from 3.0 to 9.0, the dominant Fe^{3+}-catechol complexes in the medium gradually change from mono-catechol-Fe to di-catechol-Fe and finally tris-catechol-Fe. Such a transition could be observed on UV/Vis absorption spectra, on which the peaks at 715 nm, 580 nm, and 490 nm are corresponding to mono-, di- and tris-catechol-Fe complexes. And the complexation stability also increases progressively as pH increasing

Taking use of such a transition, Jiang's group reported another approach to control drug release via coordination between metal and PDA. [424] In their research, Dox was firstly encapsulated into a ZIF-8 MOF template. Then a thin film made of dopamine-modified alginate and Fe^{3+} was synthesized on the template. In a mild condition, the ZIF-8 template was removed. During the in vitro release experiment, the nanocapsule was stable at pH higher than pH 6. In pH 5, the nanocapsule was decomposed due to the weakened Fe-catechol coordination, and the drug was released completely.

For the metal nanoparticles immobilized by phenolic group reduction, the morphology is tunable as the concentration of the metal salt solution, temperature, and solvent changed. Such a feature could be applied in the fabrication of high superficial area catalysts and sensors. The study in Cai's group found out that as the concentration of metal ions solution ($HAuCl_4$) increased, the morphology of metal particle generated on PDA surface changed from sparse large particles to homogenous small particles, then back to large particles again. [425] The temperature and solvent can also influence the immobilization. By tuning these parameters, Ma, et al. prepared Au-PDA nanoparticles with different morphologies. [426] The structures varied from core-shell large Au agglomerate structure to strawberry-like uniformly dispersed tiny Au nanoparticles (< 5nm). Due to the high surface area of the tiny Au nanoparticles, such synthesized strawberry-like nanostructure showed excellent stability and catalytic activity than other nanostructures

1.2.1.3.4. Magnetic Functionalization

Magnetism is widely applied in nanotechnology. [427] The spatial distribution of nanoparticles can be controlled via magnetic attraction. Magnetic nanoparticles can also be used to improve MRI. In addition, heat can be generated in an alternating magnetic field by magnetic nanoparticles. [428] Generally, there are two approaches to "magnetize" PDA nanoparticles: encapsulating magnetic nanoparticles in PDA and immobilizing magnetic nanoparticles on PDA. For the first method, the magnetic core was dispersed in an alkaline dopamine solution. After a while, PDA film was generated on the core by oxygen-mediated self-polymerization. Many core-shell structure magnetic nanoparticles were fabricated in this way. [429-432] After PDA coating, other modifications can be applied to fabricate a multifunctional platform.

The other method is letting iron ions precipitate on PDA to form magnetic nanoparticles, Figure 1.11 (c). Guo et al. added a mixed precursor solution containing Fe^{2+} and Fe^{3+} to PDA/reduced graphene oxide (rGO) dispersion in an alkali condition (pH 10). [415] Subsequently, the medium was preserved at 90 °C in ambient conditions for 30 min. After that, the mixture was cooled down, and Fe_3O_4-deposited PDA/RGO was collected by centrifugation and washing. Such synthesized Fe_3O_4 modified PDA/RGO showed superparamagnetism and good response to an external magnetic field.

1.2.1.3.5. Fluorescent PDA capsules

There are ample aromatic rings and π bonds on PDA, and eumelanin is known to have the fluorescent property. Considering the similar structure between eumelanin and PDA, it is also expected to observe fluorescence on PDA. The first report was published by Zhang et al. [433] They obtained worm-like PDA-based fluorescent nanoparticles (PDA-FONs) by adding H_2O_2 in a Tris-buffered solution of dopamine. Under irradiation in the range of 360 nm - 500 nm, emission from 490 nm to 560 nm can be observed. Then in vitro test was conducted. The results showed that PDA-FON has excellent biocompatibility (> 90 % cell viability with a concentration of 160 μg/ml).

Such a technique was used by Chen et al. to fabricate a fluorescent shell on PDA nanoparticles, Figure 1.12. [434] The PDA shell was first synthesized on a template core; then, the template was removed by hydrofluoric acid (HF) etching. Subsequently, a second PDA shell was synthesized on such obtained PDA nanoparticles, then H_2O_2 was added to generate a fluorescent layer. Under fluorescence microscopy, the nanoparticle showed strong fluorescence. They also optimized the fluorescence via varying the reaction time and pH of the suspension. After

processing the nanoparticles with H_2O_2 for 15 hr, the PDA nanoparticles showed the highest fluorescence in the pH 3 buffer.

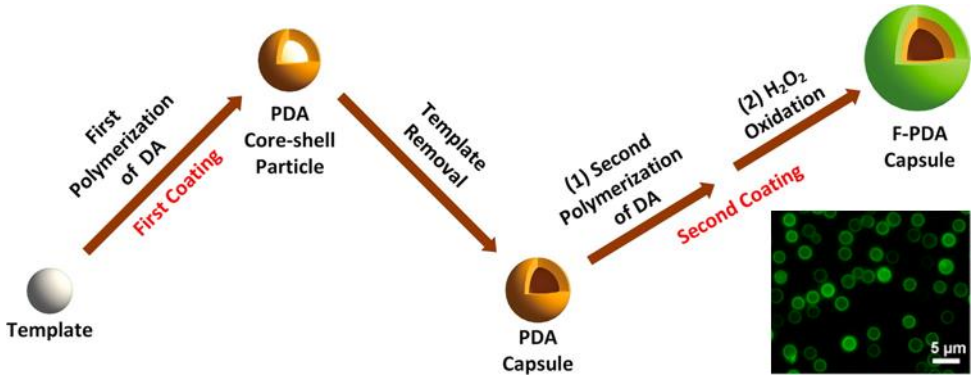

Figure 1.12 Scheme for the synthesis of fluorescent PDA (F-PDA) capsules. The inset shows a fluorescence microscopy image of F-PDA capsules [434]

Regarding dopamine as an important indicator for many nervous diseases, Yildirim et al. developed a dopamine sensing method based on the fluorescence of dopamine. [435] Via a series of optimization, they established a sensitive, selective sensing method for dopamine. The dopamine sample firstly went through 30 min oxidation in 20 mM NaOH solution. The oxidation was terminated by the addition of excess hydrochloride acid (HCl). The maximized emission was then found with 370 nm excitation. Through this method, the dopamine detection limit could be as low as 40 nM.

By investigating the mass spectra of oxidized PDA nanoparticles, Lin et al. proposed an explanation for PDA fluorescence. [436] They found out after oxidation with H_2O_2 in a strongly alkaline solution. The PDA nanoparticles were degraded into much smaller PDA dots (PD). The thermogravimetric analysis also confirmed that there were fewer cross-linking among PD remained. Furthermore, according to the mass spectrum, the m/z of PD decreased nearly one order of magnitude than PDA nanoparticles. They also found additional O-H deformation vibration on the FTIR spectrum of PD. Based on these results, they speculated that the hydroxyl radicals produced by H_2O_2 and NaOH weakened $\pi - \pi$ interactions in PDA. As a result, PDA

nanoparticles broke down into PDs. The conversion decreased fluorescence quenching. Therefore strong fluorescence was observed.

Zhao et al. prepared fluorescent PDA through another approach by weakening its intermolecular interactions. [437] In their method, polyethyleneimine (PEI) was added during PDA synthesis. The obtained polymer (PEI-PDA) showed similar fluorescence as oxidized PDA, except for a small redshift of the emission. In addition, as increasing the amount of PEI, the size of synthesized nanoparticles decreased. PEI was supposed to block the conjugation of PDA, and they can also form hydrogen bond (H-bond) with oxidative produce dopamine. Therefore, intra- and intermolecular couplings were weakened, and fluorescence was enhanced. Furthermore, they also found out metal ions, especially which have a high affinity to PEI or PDA or both, could counteract the PEI-PDA interaction. Therefore fluorescence was quenched again by adding these metal ions.

Other than fluorescent material, PDA could also be used as a fluorescence quencher. Qiang et al.'s study found out that PDA had an affinity to single-strand DNA (ssDNA), which could quench the fluorescein-labeled on DNA. [438] Adopting this interaction, they developed a DNA and protein sensing platform. In this strategy, probe DNA with a strong fluorescence emission was quenched when bound with PDA. As the target DNA or protein was introduced, the interaction between probe DNA and the target overwhelmed the affinity between probe DNA and PDA. As a result, the probe DNA was released and recovered its fluorescence.

1.2.1.3.6. Hydrophobic-Hydrophobic Interaction

This modification can be conducted by simply mixing PDA and the functional group. Cai's group mixed D-α-tocopheryl polyethylene glycol 1000 succinate (TPGS), an amphiphilic chemical,

with PDA nanoparticles in a neutral buffer. [439] After 24 hrs stirring, the TPGS modified PDA was obtained by centrifugation and washing. Due to the presence of aromatic rings on PDA, TPGS was integrated tightly on PDA via intermolecular $\pi - \pi$ interaction and hydrophobic-hydrophobic interaction. This hypothesis was proved by the differences of naked PDA and TPGS-PDA in TGA and zeta potential test. Furthermore, by adding acetone, a $\pi - \pi$ stacking breaking solvent, the zeta-potential of TPGS-PDA changed back to negative, which is similar to naked PDA. These results confirmed that it was $\pi - \pi$ interaction and hydrophobic-hydrophobic interaction loading TPGS on PDA, instead of chemical bond. In addition, they also developed a method to fabricate mesoporous PDA nanoparticles, which effectively increased the surface area of the PDA nanostructure. [440]

1.2.1.3.7. Modification via Molecular Structure

PDA modification can be achieved via a bottom-up approach, through which the monomer's structure is altered. In this way, polymers with the different repeating units could be prepared, and distinct properties could be expected. PDA is derived from the mussel adhesive protein. The excellent adhesive capability and active chemical properties are attributed to abundant catechol and amino groups. Given their function, Figure 1.13 summarizes several mussel-inspired materials. Besides the features of PDA, they also possess biodegradability and different adhesive properties.

Though melanin and its analogs are considered biocompatible, the inert chemical property and crosslinked structure make them hard to be degraded by enzymes. Therefore, the lack of a metabolism pathway leaves a potential concern. Hong et al. designed a biodegradable PDA with disulfide bonds. [442] In this study, two L-DOPA molecules were firstly connected via a disulfide

bond. The L-DOPA disulfide dimer (DOPA-SS) was then coated on a substrate in Tris buffer. Similar to PDA, all substrates turned hydrophilic after coating. The presence of disulfide bonds was confirmed by ^{1}H NMR spectra. Under a high concentration of glutathione (GSH), the thicknesses of PDA coating rapidly decreased. The signal of coating on FTIR disappeared, and the DOX loaded in PDA film was quickly released. On the spectra of quartz crystal microbalance with dissipation (QCM-D), the mass reduction of the film was also observed. All these results indicate the rapid degradation of the film synthesized via DOPA-SS. This study solved the biodegradation problem for PDA and its analogs and demonstrated the power of molecular design on PDA modification.

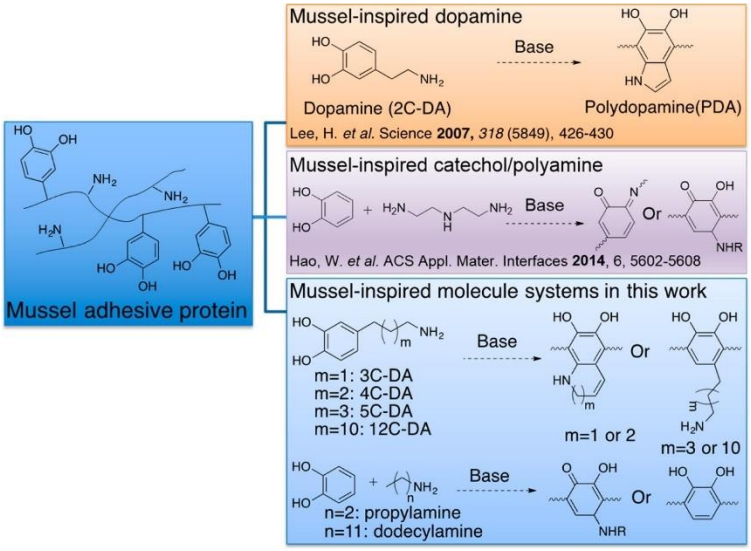

Figure 1.13 Overview of mussel-inspired materials and proposed polymer structure[441]

Repenko et al. proposed another novel strategy to synthesize excludable PDA.[443] The basic idea of the study is to avoid cross-linking during dopamine polymerization. Dopamine was firstly brominated; then, the hydroxyl and amine groups were protected using tert-butyloxycarbonyl (tBoc). Following that, a linear PDA was obtained by Kumada coupling. [444] After further oxidation in an aqueous solution, linear melanin was prepared. Due to the defined backbone, the UV/Vis spectrum of linear melanin presented two distinct peaks instead of a broad

band. Its fluorescence spectra (excited at 785 nm) showed a peak around 900 nm. Based on the spectra information, the photoacoustic excitation spectrum of the melanin was investigated. On the spectrum, a strong signal was found where blood had low absorption. Later, during the in vivo and in vitro experiment, the linear melanin showed well biocompatible, low detection limit, and high detection depth.

Though melanin has been studied for decades and PDA has been widely studied for over ten years, there are still limited types of melanin-like polymers. Hu et al. synthesized a series of dopamine-like molecules, which have catechol and amine groups, but the length of the alkyl chain linking the amine is varied. [441] They also studied the non-covalent-linked catechol and amine combinations, i.e., the chemicals with only catechol or amine were mixed to react. By adding these molecules in alkaline aqueous or hybrid solutions, polymerization all occurred. The UV/Vis spectra were investigated for products. It was found that the molecules with two or three carbon on alkyl chains had ring formed during polymerization, while molecules with longer alkyl chains had no ring formed. For noncovalent systems, there was also no ring formed. Polymerization was more dependent on Michael addition. UV/Vis spectra also displayed differences between products synthesized from aqueous solution and hybrid solutions, which implied different polymerization mechanisms, though the mechanisms are still elusive. Furthermore, they also found that polymers had similar adhesive strength, regardless of alkyl chain length and whether catechol and amine were chemically bonded. While for the coating capability, noncovalent systems were significantly weakened. This study shed light on the mechanism of dopamine polymerization and provided a reference for designing new PDA-like polymers.

Because several interactions and bindings were included in polymerization, the functionally modified dopamine molecules could also be incorporated in PDA. Gao et al. mixed

Dox, dopamine, and lactosylated dopamine (on which a lactobionic acid was linked to amine), then synthesized Dox loaded PDA nanoparticle via a one-pot polymerization. [400] The linked lactobionic acid worked as a target making PDA nanoparticles specifically bind with ricinus comunis agglutinin (RCA120). The targeting efficiency could be further tuned by changing the ratio between dopamine and lactosylated dopamine. The in vitro experiment confirmed that the modified PDA nanoparticles had no damage to cell viability, while the drug-loaded modified PDA nanoparticle had enhanced cytotoxicity.

1.2.1.3.8. Directly incorporation of functional group

Though simple chemical modification had been extensively studied, functional groups, like amine or thiol, are still needed for modifications. Recently, Lee's group developed an even more facile surface modification method with fewer limitations based on PDA. [445] In this study, agents were co-dissolved with dopamine, and then due to the broad-spectrum affinity between dopamine and materials, agents were immobilized on PDA film during PDA coating. This method was successfully applied to different substrates and various chemicals that could be co-dissolved with dopamine. For instance, an atom transfer radical polymerization (ATRP) initiator was mixed with dopamine in a methanol/water solution. Then the ATRP-PDA film was generated on a series of substrates, like noble metal, oxides, ceramics, and PTFE. After that, the polymerization was successfully initiated on all these surfaces. Immobilization of cetyltrimethylammonium bromide (CTAB) on silica substrate created an excellent antibacterial surface. While by embedding sodium hyaluronate (HA) on silica, cell adhesion was effectively improved. Due to PDA can also be prepared in alcohol, the method could even expand to some hydrophobic molecules. However, water still must be introduced during the process. Therefore, they further investigated to initiate

dopamine polymerization in a pure organic solvent to deal with the co-dissolution problem of dopamine and hydrolyzable or hydrophobic molecules. [446] The organic base, piperidine, was regarded as essential during the process. Compared with the widely used Tris and other organic bases, piperidine showed an efficient and universal catalytic effect in protic solvents, which made immobilization of water-insoluble molecule in PDA possible. In addition, this system was failed in an aprotic solvent. In other words, the presence of protons was essential during dopamine polymerization.

Chapter 2

Fabrication of Polydopamine Nanotube and Preliminary Control Release Study

2.1 Introduction

Extensive studies have been conducted exploring the effect of nanoparticle size, surface chemistry, and composition on cellular uptake and drug delivery.[447-450] Recent studies indicate that particle shape also plays a key role in controlling cellular uptake, with rods exhibiting reduced uptake by circulating phagocytes, leading to prolonged circulation time as compared to spherical particles. [234, 357, 365, 451-454] In addition to the prolonged circulation exhibited by nanorods, studies have demonstrated that high aspect ratio rods exhibit greater tumor accumulation and deeper tumor penetration. [368, 372] In vitro investigations have demonstrated low non-specific [357, 366-367, 455] and high-specific[369, 456-457] cellular uptake of nanorods. While the interaction between nanoparticle shape and physiological environment is not completely understood, and there are some studies implying the potential negative influence of rod-like shape on biocompatibility, [373, 458-459] nanoparticle shape undoubtfully plays a role in biodistribution and cellular uptake. This dependence suggests enhanced performance of anisotropic materials in targeted drug delivery.

Several methods have been developed for producing non-spherical micro/nanostructures, including microfluidics,[452, 460-462] projection photolithography,[452, 463] particle replication in non-wetting templates (PRINT),[464] film-stretching,[465] self-assembly,[371, 466-469] and template-assisted fabrication.[470] Despite the advance in shape control of micro/nanostructures, there remain significant limitations in the application of these techniques to cancer therapy. For

example, to avoid clearance by the MPS, liver, spleen, and kidney; and to capitalize on the enhanced permeability and retention of these particles by tumor cells, the optimal nanoparticle sizes are believed to be in the range of 30-200 nm.[74] Methods such as microfluidics, projection photolithography, PRINT method, and templating with porous anodic aluminum oxide produce nanoparticles outside this desired size range.[452, 464, 471-473] In addition, these methods carry relatively high synthesis costs. [8] Film stretching is a versatile technique capable of producing several geometries of polymeric nanoparticles. However, the nanoparticles obtained through film stretching are all solid, limiting the ability to load therapeutic agents.[451] Self-assembly techniques utilize the formation of micelle and vesical shaped nanostructures in a liquid colloid, and are capable of producing particles in the requisite size range. However, the specific shape and size dispersity can be difficult to control.[452] Particles derived from self-assembly, can be used as soft templates for synthesis of polymeric nanotubes as can other hard templates.[474-475] Carbon nanotubes can be surface modified with a wide variety of organic materials using both physical adsorption and chemical grafting.[476-478] However, the CNTs remain in the obtained nanoparticles. In template-assisted methods, the shape, size and polydispersity of fabricated nanostructures are largely dependent on the template utilized. These methods have been used to produce nanomaterials with various shapes, such as nanocubes, nanoellipsoids, and nanopeanuts.[479] Recently PDA nanorods have been fabricated via the use of rod-like templates such as curcumin crystals and ZnO nanorods.[480-482] However, the rods obtained are larger than the 30-200 nm range desired to avoid clearance and enhance accumulation at tumor sites. Thus, while the shape is potentially a powerful factor to enhance cancer treatment, the formation of high aspect ratio polymeric nanoparticles, particularly polymeric nanotubes, in the appropriate size range is not a simple task.

Naturally occurring silicate nanotubes, most notably halloysite, have been used as a template for inorganic nanostructures, such as nanorods, formed in the lumen, and there are numerous reports of grafting polymers to their surfaces.[483-485] Halloysite nanotubes (HNTs) are formed by the rolling of kaolinite resulting in a hollow lumen with a diameter of 12-15 nm and an overall diameter of 50-60 nm.[486-487] The tubular structure, low cost, and biologically inertness of halloysite have driven its development as a controlled release reservoir.[488-490] Unfortunately, HNTs are not biodegradable and are not removed from the circulatory system via the kidneys limiting suitability for direct drug delivery.[491] More recently, halloysite has been used to produce polymer-coated nanotubes via surface copolymerization of propyl methacrylate, ethylene glycol dimethacrylate, and methacrylic acid, and by the deposition of polypyrrole from HCl solution.[492-493]

This work leverages the simplicity of preparing conformal coatings of PDA and the availability of the low-cost natural nanotube halloysite for the facile preparation of high aspect organic nanotubes that combine the benefits of PDA with the increased circulation time and tumor uptake reported for nanorods. Residual catechol and amino groups were used to further modify the PDA surface. The pH and photothermal behavior of the particles can be used to control the release rates of therapeutic compounds loaded either during or after fabrication. The morphology and photothermal behavior of the resulting PEG-coated PDA nanotubes, as well as the loading and release characteristics of a model chemotherapeutic compound, doxorubicin (DOX), from these nanotubes, are reported. Results are compared with PDA nanospheres. Results are compared with PDA nanospheres. The resulting PDA nanotubes have potential applications as anisotropic drug delivery systems.

2.2 Experiments

2.2.1 Materials and Instrumentation

Dopamine chloride (DA) was from Beantown Chemicals. Tris(hydroxymethyl) aminomethane (Tris) was obtained from VWR Life Science. Hydrochloric acid (HCl, 10 % v/v), potassium phosphate monobasic (KH_2PO_4), ammonia (NH_3 in water, 28-30%). Halloysite nanotubes (HNT) were obtained from Bonding Chemical. Hydrofluoric acid (50%, v/v ACS grade) was obtained from BDH Chemical. All chemicals were used without further purification. Deionized (DI) water was used in all the experiments. Morphology was obtained using transmission electron microscopy (TEM; Zeiss EM10). Samples were prepared by evaporation of dispersions onto a 300 mesh formvar/carbon film from Electron Microscopy Sciences. Fourier transform infrared spectra (FTIR) were obtained via a Shimadzu IR Prestige-21 FTIR spectrometer. KBr pellets were prepared at a sample to KBr ratio of 1:100. UV-Vis spectra were obtained on an Agilent Cary 60 UV-Vis. Thermogravimetric analysis (TGA) was conducted on a Thermal Analysis TGA Q500. For every test, around 10 mg powder sample was used. The sample was ramped to 100 ℃ with a rate of 20 ℃/min. Then the sample was held isothermally at 100 ℃ for 2 minutes. The sample was then heated to 800 ℃ with a rate of 10 ℃/min. The zeta potential of PEGylated polydopamine nanoparticles was measured in 1 mM phosphate buffer (at pH 7.4) and 1 mM acetate buffer (at pH 5.0) on a ZetaSizer Nano ZS90 sizing instrument (Malvern, Worcestshire, UK).

2.2.2 Synthesis of Polydopamine Nanotubes (PDA-NT) and its PEGylation (PEG-PDA-NT)

In the first step, PDA-HNTs were obtained via deposition of PDA from an aqueous dopamine solution. In a typical synthesis, 20 mg HNT was added in 70 ml of 10 mM Tris-HCl

buffer and dispersed ultrasonically for two minutes at 100 W (QSonica LLC, Q500). The dispersion was then continuously stirred as 20 mg DA was added. The dispersion color quickly changed to pink in ~5 min., and then to dark brown over about 30 min. After 24 h stirring, the medium was completely opaque. The product (PDA-HNTs) was obtained via centrifugation (21,964g) on a Heraeus Megafuge 8 centrifuge (Thermo Scientific). The product was washed and recollected by centrifugation until the supernatant was colorless and transparent. The resulting PDA-HNTs were lyophilized on a Freezone freeze dry system (Labconco corporation). The typical mass of the product was 22.3 mg.

PDA-HNTs were surface coated with (PEG-NH_2) via Michael Addition. In a typical synthesis, 20 mg of PDA-HNT was ultrasonically dispersed (100 W, 10 s) in 20 ml of 10 mM Tris-HCl buffer (pH 8.5). Subsequently, 20 mg of mPEG-NH_2 was added to the dispersion under constant stirring. After 24 hours, PEG-PDA-HNTs were obtained by centrifugation and washing via DI H_2O repeatedly until the supernatant was colorless and transparent. The typical mass of the product was 19.98 mg.

To remove the halloysite template, 200 mg PDA-HNTs or PEG-PDA-HNTs were added to 1.52 ml HCl with mild stirring, then 0.76 ml 50% HF was added dropwise. After 24 hours of stirring at room temperature, the product was centrifuged and washed by DI H_2O repeatedly, typically six cycles, until the supernatant pH was over 5. The collected precipitate was lyophilized prior to subsequent use. The typical mass of the product was 40.09 mg.

2.2.3 Synthesis of Polydopamine Nanospheres (PDA-NS) and its PEGylation (PEG-PDA-NS)

PDA-NS were synthesized via the method reported by Liu et al. [2] In a typical synthesis, 2 ml of ammonia aqueous solution (NH_4OH, 28-30%) was added dropwise to an ethanol : water

solution (40 ml ethanol : 90 ml DI H_2O) under constant stirring at 30 °C. Subsequently, 0.5 g DA, dissolved in 10 ml DI H_2O was added. After 24 h, the product (PDA-NS) was obtained via centrifugation and washing by DI H_2O repeatedly until the supernatant was colorless and transparent. The product was lyophilized prior to further investigation. The typical mass of the product was 95.04 mg.

PDA-NS were surface coated with PEG-NH_2 via Michael Addition. A similar method was used to produce PEG-PDA-HNTs. In a typical synthesis, between 20 mg of PDA-NS was ultrasonically dispersed (100 W, 10 s) in 30 ml of 10 mM Tris-HCl buffer (pH 8.5). Subsequently, 40 mg of mPEG-NH_2 dissolved in 4 ml DI water was added to the dispersion under constant stirring. After 24 hours, PEG-PDA-NS were obtained by centrifugation and washing via DI H_2O repeatedly until the supernatant was colorless and transparent. The typical mass of the product was 30 mg.

2.2.4 The photothermal effect of PEG-PDA-NT and PEG-PDA-NS

The temperature rise of dispersions upon irradiation was used to evaluate photothermal conversion efficiency. PEG-PDA-NT or PEG-PDA-NS were placed in 1 ml DI H_2O in a 10 mm x 10 mm quartz cuvette. The temperature of the solution was monitored until the sample was at thermal equilibrium with the room. The cuvette was then irradiated with 808 nm wavelength light using a fiber light guide. Intensity at the cuvette surface was ~1 W/cm^2. A thermocouple was inserted into the medium and out of the laser path. The temperature of the dispersion was recorded every 10 seconds.

2.2.5 Drug loading of Doxorubicin on PEG-PDA-NT and PEG-PDA-NS

Loading was performed by adsorption of doxorubicin by PEG-PDA-NTs or PEG-PDA-NS from solutions (1.5, 1, 0.5, 0.25, 0.1 mg/ml) of doxorubicin in phosphate buffer (PBS; 10 mM, pH 8). PEG-PDA-NT or PEG-PDA-NP was dispersed into the solutions at a concentration of 0.5 mg/ml under magnetic stirring at room temperature. After 24 hours, the doxorubicin-loaded PEG-PDA-NT or PEG-PDA-NS (PEG-PDA-NT/Dox or PEG-PDA-NS/Dox) was collected via centrifugation and washed via fresh PBS (10 mM, pH 7.4) three times to remove extra unloaded Dox.

2.2.6 Stimuli-Responsive Drug Release

The effect of irradiation and medium pH changes were evaluated by monitoring the amount of doxorubicin released into the dispersion medium over time. In a typical experiment, to examine the effect of pH, 2 mg doxorubicin-loaded nanoparticles were added to 30 ml PBS (10 mM, pH 7.4 or pH 5) with mild stirring at room temperature. Periodically, a 3 ml release medium was collected and centrifuged (21,964 g for 1 min). The concentration of doxorubicin in the supernatant was determined by UV-Vis absorption at 480 nm and used to determine the total amount of doxorubicin released from the nanoparticles. The precipitate was dispersed in 3 ml of fresh PBS and returned to the sample. The influence of NIR on drug release was investigated using a similar methodology. In a typical experiment, 0.2 mg of doxorubicin-loaded nanoparticles were added to 3 ml PBS (10 mM, pH 7.4 or 5) with mild stirring at room temperature and placed in a quartz cuvette. NIR irradiation (808 nm, ~1 W/cm^2 at sample surface) was applied to the top of the sample for 10 minutes every 50 min. Just prior to and immediately after each irradiation cycle, a 0.2 ml sample was collected and centrifuged. After the doxorubicin concentration in the supernatant was

determined by UV-Vis, the precipitate was redispersed in the same supernatant and returned to the cuvette.

2.3 Results and Discussion

2.3.1 Synthesis of Polydopamine Nanotubes and Nanospheres

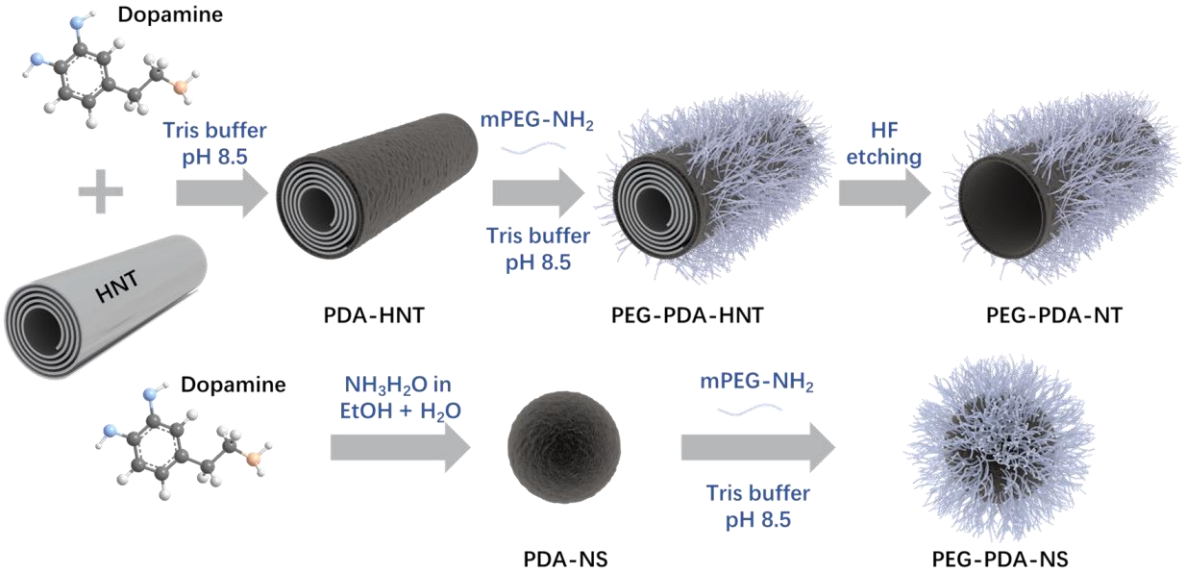

Figure 2.1 Synthesis of PDA-NT, PEG-PDA-NT. PDA-NS, PEG-PDA-NS

Figure 2.1 depicts the nanotube fabrication process. Dopamine undergoes a self-oxidation process in weak base conditions. Through a series of oxidation, cyclization, and isomerization reactions, dopamine molecules conjugate and form a conformal polydopamine coating on the suspended particles. By suspending HNTs in a dopamine solution in Tris buffer, a conformal coating on the halloysite surface was formed as the reaction proceeded. In this work, halloysite was suspended first, followed by the addition of dopamine under rapid stirring. After the addition of dopamine, the color of the medium quickly changed to pink, indicating oxidation of the catechol groups and the formation of indoles. The solution gradually turned dark brown as polymerization proceeded. Figure 2.2 (a) and (b) are TEM images of unmodified HNTs, and PDA coated halloysite, PDA-HNT. As compared to the unmodified halloysite, the coated halloysite had a larger diameter

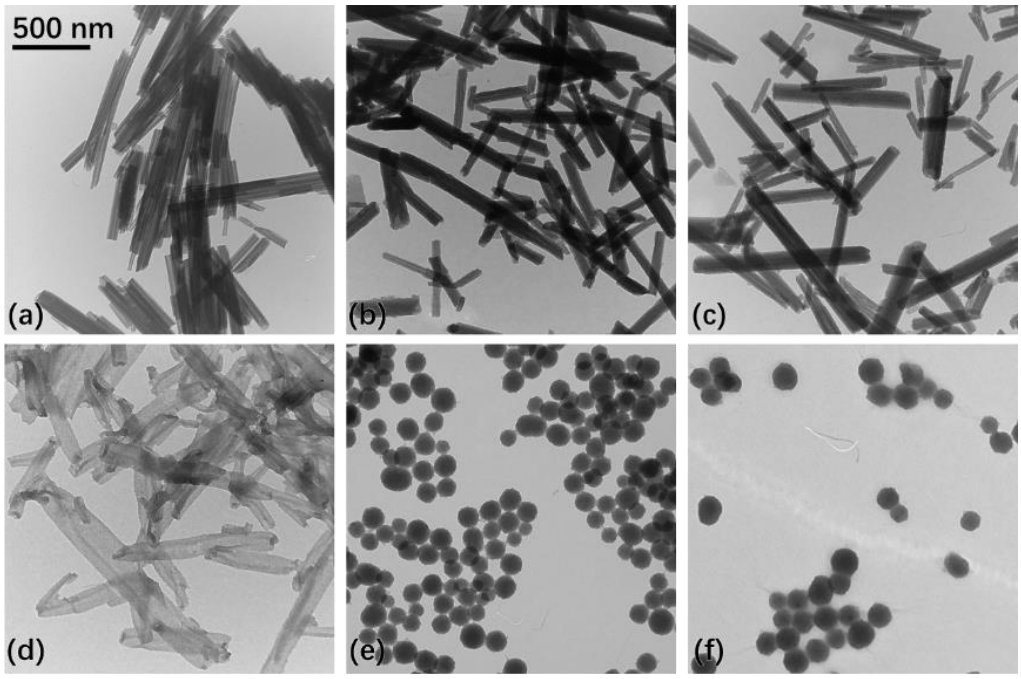

Figure 2.2 TEM images of nanotubes and nanospheres: (a) unmodified halloysite, (b) polydopamine coated halloysite, (c) polyethylene glycol surface modified polydopamine coated halloysite, (d) PEG-PDA-NT, (e) PDA-NS, and (f) PEG-PDA-NS

and a rougher surface. Further modification of the nanotube was achieved by the addition of amine-terminated PEG (M_w – 1000). The reaction between the amino-terminal group and quinone groups on the PDA coating effectively grafted PEG to the tube surface. Figure 2.2 (c) is a TEM image of PEG grafted PDA coated halloysite nanotubes, PEG-PDA-HNT. In general, the tubes had a similar diameter to PDA-HNT with similar surface roughness. Removal of the halloysite was achieved by HF etching. Figure 2.2 (d) is a TEM image of the resulting PEG-PDA bilayer nanotubes (PEG-PDA-NT). The tubes had considerably lower stiffness than halloysite, as evidenced by the appearance of bent, wrinkled, flattened, or otherwise distorted nanotubes. HNTs have both an outer and inner surface available for PDA deposition. Based on TEM images, only a single layer of PDA was left after HF etching of PDA-coated HNTs. Thus, either there was no PDA deposited on the inner surface of the halloysite, possibly due to diffusion limitations, or the PDA deposited on the inner surface of the halloysite is removed with the HNT upon etching. The diameter of pristine

HNT was 51-60 nm, the diameter of PDA coated HNTs was ~25% larger, 65-75 nm. PEG modification resulted in a small additional increase in diameter, 67-78 nm. After HF etching, possibly due to partial collapse of nanotubes into less cylindrical shapes, the width measured under TEM was 104-127 nm small enough for transport through the leaky vessel walls typical of tumors (< 200 nm) and large enough to avoid clearance by the kidneys (>10 nm).[74] Lengths obtained for the tubes ranged were 532 – 709 nm; the aspect ratios were in the range of 4.7 to 5.9. For comparison, PDA spheres, PDA-NS, and PEG-coated PDA spheres, PEG-PDA-NS, were produced. Solid spheres were selected as a comparison as they are the most studied form of PDA nanoparticles. In addition, the inner surface of hollow spheres is not directly accessible. In contrast, the inner surface of an open tube such as those produced in this work is accessible via the tube ends. The PDA spheres produced, Figure 2.2 (e) and (f), had diameters of ~115-130 nm and 145–160 nm, respectively. The thin PDA layer indicated only a single layer of PDA left after HF etching of PDA coated HNTs. Thus, either there was no PDA deposited on the inner surface of the halloysite, possibly due to diffusion limitations, or the PDA deposited on the inner surface of the halloysite is removed with the HNT upon etching. The diameter of pristine HNT was 51-60 nm, the diameter of PDA coated HNTs was ~25% larger, 65-75 nm. PEG modification resulted in a small additional increase in diameter, 67-78 nm. After HF etching, possibly due to partial collapse of nanotubes into less cylindrical shapes, the width measured under TEM was 104-127 nm small enough for transport through the leaky vessel walls typical of tumors (< 200 nm) and large enough to avoid clearance by the kidneys (>10 nm).[74] Lengths obtained for the tubes ranged were 532 – 709 nm; the aspect ratios were in the range of 4.7 to 5.9.

For comparison, PDA spheres, PDA-NS, and PEG-coated PDA spheres, PEG-PDA-NS, were produced. Solid spheres were selected as a comparison as they are the most studied form of

PDA nanoparticles. In addition, the inner surface of hollow spheres is not directly accessible. In contrast, the inner surface of an open tube such as those produced in this work is accessible via the tube ends. The PDA spheres produced, Figure 2.2 (e) and (f), had diameters of ~115-130 nm and 145–160 nm, respectively. The comparatively thin PDA layers in the prepared nanotubes versus the size of the PDA nanospheres is explained by the modulation of PDA growth in Tris buffer as seen in the work of Della Vecchia et al. [494] Under TEM, the hollow nanotubes were semi-transparent, most notably for the PEG-PDA-NT, while the solid nanospheres were opaque.

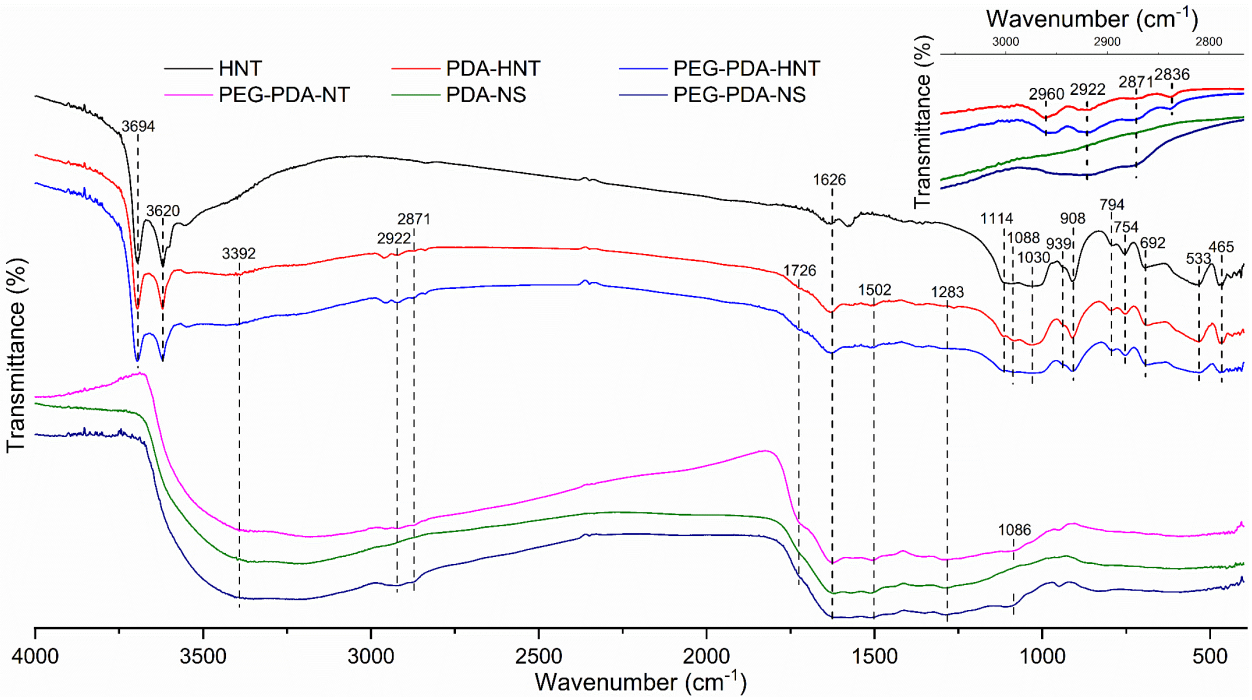

Figure 2.3 FTIR spectra of halloysite and nanomaterials produced in this work.

Representative FTIR spectra, Figure 2.3, show typical peaks for HNT in not only the pristine halloysite but also the PDA-HNT and PEG-PDA-HNT tubes. These peaks include the O-H stretching of hydroxyl groups at 3694 and 3620 cm^{-1}, as well as the deformation and stretching of Si-O, Al-O-Si, and OH in the range of 465-1114 cm^{-1}, consistent with previous studies.[483] However, after HF etching, these peaks disappeared, indicating complete removal of template. Compared with pristine halloysite, a wide arch was present in the spectra from about 1850 to 3650

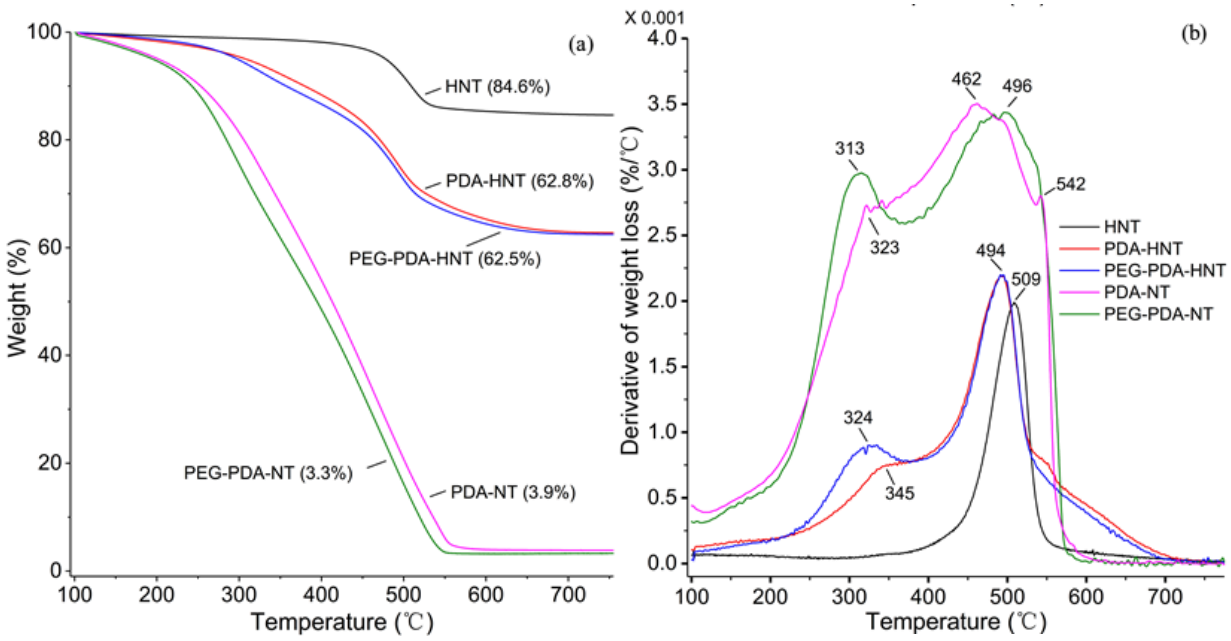

Figure 2.4 Thermogravimetric analysis of samples. (a) TGA curves for nanotubes. Numbers in parenthesis refer to residual mass at end of test. (b) Derivative of weight loss versus temperature measured by TGA of nanotubes.

cm^{-1} after the PDA coating was formed.[8, 495] This arch was more obvious after HNT etching. The peaks at 1283 cm^{-1} and 1502 cm^{-1} correspond to the stretching vibrations of C-N-, C=C, and C=NC of aromatic rings, while the peak at 1726 cm^{-1} corresponds to the stretching vibration of C=O, all indicate the presence of PDA.[8-9] After PEG modification, small peaks appeared at 2922 cm^{-1} and 2871 cm^{-1}. These are attributed to the asymmetric and symmetric stretching vibrations of $-CH_2$ in PEG.[8, 495-496] The peak at 1086 cm^{-1}, attributed to the stretching vibration of CH_2-C-O, also suggests the PEGylation of PDA. There were also two peaks at 2836 and 2960 cm^{-1} found on PDA-HNT and PEG-PDA-HNT, which disappeared after HF etching. The authors believe these peaks are associated with aliphatic C-H groups interacting with the halloysite surfaces. This interaction disappears after halloysite removal. Similar features are noted in the spectra of PDA-NS and PEG-PDA-NS.

Thermogravimetric analysis (TGA) was performed to study the composition of nanotubes, Figure 2.4. The sample weight at 100 °C was selected as the representative of samples without

adsorbed water to eliminate the interference of moisture with the analysis. For the unmodified HNT, around 15.4 % of the sample mass was lost between 450 and 550 °C, peak loss occurred at 508 °C, Figure 2.4 (b). This peak is typically assigned to the dehydroxylation of structural Al-OH groups of HNT.[496-497] Conversely, polydopamine coated halloysite exhibited mass loss between 200 and 600 °C. Pure PDA exhibits a mass loss across a broad temperature range in TGA testing, supporting the assignment of this loss peak to the presence of PDA.[7] 37.2% of the mass was lost for PDA-HNTs. Two events were responsible for this behavior, Figure 2.4 (b). The first, related to PDA degradation, was at 345 °C and the second, related to dihydroxylation of HNT, was at 494 °C. Analysis indicates that dehydroxylation accounted for 30.2% of the lost mass, while PDA degradation accounted for 69.8%. This suggests that the PDA-HNT tubes are roughly 26 wt.% PDA. Similar results were obtained after modification with polyethylene glycol; dehydroxylation accounted for 29.8% of the total weight lost, while the combined PDA and PEG degradation accounted for 70.2% of the total weight lost. The total loss was 37.5% suggesting the PEG-PDA-HNT tubes are 26.3 wt.%. After etching of the halloysite, the dehydroxylation peak largely disappears, and almost the entire mass of the sample is degraded during TGA testing, 3.9% residual mass for polydopamine nanotubes, and 3.3% residual mass for polyethylene glycol coated polydopamine nanotubes indicating the halloysite template was completely removed. This result is consistent with the TEM and FTIR analysis.

2.3.2 Photothermal Behavior of Nanoparticles and Nanotubes

Previously, Liu et al. demonstrated the high photothermal efficiency to PDA nanospheres, suggesting their applicability to photothermal therapy.[2] In this work, the photothermal performance of PEG-PDA-NT was compared with PEG-PDA-NS prepared via Liu's method,

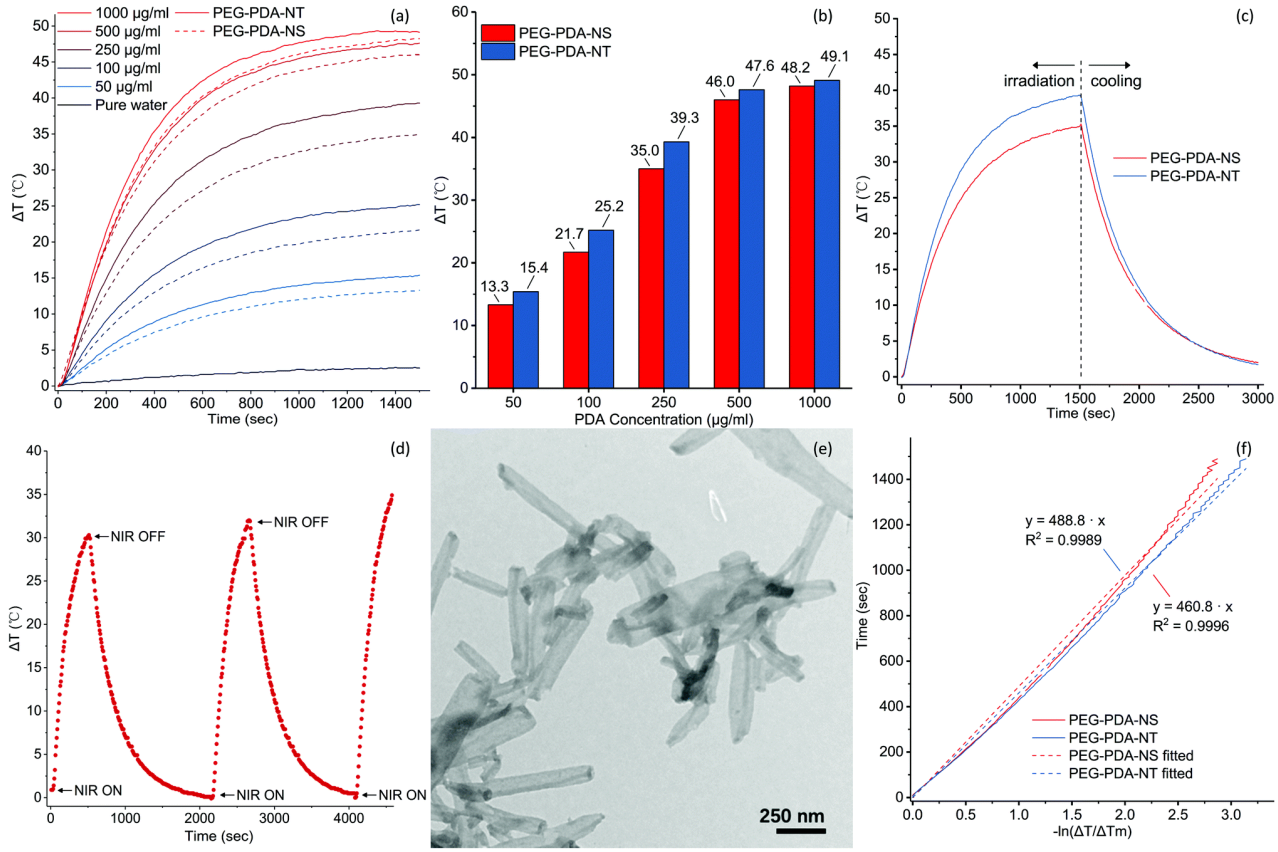

Figure 2.5 Photothermal behavior of PEG-PDA-NT and PEG-PDA-NS. (a) Temperature change over time of PEG–PDA-NT and PEG–PDA-NS dispersions in DI water upon irradiation by an 808 nm source at 1 W cm^{-2} intensity. (b) Temperature change after irradiation, same conditions, for 1000 s for PEG–PDA-NT and PEG–PDA-NS dispersions as function of mass concentration. (c) Temperature change during irradiation and cooling period for 250 µg ml^{-1} PDA nanoparticles dispersion. (d) Cyclic photothermal behavior of PEG–PDA-NT dispersion (1 mg ml^{-1}). Sample irradiated for 500 seconds by an 808 nm sources at 1 W cm^{-2} followed by no irradiation until dispersion cooled to ambient temperature (~1500 s). (e) TEM of PEG–PDA-NT after cyclic irradiation. (f) Time versus $-\ln(\Delta T/\Delta T_m)$ for cooling phase data shown in (c), used for determining *hA* values required to calculate photothermal efficiency.

Figure 2.5. As expected, the heat-up rate of NIR irradiated dispersions was largely dependent on the mass concentration of PDA, Figure 2.5 (a) and (b). At high concentrations, 1 mg/ml, the dispersions displayed a 43 °C temperature rise over 15 minutes. While dispersions at concentrations of 50 mg/ml only exhibited an increase of ~10 °C. However, for both PEG-PDA-NT and PEG-PDA-NS, the maximum temperature increase is not a linear function of concentration, Figure 2.5 (b), the apparent photothermal efficiency decreases. This decrease is possibly due to the agglomeration of the nanoparticles.

The results in Figure 2.5 (a) suggest that PEG-PDA-NT has a higher photothermal efficiency than PEG-PDA-NS. For example, at 250 μg/ml, the PEG-PDA-NS displayed a temperature change of 35.0 ℃, while the PEG-PDA-NT resulted in a 4.3 ℃ higher temperature change, 39.3 ℃, under the same conditions. Similar differences were apparent at all concentrations evaluated. The photothermal conversion efficiency, η, of both PDA nanoparticles were measured to elucidate this difference. Efficiency was calculated from:

$$\eta = \frac{hA\Delta T_{max} - Q_s}{I(1 - 10^{-A_\lambda})} \quad 2\text{-}1$$

where h is the heat transfer coefficient, A is the surface area of the container, ΔT_{max} is the maximum temperature change of PDA nanoparticle dispersions at a steady state, I is the irradiation power, A_λ is the absorbance 808 nm, and Q_s is the heat associated with the light absorbance of the solvent.[2] Q_s was calculated from $Q_s = hA\Delta T_{\text{solvent}}$, where $\Delta T_{solvent}$ is the maximum temperature change of water irradiated by the same light source at the same power intensity.

The parameter set hA was determined by fitting temperature vs. time data to the equation:

$$t = -\frac{\sum_i m_i c_{pi}}{hA} ln(\theta) \quad 2\text{-}2$$

where, m_i is the mass of component i, c_{pi} is the specific heat capacity of component i, t is time, and θ is calculated at each time increment as $(\Delta T/\Delta T_{max})$. The summation $\sum_i m_i c_{pi}$ was approximated by the mass and specific heat capacity of the solvent (water).

Data was collected as the photothermally heated sample cooled to room temperature, Figure 2.5 (c). The fits are shown in Figure 2.5 (f). The photothermal conversion efficiency of PEG-PDA-NS at 250 μg/ml was found to be 40%, the same value obtained by Liu et al.[2] The photothermal conversion efficiency for PEG-PDA-NT at the same mass concentration was found to be 42%.

Gold nanorods have been widely studied as a photothermal therapeutic agent, owing to localized surface plasmon resonance (LSPR).[498] However, according to Liu et al.'s study, gold nanorods experience significant morphology changes upon irradiation. One effect of this morphological change is a change in SPR, resulting in a reduction of photothermal energy transfer.[2] In this study, dispersion of PEG-PDA-NT (1 mg/ml) was repeatedly irradiated at an energy density of 1 W cm^{-2} with 808 nm wavelength light. The 1 mg/ml concentration of PEG-PDA-NT was selected to maximize the temperature change during the evaluation. The dispersion was irradiated for 500 seconds, followed by 1500 seconds of cooling. This irradiation-cooling cycle was repeated several times on the same sample. The temperature of the dispersion was recorded over the course of the irradiation / cooling cycles, Figure 2.5 (d). It can be seen the photothermal effect of PEG-PDA-NT was not deteriorated by previous irradiations. The highest temperature of the dispersion even increased during the second and third irradiation. This increase is believed to be due to an increased PDA concentration due to water evaporation during the test. The morphology of PDA nanotubes after repeated NIR was inspected by TEM. As shown in Figure 2.5 (e), no obvious morphological changes were observed for the PEG-PDA-NT.

2.3.3 Doxorubicin Loading Capacity

Loading of doxorubicin was accomplished by adsorption from a concentrated solution. In the aqueous solution used to load the nanoparticles, 10 mM PBS at pH 8, doxorubicin is positively charged while PDA is negatively charged, resulting in a strong driving force for the adsorption of doxorubicin by PDA.[499-501] Doxorubicin also interacts with PDA through π - π and hydrogen bonding interactions increasing binding and loading capacity.[3] In this work, solutions with various doxorubicin concentrations, 0.1 mg/ml to 1.5 mg/ml, were used to load the nanoparticles.

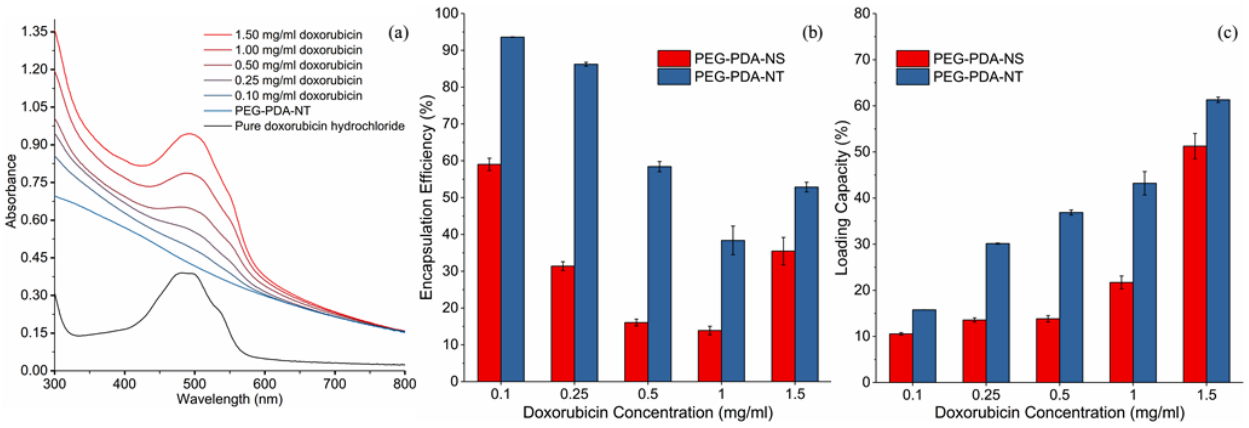

Figure 2.6 Characterization of doxorubicin loading on PDA nanoparticles. (a) UV/Vis spectra of PEG-PDA-NT/Dox loaded with different doxorubicin concentrations, pure PEG-PDA-NT, and doxorubicin hydrochloride. (b) Encapsulation efficiency of doxorubicin on PDA nanoparticles. (c) The loading capacity of doxorubicin on PDA nanoparticles. Error bars in (c) and (d) are standard error.

Two methods were used to evaluate the amount of doxorubicin loaded on the nanoparticles. First, after loading, the collected and washed nanoparticles were resuspended in Tris buffer, and UV-Vis spectra were taken. PDA exhibits a wide absorbance from 300 to 800 nm. However, adsorbed doxorubicin increases the adsorption, particularly between 450 and 550 nm. Figure 2.6 (a) shows spectra obtained from doxorubicin-loaded PEG-PDA-NT, which was washed and resuspended after loading. As the concentration of doxorubicin in the loading solution increased, the absorbance between 450 and 550 nm increased, suggesting a higher loading was achieved; dispersions with the same concentration of PEG-PDA-NT were used in each case. Due to the significant spectral overlap between PDA and doxorubicin, the comparison of the UV-Vis absorption of loaded nanoparticle dispersions is qualitative.

Quantification of doxorubicin loading was obtained by an indirect calculation. In this case, the residual doxorubicin concentration in the supernatant remaining after collection and washing of the loaded nanoparticles was used to determine the amount of doxorubicin not loaded on the nanoparticles. The encapsulation efficiency (EE) was calculated from:

$$EE = \frac{c_{LS} \cdot V_{LS} - c_S \cdot V_S}{c_{LS} \cdot V_{LS}} \times 100\% \qquad 2\text{-}3$$

where EE is the fraction of doxorubicin that was loaded onto the nanoparticles, c_{LS} is the doxorubicin concentration in the loading solution, V_{LS} is the volume of loading solution used, c_S is the doxorubicin concentration in the supernatant collected during washing, and V_S is the volume of supernatant collected during washing.

As shown in Figure 2.6 (b), as the doxorubicin concentration in the loading solution increased, the encapsulation efficiency dropped from 95% (0.1 mg/ml doxorubicin solution) to 37% (1 mg/ml doxorubicin solution). This trend was interrupted when the concentration was increased to 1.5 mg/ml, the encapsulation efficiency for PEG-PDA-NT increased to 55% at this concentration. Similar trends in the loading efficiency for PEG-PDA-NS were observed. However, at every concentration, the encapsulation efficiency for PEG-PDA-NT was higher than that for PEG-PDA-NS. This can be attributed to the higher specific area of nanotubes. The enhanced efficiency at the highest loading concentration is believed to result from diffusion of the adsorption of doxorubicin into bulk PDA. If bulk absorption plays a role in encapsulation efficiency, one expects that it is the total mass of PDA that would control loading efficiency, and there would be no significant difference between nanospheres and nanotubes. When loading solution concentrations were between 0.1 and 1.0 mg/ml, the encapsulation efficiency of PEG-PDA-NS was roughly 60% of the PEG-PDA-NT. However, when a loading solution of 1.5 mg/ml was used, the ratio increased to ~85%, supporting the hypothesis that loading shifts from a surface to a bulk effect. This effect is similar to that observed by Zeng et al. for the diffusion of Au^{3+} into a PDA shell.[425]

The loading capacity (LC) was calculated from:

$$LC = \frac{c_{LS} \cdot V_{LS} - c_S \cdot V_S}{M_{NP} + c_{LS} \cdot V_{LS} - c_S \cdot V_S} \times 100\% \quad 2\text{-}4$$

where LC is the fraction of the mass of loaded doxorubicin divided by the total mass of the nanoparticles after loading, and M_{NP} is the mass of the unloaded nanoparticles. The loading capacity of doxorubicin on nanoparticles is shown in Figure 2.6 (c). Loading capacity increased as doxorubicin concentration increased in the loading solution. For PEG-PDA-NT, the doxorubicin fraction increased from ~15.8% to ~61.3% as the loading solution doxorubicin concentration increased from 0.1 to 1.5 mg/ml. Loading with mass fractions greater than 50%, while surprising, are not unheard of for particles with large specific surface area.[227] Similar trends were noted for PEG-PDA-NS. The loading capacity of the nanospheres is lower than that of the nanotubes at all concentrations. However, the relative loading capacity, nanosphere loading capacity divided by nanotube loading capacity, does seem to be a function of doxorubicin concentration in the loading solution. When the doxorubicin concentration in the loading solution was 0.1 mg/ml, the relative loading capacity was 67%. It dropped to 34% when the doxorubicin concentration in the loading medium was 0.5 mg/ml and increased to 84% at a doxorubicin concentration in the loading medium of 1.5 mg/ml. This behavior supports the idea that loading shifts from a surface- to bulk-driven phenomena at higher doxorubicin concentrations.

2.3.4 Release from Polydopamine Nanoparticles

Normally, the pH of blood is around 7.4, while in tumors, the pH drops to lower than 6.6; the pH of endosomes is in the range of 6.5 to 5.0. [164, 502-503] Therefore, pH change is commonly used to trigger the local release of therapeutic compounds. Under weak acidic conditions, such as those found in endosomes, the release rate of doxorubicin from the PDA nanoparticles produced in this work was faster and reached a higher level of completion. For tubes,

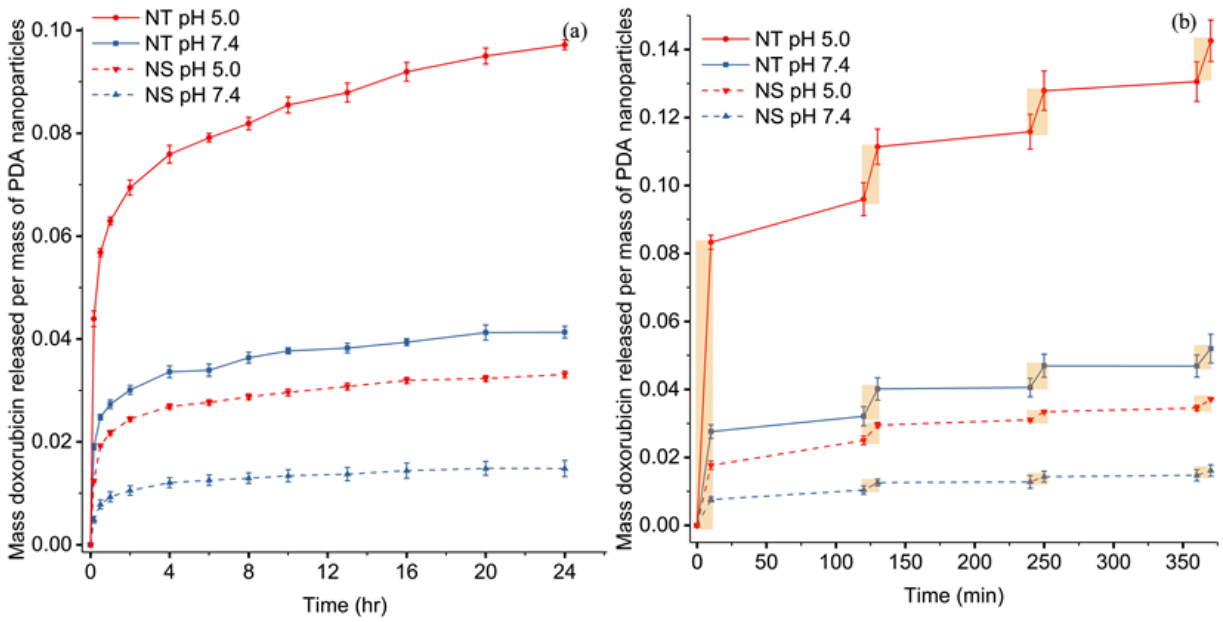

Figure 2.7 Release behavior of PEG-PDA-NT and PEG-PDA-NS. (a) Fraction of loaded doxorubicin released over time at two pHs. (b) Fraction of loaded doxorubicin released over time when vessel is cyclically irradiated at 1W/cm2 by an 808 nm source. Highlighted rectangles indicate time sample is being irradiated. All error bars are standard error.

after 24 h, ~55% of loaded doxorubicin was released when the media was at pH 5.0, while only ~17% doxorubicin was released in neutral pH. For spheres, the fraction released at the same time was ~45% at pH 5.0, while only ~14% was released at neutral pH. The fraction of doxorubicin released from the tubes was ~20% higher than exhibited by the spheres at both pHs evaluated. The pH effect is similar to that reported by Wang *et al.* for polydopamine–gadolinium–metallofullerene. [504] In that work, differences in release rates were related to the change in the zeta potential of the PDA nanoparticles. The zeta potential of PDA is a strong function of pH. At pH 5.0, the zeta potential of the tubes and spheres was −19.6 mV and −20.3 mV, respectively, while at a pH of 7.4, the zeta potential of the tubes and spheres was −32.2 mV and −39.3 mV, respectively. The difference in zeta potential did not have a significant effect on the difference in the fraction of doxorubicin released in the present study. This suggests that the increased release rate for the PDA nanotubes is related to the increased surface area of tubes vs. spheres. Furthermore, as the PDA nanotubes had a higher loading capacity, Figure 2.6, the amount of doxorubicin

released per unit mass of PDA in the nanoparticles was considerably higher for nanotubes than for nanospheres. Figure 2.7 (a) shows the mass of doxorubicin released per mass of PDA in the nanoparticles as a function of time and pH of the release medium for PDA nanoparticles loaded in a 0.5 mg ml^{-1} doxorubicin solution. Under this loading condition, the PDA nanotubes had ~2.5 times the loading capacity of the PDA nanospheres. The mass of doxorubicin released for spheres is less than half of that delivered by the tubes at both high and low pH.

Figure 2.7 (b) shows the effect of NIR irradiation on the release of doxorubicin from PEG–PDA-NT. Samples were placed in a quartz cuvette and irradiated (808 nm, 1 W cm^{-2}) for 10 minutes every two hours. The mass of doxorubicin released was measured just before and just after each irradiation cycle. Under both pH conditions, NIR irradiation induced a burst of release. When the irradiation was removed, release rates seemed to slow or reverse. The overall doxorubicin release rate and the effect of NIR irradiation were higher for low pH media. The samples were immersed in a water bath to limit the temperature increase of the dispersion during irradiation. However, the strong NIR adsorption by PDA is not affected. This energy adsorption increases the particle temperature disrupting hydrogen and π–π bonding and shifting the equilibrium toward unbound doxorubicin. The increased temperature also increases local diffusion rates increasing doxorubicin release. In this test, the release media was not refreshed; perfect sink conditions were not maintained. Thus, during the portion of the cycle without NIR irradiation, the doxorubicin could be reabsorbed by the particles, resulting in the apparent decrease in the mass released seen for some samples.

2.4 Conclusion in the Chapter

Hollow bilayer polyethylene glycol polydopamine nanotubes were prepared via the use of halloysite as a sacrificial template. The abundant catechol and amino groups on polydopamine enable surface coating of halloysite under mild conditions and enable grafting of polyethylene glycol on the outer surface by a Michael Addition mechanism. The halloysite core prevents similar grafting on the inner surface of the polydopamine layer resulting in a bilayer nanotube after the template is removed. The prepared tubes exhibited excellent photothermal behavior. Compared to PEG-coated polydopamine spheres, the nanotubes displayed significantly higher loading capacity of a model cancer therapeutic, doxorubicin. The tubular shape and size range of the nanotubes suggest they would exhibit good circulation lifetime and high specific uptake by tumor cells. It was demonstrated that the release of doxorubicin could be controlled by media pH and NIR irradiation. The combination of excellent photothermal efficiency, pH and NIR activated release, the potential for the shape-dependent enhancement of circulatory time and preferential tumor uptake make these nanotubes a promising drug delivery platform for combined chemo-photothermal therapy. The facile approach to PDA nanotube production should stimulate further research on the utility of anisotropic PDA nanoparticles in cancer therapy and other biomedical applications. The work reported here enables studies on the effect of anisotropy on the biocompatibility and toxicity of PDA and provides key in vitro data to motivate in vivo evaluations of PDA nanotubes.

Chapter 3

Bowl-Shaped Polydopamine Nanocapsules: Control of Morphology via Template Free Synthesis

3.1 Introduction

Nanoparticles are regularly produced in relatively simple shapes such as spheres, rods, and wires and applied to applications in the biomedical and environmental fields as drug delivery particles, photothermal agents, enhanced catalysts, electrochemical agents, and signal-enhancement agents. [406, 421, 492, 505-508] While synthesis of asymmetric nanostructures is not as simple as it is for spherical nanoparticles, the range of synthesized nanoparticle morphologies has steadily grown to include more exotic shapes such as acorn-shaped, dumbbell-shaped, tubes, ellipsoids, regular tetrahedra, and regular icosahedra. [509-512] Bowl-shaped nanoparticles (nanobowls) have a high specific surface area and high packing density making them an exciting candidate for signal detection, biomedical, energy storage, and catalyst applications. [513-516] There are three main template-assisted methods used to produce nanobowls. The most widely used technique utilizes an array of spherical nanoparticles as a template. The nanobowls are obtained by depositing additional material on one side of the array, followed by template removal. [517-522] A second technique "grows" the nanobowls asymmetrically on nanoparticles as seeds through a process similar to the Volmer-Weber growth mode.[523-524] Droplets formed in immiscible liquids can be used as seeds. Instead of layer growth, deposited materials grow as isolated "islands" on the surface of droplets. [525] The nanobowls are then obtained by the removal of the immiscible liquid. For the third technique, nanobowls can also be obtained from collapsed vesicles, which are formed on either soft templates (immiscible liquid droplets) [526] or hard

templates (sacrificial nanospheres). [398, 527-529] Inspired by the formation of liposomes, the addition of water to colloidal solutions of amphiphilic copolymers have also been demonstrated to produce nanobowls. [530-532] The evaporation of the organic solvent from the colloidal nanoparticles results in the "collapse" of the particles into a bowl shape. Nanobowls can also be prepared through lyophilization. In this technique, the polymer is dissolved in an organic solvent which is then dispersed in water. The system is then freeze-dried. During lyophilization, evaporation of the organic solvent results in the formation of a cavity or hole in the polymer nanospheres. [533-534] Finally, for metal oxides, Ostwald ripening was used by He et al. to prepare bowl-like nanoparticles. [535] However, all of these methods are typically time-consuming and labor-intensive; many of them require multiple steps. Also, in templated synthesis methods, the size and dispersity of the nanoparticles produced are highly correlated to the size and dispersity of the template used. For example, polystyrene beads are typically used as templates for nanobowl fabrication. However, these particles are usually in the 500 – 2000 nm range. Thus, the produced nanobowls are significantly larger than the optimum size for drug delivery. [74] The additional solvents and chemicals used for the removal of templates in template-assisted synthesis methods may also be a safety concern in biomedical applications. [536] Furthermore, for drug delivery applications, the payloads may be inactivated during template removal, directly impacting the efficacy of the nanocarrier. [537] Therefore, particularly for biomedical applications, rapid template-free methods for nanocapsule and nanobowl fabrication are desired.

One material that has attracted considerable interest for biomedical applications in recent years is polydopamine (PDA). Messersmith's group synthesized PDA by polymerizing dopamine under mild base conditions in 2007. [386] The numerous catechol and amino groups present in PDA endow it with excellent adhesion to many materials and provide a facile method for

attachment of functional groups through Michael addition or Schiff base reactions. [387, 538-540] Additionally, excellent biocompatibility and aromatic group content make PDA a promising material in biomedical and electrical applications. [2, 541-543] While spheres are by far the most studied shape of PDA, there have been some recent reports on the synthesis and properties of rod-like [399] and tube-like [481, 544] PDA nanostructures. Template-assisted techniques have been explored to produce bowl-shaped PDA structures. [545-548] However, these methods have all resulted in large particles, on the order of 260 nm to 4 mm, and are time-consuming. In addition, the templates used or the solvents used may raise biocompatibility issues when removed. Recently, biocompatible poly(acrylic acid) nanoparticles have been used as templates for PDA nanobowl synthesis. [470, 549-550] While the particles produced are smaller, on the order of 150 – 200 nm, and the materials used are biocompatible, the multiple-step fabrication process inherent in template-assisted synthesis still makes the preparation process complicated and time-consuming.

Recently, Ni et al. prepared hollow PDA nanocapsules approximately 200 nm in diameter in a mixed solution of water and tetrahydrofuran. [551] The authors attributed the hollow structure obtained to the microphase-separated complexes that formed in the reaction medium. However, the reaction was slow, possibly as THF is a non-protic solvent, [446] and the hollow particles were only obtained after 36 to 72 hours. In addition, while they were able to synthesis nanocapsules, the products exhibited poor morphological control and size homogeneity. Also, after a period of storage, the particles aggregated. Yan et al. reported the formation of solid PDA nanoparticles in alcohol/water solvent.[552] They mention the observation of one particle with a hole when isopropyl alcohol was used as a co-solvent but did not report further investigation of this phenomenon. Herein, a rapid one-pot synthesis method of PDA nanocapsules and nanobowls is reported. PDA nanocapsules were prepared in weakly alkaline ethanol/water solution in two hours.

After drying in ambient conditions, nanobowls were obtained. Compared with previously reported methods for PDA bowl-like structure fabrication, the process used in this study is straightforward, fast, uses biocompatible materials, and does not require a template. Furthermore, the morphology of the nanocapsules produced is tunable by varying the reaction conditions. The size of the nanobowls produced is between 80 – 120 nm. To the best of the authors' knowledge, there are no previous reports of such small PDA bowl-shaped nanoparticles rapidly synthesized through a template-free method. The utilization of naturally occurring ethanol nanodroplets makes this method simple, low-cost and biofriendly, and have great potential in catalyst, energy storage, and biomedical applications.

3.2 Experiments

3.2.1 Materials

Dopamine chloride (DA, ≥ 99%) was obtained from Beantown Chemicals. Tris(hydroxy methyl) aminomethane (Tris, ultrapure 99.9%) was obtained from VWR Life Science. Ethanol (EtOH, ACS grade ≥ 99.5%) and methanol (MeOH, HPLC grade ≥ 99.8%) were obtained from BDH Chemicals. Iso-propanol (histology grade ≥ 99%) was obtained from MilliporeSigma. All chemicals were used without further purification. Deionized (DI, ultrapure Type 1) water was used in all experiments.

3.2.2 Characterizations

The morphology and structure of nanocapsules were characterized by transmission electron microscopy (TEM, Zeiss EM10, Germany) and scanning electron microscopy (SEM, JEOL JSM – 7000F, JEOL). The TEM microscopy was conducted at an accelerating voltage of 60 kV. The

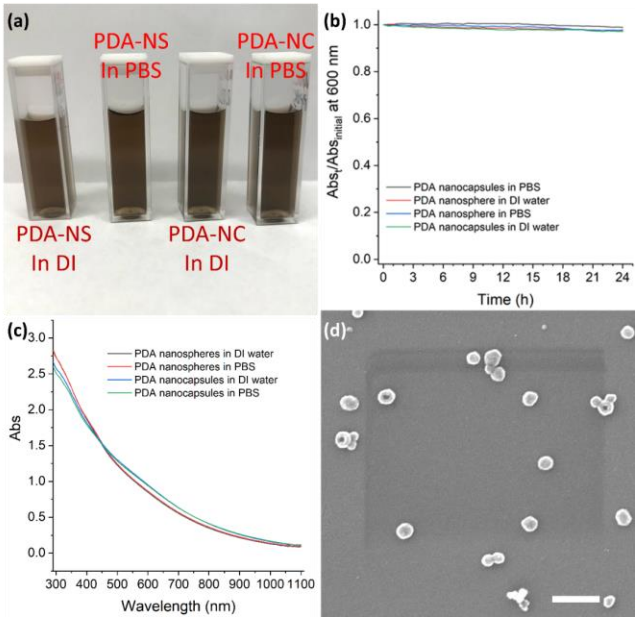

Figure 3.1 Hydrophilic property and stability of PDA nanocapsules in water. (a) Photos of nanoparticle dispersions from left to right: PDA nanospheres in DI water, PDA nanospheres in phosphate buffer solution, PDA nanocapsules in DI water, and PDA nanocapsules in phosphate buffer. All dispersions contain 200 μg/ml of PDA. The image was taken 24 hours after the particles were redispersed. (b) Normalized absorbance at 600 nm vs time for each dispersion shown in (a). The normalized values were calculated using the absorbances at each time divided by the initial absorbances of respective PDA nanoparticle dispersions. (c) UV/Visible spectra of four PDA nanoparticle dispersions shown in (a). (d) SEM image of PDA nanocapsules produced using 30 % EtOH, 0.3 mg/ml DA in unsealed containers with 0.606 mg/ml Tris). The scale bars in images represents 300 nm.

specimens for TEM were prepared by drying a droplet of nanocapsule suspension diluted with EtOH on a copper grid under ambient temperature and atmospheric pressure. The size distributions were obtained by measuring at least 100 randomly selected nanocapsules in the TEM images using image software (ImageJ, National Institutes of Health, Bethesda, MD, USA). The wall thicknesses of uncollapsed hollow nanocapsules were calculated from the inner and outer diameters of the imaged nanocapsules. For collapsed particles, the wall thicknesses were directly measured in relevant images. The numbers of solid (nanospheres) and hollow nanoparticles (nanocapsules) for each reaction time were counted in TEM images taken at randomly selected sites on the prepared grids. SEM was performed at an accelerating voltage of 20 kV. The samples for SEM were prepared by drying a droplet of diluted nanocapsule/water dispersion on a piece of silica wafer

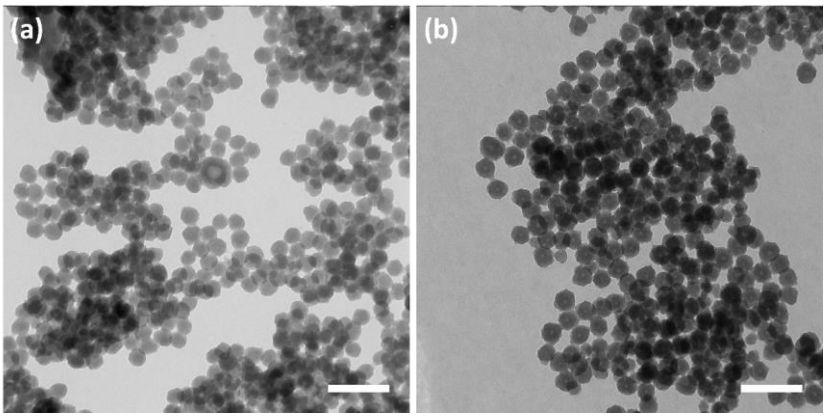

Figure 3.2 TEM images of hollow PDA capsules prepared in unsealed containers with 0.606 mg/ml Tris, 0.3 mg/ml DA and (a) 30 % methanol or (b) 30 % iso-propanol. The scale bars in images represents 200 nm.

under ambient temperature and atmospheric pressure. The wafer was then attached to an SEM mount. The numbers of collapsed nanocapsules (nanobowls) and uncollapsed nanocapsules were counted in SEM images taken at randomly selected sites on the prepared wafers. The PDA nanoparticles are hydrophilic, and the nanoparticle dispersions are stable in water and pH 7.4 phosphate buffer solutions over 24 hours, as shown in Figure 3.1 (b). The TEM samples were prepared in EtOH to reduce the surface tension between the TEM grid and dispersion solvent. However, the PDA nanoparticles gradually precipitate in an organic solvent like EtOH. Therefore the nanoparticles moderately aggregated under TEM. Under SEM, the nanoparticles are dispersed well using water as dispersion solvent, Figure 3.1 (b). The 0 vol.%, 5 vol.%, 10 vol.%, 20 vol.%, 30 vol.% EtOH aqueous solutions containing 0.606 mg/ml Tris and DI water were investigated using dynamic light scattering (DLS, Nano ZS90, Malvern, Worcestershire, UK) measurement. The composition of hollow PDA nanocapsules and solid PDA nanoparticles were characterized by Fourier transform infrared spectra (FTIR, Shimadzu IRPrestige-21 FTIR spectrometer, Japan). The KBr pellets were prepared at a sample to KBr mass ratio of 1:100.

3.2.3 Synthesis of Hollow Polydopamine Nanocapsules

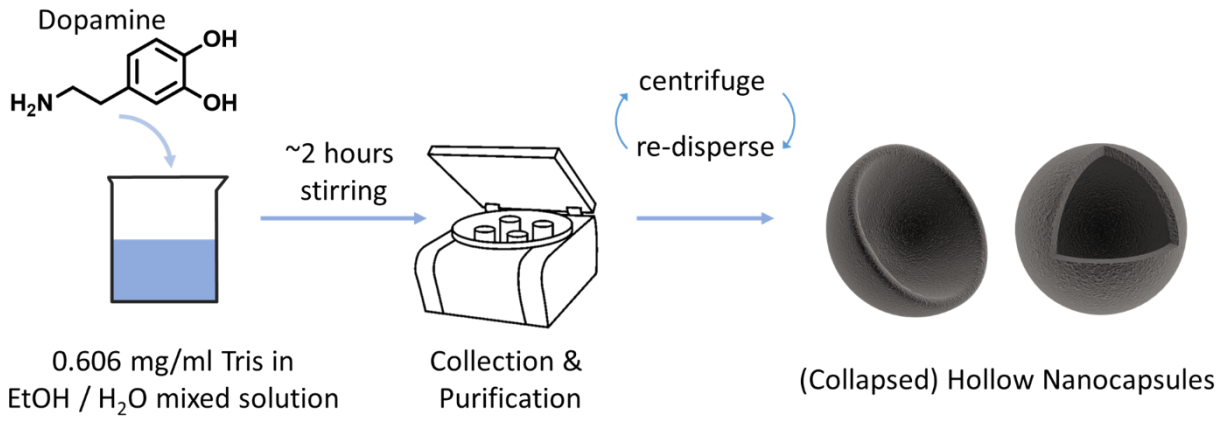

Figure 3.3 Preparation and purification of polydopamine hollow nanocapsules.

The simple synthesis process used in this work is depicted in Figure 3.3. In a typical synthesis to produce nanocapsules, 6 mg DA was added to 20 ml of 20 vol.% EtOH aqueous solution with 0.606 mg/ml Tris. The reactants were stirred using a magnetic stirrer for 2 hours. The polydopamine nanocapsules produced were collected by centrifugation (21,912 g, for 10 minutes), purified by dispersing in DI water and centrifuging three times, and finally dispersed in DI water. Various concentrations of DA (0.3, 0.6, and 0.9 mg/ml) and different solvent compositions (5 to 30 vol.% EtOH) were evaluated. Sealing some reaction vials with parafilm and leaving others open to the atmosphere was used to investigate oxygen influence. The reaction medium gradually changed from colorless to dark brown regardless of the concentrations of reactants or the final particle morphology. This change is typical for the self-polymerization of DA that occurs through oxidization and cyclization of the catechol groups and the formation of indoles.[386] Nanocapsules were also synthesized in 20% iso-propanol (3-hour reaction) and 20% methanol (1-hour reaction) with 0.3 mg/ml DA and 0.606 mg/ml Tris added. However, the products were not as uniform as those produced in the ethanol/water system, in Figure 3.2. Thus, this report focuses on the production of nanocapsules and nanobowls using an ethanol-water mixed solvent.

3.2.4 Statistical analysis

All statistical analysis was performed using SAS® OnDemand for Academics. The significance level, α, is set at 0.05.

3.3 Results and Discussion

3.3.1 Formation of Thicker Wall on Vessels with Increasing DA Concentration.

The morphology of particles obtained via synthesis with different concentrations of DA in the reaction medium is shown in Figure 3.4. A hollow structure is observed in TEM images, Figure 3.4 (a-c). In the sample prepared with a 0.3 mg/ml DA concentration, Figure 3.4 (a), almost every nanoparticle has a hollow structure. Only three solid nanospheres can be found. Synthesis using higher DA concentrations, 0.6 mg/ml and 0.9 mg/ml, Figure 3.4 (b) and (c), results in smaller hollow-core sizes and increased wall thickness. This trend is consistent with Ball et al.'s observation that the thicknesses of polydopamine films deposited on substrates are proportional to

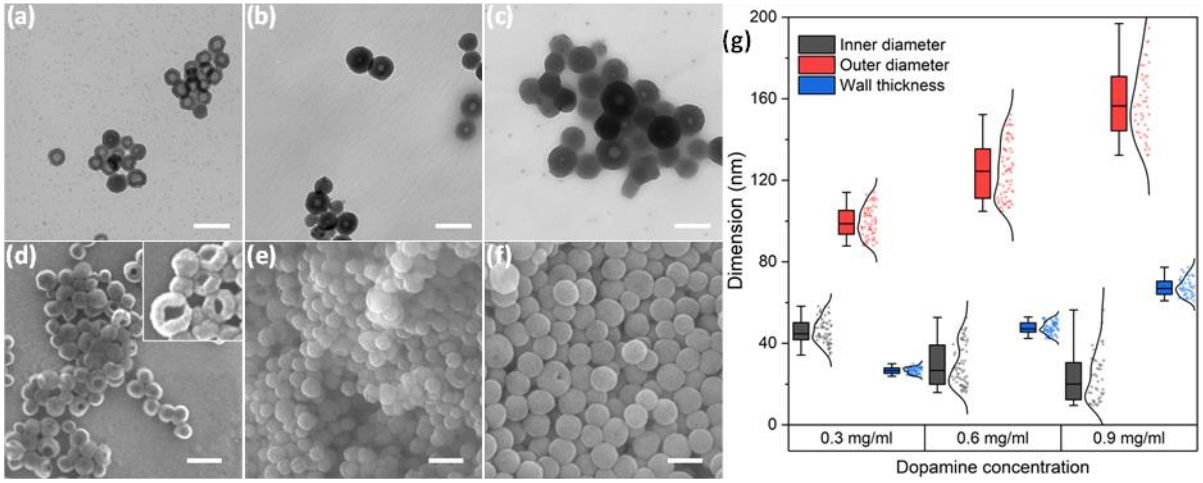

Figure 3.4 PDA capsules prepared in unsealed EtOH/H_2O (EtOH 30 vol %) solution for 6 hours with 1.212 mg/ml Tris and different concentrations of DA. (a, b, c) TEM images, (d, e, f) SEM images, (a and d) 0.3 mg/ml dopamine, (b and e) 0.6 mg/ml dopamine, (c and f) 0.9 mg/ml dopamine, and (g) characteristic dimensions of capsules obtained. The scale bar in images represents 200 nm. Dimensions in (g) were obtained by measurement of more than 100 random particles at each condition using ImageJ.

the initial concentration of dopamine.[553] The fraction of solid nanospheres also increases as the DA concentration increases. The distribution of inner and outer diameters of the hollow particles determined from TEM images is provided in Figure 3.4 (g). The walls become thicker by simultaneously increasing the overall particle diameter and decreasing the interior void space, i.e., the particles grow in both the inner and outer direction. The variability in particle size and void size also increases with increasing DA concentration. Bowl-like morphology is not clear in TEM images but is readily apparent in SEM images, Figure 3.4 (d-f). This morphology is believed to be the result of the nanocapsules collapsing during the drying process. As the DA concentration is increased, the fraction of bowl-like nanocapsules declines, suggesting that the thick-walled nanocapsules are more mechanically stable and unable to collapse. At a DA concentration of 0.3 mg/ml particles with diameters on the order of 99 nm (SD 7 nm) and wall thickness of 27 nm (SD 2 nm) were obtained, and many collapsed particles, bowl-like nanocapsules, can be seen in the SEM image, Figure 3.4 (d). However, at a DA concentration of 0.9 mg/ml particles with diameters on the order of 159 nm (SD 17 nm) and wall thickness of 68 nm (SD 4 nm) were obtained, and only one bowl-like structure is seen in the SEM image, Figure 3.4 (f), suggesting that there is a wall thickness above which the obtained nanocapsules cannot collapse to bowl-like morphology.

3.3.2 Synthesis of Pure Nanocapsules

Many established solid PDA nanosphere synthesis methods require a reaction time of at least 12 hours. [2-5, 243, 400, 554-555] However, the process reported here produces a blend of both solid nanospheres and hollow nanocapsules in a relatively short time. Literature suggests that lower base content results in a slower polymerization of DA. [556] When the Tris concentration was reduced to 0.606 mg/ml, the fraction of solid nanospheres produced decreased, Figure 3.6. A

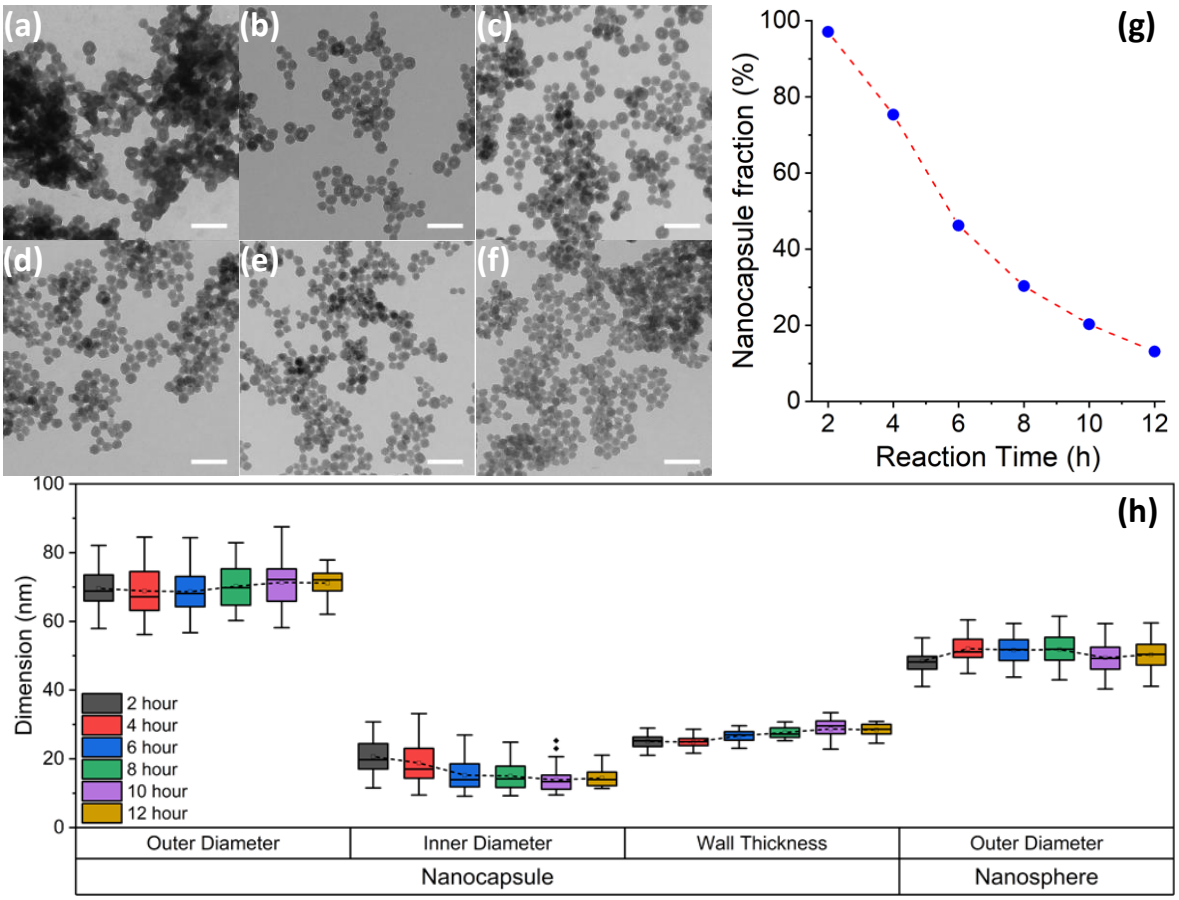

Figure 3.5 TEM images of hollow PDA nanocapsules collected in different time. (a) 2 hours, (b) 4 hours, (c) 6 hours, (d) 8 hours, (e) 10 hours, and (f) 12 hours. (g) Fraction of nanocapsules as a function of reaction time. (h) Characteristic dimensions of particles produced. The means are connected with dashed line to help vision comparison. Dimensions for these particles were obtained by measurement of more than 100 particles at each reaction time using ImageJ. All reactions were conducted in unsealed containers using 5 mM Tris concentration in a 30 vol.% EtOH solution, and 0.3 mg/ml DA. The scale bars in TEM images represent 200 nm.

comparison of samples synthesized using reaction times between 2 and 12 hours was used to evaluate the effect of reaction time on the fraction of nanocapsules produced. TEM images of the nanoparticles obtained for each reaction time are provided in Figure 3.5 (a-f). The fraction of hollow particles produced decreases as the reaction time increases. In Figure 3.5 (a), nearly all the nanostructures have hollow cores and are nanocapsules, while in Figure 3.5 (f), the majority of nanoparticles are solid nanospheres. Counts of nanocapsules versus solid particles observed via TEM were used to estimate the fraction of nanocapsules produced vs. reaction time, Figure 3.5 (g).

At two hours of reaction, approximately 97% of the particles produced were nanocapsules. At 6 hours reaction time, less than 50% of the particles were nanocapsules. At 12 hours reaction time, the fraction of nanocapsules was ~13%.

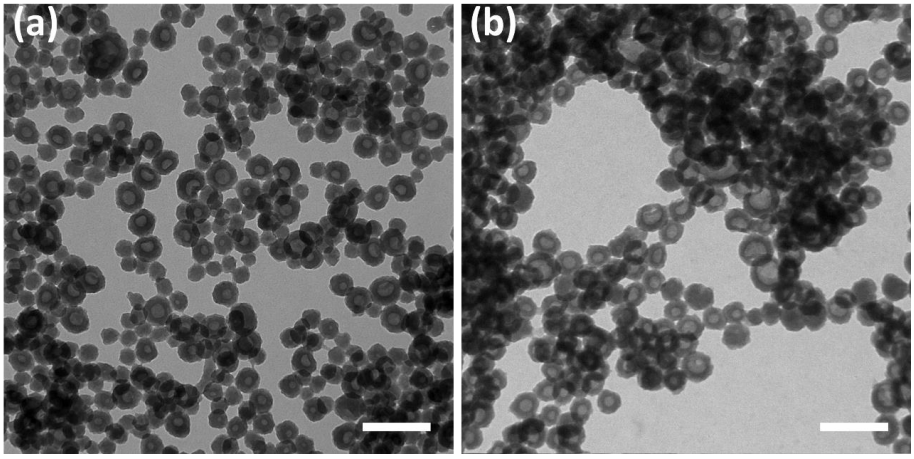

Figure 3.6 TEM images of PDA capsules prepared with 1.212 mg/ml (a) and 0.606 mg/ml (b) Tris in 30 % EtOH solutions with 0.3 mg/ml DA. The scale bars represent 200 nm.

Characteristic dimensions of the obtained particles are presented in Figure 3.5 (h). Both the outer diameter, ~70 nm, and the wall thickness, 26 nm, of the nanocapsules produced remain relatively constant over the 12 hours of the reaction. This result is in line with Ball et al., who found that that the deposition of polydopamine from solution is quick and that the thickness of deposited polydopamine layers is stabilized at a constant value after a short time. [553] In contrast, the diameter of the solid nanosphere produced was stabilized after ~4 hours at ~50 nm. The fact that there are few nanospheres present after 2 hours of reaction suggests that nanosphere formation is slower or starts later than the formation of the nanocapsules. To further investigate the dimension growth with reaction time, analysis of variance (ANOVA) was conducted to the four groups of dimensions in Figure 3.5 (h). The data in each group show heteroscedasticity problems in Levene's test. Thus Welch's ANOVA is used. Except for the outer diameters of nanocapsules, the means of dimension measurements are unequal. The paired comparisons in adjacent timepoints were conducted via t-test. Then the overall trend of dimension changes was revealed via fitting the

dimensions by reaction time with a linear regression model. These analysis results were shown in Table 3.1. It can be found that for nanocapsules, the outer diameter increase was slow and not significant after 2 hours. While their inner diameters continuously reduced until 8 hours. As a result, the wall thickness showed a significant growth rate during the reaction period. For the nanospheres, the outer diameter changes in a non-monotonous way. The measurements at 4-8 hours were larger than the rest time. The time regression coefficient shows a negative value. We are not clear about the reason for this observation. Other than measurement errors, one possible reason is that during the 4-8 hours, both nanospheres and nanocapsules are largely dispersed in the medium, parts of nanocapsules were mistakenly regarded as nanospheres, and led to overestimation of the nanosphere dimensions. Furthermore, the small coefficicent indicates the weak effect of reaction time on nanosphere dimensions.

Table 3.1 Statistic analysis of reaction on nanoparticle dimension change

Dimension	P-value of Levene's test	P-value of Welch's ANOVA	Satterthwaite t-test[a]	time coefficient[b]	P-value of time coefficient[c]	Pearson corr coef
Nanocapsule Outer diameter	0.0004	0.0857	$d_{2h} \approx d_{4h} \approx d_{6h} \approx d_{8h} \approx d_{10h} \approx d_{12h}$	0.21016	0.0535	0.08180
Nanocapsule Inner diameter	<0.0001	<0.0001	$d_{2h} > d_{4h} > d_{6h} \approx d_{8h} \approx d_{10h} \approx d_{12h}$	-0.80751	<0.0001	-0.36817
Nanocapsule Wall thickness	<0.0001	<0.0001	$d_{2h} \approx d_{4h} < d_{6h} < d_{8h} < d_{10h} \approx d_{12h}$	0.4755	<0.0001	0.55045
Nanosphere Outer diameter	0.0252	<0.0001	$d_{2h} < d_{4h} \approx d_{6h} \approx d_{8h} > d_{10h} < d_{12h}$	-0.22487	<0.0001	-0.13811

[a] "≈" indicates the null hypothesis of a two-sided t-test is accepted. "<" or ">" indicate the alternative hypothesis of a one-sided lower-tail or upper-tail is accepted.
[b,c] Linear regression results of dimension by reaction time.

Interestingly, the average radius of the nanospheres, 25 nm, is like the wall thickness of nanocapsules, 26 nm. As both nanoparticles are formed through precipitation of PDA, their similar thicknesses (radii for the nanospheres) are probably determined by the same initial DA

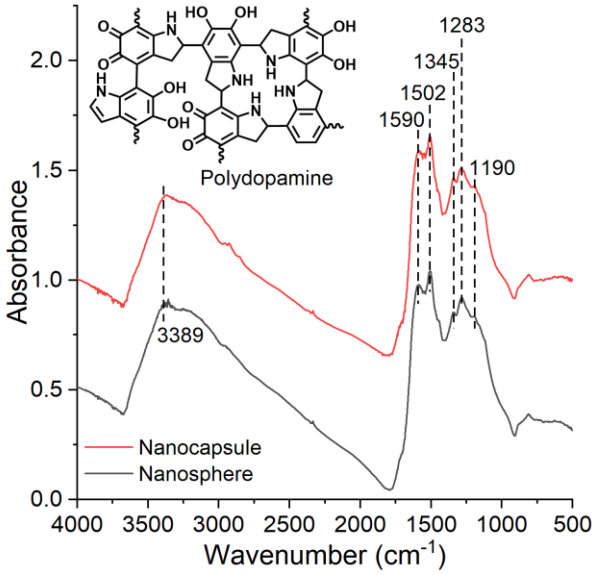

Figure 3.7 FTIR spectra of PDA nanocapsules and nanospheres. The wide peak at 3389 cm^{-1} is attributed to the stretching vibration of phenolic -OH and N-H groups. [7] The peak at 1590 and 1345 cm^{-1} correspond to bending of N-H and O-H groups. At 1726 cm^{-1}, the peak indicates stretching vibration of C=O, and the aromatic C=C bending is present at 1502 cm^{-1}. [8] Additionally, the peaks at 1283 cm^{-1} and 1190 cm^{-1} indicate the stretching of C-N. [9]

concentration. FTIR spectra obtained for nanocapsules and nanospheres, Figure 3.7, confirms that though synthesized into different morphologies, both nanoparticles have the same chemical composition. The inner diameter of the nanocapsules decreased over the first six hours of reaction, from 21 nm to 15 nm. This suggests that the overall reaction proceeds via two phases. First, DA polymerizes and precipitates onto the surface of nanodroplets in the EtOH/H_2O solution. The nanodroplet diameter and thickness of this deposition layer establishes the outer diameter of the nanocapsules. The process is primarily completed in the first 2 hours. In the following phase, additional DA that polymerizes in the bulk solution forms solid nanospheres through a process of aggregation. These aggregates are stabilized at a diameter of ~50 nm, and further DA polymerization in the bulk solution results in more nanospheres. This process continuously produces solid nanospheres through the reaction. As the reaction proceeds, the DA trapped in the nanodroplet polymerizes and precipitates onto the inner surface of the nanocapsule, increasing the nanocapsule wall thickness. This process lasts until the DA trapped inside the nanocapsule is

depleted and takes ~ 6 hours. The longer time for this process compared to the initial deposition of the nanocapsule shell can be attributed to the slower DA polymerization observed in EtOH compared to H_2O.[446, 557]

3.3.3 Effect of EtOH Volume Fraction on Nanocapsule Formation

The synthesis was also conducted using a range of EtOH contents. Without the presence of EtOH, no nanocapsules were formed, and only solid nanospheres were obtained, Figure 3.8 (a). At low EtOH fractions, 5 vol.% and 10 vol.%, lots of nanocapsules were formed. The inner diameter, outer diameter, and wall thickness of the particles produced using 5 vol.% and 10 vol.% EtOH fractions are similar, Figure 3.8 (b), (c), and (g). However, as the EtOH content is increased to 20 vol.%, the size of the particles dramatically increases, Figure 3.8 (d) and (g). At EtOH content of 30 vol.%, the average particle size is smaller than that at 20 vol.%, but there are still a considerable number of large particles present, Figure 3.8 (e) and (g). Surprisingly, while the sizes of the particles increased with increased EtOH content, the capsule wall thickness remains relatively constant at around 23 nm, Figure 3.8 (g), which further confirms it is the initial DA concentration that determines the wall thickness of nanocapsules.

To evaluate the hypothesis that PDA nanocapsules form around EtOH nanodroplets, EtOH/H_2O mixed solutions with 5 mM Tris and without the addition of DA were investigated via DLS, Figure 3.8 (f). Interestingly, the relative size distributions of nanodroplets in the reaction medium are consistent with the relative size of nanocapsules formed in these solutions upon the addition of DA, Figure 3.8 (h). A positive correlation can be observed in the inset graph. The reaction media with the largest droplet size, 316 nm in 20 vol.% EtOH, produced the largest

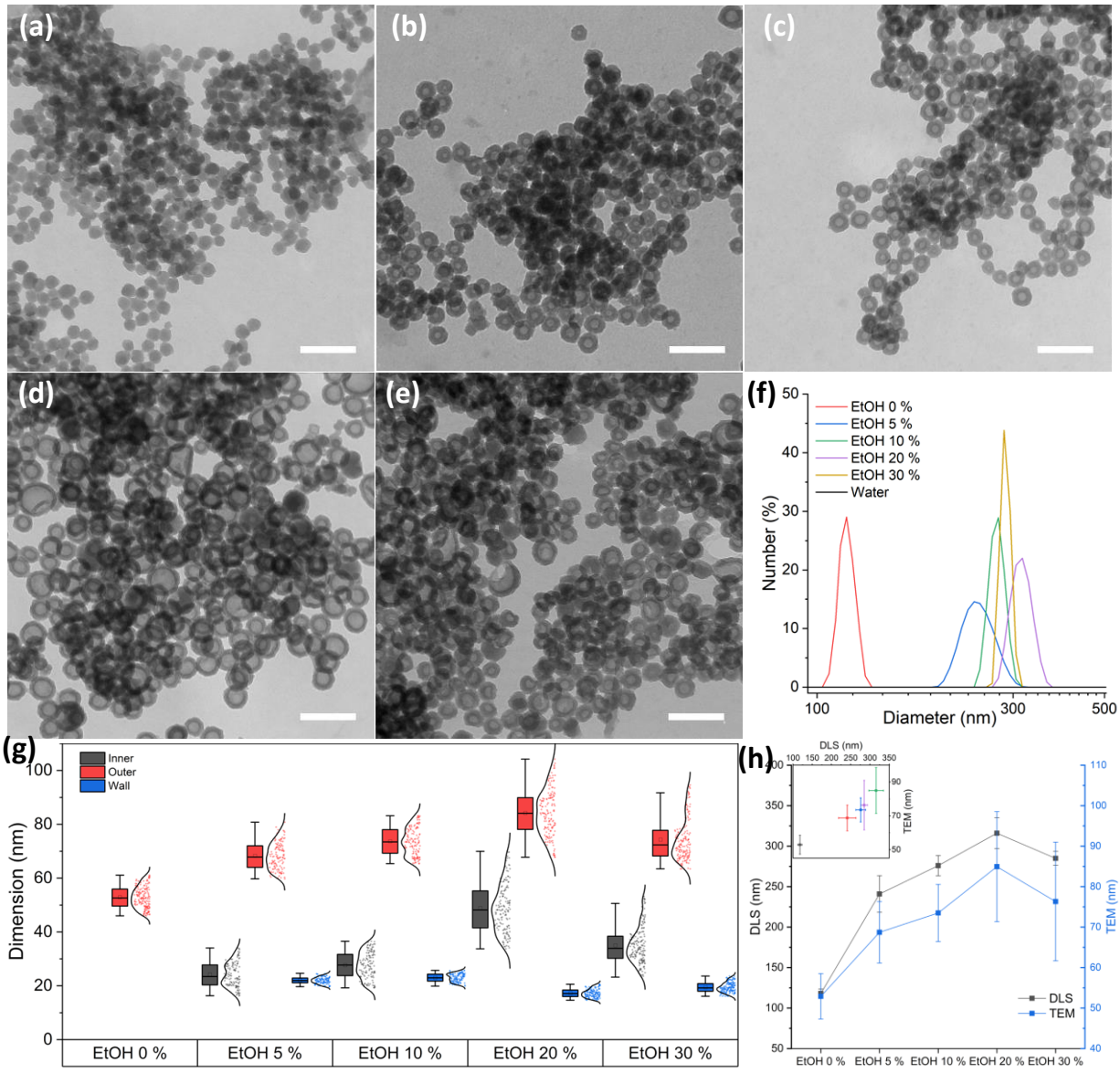

Figure 3.8 TEM images of PDA nanocapsules prepared in unsealed 0.606 mg/ml Tris in EtOH/H_2O solutions, 0.3 mg/ml DA and different EtOH composition (a) 0 vol.%, (b) 5 vol.%, (c) 10 vol.%, (d) 20 vol.%, and (e) 30 vol.%. (f) Droplet size distributions obtained via DLS. (g) Nanocapsule dimensions obtained by measurement of more than 100 random particles in TEM images using ImageJ. (h) Comparison of droplet size and particle outer diameters as a function of EtOH content. The inset graph is the plot of DLS measurements by TEM measurements. The error bars are standard deviation. The scale bars in TEM images above represent 200 nm.

nanocapsules, 84 nm outer diameter. While the reaction media with the smallest droplet size, 241 nm in 5 vol.% EtOH, produced the smallest nanocapsules, 68 nm outer diameter. In Tris solutions without EtOH, much smaller droplets, 118 nm, were detected. Conducting the reaction in this

media produces only solid nanospheres with a diameter of 53 nm. As a control, the water used in this work was also tested by DLS, and no particles or "droplets" were observed via DLS. The presence of Tris allows the formation of droplets upon the addition of EtOH in this system. When only Tris is present in the system, polymerization of the DA to PDA produces nucleated particles that grow as the reaction continues. In comparison, when EtOH is added, PDA is deposited at the droplet interface resulting in the formation of nanocapsules. DLS measures the hydrodynamic size, while TEM measurements are of solids in a desiccated state. As a result, DLS measures of diameter can be 2 to 5 times that obtained from TEM imaging, even for ceramic particles.[558] Though the DLS measures of droplet size are larger than the diameters of the obtained particles, the correlation between droplet size and particle dimensions suggests that the droplet size is critical in determining the morphology of the obtained particle. Also, EtOH seems to be a prerequisite for the formation of hollow particles.

Table 3.2 Calculated specific surface areas of the particles produced in this work

No.	Nanoparticle	Preparation condition	Outer radius (nm)	Inner radius (nm)	Mass-based surface area (x 10^6 m^2/g)	Volume-based surface area (x 10^7 m^{-1})
1	Uncollapsed nanocapsule	0.15 mg/ml DA, 20 % EtOH, sealed	35.62[a]	24.84[b]	1.06	8.42
2	Collapsed nanocapsule	0.15 mg/ml DA, 20 % EtOH, sealed	35.62[a]	24.84[b]	1.06	12.7
3	Uncollapsed nanocapsule	0.3 mg/ml DA, 20 % EtOH, unsealed	42.01[a]	21.68[b]	0.69	7.14
4	Solid nanoparticle	0.3 mg/ml DA, 0 % EtOH, unsealed	26.46		0.95	11.3
5	70 nm-diameter solid particle [1-3]		35		0.71	8.57
6	100 nm-diameter solid particle [4-6]		50		0.5	6

[a] The outer radii were obtained by taking the mean value of measurement of 50 random nanocapsules at the corresponding conditions using ImageJ. For sample 1 and 2, only spherical (uncollapsed) nanocapsules were measured.
[b] The inner radii were obtained by subtract the mean wall thicknesses from the outer radii at the corresponding conditions.

3.3.4 Formation of Bowl-like Nanocapsules with Low DA Concentration

Compared with nanocapsules, collapsed bowl-like structures have a smaller particle volume and a larger specific surface area, Table 3.2 (the density is used according to Bernsmann et al.'s work [559]). When the wall thickness of the nanocapsules is thin enough, it can be expected that the particles will collapse into a bowl-like morphology as the solvent trapped in the capsule evaporates. Such morphology is shown in the SEM images in Figure 3.9. The collapse can also be observed via TEM, Figure 3.10. Two reaction conditions were evaluated for their effect on the fraction of collapsed nanocapsules. First, to limit the wall thickness and increase the fraction of collapsed particles, the amount of DA used in the synthesis was reduced, Figure 3.9 (a-c) and Figure 3.10 (a-c). Second, oxygen is known to be critical for dopamine polymerization.[560] The effect of limiting oxygen availability during the reaction on nanocapsule collapse was evaluated by conducting the reaction in sealed vessels. The number fraction of collapsed nanocapsules vs.

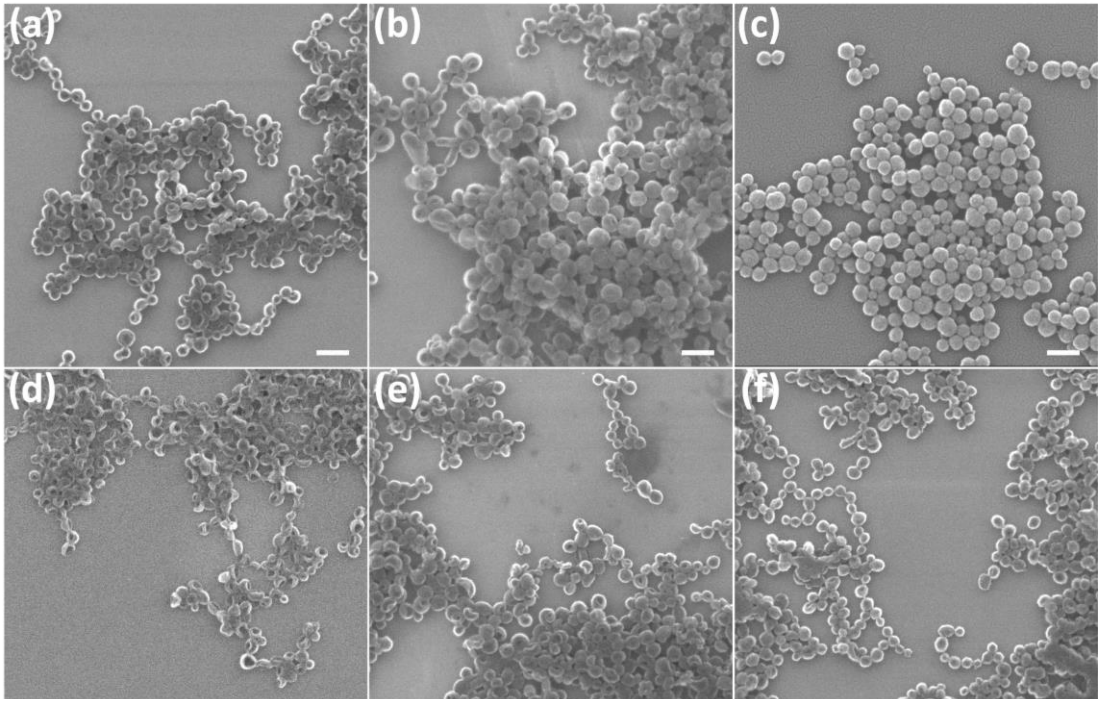

Figure 3.9 SEM images of PDA capsules prepared in 5 mM Tris in EtOH/H_2O (EtOH 20 vol.%) solution in unsealed reaction vessels (a) 0.15 mg/ml, (b) 0.2 mg/ml, (c) 0.3 mg/ml DA, and in sealed reaction vessels (d) 0.15 mg/ml, (e) 0.2 mg/ml, (f) 0.3 mg/ml DA. The scale bars represent 200 nm.

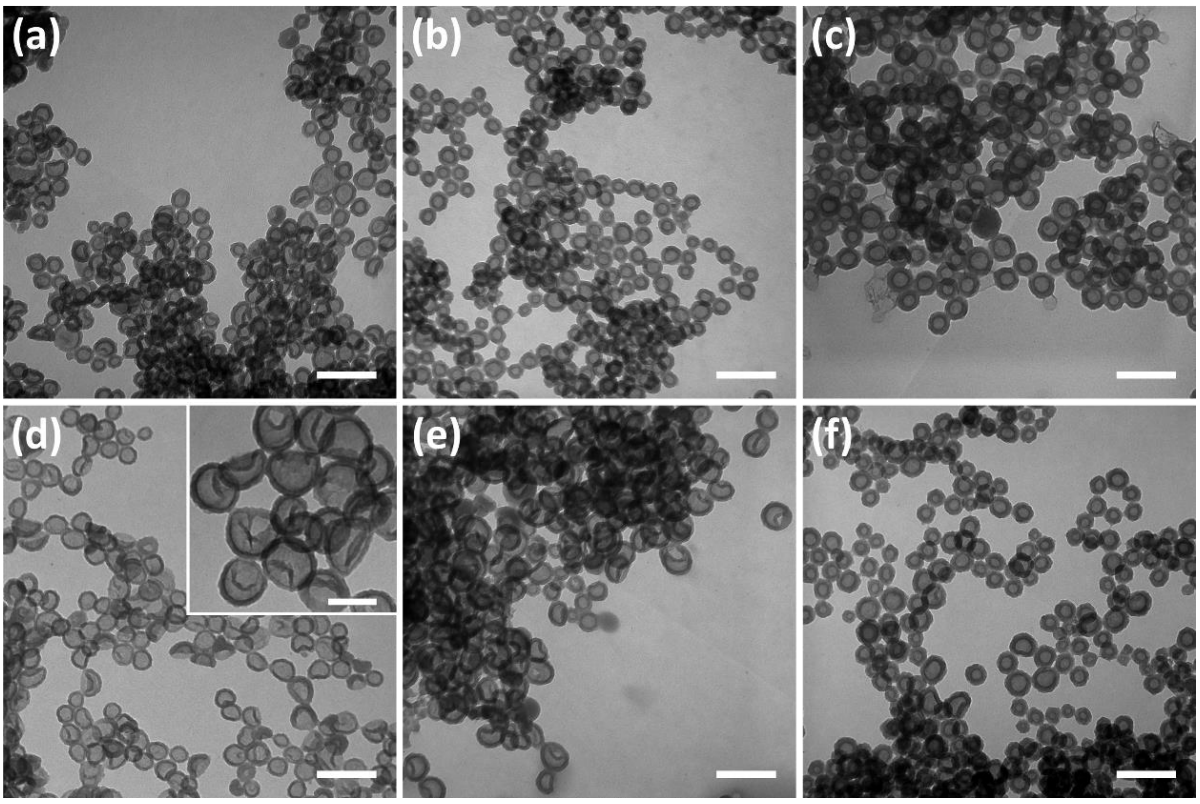

Figure 3.10 TEM images of PDA capsules prepared in unsealed EtOH/H_2O (EtOH 30 vol %) solution with 0.606 mg/ml Tris and (a) 0.15 mg/ml, (b) 0.2 mg/ml, (c) 0.3 mg/ml DA, and hollow PDA capsule prepared in sealed EtOH/H_2O (EtOH 30 vol %) solution with 0.606 mg/ml Tris and (d) 0.15 mg/ml, (e) 0.2 mg/ml, (f) 0.3 mg/ml DA. The scale bars in images represent 200 nm. The inset in (d) is a high-resolution image of collapsed nanocapsules under TEM, the scale bar represents 100 nm.

the nanocapsule wall thickness at various DA concentrations is shown in Figure 3.11. Data is presented for both sealed and unsealed reaction conditions. As the concentration of DA used in the synthesis was decreased, the fraction of collapsed nanocapsules observed increased. In unsealed containers, when 0.15 mg/ml DA was used in the synthesis, around 56 % of the produced nanocapsules were collapsed. In comparison, when 0.3 mg/ml DA was used in the synthesis, no collapsed nanocapsules were observed. Under these conditions, the high DA concentration in the reaction medium results in nanocapsules with large wall thickness. These nanocapsules are mechanically strong enough to withstand the capillary forces during drying and remain uncollapsed. Then the reaction was conducted in sealed containers to evaluate the effect of oxygen. Limiting oxygen resulted in significantly higher fractions of collapsed nanocapsules, Figure 3.9

(d-f), Figure 3.10 (d-f), and Figure 3.11. Over 90% of particles were completely collapsed to a bowl-like morphology when the nanocapsules were produced in sealed containers with 0.15 mg/ml DA added, compared to 56% when the same reactant concentrations were used in unsealed containers, Figure 3.11. Similar improvements are seen when 0.2 mg/ml and 0.3 mg/ml DA were reacted in sealed containers as compared to unsealed containers. In all cases, the mean wall thickness is decreased by 1-3 nm over the wall thickness obtained in unsealed containers. ANOVA analysis supports the hypothesis that both decreasing the amount of dopamine added and sealing the containers reduces the wall thickness of the produced nanocapsules, $p < 0.05$, but that there is no interaction effect between two factors, $p > 0.05$, as shown in Table 3.3.

Table 3.3 Two-way ANOVA of concentration and seal condition on wall thickness.

Source	DF	Type III SS	Mean Square	F Value	Pr > F
DA concentration	2	13253.98287	6626.99143	2524.87	<.0001
seal condition	1	604.48915	604.48915	230.31	<.0001
*DA concentration * seal condition*	2	3.02529	1.51265	0.58	0.5621

A comparison on the fraction of nanocapsules collapsed for sealed containers using 0.3 mg/ml DA and unsealed containers using 0.2 mg/ml DA (or sealed containers using 0.2 mg/ml DA and unsealed containers using 0.15 mg/ml) suggest that wall thickness is not the only factor in determining the likelihood of nanocapsule collapse. In this case, the larger average wall thickness particles exhibited a larger fraction of collapse, Figure 3.11. Polydopamine is formed through a series of covalent and noncovalent interactions.[561] Oxidation of DA enhances covalent bonding, which likely makes the nanostructure more rigid and results in fewer collapsed nanocapsules. In comparison, restricting oxygen limits oxidation, and covalent bonding is reduced. Thus, restricting oxygen results in a weaker material and leads to a higher rate of collapse. Consequently, to produce fully collapsed nanocapsules, both DA and oxidant should be limited. In this study, 0.15 mg/ml DA reacted in sealed vessels resulted in over 90 % collapsed nanocapsules. Considering some of

the collapsed nanocapsules may be regarded as uncollapsed because they face towards the wafer, probably almost all nanocapsules prepared in this condition were collapsed. The critical wall thickness for collapse is assumed to be the average wall thickness of the particles when 50% collapse. This critical wall thickness was found by interpolating the data shown in Figure 3.11 and was found to be ~13 nm for nanocapsules produced in unsealed containers and ~19 nm for nanocapsules produced in sealed containers.

The obtained PDA nanobowls are significantly smaller than those reported previously in the literature. In this work, nanobowls with diameters on the order of 35 - 40 nm are obtained. This is significantly smaller than the nanobowl dimensions typically reported, 260 nm to 4 mm,[545-548] and roughly one-fourth that of the smallest previously reported PDA nanobowls, 150 nm.[470, 550, 562] In addition, the process reported here eliminates the need for the removal of hard templates and uses environmentally benign solvents.

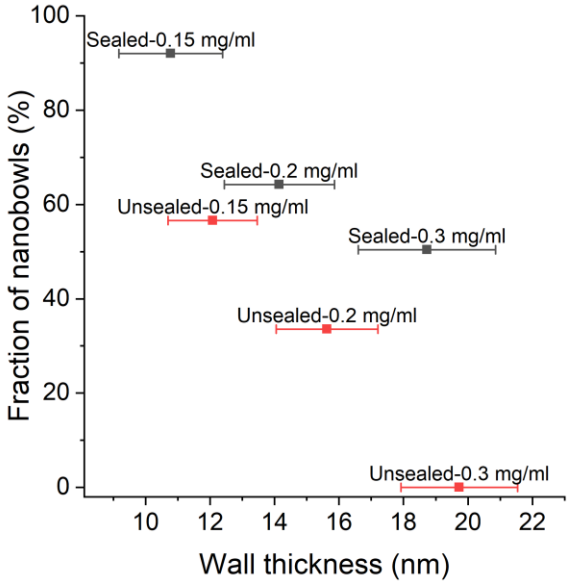

Figure 3.11 The number percentage of collapsed nanocapsules and the wall thickness of nanocapsules prepared in unsealed/sealed 20 vol % EtOH solution with 0.606 mg/ml Tris and 0.15, 0.2, 0.3 mg/ml DA. The thicknesses were obtained by measurement of more than 100 random nanocapsules at each condition using ImageJ. The error bars are standard deviation.

3.3.5 Mechanism of Nanocapsule Formation

Previous reports of droplets in miscible solvent mixtures include those reported in water 1,4-dioxane solutions, [563] and water THF solutions. [551, 563] Ni et al. proposed a mechanism for the formation of hollow nanoparticles based on the dynamic formation of THF droplets based on a microphase separation. During polymerization, small PDA nanoparticles form and deposit on the surface of the droplets.[551] Yan et al. used a water-ethanol (or iso-propanol) solution and long reaction times, 3 days, to produce PDA solid nanospheres. [552] Furthermore, they suggest that the presence of ethanol in the solvent reduces the polymerization rate of DA. In this work, as demonstrated via DLS measurements, there are nanodroplets present in the Tris EtOH/H_2O solutions. A proposed mechanism for nanocapsule formation and subsequent collapse for nanoparticles formed in Tris EtOH/H_2O solutions is shown in Figure 3.12. The process begins with the microphase separation of Tris EtOH/H_2O solutions. Upon the addition of DA to these solutions, self-polymerization begins. As the solubility of the DA is lower in EtOH than in H_2O solution, [564] PDA precipitates at the interface of the droplets forming nanocapsules early in the reaction. Continued polymerization of the DA present in the nanocapsule core results in the nanocapsule wall thickness increasing until the DA is depleted. This final process is slow compared to the initial formation of the shell because DA polymerization in EtOH is slow. [446, 557] As a result, the full wall thickness of the nanocapsules is not achieved until about 6 hours. At longer reaction times, polydopamine aggregates start to nucleate and grow to solid PDA nanospheres in the bulk solution. Over time these solid nanospheres dominate in the reaction products. As a result, at long reaction times, the dominant product is solid nanospheres. Short reaction times, lower DA concentrations, and sealing the containers to restrict oxygen favor a high fraction of thin-walled nanocapsules. As EtOH is removed from the nanocapsules on drying, the

capsules collapse to nanobowls. This process mirrors the formation of microscopic bowl-shaped particles from hollow THF filled PDA nanoparticles observed by Lei et al.[545, 552]

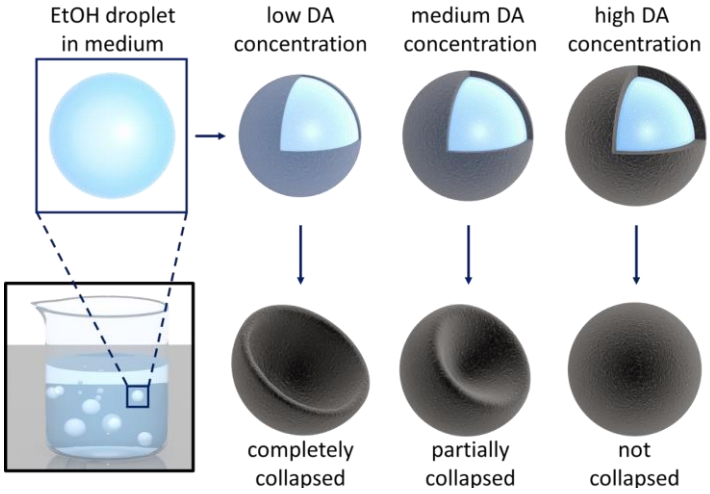

Figure 3.12 Formation of hollow PDA nanocapsules and collapse of thin-walled PDA shells

3.4 Conclusion in the Chapter

In this study, a rapid one-pot template-free method for PDA bowl-like nanostructure was demonstrated. Addition of DA to Tris - EtOH/H_2O solutions produces hollow PDA nanocapsules (80-120 nm) in 1-2 hours. The collapse of these nanocapsules results in particles with a bowl-like shape. The morphology of the nanocapsules produced can be controlled by altering the DA concentration and EtOH content. The mechanism of formation of the nanocapsules is related to the nanodroplets present in the reaction medium. The nanocapsule size is directly related to the reaction medium droplet size. As for collapse, a nanocapsule with a thinner wall is more likely to collapse to a bowl-like structure. In addition, limiting oxygen supply by conducting the reaction in sealed containers increases the likelihood of nanocapsule collapse. The facile synthesis method reported here and the morphological control to the product paves the way to explore bowl-like PDA nanocapsules for biomedical, environmental, catalyst, and electrochemical applications. This template-free morphology-controllable method for PDA bowl-like nanostructure is expected to inspire novel strategies for functional nanostructure synthesis.

Chapter 4

Fabrication of Janus Hollow Polydopamine Nanotubes as a Multiple-Responsive Drug Delivery System

4.1 Introduction

Cancer is the second leading cause of death in the United States. In 2019, 21 % of deaths were due to malignant neoplasms. [565] A conventional and most widely used strategy is chemotherapy. [566] However, the problems like adverse effects, systemic toxicity, and multi-drug resistance after repeated drug administrations may reduce therapeutic efficiency, discontinuation of treatment, or even failure in therapy. [567] Extensively novel nanostructures have been therefore developed as drug delivery systems (DDS). [568] With the application of advanced nanoparticle DDS, not only have these drawbacks been mitigated, but the precise control release of medicines also improves therapeutic efficiency. The delivery technique is also valuable for applying macromolecular therapeutic agents, which can encounter degradation, clearance, and cell internalization problems when administrated. [569] Furthermore, nanotechnology and medicine research advances make it possible to integrate photodynamic therapy, photothermal therapy, nitric oxide therapy, and cocktail strategy with the chemotherapy on DDS. [570] In addition to treatment, real-time and non-invasive tracking of the DDS after administration is also meaningful for both the spatial control release of therapeutic agents and the cancer study. [571-572] A multifunctional drug delivery nanoplatform is therefore highly desirable.

Excellent material for this purpose is polydopamine. Messersmith's team first reported it in 2007. [573] The polymer can be synthesized and coated on almost all materials in mild

conditions.[387] Its excellent biocompatibility has been demonstrated through in vitro and in vivo methods. [2, 9] And in the presence of reactive oxygen species, the melanin-like material can be gradually degraded. [574] Like melanin, polydopamine has a significant photothermal effect, making it a naturally photothermal therapeutic agent and can be used in combination with thermoresponsive systems.[2, 575] The change of zeta-potential between pH 7.4 and 5.5 can be used as a pH control release strategy.[576] Polydopamine nanostructures are also suitable for imaging applications. On one side, polydopamine becomes fluorescent after processed with oxygen species, which can be applied in a cell assay. [433-436] On the other side, metal nanoparticles can be precipitated on polydopamine via catechol groups for magnetic resonance imaging (MRI). [416] Additionally, after the synthesis of polydopamine, the amino and catechol group residues make the further modification easily achieved. [577-578] Therefore, the polydopamine-based multifunctional nanostructures have aroused great interest in medicine application.

Due to the simplicity in fabrication, the predominant DDS are spherical structures. Many studies have been conducted on the size and the surface property influences of nanoparticle circulation, tumor accumulation, and cell internalization. [447-450] Several studies indicate that the flexible nanoparticles with a high aspect ratio (AR) may present unique advantages in these processes. Mitragotri's team conducted early exploration. [357, 451-452] In these studies, rigid microparticles with different AR and shapes were fabricated with polystyrene (PS) and used to prepare the medium for macrophages incubation. They found that whether the internalization can be initiated depends on the local dimension in contact with macrophages. In contrast, the particle size determines if the internalization can be accomplished. Geng et al. demonstrated the extended circulation life of flexible filament-shaped micelles (filomicelles). [365] Their in vitro studies

found that the capture efficiency of filomicelles by macrophages reduced with the nanostructure length in both static and dynamic conditions. They attributed the observation to, on one side, the cooperative inhibition binding between macrophages and filomicelles, on the other side, the hydrodynamic force of fluid. During the in vivo study, the extended circulation life was also observed with increasing the filomicelle length. Recently, the superior circulation performance of filomicelles than spherical micelles was also observed in Li et al.'s work. [371] However, when the nanoparticles are decorated with target ligands to cells, the internalization could be enhanced. In Barua et al.'s study, the trastuzumab ligand modified PS nanorod showed significantly higher cell uptake than the spherical controls.[369] For flexible structures, Zhang et al. demonstrated a similar effect, i.e., the folate decorated filomicelles achieved higher KB cell accumulation than spherical micelles. [370] This contrast is because more ligands available on high AR nanostructures could facilitate the cell uptake process through multivalent binding of nanoparticles to cells. In addition to the effect of cell-nanoparticle interaction, a recent simulation study by Cooley et al. found that shapes can also influence the distribution and margination of nanoparticles in blood flow.[579] Moreover, the high AR may show an advantage in cell uptake and transport across intestinal cells during oral drug delivery.[361] Nonetheless, high AR may present higher organ accumulation during circulation, like lungs and spleen, which is undesirable in drug delivery and can lead to systemic toxicity.[373, 580-581] Overall, given the relatively limited studies of non-spherical DDS and the intriguing effect of shape in drug delivery, the high AR DDS is worth well for further investigation.

Several methods have been developed to fabricate non-spherical nanostructures, including replication in non-wetting templates (PRINT),[464] microfluidics, [460] projection photolithography, [582] film-stretching, [465] solvent evaporation, [583] self-assembly, [371,

466-469], and template-assisted fabrication. [470] These methods have their respective advantages and limitations. The first four methods can produce non-spherical particles with uniform shapes and dimensions. However, the PRINT and projection photolithography need sophisticated instruments, especially for the drug delivery purpose, which requires the particle size to fall into 30-200 nm. [74] Moreover, microfluidics cannot produce particles below a micron. [584] As for film-stretching, though the method is simple and can easily adjust the AR of prepared particles, it is suitable for preparing rigid solid thermoplastic particles.[363] The solvent evaporation and self-assembly method can be facilely conducted in a lab, but the regularity and repeatability of products are not as good as previous methods. Their dimension and geometries cannot be easily tuned as prior methods. Then for the template-assisted fabrication, the size, shape, and quality of nanostructures are primarily dependent on the template and the coating material. For example, by using porous anodic aluminum oxide (AAO), Chen et al. synthesized nanotubes with the diameter of 200 nm. [473] And Gao et al. using the reverse micelle prepared nickel hydrazine as a template synthesized hollow silica nanorods with diameters in 10-20 nm.[585] However, it is still difficult to prepare nanoparticles with more sophisticated structure. The previous methods can only synthesize either solid or hollow structures. The Chen et al.'s method could prepare nanotubes with accessible lumen, but the size of the template limits its application in drug delivery.

We prepared hollow nanorods with halloysite nanotube as the template and polydopamine as the template material in our previous work.[586] However, on one side, the structure is still a simple hollow nanorod without accessible lumen; on the other side, the structure can be collapsed in the desiccated condition. This work reports a halloysite-sonication-etching method to prepare robust hollow polydopamine nanotubes with the accessible lumen. The staged approach also makes the different modifications to the inner and outer surface of polydopamine nanotubes

possible. To demonstrate the feature, we decorated poly(ethylene glycol) (PEG) and Poly(N-isopropylacrylamide) (PNIPAM) on both layers respectively to enhance the hydrophilicity and biocompatibility and add thermal responsiveness to the nanotube. Aiming to develop the structure as a smart DDS, we precipitated superparamagnetism Fe_3O_4 on the particles to endow it with the magnetic response. Furthermore, to demonstrate its potential application in control release, the doxorubicin (DOX) release profiles from the nanotubes in the exposure of near-infrared laser, magnetic field, and different pH conditions were provided.

4.2 Experiments

4.2.1 Materials

Dopamine chloride (DA), succinic anhydride (SA, 99%), iron(II) sulfate heptahydrate ($Fe_2SO_4 \cdot 7H_2O$, 98%), 1-(3-dimethylaminopropyl)-3-ethylcarbodiimide hydrochloride (EDC HCl, 98 %), 4-(dimethylamino)pyridine (DMAP, 99%), tetrahydrofuran (THF, stabilized, HPLC grade), bisacrylamide (MBA) and iron(III) chloride ($FeCl_3$, 98%) were obtained from BeanTown Chemicals. N-Isopropylacrylamide (NIPAM, 98%), N-hydroxysuccinimide (NHS, 98%) were purchased from Tokyo Chemical Industry. β -(N-Morpholino)ethanesufonic acid (MES) monohydrate (MES, 98%) was bought from JT Baker. Poly(ethylene glycol) 2000 (PEG), sodium phosphate (Na_2HPO_4), chloroform ($CHCl_3$, HPLC grade) and doxorubicin were obtained from MilliporeSigma. Sodium chloride (NaCl) was obtained from Fisher Scientific. Halloysite nanotubes (HNT) were obtained from Bonding Chemical. Hydrofluoric acid (50%, v/v ACS grade), hydrochloric acid (HCl, 10 % v/v), ethylene glycol (EG, semi grade, 99%), ethanol (EtOH, ACS grade, 99.5%) and ammonia ($NH_3 \cdot H_2O$ in water, 28-30%) was obtained from BDH Chemicals. 2,2'-(Diazene-1,2-diyl)bis(2-methylpropionamidine)dihydrochloride (V50, 95%) was purchased

from Matrix Scientific. Nucleopore hydrophilic membrane (pore size: 0.4 μm) was purchased from Cytiva. All chemicals were used without further purification. Deionized (DI, ultrapure type 1) water was used in all the experiments.

4.2.2 Characterizations

Morphology of nanostructures was obtained using transmission electron microscopy (TEM, Zeiss EM10, Germany) and scanning electron microscopy (SEM, JEOL JSM-7000F). TEM was conducted at an accelerating voltage of 60 kV. The specimens for TEM were prepared by drying a droplet of nanoparticles suspension diluted with EtOH on a 300 mesh formvar/carbon film from Electron Microscopy Sciences. The PDA shell thickness distributions were obtained by measuring over 40 randomly selected nanotubes in the TEM images using the image analysis software (ImageJ, National Institutes of Health, Bethesda, MD, USA). SEM was performed at an accelerating voltage of 20 kV. The samples for SEM were prepared by attaching lyophilized nanoparticles to the conductive tapes. Fourier transform infrared spectra (FTIR) were obtained via a Shimadzu IR Prestige-21 FTIR spectrometer. KBr pellets were prepared at a sample to KBr ratio of 1:100. UV-Vis spectra were obtained on an Agilent Cary 60 UV-Vis, doxorubicin concentration in solution was obtained by measuring absorbance at 480 nm. The turbidity test was conducted by measuring the absorbance at 600 nm of 0.2 mg/mL nanoparticle dispersions in pH 7.4 PBS solution under 25 and 55 °C. The surface charge and hydrodynamic dimension of nanoparticles in DI water were measured by a ZetaSizer Nano ZS90 sizing instrument (Malvern, Worcestshire, UK).

4.2.3 Synthesis of PEG-SA

Carboxyl groups were grafted on the terminals of PEG via a modified esterification method. [587] In a typical reaction, 33 g PEG, 6.9 g SA and 1.687 g DMAP were dissolved in 220 ml THF at room temperature. The solution was stirred in a 50 $°C$ water bath. The reaction was lasted 72 hours, during which the solution gradually changed from clear and transparent to white semitransparent. Next, the THF was entirely removed by evaporation and evacuation. To purify the PEG-SA and remove the unreacted SA, 35 ml of $CHCl_3$ was then added to the container with the obtained product, and the suspension was kept shaking for 2 d. Finally, the suspension was centrifuged on a Heraeus Megafuge 8 (Thermo Scientific) at 4500 RPM for 5 hours. The supernate was kept, and the $CHCl_3$ was removed by evaporation. The residual solid is PEG-SA.

4.2.4 Synthesis of Polydopamine-Halloysite Nanotubes (PDA-HNT)

To prepare the PDA-HNT, 1 g template HNT was first dispersed in 200 mL DI water using a sonicator. DA can rapidly form oligomer and aggregate in neutral or basic aqueous solution; thus, to ensure a homogenous shell can be formed on HNT, the DA solution was prepared by dissolving 4 g DA in 200 mL 0.1 % (v/v) HCl aqueous solution. Then both solutions were combined in a 2 L flask. Next, 1.6 L DI water, 3.8 mL HCl and 1.36 mL $NH_3 \cdot H_2O$ were added to the container. The pH of the medium should be around 8.7 at this time. After 48-hour mild stirring, $NH_3 \cdot H_2O$ was used to adjust the medium pH to 8.7, and the stirring was continued for another 48 hours. The PDA-HNT was collected using vacuum filtration to process the medium through the 0.4 μm nucleopore membranes. The residue was then dispersed in DI water and filtered again for 3-5 cycles until the filtrate was colorless. Finally, the PDA-HNT product was dispersed in 650 ml DI water for further use.

4.2.5 Fragment of PDA-HNT

To make the lumen of the PDA nanotube accessible, the PDA-HNT was fragmented by a sonicator. In this process, 15 ml PDA-HNT suspension was transferred to a polypropylene test tube to allow the probe of sonicator immersed in the liquid. Then the suspension was sonicated for four hours at 350 W (QSonica LLC, Q500). After the processing, the suspension was centrifuged at 700 g for 1.5 h. The precipitate was kept and further purified by dispersion and centrifuge at 21,694 g for 1.5 min until the supernate became colorless. The fragmented PDA-HNT was then dispersed in 7.5 ml DI water.

4.2.6 Outer Modification of PDA-HNT with PEG-SA and Template Removal

The outer layer modification of PDA-HNT was performed through EDC/NHS conjugation. In a typical reaction, 9 g PEG-SA, 1.52 g EDC, and 3.39 g NHS were dissolved in 100 mL of 100 mM MES solution. After adjusting the pH to 5.35, the solution was stirred at 400 RPM for 15 min. Next, 30 mL of fragmented PDA-HNT suspension was dispersed in 70 mL of 100 mM Na_2HSO_4 solution. The dispersion was combined with the MES solution, and the pH was adjusted to 7.4. The reaction medium was stirred at 400 RPM for 24 h. Then the product was collected using the filtration membrane and purified through 4 cycles of centrifuge and dispersion, after which the PEG-SA attached PDA-HNT (PEG-PDA-HNT) was dispersed in 30 mL DI water.

After the outer modification, the HNT template was removed via HF. In this process, the nanotubes in 30 mL of the above suspension were collected through centrifugation and dispersed in 6 mL DI water, then 1.5 mL HCl and 0.45 mL HF was added to the medium. The suspension rapidly converted from black to brown and gas bubbles were generated in the liquid. After mild stirring for 6 h, the etched samples were collected through centrifugation (21,694 g, 2 min), then

exhaustively purified through 5 cycles of re-dispersion and centrifuge. PEG-SA attached PDA nanotubes (PEG-PDA-NT) were dispersed in 15 mL DI water, and the concentration of PDA nanotubes was estimated via the calibrated PDA curve for further use.

4.2.7 Calibration of PDA Nanotube UV-Visible Curve

To keep PDA nanotubes well dispersed in an aqueous solution and to conveniently quantify the amount of PDA nanotubes, the UV-visible concentration curve of the PDA nanotube was calibrated. In short, 20 mL PEG-PDA-NT was evenly divided into two batches. One batch was lyophilized with the Freezone system (Labconco corporation), and the obtained powder was weighed to obtain the mass of one batch. The other batch was diluted in different times and measured with UV-visible spectroscopy. A calibration curve of PEG-PDA-NT dispersion at 600 nm was therefore obtained.

4.2.8 Inner Modification of PEG-PDA-NT with V50 and in situ NIPAM Polymerization

To decorate the inner layer of nanotubes with the thermoresponsive polymer, poly(N-isopropylacrylamide) (PNIPAM), the initiator, V50, was firstly attached on the inner surface via Michael addition. In this process, 10 mg PEG-PDA-NT was dispersed in 15 ml DI water. 1.87 g V50 was added to the dispersion. After the pH was adjusted to 9.5, the reaction lasted 24 h with 400 RPM. The V50 attached PEG-PDA-NT was collected using nucleopore membrane and purified through several cycles of redispersion and centrifuge. The obtained product (PEG-PDA-V50) was dispersed in 10 ml EtOH and stored in the freezer to avoid degradation of V50.

Then the PNIPAM was synthesized on the nanotubes using the attached V50 as the initiator. In a 150 mL round-bottom flask, 100 mL of EtOH, 10 mg PEG-PDA-V50, 20 mg MBA, and 24 g

NIPAM were added. After two-min stirring, the NIPAM and MBA were wholly dissolved in the medium. Then the flask was stirred and heated in an oil bath at 90 $°C$ under a nitrogen atmosphere. The reaction lasted 12 h. Finally, the product was collected using a nucleopore membrane and purified through several cycles of redispersion and centrifuge. The obtained product (PEG-PDA-PNIPAM) was dispersed in 10 ml EG for further use.

4.2.9 Precipitation of Fe_3O_4 Magnetic Nanoparticles on PEG-PDA-PNIPAM

Fe_3O_4 nanoparticles were precipitated via a hydrothermal method to endow magnet response to the nanotubes. Before the reaction, $FeCl_3$ and $FeSO_4 \cdot 7H_2O$ were dissolved in EG to prepare 53 mM $FeCl_3$ solution and 36 mM $FeSO_4$. Next, 3 mg PEG-PDA-PNIPAM was dispersed with 9 ml EG in a 20 ml Teflon tube. 0.4 mL $FeSO_4$ solution and 0.4 mL $FeCl_3$ solution were added in the EG suspension. The medium was stirred at room temperature for 0.5 h. After 1 mL $NH_3 \cdot H_2O$ was dropwise added, the medium was stirred for another 0.5 h. Then the Teflon tube was put in a hydrothermal autoclave reactor and heated to 205 °C for 8 hours. After the reactor cooled down, the reaction medium was transferred to a centrifuge tube. Next, the Fe_3O_4 magnetic nanoparticle attached PEG-PDA-PNIPAM (mag-PEG-PDA-PNIPAM) was purified through 3 cycles of centrifuge and redispersion with DI water. Finally, the product was dispersed in 6 ml DI water for further study.

4.2.10 Drug Loading of DOX on Nanotube Samples

Loading was performed by adsorption of DOX by 0.5 mg/ml of PDA-NT, PEG-PDA-NT, PEG-PDA-PNIPAM, or mag-PEG-PDA-NTs from DOX solution (0.5 mg/ml in DI water) under mild shaking at room temperature. After 12 h, the DOX loaded samples (PDA-NT/DOX, PEG-

PDA-NT/DOX, PEG-PDA-PNIPAM/DOX, or mag-PEG-PDA-PNIPAM/DOX) was collected via centrifugation and washed via fresh phosphate buffer solution (PBS, 10 mM at pH 5.5) three times to remove extra unloaded DOX.

4.2.11 Temperature Effect on DOX Release from Nanotubes

The effect of PEG and PNIPAM modification on the loading and release profile of DOX were evaluate by dispersing 0.25 mg of the DOX loaded samples (PDA-NT, PEG-PDA-NT, and PEG-PDA-PNIPAM) in a 1 mL release medium (10 mM PBS at pH 7.4 or pH 5.5). The release medium was centrifuged, and 0.8 ml supernate was used for DOX concentration measurement with an interval of one hour. Then 0.8 ml fresh PBS was added to the medium. In the first 6 h, the medium was shaken at room temperature. After that, the release medium was shaken in 50 °C water bath for another 6 h.

4.2.12 Stimuli Effect on the Release Profile of Mag PEG-PDA-PNIPAM

The effect of near-infrared irradiation (NIR), static magnetic field, and medium pH were evaluated by monitoring the amount of doxorubicin released into the medium over time. In a typical experiment, a DOX-loaded sample containing 0.25 mg PDA was dispersed to 1 ml PBS (10 mM, pH 7.4 or 5) with mild shaking at room temperature and placed in a 2 mL microcentrifuge tube. If the static magnetic field effect was studied, a magnet was placed below the centrifuge tube. If the NIR effect was studied, the irradiation (808 nm, ~1 W/cm^2) was applied from the top of the liquid for 10 minutes every 50 min, and the measurement was conducted immediately after irradiation. The measurement was conducted every hour. 0.8 mL of release medium was collected and centrifuged (21,964 g for 2 min). Then the supernate was used to measure DOX concentration.

After that, the precipitate was redispersed in the 0.8 mL fresh PBS and returned to the cuvette. The influence of NIR on drug release was investigated using a similar methodology.

4.2.13 Statistical Analysis

All statistical analysis was performed using SAS® OnDemand for Academics. The significance level, α, is set at 0.05. All the error bars are standard errors except Figure 4.3.

4.3 Results and Discussion

4.3.1 Fabrication of Robust Hollow Polydopamine Nanotubes

Figure 4.2 depicts the nanotube fabrication process. Dopamine undergoes a self-oxidation process in the alkaline condition. [573] By suspending HNTs in the dopamine solution, the polydopamine precipitates on the halloysite surface, forming a continuous polymer shell. In this work, halloysite and dopamine were mixed in an acidic condition. After the pH was raised to 8.7,

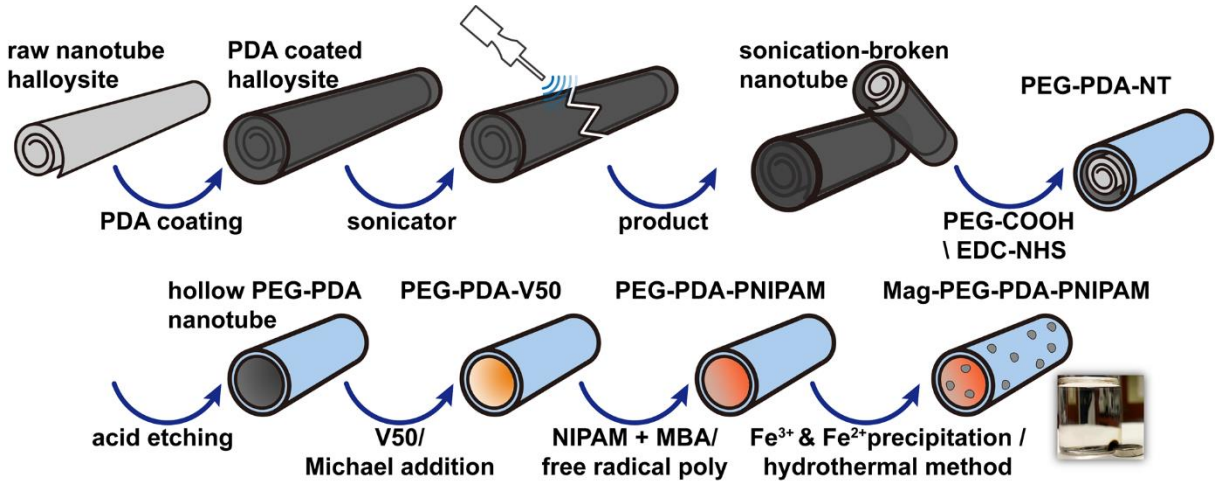

Figure 4.1 The synthesis procedure of the mag-PEG-PDA-PNIPAM nanotubes. The procedure begins with the formation of a conformal coating of polydopamine on halloysite nanotubes. Surface modification of the polydopamine is achieved through reaction with carboxyl terminated PEG-SA. The HNT template is then removed by etching with HF. The initiator V50 is next integrated on the inner surface of the nanotubes, followed by in situ synthesis of PNIPAM, the inner lumen modification was accomplished. Finally, the Fe_3O_4 was precipitated on the nanotubes through hydrothermal method. The image at right bottom corner indicates the particles attracted by the magnet.

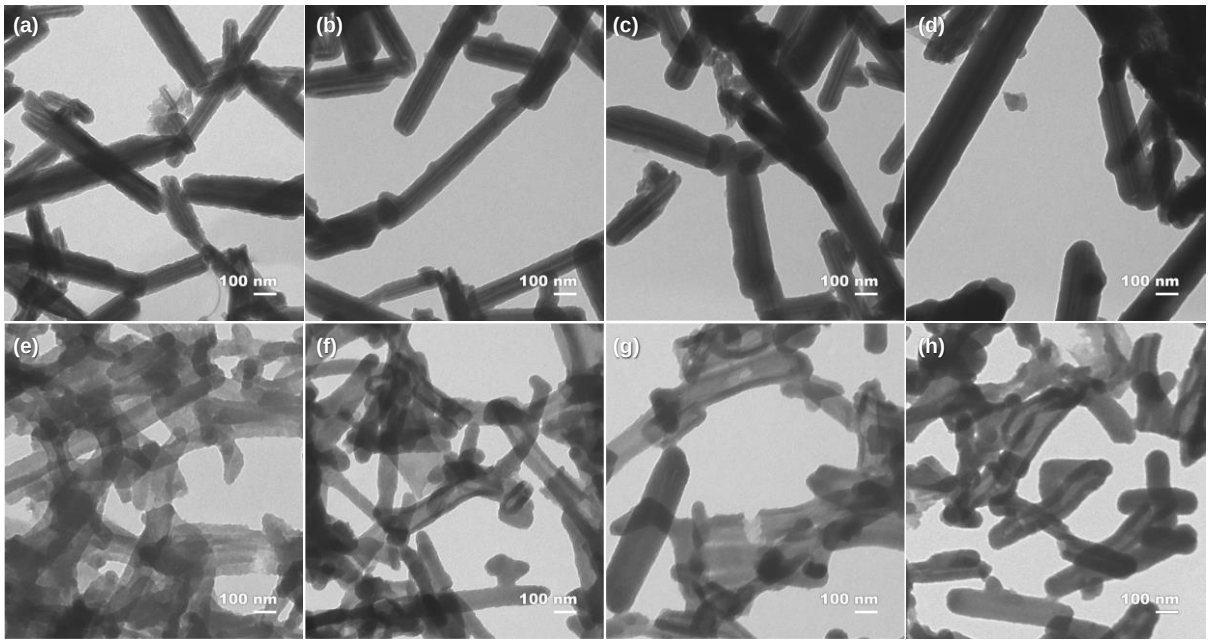

Figure 4.2 TEM images of PDA-HNT synthesized with different DA/HNT ratio and the corresponding nanotubes with HNT etched: (a-d) PDA-HNT prepared with the mass ratio of DA and HNT as 1, 2, 3, 4; (e-h) the corresponding HF-etched PDA-HNT samples from above.

the color of the medium quickly changed to pink, indicating oxidation of the catechol groups and the formation of indoles. The solution gradually turns dark brown as polymerization proceeds. The PDA-HNT composite and the corresponding etched samples were shown in Figure 4.2. The samples were prepared by keeping HNT concentration constant in a medium as 0.5 mg/mL and increasing the DA amount. In Figure 4.2 (a-d), it can be observed that the PDA shell thickness increased as more DA was added. While after the PDA-HNT samples were etched, the products present different morphology. In Figure 4.2 (e), all the nanotubes collapsed as strips lying on the TEM grid. In Figure 4.2 (f), some nanotubes preserve the tubular structure, while others still collapsed to strip. In Figure 4.2 (g), more tubular structures can be found. While in Figure 4.2 (h), the walls of nanotubes become very thick, and they aggregate on the TEM grid. To quantify the effect of DA:HNT ratio on PDA shell thickness, we measured the parameter of samples and plotted it in Figure 4.3. In Figure 4.3 (a), the thickness increases linearly with the DA:HNT ratio from 1 to 4. The thickness increases less when further the DA:HNT ratio is 6. In addition, the variance of

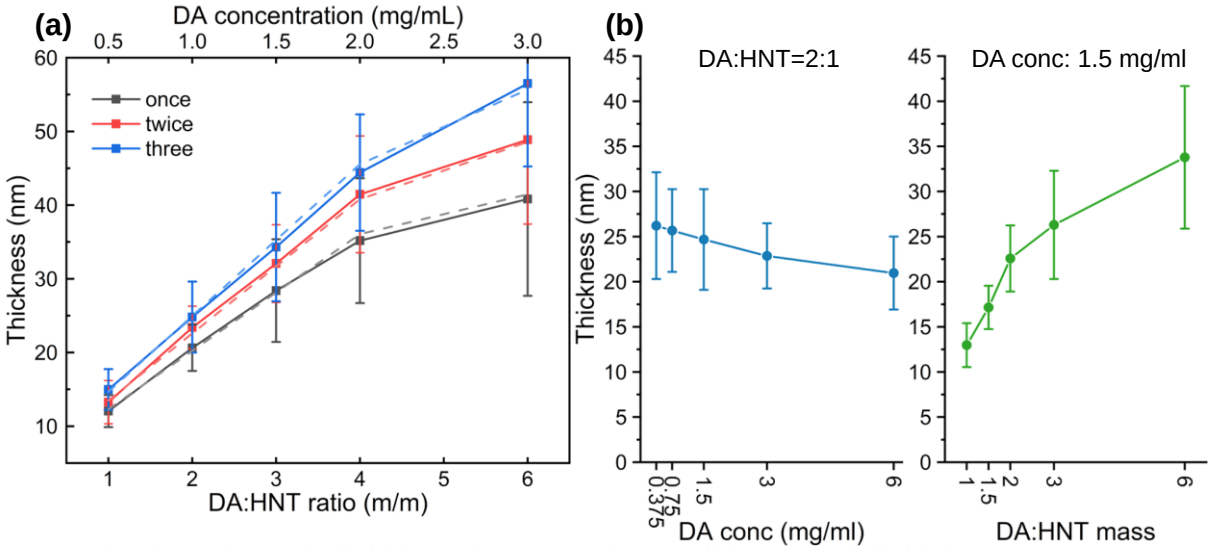

Figure 4.3 The plots of PDA shell thickness by preparation conditions. (a) Shell thickness vs DA:HNT mass ratio. The DA concentration is also altered in different ratios. And the colors indicate the times of pH adjustments during reaction. The dashed lines are predicted curves from linear spline model. The error bars are standard deviations. (b) The shell thickness change with only DA concentration change (left) or DA:HNT ratio change (right). The error bars are standard deviations.

shell thickness is also increased as its value. We found that the pH value of the reaction medium dropped around 7 after 24 hours during the reaction. The higher the DA:HNT ratio, the lower the pH at this time. For the reaction with DA:HNT as 6, the pH dropped to 5.8. These conditions were not favorable for PDA polymerization. Therefore, we re-adjusted the pH to 8.7 and kept stirring for another 24 h and obtained the red curve. This operation was conducted once more to obtain the blue curve. During the process, the pH drops were found less for the reaction with less DA used. Moreover, the more times the pH adjustments were conducted, the less the pH drop. The reduced pH drop can be attributed to less DA, or DA oligomer remained in the medium. As a result, fewer protons were released in the DA polymerization reaction. This can also be reflected in the less thickness increase from the blue relative to the red curve than the red relative to the black curve. Furthermore, after twice pH re-adjustment, the increase of shell thickness almost returned to the linear relationship with the DA:HNT ratio. Given the linear trend at 1-4 ratio, the knot at ratio 4, and the increasing variance as the thickness increase, a linear spline regression model with

weighted least square method was fitted as shown in Table 4.1. According to the model, the DA:HNT ratio is the factor that determines the thickness. When the ratio above is 4, the effect of the ratio on thickness increase reduced significantly. Additionally, the pH adjustment time also influences the slope, i.e., the ratio effect on thickness increase. Due to only limited experimental conditions tested, the model cannot describe the nature of PDA shell growth on PDA-HNT. For example, the thickness should be 0 instead of 4.39172 nm when the ratio is 0. The high R^2 (0.8165) and the excellent fit of the predicted curve to the experiment date shown by the dashed line in Figure 4.3 (a) indicate the linear model is reliable within the experiment conditions and can be used to obtain a PDA shell with the desired thickness.

Table 4.1 Linear spline model of PDA shell thickness on PDA-HNT.

Variable	Parameter Estimate	Standard Error	t Value	Pr > |t|
$\boldsymbol{Intercept}$	4.39172	0.28769	15.27	<.0001
$\boldsymbol{ratio}$	6.73549	0.20161	33.41	<.0001
$(\boldsymbol{ratio}-\boldsymbol{4})_+$	-5.22279	0.47689	-10.95	<.0001
$\boldsymbol{ratio} * \boldsymbol{adjustment\_times}$	1.18493	0.06915	17.14	<.0001

However, it should be noted in the above conditions. The DA concentration was increased as the DA:HNT ratio. To discriminate the contribution of both parameters to the thickness increase, we solely altered one parameter and obtained Figure 4.3 (b). As the DA concentration increases from 0.375 mg/mL to 6 mg/mL, the shell thickness reduces slightly from 26 nm to 23 nm. One possible reason is that the oxygen in the reaction medium is relatively insufficient in a high DA concentration situation. Therefore, the PDA formation and precipitation were minified. While the DA:HNT ratio increased from 1 to 6, the thickness was significantly increased from 13 nm to 34 nm. Therefore, it can be concluded that the ratio between DA and HNT determines the shell thickness. According to Figure 4.2, a robust hollow nanotube can be obtained after etching when the shell is thick enough.

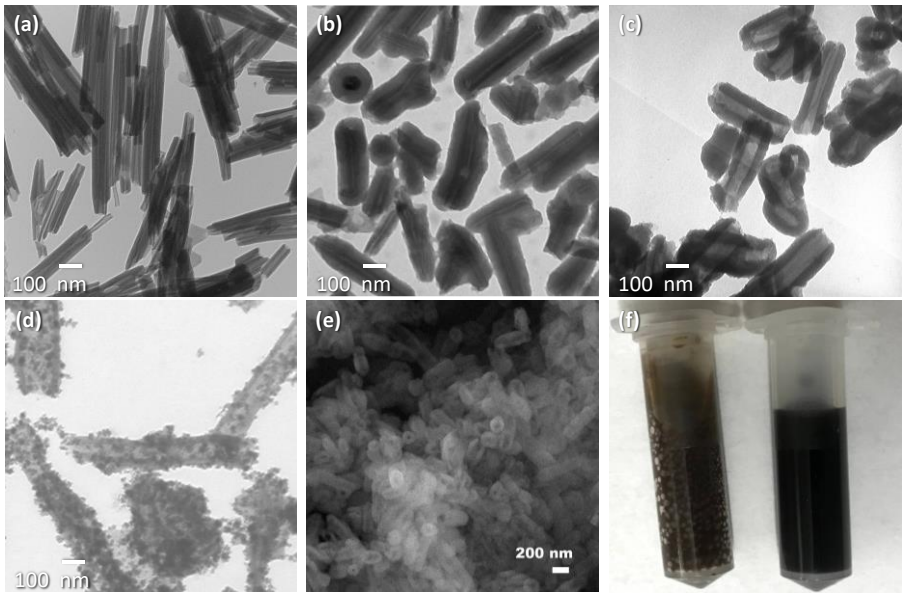

Figure 4.4 TEM images of (a) pristine HNT, (b) PDA-HNT, (c) fragmented PDA-NT, (d) mag PEG-PDA-PNIPAM nanotubes; (e) SEM image of fragmented PDA-NT; (f) sonicated (left) and un-sonicated (right) PDA-HNT during HF etching.

The thick PDA shell can be obtained by optimizing the ratio between DA and HNT, given the results from above. However, as shown in Figure 4.2 (h), a too thick PDA shell may produce nanocapsules rather than nanotubes with an accessible lumen. Previously, Rong et al. fragmented HNT via sonication to obtain uniform nanotubes. [588] Herein, the sonication was introduced to fragment PDA-HNT so that accessible lumen could be obtained after HF etching. As shown in Figure 4.4 (c), the length of PDA-HNT reduced after the sonication process. When HF was added to the PDA-HNT dispersion, gas bubbles were violently generated in the fragmented sample. In contrast, the sample without sonication processing did not show an apparent phenomenon, Figure 4.4 (f). The different phenomena can be attributed to the HF could directly react with HNT exposed in the medium and generated SiF_4 gas. In the un-fragmented sample, the HF must diffuse through the PDA shell to react with HNT, and the gradually generated SiF_4 could be dissolved or hydrolyzed in water. After a series of modifications, the mag PEG-PDA-PNIPAM was obtained, as shown in Figure 4.4 (d). Due to part of the PDA degraded in the hydrothermal reaction, the

thickness of PDA reduced than that in Figure 4.4 (c), but the tubular structure preserved under TEM.

4.3.2 Separated Modification on Both Surfaces of PDA Nanotubes

Due to the presence of HNT before etching in the PDA-HNT, the outer and inner surfaces can be separately modified to achieve a Janus tubular structure. In this work, PEG-SA was conjugated on the outer surface via EDC/NHS reaction. After HNT was removed, the inner surface was firstly attached with V50 via Michael addition. Then PNIPAM was in situ synthesized at the inner layer using V50 as the initiator. Representative FTIR spectra are shown in Figure 4.5. Typical peaks for PDA are observed on all the three curves, which include a wide arch centered at 3385 cm^{-1} indicating the O-H, N-H, and C-H stretching, [8, 495] the peaks at 1291 cm^{-1} due to the C-N stretching on the aromatic ring and 1510 cm^{-1} induced by C=C stretching along with the peak at 1721 cm^{-1} because of the C=O stretching.[8-9] After PEG modification, small peaks appear at 2963, 2932, and 2877 cm^{-1}. These are attributed to the asymmetric and symmetric stretching

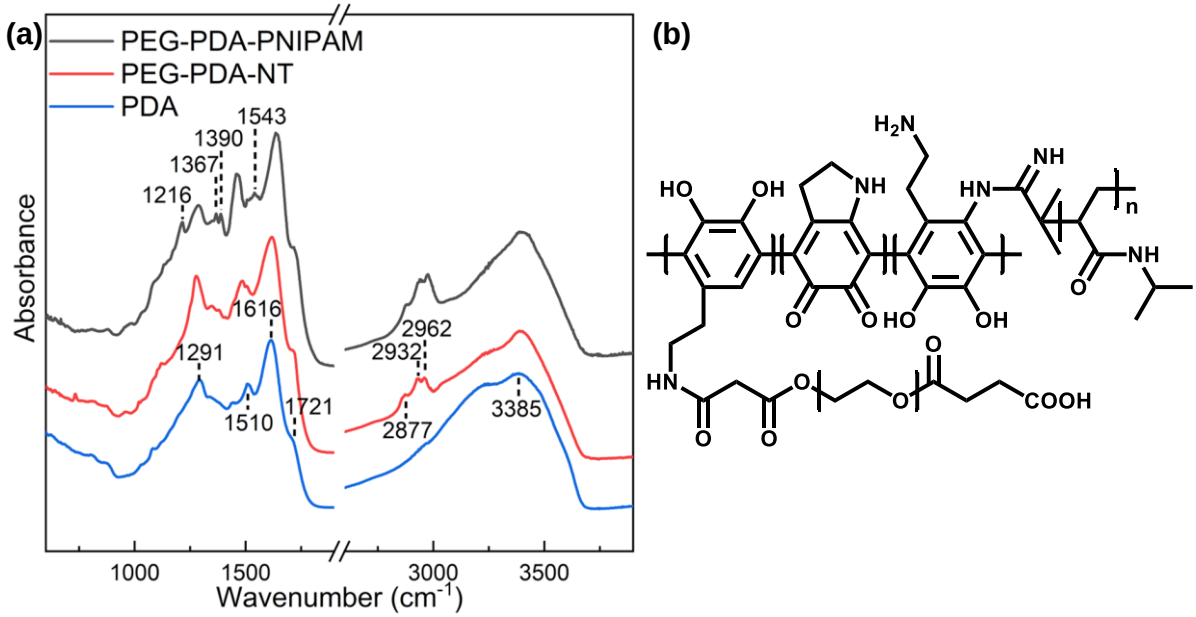

Figure 4.5 (a) FTIR of polydopamine nanotube (PDA-NT), PEG-PDA-NT and PEG-PDA-PNIPAM (b) chemical structure of PEG-PDA-PNIPAM

vibrations of -C-H on PEG.[8, 495-496] After the PNIPAM was decorated, two small peaks arise at 1367 and 1390 cm^{-1}, corresponding to the C-H bending of methyl groups PNIPAM. [589] The peak at 1216 cm^{-1} is due to the C-N stretching vibrations. Finally, the peak at 1543 and 1616 cm^{-1} can be attributed to N-H bending. The peak at 1616 cm^{-1} also appears on the other two curves; thus, it could indicate N-H bending on the amine. After PNIPAM was decorated, the peak at 1543 cm^{-1} might be due to the N-H bending on the amide. These observations indicate that both polymers were decorated on the nanotubes.

Though both polymers present on nanotubes, it is unclear if they are distributed as expected on the inner and outer surface, respectively. Considering the thermal response of PNIPAM, the dimension of PEG -PDA-PNIPAM and the nanotubes with only PNIPAM modification (PDA-PNIPAM) were investigated using DLS as in Figure 4.6 (a). Both samples were dispersed in DI water, respectively. At 25 °C, PDA-PNIPAM showed a slightly larger hydrodynamic diameter than PEG-PDA-PNIPAM, which can be attributed to the different modifications of nanotubes' outer surface. The z-average dimensions can match the sizes observed from the distribution. Moreover, the polydispersity indexes (PDI) are very close for both particles. However, as the temperature increased to 55 °C, the size distribution of PDA-PNIPAM shows a noticeable reduction, while its z-average dimension becomes over 1000 nm, indicating the agglomeration among nanotubes. Furthermore, the PDI increased to 0.82, which resulted from the distinct dimension difference between nanotubes and nanotube agglomeration in the medium. While for PEG-PDA-PNIPAM, the dimension reduced slightly at elevated temperature. The z-average dimension can still match the distribution, and there is no apparent change for the PDI. The results are consistent with the turbidity test, which measures the fraction of nanoparticles that remain in the medium at different temperatures. As shown in Figure 4.6 (b), at 25°C, PDA-NT and PEG-

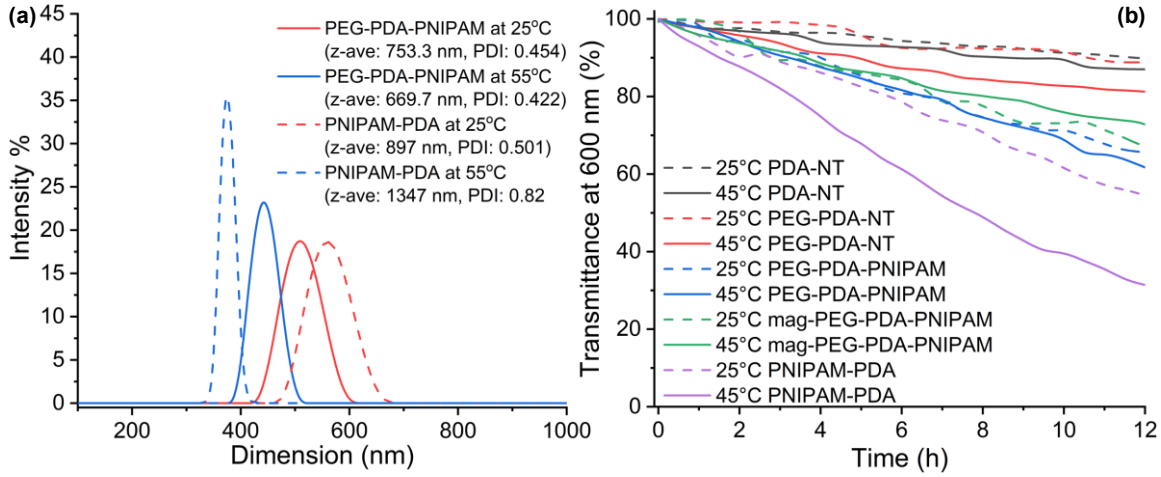

Figure 4.6 (a) DLS results of PDA-PNIPAM and PEG-PDA-PNIPAM at 25°C and 55°C, (b) Absorbance at 600 nm of 0.2 mg/ml nanoparticle dispersions in pH 7.4 PBS at 25°C and 55°C.

PDA-NT kept stable in medium, the PEG-PDA-PNIPAM and mag-PEG-PDA-PNIPAM precipitated at a slow rate, and the PNIPAM-PDA precipitated at a moderate rate. While evaluated to 45°C, the precipitation rates of PDA-NT, PEG-PDA-NT, PEG-PDA-PNIPAM, and mag-PEG-PDA-PNIPAM did not change a lot. As a contrast, the PNIPAM-PDA nanoparticles precipitated rapidly in the medium. These results demonstrate that grafted PEG prevents the modification of PNIPAM on the outer surface and protects nanotubes from agglomeration at an elevated temperature.

4.3.3 Loading of Doxorubicin

DOX was used as the model drug to evaluate the loading capacity of nanotubes. The loading process was accomplished by dispersing 0.25 mg nanotubes in 0.5 ml of 0.5 mg/ml DOX solution. After 12 h, the loaded samples were washed three times with pH 5 PBS buffer. The DOX concentrations in the loading medium and the washing mediums were used to calculate the unloaded DOX. The loading capacity (LC) and encapsulation efficiency (EE) were then calculated as below:

$$LC = \frac{m_{DOX}}{m_{DOX} + m_{NT}} \times 100\% \quad 4\text{-}1$$

$$EE = \frac{m_{DOX}}{m_{DOX\ initial}} \quad 4\text{-}2$$

where m_{NT} is the mass of nanotubes, m_{DOX} is the mass of DOX loaded, $m_{DOX\ initial}$ is the mass of DOX initially added.

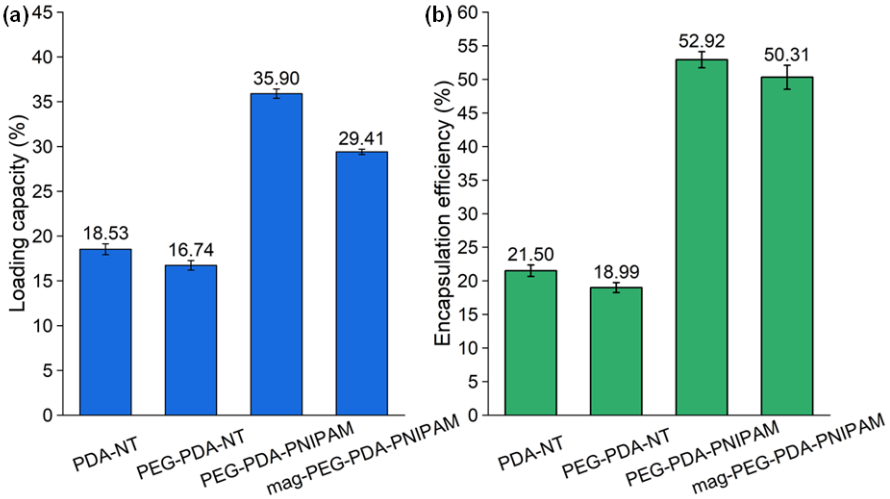

Figure 4.7 DOX loading capacity (a) and encapsulation efficiency (b) of PDA-NT, PEG-PDA-NT, PEG-PDA-PNIPAM and mag-PEG-PDA-PNIPAM. The error bars are standard error.

Figure 4.7 shows the loading capacity and encapsulation efficiency calculated for the four samples. Under pH 8.4, DOX presents as a cation, and due to the abundant catechol, the PDA nanoparticles possess a negative charge at the neutral condition. [590] Furthermore, considering the possible influence of zeta-potential on DOX loading, the zeta-potentials of samples in neutral pH were measured and listed in Table 4.2. After the nanoparticle was partially neutralized after PEG decoration, PEG-PDA-NT has slightly dropped LC and EE than PDA-NT. However, after PNIPAM was attached, both values significantly increased. On one side, the nanotubes became more negative after modification; on the other side, a network may be formed in the nanotubes

Table 4.2 Zeta-potential of PDA-NT, PEG-PDA-NT, PEG-PDA-PNIPAM and mag-PEG-PDA-PNIPAM at pH 7.

Sample	Zeta-potential (mV)
PDA-NT	-35.5
PEG-PDA-NT	-20.8
PEG-PDA-PNIPAM	-30.5
mag-PEG-PDA-PNIPAM	-22.0

with the MBA crosslinker used during the PNIPAM polymerization, which can trap more DOX on the surface of PDA. After the Fe_3O_4 was decorated via hydrothermal approach, the zeta-potential raised from -30.5 mV to -22 mV, but the high LC and EE preserved as 29.41% and 50.31 %.

4.3.4 Release Behavior

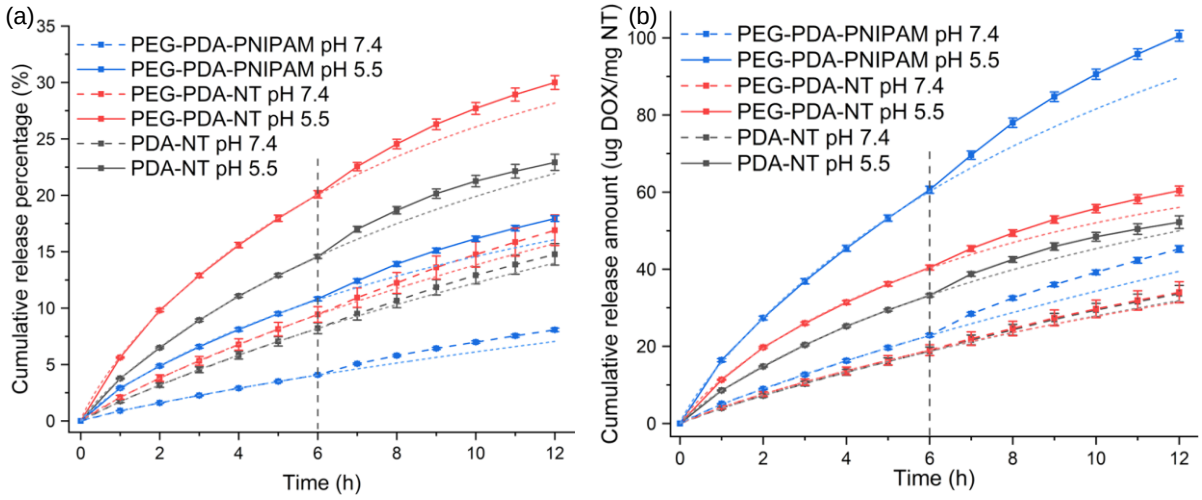

Figure 4.8 Release behavior of PDA-NT, PEG-PDA-NT, PEG-PDA-PNIPAM: (a) DOX release plot in cumulative release percentage by time. (b) DOX release plot in cumulative release amount by time. In the first 6 h, the samples were mildly shaken at room temperature; after that, the samples were shaken in 45°C. The short dash lines are the Weibull models fitted using the data in the first 6 h and extrapolated to 12 h. All error bars are standard error.

In this work, the release profiles were measured by dispersing 0.25 mg loaded samples in 1 ml PBS buffer (pH 7.4 or 5.5) and taking 0.8 mL medium to measure the DOX concentration in the medium, then refill 0.8 mL fresh buffer to the containers. Previously, it was found that the presence of PNIPAM significantly enhanced the DOX loading capacity of nanotubes. In this part, we first tested if the PNIPAM could work as the thermal responsive structure to influence DOX release at an elevated temperature. In Figure 4.8 (a), less fraction of DOX was released from PEG-PDA-PNIPAM than PEG-PDA-NT and PDA-NT at pH 7.4. While in pH 5.5 medium, the DOX release fraction from PEG-PDA-PNIPAM was like PDA-NT and less than PEG-PDA-NT. At

elevated temperature in the last 6 h, the changes of DOX release rate were slight for three samples. To compare the release in the first 6 h, Weibull models were fitted using the first 6 h data and extrapolated to 12 h. Though it is hard to interpret the parameter from the empirical model. the flexibility of the model can achieve a good fitting of the data and provide a more credible extrapolation. As shown in the short dash line in Figure 4.8, the fitting curves of the Weibull model almost completely overlap the data in the first 6 h. In the last 6 h, the data values were higher than the extrapolated values, which indicates the heating accelerated release. For the PNIPAM modified samples, the differences between extrapolated values and data values were higher than that for PDA-NT and PEG-PDA-NT. The observation present on both the percentage scale and amount scale. Therefore, in addition to the high-temperature-induced release acceleration, the thermal responsiveness of PNIPAM also contributes to the DOX release. Furthermore, by converting the DOX release fraction to release amount, the highest DOX release amount was achieved for PEG-PDA-PNIPAM at pH 5.

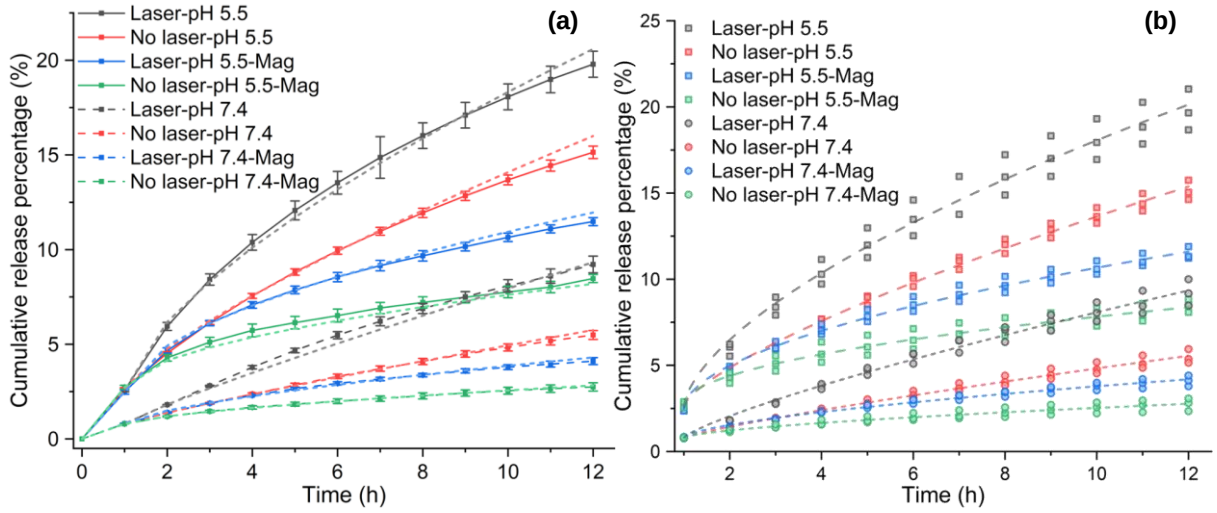

Figure 4.9 The release profiles of DOX from mag-PEG-PDA-PNIPAM measured with altering pH, applying magnetic field and irradiating NIR laser: (a) profiles plotted by average and standard deviation at respective conditions, the dashed lines are predicted results of final linear mixed model, the error bars indicate standard error; (b) scatter plots of raw data and the Korsmeyer-Peppas model fittings using the data from 1 h to 12 h. The release in the first hour was conducted with mild shaking at room temperature, after which the magnetic field or laser was applied.

The release tests were then conducted by altering pH, applying a magnetic field, and irradiating the NIR laser to investigate the control release performance of the multi-functional nanotube, mag-PEG-PDA-PNIPAM. The release profiles were plotted in Figure 4.9. In the first hour, all samples were released in the same conditions, with mild shaking at room temperature. Therefore except for the pH resulting difference, DOX was released similarly from each sample. Then the NIR or magnetic field was applied to alter the release profile. The NIR laser and the low pH condition significantly enhanced the DOX release, while magnetic field attraction reduced the DOX release. Then the DOX release model was investigated by fitting the release profiles to different drug release models. Because DOX was loaded via adsorption, the PDA and PNIPAM are not degradable in the release medium. Three models based on diffusion mechanism were used here, i.e., zero-order model, Higuchi model, and Korsmeyer-Peppas model.

It should be noted that due to the release in the first hour, other than pH values, all samples were released in the same conditions. The stimuli were applied start after one hour. When fitting the models, all release values were reduced by the release value measured at the first hour. By comparing the adjusted R squares of each model in every release condition, Table 4.3, Korsmeyer-Peppas models show the best performance in most cases. In Table 4.4, the parameters of the Korsmeyer-Peppas models were listed. Generally, the n value reflects the diffusion type of the

Table 4.3 Adjusted R^2 of release profiles fitted via zero order, Higuchi and Korsmeyer-Peppas models respectively. The bold value indicates the highest adjust R^2 at the corresponding condition.

Release profiles	Zero order	Higuchi	Korsmeyer-Peppas
pH 5.5 + laser	0.87393	0.95853	0.97499
pH 5.5	0.94903	0.94445	0.99233
pH 5.5 + mag + laser	0.79628	0.98366	0.98525
pH 5.5 + mag	0.72506	0.94092	0.9393
pH 7.4 + laser	0.95968	0.91141	0.98055
pH 7.4	0.96773	0.89896	0.98027
pH 7.4 + mag + laser	0.88239	0.95669	0.9765
pH 7.4 + mag	0.81322	0.87872	0.89457

release process; the k value indicates the release rate. The k values of the models are consistent with Figure 4.9. In both pH conditions, the laser condition resulted in the highest k value, 0.152 in pH 5.5 and 0.049 in pH 7.4. The conditions in presence of magnetic field and no laser applied have the lowest k values, 0.065 in pH 5.5 and 0.016 in pH 7.4. While the conditions with magnetic field and laser applied along with the conditions without both stimuli had comparable k values. In terms of n, the value in presence of laser is lower, indicating a diffusion close to Fickian mode. For example, the n value in pH 5.5 without magnetic field is 0.626 vs. 0.733, and in pH 7.4 without magnetic field, it is 0.800 vs 0.838. And in the presence of a magnetic field, the n value is smaller. By comparison of the conditions, in pH 5.5, the presence of magnetic field reduces the values around 0.5 from about 0.65. In pH 7.4, the magnetic field leads to the n value around 0.63 than about 0.8 without magnetic field. Furthermore, the lower pH value results in a smaller n value.

For the drug release model of the continuum system, two interfaces present, as shown in Figure 4.10. In the Higuchi model, the drug delivery reservoir (or the polymer matrix) does not

Table 4.4 Fitted Korsmeyer-Peppas models of release profiles.

Profiles	Parameter	Value	Standard Error	P value
pH 5.5 + laser	n	0.62616	2.78E-02	0
	k	0.03913	2.24E-03	0
pH 5.5	n	0.73308	0.01736	0
	k	2.19E-02	7.93E-04	0
pH 5.5 + mag + laser	n	0.53901	1.83E-02	0
	k	2.51E-02	9.29E-04	0
pH 5.5 + mag	n	0.50928	3.62E-02	8.88E-16
	k	1.66E-02	1.21E-03	2.00E-15
pH 7.4 + laser	n	0.80027	0.03037	0
	k	0.01254	8.00E-04	0
pH 7.4	n	0.83803	0.03191	0
	k	0.00638	4.29E-04	2.22E-16
pH 7.4 + mag + laser	n	0.63879	0.02702	0
	k	0.00731	4.06E-04	0
pH 7.4 + mag	n	0.64045	0.05941	1.65E-12
	k	0.00424	5.19E-04	1.52E-09

swell or dissolve. Thus, the interface between undissolved or unswelling and dissolved or swelling polymer matrix is the interface of sink and reservoir. And it does not move during the release process, i.e., the $v_{inter} = 0$. [591] While the interface between undissolved drug and dissolved drug in the drug delivery reservoir keeps moving towards the core of the reservoir. Therefore, in the release described by Higuchi, we have a Fickian diffusion-controlled process with $v_{front} \gg v_{inter}$, as shown in Figure 4.10 (a). During the Fickian diffusion release, the drug release fraction is proportional to square root of time. And it is proved even in a system that the $c_0 < c_{satu}$, such a release-time relation still presents.[591] While in the zero-order release process, it is assumed the drug molecules in swelling or dissolved state matrix have rapid diffusion rate and the movement speed of the undissolved-dissolved or unswelling-swelling interface, v_{inter}, is much higher than the v_{front} of undissolved-dissolved-drug front, i.e., $v_{inter} \gg v_{front}$. In other words, the rate determined process is the swelling or dissolving rate of polymer reservoir rather than the Fickian diffusion of drug molecules, as shown in Figure 4.10 (b). Therefore, this process is also called non-Fickian release. In most practical cases, the release is closer to an intermediate process like Figure 4.10 (c). Though it is pointed out that the continuum models cannot perfectly describe release on nanosystems. [592] Two effects still can be considered determining the release pattem

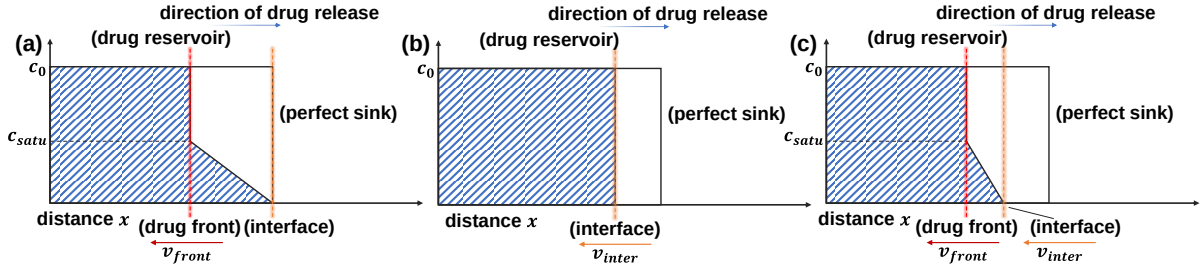

Figure 4.10 Illustration of drug concentration-distance-profile of Higuchi model (a), zero order model (b) and the anomalous diffusion situation (c). c_0 is the initial concentration of drug in the drug reservoir; c_{satu} is the saturated drug concentration in medium; v_{front} is the speed of drug front; v_{inter} is the speed of the interface where the concentration of drug is the same as that in medium. Red line is the interface between undissolved and dissolved drug. Orange line is the interface between undissolved or unswelling and dissolved or swelling polymer matrix.

of nanoparticles that load drug via adsorption. One is the rate of the drug molecules diffusion in nanoparticle, r_{diff}; the other is the rate the equilibrium position moves towards the nanoparticle core, r_{inter}. Figure 4.11 (a) and (b) illustrate the conditions of $t = 0$ and $t = \infty$. After infinite time, the drug distribution in nanoparticle is homogenous and in equilibrium with the medium. This can be achieved via diffusion of drug molecules in nanoparticles and dissolution at the surface of nanoparticle, in which case we have $r_{\text{diff}} \gg r_{\text{inter}}$. Alternately, the equilibrium achieves via the equilibrium position moves from nanoparticle surface to the core, i.e., $r_{\text{diff}} \ll r_{\text{inter}}$. In the first case, the release profile is closer to the Fickian diffusion release and $n = 0.5$ in the Korsmeyer-Peppas model. In the other case, the release profile is closer to zero-order release and $n = 1$ in Korsmeyer-Peppas. Based on previous analysis, for our system, we propose the following explanation for the changes of n values due to stimuli. The NIR on one side could enhance the mobility of drug molecules, which can improve the r_{diff}. On the other side, the PNIPAM on the surface of nanotubes shrinks and turns hydrophobic, which prevent molecules transport across the nanotube surface and reduce the r_{inter}. In the magnetic field, the nanotubes can no longer disperse

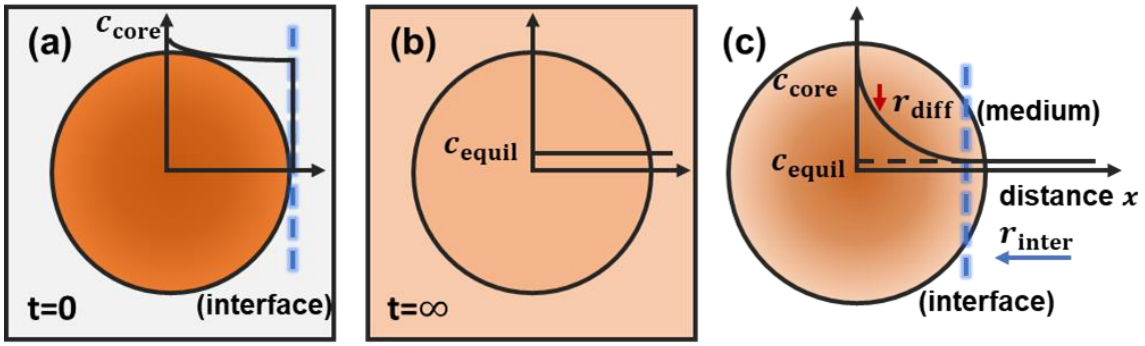

Figure 4.11 Illustration of drug release from nanoparticle: initial state of release (a), equilibrium achieved after infinite time (b) and drug concentration-distance-profile of nanoparticles (c). c_{core} is the drug concentration in the core of nanoparticle; c_{equil} is the drug concentration that is achieved in drug reservoir with the release medium in sink; r_{inter} is the motion rate of the interface between equilibrium and non-equilibrium parts in a nanoparticle; r_{diff} is the diffusion rate of drug molecules in a nanoparticle. (Note for simplicity, the c_{equil} is equal to the drug concentration in medium, while in fact, due to the chemical potential, the nanoparticles with strong attractive force to drug molecules may have c_{equil} than higher than the drug concentration in medium.)

in the release medium; instead, they are attracted at the bottom of the release medium. The molecules need to diffuse across the nanotube's surface and through the accumulated nanotubes to achieve equilibrium. This change slows down the molecule transport across the nanotube surface and leads to r_{inter} reduction. In lower pH, the PDA turns more positive, which reduces its attractive force with DOX cations. Thus, the mobility of DOX molecules is enhanced and r_{diff} increases. Therefore, in the presence of the above three stimuli, the n turns out to be reduced.

To further quantify the stimuli effects on release profiles, the Korsmeyer-Peppas model is converted to its logarithm form, i.e., $\ln\left(\frac{M_t}{M_\infty}\right) = \ln(k) + n \cdot \ln(t)$. Due to the $\ln(0)$ is undefined, the measurements at 1 h were abandoned. In this way, the influences of stimuli could be integrated as variables that can influence the slope and intercept of a linear regression model. Considering the possible interactions among stimuli and time, the full model should be:

Table 4.5 Full model of release profile in presence of three stimuli

Variable	Parameter Estimate	Standard Error	t Value	Pr > |t|
$\boldsymbol{Intercept}$	-5.14105	0.03948	-130.22	<.0001
$\boldsymbol{ln(t)}$	0.88242	0.02266	38.95	<.0001
$\boldsymbol{laser}$	0.61371	0.05583	10.99	<.0001
$\boldsymbol{magnet}$	-0.37056	0.05583	-6.64	<.0001
$\boldsymbol{pH5}$	1.21608	0.05583	21.78	<.0001
$\boldsymbol{laser * magnet}$	-0.15433	0.07896	-1.95	0.0518
$\boldsymbol{pH5 * magnet}$	0.15629	0.07896	1.98	0.0489
$\boldsymbol{pH5 * laser}$	-0.0172	0.07897	-0.22	0.8277
$\boldsymbol{pH5 * laser * magnet}$	-0.05604	0.11167	-0.5	0.6162
$\boldsymbol{\ln(t) * laser}$	-0.00424	0.03204	-0.13	0.8949
$\boldsymbol{\ln(t) * magnet}$	-0.22095	0.03204	-6.9	<.0001
$\boldsymbol{\ln(t) * pH5}$	-0.09387	0.03204	-2.93	0.0037
$\boldsymbol{\ln(t) * pH5 * magnet}$	-0.03796	0.04532	-0.84	0.4031
$\boldsymbol{\ln(t) * pH5 * laser}$	-0.11181	0.04533	-2.47	0.0143
$\boldsymbol{\ln(t) * laser * magnet}$	0.05277	0.04532	1.16	0.2454
$\boldsymbol{\ln(t) * pH5 * laser * magnet}$	0.10847	0.0641	1.69	0.0918

$$y_i = \beta_0 + \beta_1 laser_i + \beta_2 magnet_i + \beta_3 pH5_i + \beta_4 \ln(t_i) + \beta_5 laser_i * magnet_i + \beta_6 laser_i * pH5_i + \beta_7 magnet_i * pH5_i + \beta_8 laser_i * \ln(t_i) + \beta_9 magnet_i * \ln(t_i) + \beta_{10} pH5_i * \ln(t_i) + \beta_{11} laser_i *$$

$magnet_i * \ln(t_i) + \beta_{12} laser_i * pH5_i * \ln(t_i) + \beta_{13} magnet_i * pH5_i * \ln(t_i) + \beta_{14} laser_i * magnet_i * pH5_i * \ln(t_i) + \epsilon_i \quad (i = 1,2,3 \dots 11)$

where the y_i is the value of $\ln\left(\frac{M_t}{M_\infty}\right)$ at $(i+1)$th measurement, $laser_i$ is 1 if NIR laser is applied before the measurement; otherwise, it is 0. Similarly, $magnet_i$ is 1 if a magnet is placed under the release medium and $pH5_i$ is 1 if the release is conducted in pH 5 medium.

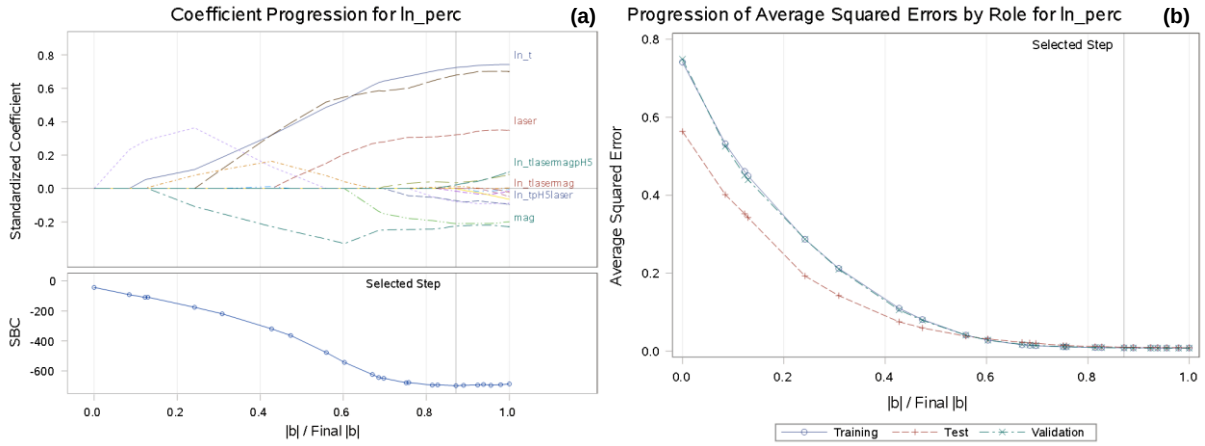

Figure 4.12 LASSO method result (a) the progression of coefficients (top) and Schwarz Bayesian information criterion (smaller is better, bottom) by the norm of coefficients, (b) the progression of averaged squared error (ASE) on training, validation and test data.

The full model is in Table 4.5. The regression achieves a high adjusted R^2 (0.9889). However, the interaction terms might lead to the collinearity problem, and some terms were found not significant, as shown in Table 4.5. The least absolute shrinkage and selection operator (LASSO) method was used to shrink the coefficients and select variables. In this step, Schwarz Bayesian information criterion (SBC) was used to choose the model. The dataset was participated into training, validation, and test data by the ratio 6:3:1, as in Figure 4.12. And four terms, $pH5 * laser$, $laser * magnet * pH5$, $\ln(t) * pH5 * magnet$, $\ln(t) * laser * magnet$, were excluded. However, it was found the residuals are inconsistent at different response values, as shown in Figure 4.13 (a). Given that the same release profile measurements were conducted repeatedly on the same sample, the longitudinal regression is appropriate for this data, which can also deal with the heteroscedastic problem as in Figure 4.13. By fitting the data with the terms in the reduced

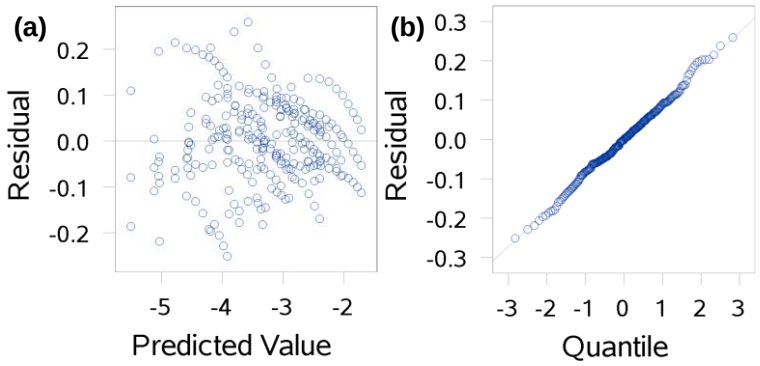

Figure 4.13 Diagnostics plots of the reduced model: (a) residual vs. predicted value, (b) residual vs. quantile.

model using linear mixed model, it was found three more terms, $laser * magnet$, $pH5 * magnet$, $\ln(t) * laser$, still had nonsignificant p values. After removed them, the final reduced model is shown in Table 4.6 and Table 4.7. The full model and reduced model estimated via the maximum likelihood method were also compared by the Chi-square likelihood ratio test. No significant difference was found with a p-value of 0.203. In addition, the random effects among release profiles were included in the linear mixed model. It can be found in Table 4.6 the within-subject error variance ($Var(\hat{\epsilon}_{ij}) = 0.001627$) is small relative to the between-subject variance of the intercepts ($Var(\hat{b}_{1i})$=0.01459). Given the final model, the Korsmeyer-Peppas model for the nanosystem can be expressed as:

$$\frac{M_t}{M_\infty} = \mathrm{k} \cdot \mathrm{t}^{\mathrm{n}} = \exp(-5.1387 + 0.5448laser - 0.3836magnet + 1.2716pH5)$$

$$\cdot\, t^{0.8893 - 0.2125magnet - 0.1171pH5 - laser \cdot pH5(0.1013 - 0.1045magnet)}$$

The excellent fit of the model to the experimental data can be observed on the dashed line in Figure 4.9 (a). From the model, the acceleration effect of low pH and laser, as well as the deceleration effect of magnet in DOX release, can be observed in the exponential function. For the release mode, when no stimulus is applied, the n value is 0.8893, indicating a tendency of zero-

Table 4.6 Reduced model of release profile in presence of three stimuli

Variable	Parameter Estimate	Standard Error	t Value	Pr > |t|
$\boldsymbol{Intercept}$	-5.1387	0.04898	-104.92	<.0001
$\boldsymbol{\ln(t)}$	0.8893	0.01742	51.04	<.0001
$\boldsymbol{laser}$	0.5448	0.04305	12.66	<.0001
$\boldsymbol{magnet}$	-0.3836	0.05080	-7.55	<.0001
$\boldsymbol{pH5}$	1.2716	0.05080	25.03	<.0001
$\boldsymbol{\ln(t) * magnet}$	-0.2125	0.02127	-9.99	<.0001
$\boldsymbol{\ln(t) * pH5}$	-0.1171	0.02276	-5.15	<.0001
$\boldsymbol{\ln(t) * pH5 * laser}$	-0.1013	0.02885	-3.51	0.0005
$\boldsymbol{\ln(t) * pH5 * laser * magnet}$	0.1045	0.03375	3.10	0.0022

order release. While in the presence of magnet and low pH, the term is reduced. The laser can only reduce the n term significantly in low pH, which can be attributed to the more sensitive thermal response of PNIPAM in low pH conditions, as observed in Gao's study.[593] However, we are not clear about the last positive term related to the magnet in the model, which indicates the higher n value at pH 5.5 with magnetic field and laser applied than the ones without laser irradiation. Nevertheless, one possibility is that the DOX release was closed to equilibrium in this situation. The Korsmeyer-Peppas model is applicable for the first 60 % of a release curve; as the release approaching the equilibrium, the model becomes inappropriate. As a result, the deviation of the profile from the model is observed.

Table 4.7 Covariance parameter estimates of the reduced model.

Covariance Parameter	Estimate	Standard Error	Z Value	Pr Z
$\boldsymbol{Var(\hat{b}_{1i})}$	0.01459	0.004903	2.98	0.0015
$\boldsymbol{Cov(\hat{b}_{1i}, \hat{b}_{2i})}$	-0.00348	0.001611	-2.16	0.0307
$\boldsymbol{Var(\hat{b}_{2i})}$	0.001994	0.000729	2.73	0.0031
$\boldsymbol{Var(\hat{\epsilon}_{ij})}$	0.001627	0.000157	10.37	<.0001

4.4 Conclusion in the Chapter

Robust hollow polydopamine nanotubes with accessible lumen were synthesized in this work through the halloysite-sonication-etch approach. Due to the exposure of inner and outer

layers of nanotubes in different steps, both surfaces can be modified separately. To demonstrate the feature, PEG and PNIPAM were decorated on the outer and inner surfaces, respectively. The PEG was attached via EDC/NHS conjugation, and the PNIPAM was in situ polymerized by the pre-decorated initiator, V50. Compared to nanotubes with PNIPAM attached but without PEG, the PEG layer can effectively prevent agglomeration among nanotubes. In addition, the presence of PNIPAM remarkably improved the loading capacity of DOX on the nanotube. The increased loading capacity also leads to a higher release amount. It can be confirmed that besides temperature-enhanced release, the PNIPAM also promotes the DOX release. Finally, the Fe_3O_4 magnetic nanoparticles were precipitated on the surface of nanotubes, which endowed a magnetic response to the nanotube. The influences of pH, magnetic field, and laser on release profile were investigated. The lower pH and laser can enhance DOX release, while magnetic nanoparticles prevent the release. By fitting with the Korsmeyer-Peppas model, it is found that the lower pH, magnetic field, and laser can alter the release profile to a more Fickian diffusion release pattern. Furthermore, the influences were quantified through a linear mixed model. After all, the tri-responsive nanosystem is expected to behave as a smart multifunctional drug delivery nanoplatform. Moreover, the anisotropic morphology also makes it valuable to investigate the shape effect during drug delivery.

Chapter 5

Summary and Future Work

In the previous study, two kinds of intriguing nanoparticles, nanocapsules and nanotubes have been fabricated based on polydopamine. Both particles possess hollow and flexible structures, which are of great interest for biomedical application. The nanocapsules were fabricated using microphase separation of alcohol/water system. The concentration of alkaline and dopamine, the contents of alcohol, reaction time, and the supplication of oxygen could all influence the composition and morphology of final products. With a well-engineered parameter, the anisotropic bowl-like nanocapsule could even be obtained. Compared to other methods, this approach is featured with simplicity in operation and the pretty small dimension of the product. The other novel polydopamine structure is the nanotube. In the preliminary study, the photothermal effect, as well as the pH- and photo-controlled doxorubicin release, have been demonstrated. Through a halloysite-sonication-etching approach, a hollow flexible tubular structure with accessible lumen could be obtained. Due to the separated exposure of the surfaces to the surroundings, both the outer and the inner layers of the nanotubes could be modified with different functional groups. As a proof-of-concept study, polyethylene glycol and poly(N-isopropylacrylamide) were grafted. Furthermore, the different hydrophilicity from single-polymer-attached nanotubes was observed. With the Fe_3O_4 nanoparticle attached, a tri-responsive nanostructure was obtained. Finally, the controlled release profiles of doxorubicin from the nanotube under three stimuli were investigated, and a regression model was fitted. The model could precisely predict the release performance of

DOX in the presence of stimuli, also quantify and deepen our understanding of the stimuli effect on drug release from the system.

Nonetheless, plenty of works are still needed to turn these polydopamine nanoparticles into practical applications. For the nanocapsules, though the fabrication method is simple, the yield is relatively low due to first the requirement of low polydopamine concentration, second the low-efficiency purification method. One solution is to collect the product via filtration with a nucleopore membrane. However, too large pore size will lose all the product; too small pore size will withhold the oligomer in medium and result in agglomerated products. In addition to the collection method, the specific surface area should be measured. Though mathematical calculation indicates the hollow and collapsed structure may have a larger surface area than solid spheres, the parameter has not been demonstrated via experiment yet. One of the reasons is the low yield in this method. Nevertheless, once these issues are resolved, the hollow polydopamine nanostructure prepared with a facile method is of great interest in the biomedical and electrochemical fields.

Furthermore, due to the inner surface modification, the polydopamine nanotubes still rely on a free radical polymerization to decorate thermoresponsive polymer. The free radical dispersed in the medium can still lead to the formation of crosslinked poly(N-isopropylacrylamide) on the outer surface of the nanotubes, which results in the reduced stability of nanoparticle in PBS medium. In addition, the molecular structure and molecular weight are hard to control in this method. To make the inner "basket" polymer synthesis more controllable, a more advanced living polymerization method should be attempted, which can confine the polymerization occurring only at the inner surface and have a well-controlled crosslink structure. Given a dense network formed in the lumen, small molecular drugs and macromolecular agents are both expected to be loaded on the system. On the other side, though polydopamine is regarded theoretically biodegradable, the

degradation usually requires an alkaline condition or abundant reactive oxygen species, which are peculiar in cells. Due to the critical functional group in dopamine polymerization is catechol and amine, the modified molecules with both groups present also possess the "self-polymerization" property. To enhance the degradability of the system, modification of the dopamine monomer should be conducted, which can even provide additional responsiveness to the system. Furthermore, to make it clinically practical, the in vitro and in vivo test should indeed be conducted on the system.

Though polydopamine nanostructures have been researched for several years, most studies are conducted based on conventional spherical structures. The non-spherical structures studied in this work can provide large surface area, additional modification space and are expected to have different biodistribution due to the shape effect. Therefore there is still expansive research room in the future.

References

[1] Wang, X.; Wang, C.; Wang, X.; Wang, Y.; Zhang, Q.; Cheng, Y., A Polydopamine Nanoparticle-Knotted Poly(ethylene glycol) Hydrogel for On-Demand Drug Delivery and Chemo-photothermal Therapy. *Chemistry of Materials* **2017,** *29* (3), 1370-1376.

[2] Liu, Y.; Ai, K.; Liu, J.; Deng, M.; He, Y.; Lu, L., Dopamine-Melanin Colloidal Nanospheres: An Efficient Near-Infrared Photothermal Therapeutic Agent for In Vivo Cancer Therapy. *Advanced Materials* **2013,** *25* (9), 1353-1359.

[3] Wang, X.; Zhang, J.; Wang, Y.; Wang, C.; Xiao, J.; Zhang, Q.; Cheng, Y., Multi-responsive photothermal-chemotherapy with drug-loaded melanin-like nanoparticles for synergetic tumor ablation. *Biomaterials* **2016,** *81*, 114-124.

[4] Zhou, Z.; Yan, Y.; Hu, K.; Zou, Y.; Li, Y.; Ma, R.; Zhang, Q.; Cheng, Y., Autophagy inhibition enabled efficient photothermal therapy at a mild temperature. *Biomaterials* **2017,** *141*, 116-124.

[5] Wang, S.; Lin, J.; Wang, Z.; Zhou, Z.; Bai, R.; Lu, N.; Liu, Y.; Fu, X.; Jacobson, O.; Fan, W.; Qu, J.; Chen, S.; Wang, T.; Huang, P.; Chen, X., Core–Satellite Polydopamine–Gadolinium-Metallofullerene Nanotheranostics for Multimodal Imaging Guided Combination Cancer Therapy. *Advanced Materials* **2017,** *29* (35), 1701013.

[6] Zhong, X.; Yang, K.; Dong, Z.; Yi, X.; Wang, Y.; Ge, C.; Zhao, Y.; Liu, Z., Polydopamine as a Biocompatible Multifunctional Nanocarrier for Combined Radioisotope Therapy and Chemotherapy of Cancer. *Advanced Functional Materials* **2015,** *25* (47), 7327-7336.

[7] Luo, H.; Gu, C.; Zheng, W.; Dai, F.; Wang, X.; Zheng, Z., Facile synthesis of novel size-controlled antibacterial hybrid spheres using silver nanoparticles loaded with poly-dopamine spheres. *RSC Advances* **2015,** *5* (18), 13470-13477.

[8] Yah, W. O.; Xu, H.; Soejima, H.; Ma, W.; Lvov, Y.; Takahara, A., Biomimetic Dopamine Derivative for Selective Polymer Modification of Halloysite Nanotube Lumen. *Journal of the American Chemical Society* **2012,** *134* (29), 12134-12137.

[9] Liu, X.; Cao, J.; Li, H.; Li, J.; Jin, Q.; Ren, K.; Ji, J., Mussel-Inspired Polydopamine: A Biocompatible and Ultrastable Coating for Nanoparticles in Vivo. *ACS Nano* **2013,** *7* (10), 9384-9395.

[10] Ding, H.; Wang, X.; Zhang, S.; Liu, X., Applications of polymeric micelles with tumor targeted in chemotherapy. *Journal of Nanoparticle Research* **2012,** *14* (11), 1254.

[11] Milovanovic, M.; Arsenijevic, A.; Milovanovic, J.; Kanjevac, T.; Arsenijevic, N., Chapter 14 - Nanoparticles in Antiviral Therapy. In *Antimicrobial Nanoarchitectonics*, Grumezescu, A. M., Ed. Elsevier: 2017; pp 383-410.

[12] Wang, H.; Wang, Y.; Chen, Y.; Jin, Q.; Ji, J., A biomimic pH-sensitive polymeric prodrug based on polycarbonate for intracellular drug delivery. *Polymer Chemistry* **2014,** *5* (3), 854-861.

[13] Yang, B.; Lv, Y.; Zhu, J.-y.; Han, Y.-t.; Jia, H.-z.; Chen, W.-h.; Feng, J.; Zhang, X.-z.; Zhuo, R.-x., A pH-responsive drug nanovehicle constructed by reversible attachment of cholesterol to PEGylated poly(l-lysine) via catechol–boronic acid ester formation. *Acta Biomaterialia* **2014,** *10* (8), 3686-3695.

[14] Van Domeselaar, G. H.; Kwon, G. S.; Andrew, L. C.; Wishart, D. S., Application of solid phase peptide synthesis to engineering PEO–peptide block copolymers for drug delivery. *Colloids and Surfaces B: Biointerfaces* **2003,** *30* (4), 323-334.
[15] Adams, M. L.; Kwon, G. S., The effects of acyl chain length on the micelle properties of poly(ethylene oxide)-block-poly(N-hexylL-aspartamide)-acyl conjugates. *Journal of Biomaterials Science, Polymer Edition* **2002,** *13* (9), 991-1006.
[16] Shan, X.; Mao, J.; Long, M.; Ahmed, K. S.; Sun, C.; Qiu, L.; Chen, J., Influence of polyethylene glycol molecular weight on the anticancer drug delivery of pH-sensitive polymeric micelle. *Journal of Applied Polymer Science* **2019,** *136* (32), 47854.
[17] Fernandez-Villamarin, M.; Sousa-Herves, A.; Porto, S.; Guldris, N.; Martínez-Costas, J.; Riguera, R.; Fernandez-Megia, E., A dendrimer–hydrophobic interaction synergy improves the stability of polyion complex micelles. *Polymer Chemistry* **2017,** *8* (16), 2528-2537.
[18] Li, Y.; Xiao, K.; Luo, J.; Xiao, W.; Lee, J. S.; Gonik, A. M.; Kato, J.; Dong, T. A.; Lam, K. S., Well-defined, reversible disulfide cross-linked micelles for on-demand paclitaxel delivery. *Biomaterials* **2011,** *32* (27), 6633-6645.
[19] Shi, Y.; van der Meel, R.; Theek, B.; Oude Blenke, E.; Pieters, E. H. E.; Fens, M. H. A. M.; Ehling, J.; Schiffelers, R. M.; Storm, G.; van Nostrum, C. F.; Lammers, T.; Hennink, W. E., Complete Regression of Xenograft Tumors upon Targeted Delivery of Paclitaxel via Π–Π Stacking Stabilized Polymeric Micelles. *ACS Nano* **2015,** *9* (4), 3740-3752.
[20] Wang, J.; Jiang, M., Polymeric Self-Assembly into Micelles and Hollow Spheres with Multiscale Cavities Driven by Inclusion Complexation. *Journal of the American Chemical Society* **2006,** *128* (11), 3703-3708.
[21] Shi, Y.; van Steenbergen, M. J.; Teunissen, E. A.; Novo, L. s.; Gradmann, S.; Baldus, M.; van Nostrum, C. F.; Hennink, W. E., Π–Π Stacking Increases the Stability and Loading Capacity of Thermosensitive Polymeric Micelles for Chemotherapeutic Drugs. *Biomacromolecules* **2013,** *14* (6), 1826-1837.
[22] Kim, S. H.; Tan, J. P. K.; Nederberg, F.; Fukushima, K.; Colson, J.; Yang, C.; Nelson, A.; Yang, Y.-Y.; Hedrick, J. L., Hydrogen bonding-enhanced micelle assemblies for drug delivery. *Biomaterials* **2010,** *31* (31), 8063-8071.
[23] Dong, X.; Guo, X.; Liu, G.; Fan, A.; Wang, Z.; Zhao, Y., When self-assembly meets topology: an enhanced micelle stability. *Chemical Communications* **2017,** *53* (27), 3822-3825.
[24] Bronich, T. K.; Keifer, P. A.; Shlyakhtenko, L. S.; Kabanov, A. V., Polymer Micelle with Cross-Linked Ionic Core. *Journal of the American Chemical Society* **2005,** *127* (23), 8236-8237.
[25] Chen, J.; Ouyang, J.; Kong, J.; Zhong, W.; Xing, M. M., Photo-cross-linked and pH-Sensitive Biodegradable Micelles for Doxorubicin Delivery. *ACS Applied Materials & Interfaces* **2013,** *5* (8), 3108-3117.
[26] Deng, H.; Liu, J.; Zhao, X.; Zhang, Y.; Liu, J.; Xu, S.; Deng, L.; Dong, A.; Zhang, J., PEG-b-PCL Copolymer Micelles with the Ability of pH-Controlled Negative-to-Positive Charge Reversal for Intracellular Delivery of Doxorubicin. *Biomacromolecules* **2014,** *15* (11), 4281-4292.
[27] Jin, Y.; Song, L.; Su, Y.; Zhu, L.; Pang, Y.; Qiu, F.; Tong, G.; Yan, D.; Zhu, B.; Zhu, X., Oxime Linkage: A Robust Tool for the Design of pH-Sensitive Polymeric Drug Carriers. *Biomacromolecules* **2011,** *12* (10), 3460-3468.

[28] Hu, J.; He, J.; Zhang, M.; Ni, P., Precise modular synthesis and a structure–property study of acid-cleavable star-block copolymers for pH-triggered drug delivery. *Polymer Chemistry* **2015,** *6* (9), 1553-1566.
[29] Su, Z.; Chen, M.; Xiao, Y.; Sun, M.; Zong, L.; Asghar, S.; Dong, M.; Li, H.; Ping, Q.; Zhang, C., ROS-triggered and regenerating anticancer nanosystem: An effective strategy to subdue tumor's multidrug resistance. *Journal of Controlled Release* **2014,** *196*, 370-383.
[30] Sun, H.; Guo, B.; Cheng, R.; Meng, F.; Liu, H.; Zhong, Z., Biodegradable micelles with sheddable poly(ethylene glycol) shells for triggered intracellular release of doxorubicin. *Biomaterials* **2009,** *30* (31), 6358-6366.
[31] Zhu, W.; Wang, Y.; Cai, X.; Zha, G.; Luo, Q.; Sun, R.; Li, X.; Shen, Z., Reduction-triggered release of paclitaxel from in situ formed biodegradable core-cross-linked micelles. *Journal of Materials Chemistry B* **2015,** *3* (15), 3024-3031.
[32] Tong, R.; Lu, X.; Xia, H., A facile mechanophore functionalization of an amphiphilic block copolymer towards remote ultrasound and redox dual stimulus responsiveness. *Chemical Communications* **2014,** *50* (27), 3575-3578.
[33] Rao, J.; Khan, A., Enzyme Sensitive Synthetic Polymer Micelles Based on the Azobenzene Motif. *Journal of the American Chemical Society* **2013,** *135* (38), 14056-14059.
[34] Liu, G.-Y.; Chen, C.-J.; Li, D.-D.; Wang, S.-S.; Ji, J., Near-infrared light-sensitive micelles for enhanced intracellular drug delivery. *Journal of Materials Chemistry* **2012,** *22* (33), 16865-16871.
[35] Xiao, C.; Ding, J.; Ma, L.; Yang, C.; Zhuang, X.; Chen, X., Synthesis of thermal and oxidation dual responsive polymers for reactive oxygen species (ROS)-triggered drug release. *Polymer Chemistry* **2015,** *6* (5), 738-747.
[36] Ling, D.; Park, W.; Park, S.-j.; Lu, Y.; Kim, K. S.; Hackett, M. J.; Kim, B. H.; Yim, H.; Jeon, Y. S.; Na, K.; Hyeon, T., Multifunctional Tumor pH-Sensitive Self-Assembled Nanoparticles for Bimodal Imaging and Treatment of Resistant Heterogeneous Tumors. *Journal of the American Chemical Society* **2014,** *136* (15), 5647-5655.
[37] Quadir, M. A.; Morton, S. W.; Deng, Z. J.; Shopsowitz, K. E.; Murphy, R. P.; Epps, T. H.; Hammond, P. T., PEG–Polypeptide Block Copolymers as pH-Responsive Endosome-Solubilizing Drug Nanocarriers. *Molecular Pharmaceutics* **2014,** *11* (7), 2420-2430.
[38] Guo, X.; Li, D.; Yang, G.; Shi, C.; Tang, Z.; Wang, J.; Zhou, S., Thermo-triggered Drug Release from Actively Targeting Polymer Micelles. *ACS Applied Materials & Interfaces* **2014,** *6* (11), 8549-8559.
[39] Chen, S.; Li, Y.; Guo, C.; Wang, J.; Ma, J.; Liang, X.; Yang, L.-R.; Liu, H.-Z., Temperature-Responsive Magnetite/PEO−PPO−PEO Block Copolymer Nanoparticles for Controlled Drug Targeting Delivery. *Langmuir* **2007,** *23* (25), 12669-12676.
[40] Cheng, Y.; Hao, J.; Lee, L. A.; Biewer, M. C.; Wang, Q.; Stefan, M. C., Thermally Controlled Release of Anticancer Drug from Self-Assembled γ-Substituted Amphiphilic Poly(ε-caprolactone) Micellar Nanoparticles. *Biomacromolecules* **2012,** *13* (7), 2163-2173.
[41] Rapoport, N.; Nam, K.-H.; Gupta, R.; Gao, Z.; Mohan, P.; Payne, A.; Todd, N.; Liu, X.; Kim, T.; Shea, J.; Scaife, C.; Parker, D. L.; Jeong, E.-K.; Kennedy, A. M., Ultrasound-mediated tumor imaging and nanotherapy using drug loaded, block copolymer stabilized perfluorocarbon nanoemulsions. *Journal of Controlled Release* **2011,** *153* (1), 4-15.
[42] Gao, Z.; Fain, H. D.; Rapoport, N., Ultrasound-Enhanced Tumor Targeting of Polymeric Micellar Drug Carriers. *Molecular Pharmaceutics* **2004,** *1* (4), 317-330.

[43] Husseini, G. A.; Myrup, G. D.; Pitt, W. G.; Christensen, D. A.; Rapoport, N. Y., Factors affecting acoustically triggered release of drugs from polymeric micelles. *Journal of Controlled Release* **2000,** *69* (1), 43-52.
[44] Wu, P.; Jia, Y.; Qu, F.; Sun, Y.; Wang, P.; Zhang, K.; Xu, C.; Liu, Q.; Wang, X., Ultrasound-Responsive Polymeric Micelles for Sonoporation-Assisted Site-Specific Therapeutic Action. *ACS Applied Materials & Interfaces* **2017,** *9* (31), 25706-25716.
[45] Zhang, H.; Xia, H.; Wang, J.; Li, Y., High intensity focused ultrasound-responsive release behavior of PLA-b-PEG copolymer micelles. *Journal of Controlled Release* **2009,** *139* (1), 31-39.
[46] Wang, J.; Pelletier, M.; Zhang, H.; Xia, H.; Zhao, Y., High-Frequency Ultrasound-Responsive Block Copolymer Micelle. *Langmuir* **2009,** *25* (22), 13201-13205.
[47] Xuan, J.; Boissière, O.; Zhao, Y.; Yan, B.; Tremblay, L.; Lacelle, S.; Xia, H.; Zhao, Y., Ultrasound-Responsive Block Copolymer Micelles Based on a New Amplification Mechanism. *Langmuir* **2012,** *28* (47), 16463-16468.
[48] Zhou, Z.; Tang, J.; Sun, Q.; Murdoch, W. J.; Shen, Y., A multifunctional PEG–PLL drug conjugate forming redox-responsive nanoparticles for intracellular drug delivery. *Journal of Materials Chemistry B* **2015,** *3* (38), 7594-7603.
[49] Wang, C.; Wang, Z.; Zhang, X., Amphiphilic Building Blocks for Self-Assembly: From Amphiphiles to Supra-amphiphiles. *Accounts of Chemical Research* **2012,** *45* (4), 608-618.
[50] Zhou, J.; Yu, G.; Huang, F., Supramolecular chemotherapy based on host–guest molecular recognition: a novel strategy in the battle against cancer with a bright future. *Chemical Society Reviews* **2017,** *46* (22), 7021-7053.
[51] Xu, X.; Li, Y.; Li, H.; Liu, R.; Sheng, M.; He, B.; Gu, Z., Smart Nanovehicles Based on pH-Triggered Disassembly of Supramolecular Peptide-Amphiphiles for Efficient Intracellular Drug Delivery. *Small* **2014,** *10* (6), 1133-1140.
[52] Song, N.; Lou, X.-Y.; Ma, L.; Gao, H.; Yang, Y.-W., Supramolecular nanotheranostics based on pillarenes. *Theranostics* **2019,** *9* (11), 3075-3093.
[53] Zhou, J.; Chen, M.; Diao, G., Magnetic-Responsive Supramolecular Vesicles From Self-Organization of Amphiphilic Pillar[5]arene and Application in Controlled Release. *ACS Applied Materials & Interfaces* **2014,** *6* (21), 18538-18542.
[54] Cao, Y.; Zou, X.; Xiong, S.; Li, Y.; Shen, Y.; Hu, X.; Wang, L., Supramolecular Prodrug Micelles Constructed by Drug-Drug Conjugate with Water Soluble Pillar[6]arene for Controllable and Rapid Drug Release. *Chinese Journal of Chemistry* **2015,** *33* (3), 329-334.
[55] Zhou, Y.; Jie, K.; Huang, F., A redox-responsive selenium-containing pillar[5]arene-based macrocyclic amphiphile: synthesis, controllable self-assembly in water, and application in controlled release. *Chemical Communications* **2017,** *53* (59), 8364-8367.
[56] Huang, X.; Du, X., Pillar[6]arene-Valved Mesoporous Silica Nanovehicles for Multiresponsive Controlled Release. *ACS Applied Materials & Interfaces* **2014,** *6* (22), 20430-20436.
[57] Tan, L.-L.; Song, N.; Zhang, S. X.-A.; Li, H.; Wang, B.; Yang, Y.-W., Ca2+, pH and thermo triple-responsive mechanized Zr-based MOFs for on-command drug release in bone diseases. *Journal of Materials Chemistry B* **2016,** *4* (1), 135-140.
[58] Bangham, A. D.; De Gier, J.; Greville, G. D., Osmotic properties and water permeability of phospholipid liquid crystals. *Chemistry and Physics of Lipids* **1967,** *1* (3), 225-246.

[59] Akbarzadeh, A.; Rezaei-Sadabady, R.; Davaran, S.; Joo, S. W.; Zarghami, N.; Hanifehpour, Y.; Samiei, M.; Kouhi, M.; Nejati-Koshki, K., Liposome: classification, preparation, and applications. *Nanoscale research letters* **2013,** *8* (1), 102-102.
[60] Otake, K.; Shimomura, T.; Goto, T.; Imura, T.; Furuya, T.; Yoda, S.; Takebayashi, Y.; Sakai, H.; Abe, M., Preparation of Liposomes Using an Improved Supercritical Reverse Phase Evaporation Method. *Langmuir* **2006,** *22* (6), 2543-2550.
[61] Corace, G.; Angeloni, C.; Malaguti, M.; Hrelia, S.; Stein, P. C.; Brandl, M.; Gotti, R.; Luppi, B., Multifunctional liposomes for nasal delivery of the anti-Alzheimer drug tacrine hydrochloride. *Journal of Liposome Research* **2014,** *24* (4), 323-335.
[62] Dos Santos, N.; Cox, K. A.; McKenzie, C. A.; van Baarda, F.; Gallagher, R. C.; Karlsson, G.; Edwards, K.; Mayer, L. D.; Allen, C.; Bally, M. B., pH gradient loading of anthracyclines into cholesterol-free liposomes: enhancing drug loading rates through use of ethanol. *Biochimica et Biophysica Acta (BBA) - Biomembranes* **2004,** *1661* (1), 47-60.
[63] Hwang, S.; Maitani, Y.; Qi, X.-R.; Takayama, K.; Nagai, T., Remote loading of diclofenac, insulin and fluorescein isothiocyanate labeled insulin into liposomes by pH and acetate gradient methods. *International Journal of Pharmaceutics* **1999,** *179* (1), 85-95.
[64] Han, H. D.; Lee, A.; Song, C. K.; Hwang, T.; Seong, H.; Lee, C. O.; Shin, B. C., In vivo distribution and antitumor activity of heparin-stabilized doxorubicin-loaded liposomes. *International Journal of Pharmaceutics* **2006,** *313* (1), 181-188.
[65] Abraham, S. A.; Edwards, K.; Karlsson, G.; Hudon, N.; Mayer, L. D.; Bally, M. B., An evaluation of transmembrane ion gradient-mediated encapsulation of topotecan within liposomes. *Journal of Controlled Release* **2004,** *96* (3), 449-461.
[66] Sioud, M.; Sørensen, D. R., Cationic liposome-mediated delivery of siRNAs in adult mice. *Biochemical and Biophysical Research Communications* **2003,** *312* (4), 1220-1225.
[67] Ruozi, B.; Battini, R.; Montanari, M.; Mucci, A.; Tosi, G.; Forni, F.; Vandelli, M. A., DOTAP/UDCA vesicles: novel approach in oligonucleotide delivery. *Nanomedicine: Nanotechnology, Biology and Medicine* **2007,** *3* (1), 1-13.
[68] Engudar, G.; Schaarup-Jensen, H.; Fliedner, F. P.; Hansen, A. E.; Kempen, P.; Jølck, R. I.; Kjaer, A.; Andresen, T. L.; Clausen, M. H.; Jensen, A. I.; Henriksen, J. R., Remote loading of liposomes with a ¹²⁴I-radioiodinated compound and their in vivo evaluation by PET/CT in a murine tumor model. *Theranostics* **2018,** *8* (21), 5828-5841.
[69] Sur, S.; Fries, A. C.; Kinzler, K. W.; Zhou, S.; Vogelstein, B., Remote loading of preencapsulated drugs into stealth liposomes. *Proc Natl Acad Sci U S A* **2014,** *111* (6), 2283-2288.
[70] Vemuri, S.; Rhodes, C. T., Development and Characterization of a Liposome Preparation by a pH-Gradient Method. *Journal of Pharmacy and Pharmacology* **1994,** *46* (10), 778-783.
[71] Zucker, D.; Marcus, D.; Barenholz, Y.; Goldblum, A., Liposome drugs' loading efficiency: A working model based on loading conditions and drug's physicochemical properties. *Journal of Controlled Release* **2009,** *139* (1), 73-80.
[72] Fritze, A.; Hens, F.; Kimpfler, A.; Schubert, R.; Peschka-Süss, R., Remote loading of doxorubicin into liposomes driven by a transmembrane phosphate gradient. *Biochimica et Biophysica Acta (BBA) - Biomembranes* **2006,** *1758* (10), 1633-1640.
[73] Zununi Vahed, S.; Salehi, R.; Davaran, S.; Sharifi, S., Liposome-based drug co-delivery systems in cancer cells. *Materials Science and Engineering: C* **2017,** *71*, 1327-1341.

[74] Sun, T.; Zhang, Y. S.; Pang, B.; Hyun, D. C.; Yang, M.; Xia, Y., Engineered Nanoparticles for Drug Delivery in Cancer Therapy. *Angewandte Chemie International Edition* **2014,** *53* (46), 12320-12364.
[75] Al-Ahmady, Z.; Kostarelos, K., Chemical Components for the Design of Temperature-Responsive Vesicles as Cancer Therapeutics. *Chemical Reviews* **2016,** *116* (6), 3883-3918.
[76] Crowe, L. M.; Crowe, J. H.; Rudolph, A.; Womersley, C.; Appel, L., Preservation of freeze-dried liposomes by trehalose. *Archives of Biochemistry and Biophysics* **1985,** *242* (1), 240-247.
[77] Pietzyk, B.; Henschke, K., Degradation of phosphatidylcholine in liposomes containing carboplatin in dependence on composition and storage conditions. *International Journal of Pharmaceutics* **2000,** *196* (2), 215-218.
[78] Rudolphi-Skórska, E.; Filek, M.; Zembala, M., The Effects of the Structure and Composition of the Hydrophobic Parts of Phosphatidylcholine-Containing Systems on Phosphatidylcholine Oxidation by Ozone. *The Journal of Membrane Biology* **2017,** *250* (5), 493-505.
[79] Alhajlan, M.; Alhariri, M.; Omri, A., Efficacy and Safety of Liposomal Clarithromycin and Its Effect on Pseudomonas aeruginosa Virulence Factors. *Antimicrobial Agents and Chemotherapy* **2013,** *57* (6), 2694-2704.
[80] Chen, X.; Zhang, Y.; Tang, C.; Tian, C.; Sun, Q.; Su, Z.; Xue, L.; Yin, Y.; Ju, C.; Zhang, C., Co-delivery of paclitaxel and anti-survivin siRNA via redox-sensitive oligopeptide liposomes for the synergistic treatment of breast cancer and metastasis. *International Journal of Pharmaceutics* **2017,** *529* (1), 102-115.
[81] El-Nesr, O. H.; Yahiya, S. A.; El-Gazayerly, O. N., Effect of formulation design and freeze-drying on properties of fluconazole multilamellar liposomes. *Saudi Pharmaceutical Journal* **2010,** *18* (4), 217-224.
[82] Semple, S. C.; Chonn, A.; Cullis, P. R., Influence of Cholesterol on the Association of Plasma Proteins with Liposomes. *Biochemistry* **1996,** *35* (8), 2521-2525.
[83] Gaber, M. H.; Hong, K.; Huang, S. K.; Papahadjopoulos, D., Thermosensitive Sterically Stabilized Liposomes: Formulation and in Vitro Studies on Mechanism of Doxorubicin Release by Bovine Serum and Human Plasma. *Pharmaceutical Research* **1995,** *12* (10), 1407-1416.
[84] Riaz, K. M.; Riaz, A. M.; Zhang, X.; Lin, C.; Wong, H. K.; Chen, X.; Zhang, G.; Lu, A.; Yang, Z., Surface Functionalization and Targeting Strategies of Liposomes in Solid Tumor Therapy: A Review. *International Journal of Molecular Sciences* **2018,** *19* (1).
[85] Kim, C. H.; Lee, S. G.; Kang, M. J.; Lee, S.; Choi, Y. W., Surface modification of lipid-based nanocarriers for cancer cell-specific drug targeting. *Journal of Pharmaceutical Investigation* **2017,** *47* (3), 203-227.
[86] Nag, O. K.; Yadav, V. R.; Hedrick, A.; Awasthi, V., Post-modification of preformed liposomes with novel non-phospholipid poly(ethylene glycol)-conjugated hexadecylcarbamoylmethyl hexadecanoic acid for enhanced circulation persistence in vivo. *International journal of pharmaceutics* **2013,** *446* (1-2), 119-129.
[87] Uster, P. S.; Allen, T. M.; Daniel, B. E.; Mendez, C. J.; Newman, M. S.; Zhu, G. Z., Insertion of poly(ethylene glycol) derivatized phospholipid into pre-formed liposomes results in prolonged in vivo circulation time. *FEBS Letters* **1996,** *386* (2-3), 243-246.

[88] Moreira, J. N.; Ishida, T.; Gaspar, R.; Allen, T. M., Use of the Post-Insertion Technique to Insert Peptide Ligands into Pre-Formed Stealth Liposomes with Retention of Binding Activity and Cytotoxicity. *Pharmaceutical Research* **2002,** *19* (3), 265-269.
[89] Nag, O. K.; Awasthi, V., Surface Engineering of Liposomes for Stealth Behavior. *Pharmaceutics* **2013,** *5* (4), 542-569.
[90] Xu, H.; Paxton, J. W.; Wu, Z., Enhanced pH-Responsiveness, Cellular Trafficking, Cytotoxicity and Long-circulation of PEGylated Liposomes with Post-insertion Technique Using Gemcitabine as a Model Drug. *Pharmaceutical Research* **2015,** *32* (7), 2428-2438.
[91] Mack, K.; Rüger, R.; Fellermeier, S.; Seifert, O.; Kontermann, R. E., Dual Targeting of Tumor Cells with Bispecific Single-Chain Fv-Immunoliposomes. *Antibodies* **2012,** *1* (2), 199-214.
[92] Ta, T.; Porter, T. M., Thermosensitive liposomes for localized delivery and triggered release of chemotherapy. *Journal of Controlled Release* **2013,** *169* (1), 112-125.
[93] Mills, J. K.; Needham, D., Lysolipid incorporation in dipalmitoylphosphatidylcholine bilayer membranes enhances the ion permeability and drug release rates at the membrane phase transition. *Biochimica et Biophysica Acta (BBA) - Biomembranes* **2005,** *1716* (2), 77-96.
[94] Needham, D.; Anyarambhatla, G.; Kong, G.; Dewhirst, M. W., A New Temperature-sensitive Liposome for Use with Mild Hyperthermia: Characterization and Testing in a Human Tumor Xenograft Model. *Cancer Research* **2000,** *60* (5), 1197-1201.
[95] Evjen, T. J.; Nilssen, E. A.; Fowler, R. A.; Røgnvaldsson, S.; Brandl, M.; Fossheim, S. L., Lipid membrane composition influences drug release from dioleoylphosphatidylethanolamine-based liposomes on exposure to ultrasound. *International Journal of Pharmaceutics* **2011,** *406* (1), 114-116.
[96] Lin, H.-Y.; Thomas, J. L., Factors Affecting Responsivity of Unilamellar Liposomes to 20 kHz Ultrasound. *Langmuir* **2004,** *20* (15), 6100-6106.
[97] Buchanan, K. D.; Huang, S.-L.; Kim, H.; McPherson, D. D.; MacDonald, R. C., Encapsulation of NF-κB decoy oligonucleotides within echogenic liposomes and ultrasound-triggered release. *Journal of Controlled Release* **2010,** *141* (2), 193-198.
[98] Nappini, S.; Bombelli, F. B.; Bonini, M.; Nordèn, B.; Baglioni, P., Magnetoliposomes for controlled drug release in the presence of low-frequency magnetic field. *Soft Matter* **2010,** *6* (1), 154-162.
[99] Amstad, E.; Kohlbrecher, J.; Müller, E.; Schweizer, T.; Textor, M.; Reimhult, E., Triggered Release from Liposomes through Magnetic Actuation of Iron Oxide Nanoparticle Containing Membranes. *Nano Letters* **2011,** *11* (4), 1664-1670.
[100] Podaru, G.; Ogden, S.; Baxter, A.; Shrestha, T.; Ren, S.; Thapa, P.; Dani, R. K.; Wang, H.; Basel, M. T.; Prakash, P.; Bossmann, S. H.; Chikan, V., Pulsed Magnetic Field Induced Fast Drug Release from Magneto Liposomes via Ultrasound Generation. *The Journal of Physical Chemistry B* **2014,** *118* (40), 11715-11722.
[101] Lin, C.-Y.; Javadi, M.; Belnap, D. M.; Barrow, J. R.; Pitt, W. G., Ultrasound sensitive eLiposomes containing doxorubicin for drug targeting therapy. *Nanomedicine: Nanotechnology, Biology and Medicine* **2014,** *10* (1), 67-76.
[102] Javadi, M.; Pitt, W. G.; Tracy, C. M.; Barrow, J. R.; Willardson, B. M.; Hartley, J. M.; Tsosie, N. H., Ultrasonic gene and drug delivery using eLiposomes. *Journal of Controlled Release* **2013,** *167* (1), 92-100.

[103] Deng, Z.; Yan, F.; Jin, Q.; Li, F.; Wu, J.; Liu, X.; Zheng, H., Reversal of multidrug resistance phenotype in human breast cancer cells using doxorubicin-liposome–microbubble complexes assisted by ultrasound. *Journal of Controlled Release* **2014,** *174*, 109-116.
[104] Chung, M.-F.; Chen, K.-J.; Liang, H.-F.; Liao, Z.-X.; Chia, W.-T.; Xia, Y.; Sung, H.-W., A Liposomal System Capable of Generating CO2 Bubbles to Induce Transient Cavitation, Lysosomal Rupturing, and Cell Necrosis. *Angewandte Chemie International Edition* **2012,** *51* (40), 10089-10093.
[105] Sun, Q.; Kang, Z.; Xue, L.; Shang, Y.; Su, Z.; Sun, H.; Ping, Q.; Mo, R.; Zhang, C., A Collaborative Assembly Strategy for Tumor-Targeted siRNA Delivery. *Journal of the American Chemical Society* **2015,** *137* (18), 6000-6010.
[106] Yavlovich, A.; Singh, A.; Tarasov, S.; Capala, J.; Blumenthal, R.; Puri, A., Design of liposomes containing photopolymerizable phospholipids for triggered release of contents. *Journal of Thermal Analysis and Calorimetry* **2009,** *98* (1), 97.
[107] Chen, H.; Zhang, H.; Thor, D.; Rahimian, R.; Guo, X., Novel pH-sensitive cationic lipids with linear ortho ester linkers for gene delivery. *European Journal of Medicinal Chemistry* **2012,** *52*, 159-172.
[108] Thamphiwatana, S.; Gao, W.; Pornpattananangkul, D.; Zhang, Q.; Fu, V.; Li, J.; Li, J.; Obonyo, M.; Zhang, L., Phospholipase A2-responsive antibiotic delivery via nanoparticle-stabilized liposomes for the treatment of bacterial infection. *Journal of Materials Chemistry B* **2014,** *2* (46), 8201-8207.
[109] Castelli, D. D.; Boffa, C.; Giustetto, P.; Terreno, E.; Aime, S., Design and testing of paramagnetic liposome-based CEST agents for MRI visualization of payload release on pH-induced and ultrasound stimulation. *JBIC Journal of Biological Inorganic Chemistry* **2014,** *19* (2), 207-214.
[110] Torres, E.; Mainini, F.; Napolitano, R.; Fedeli, F.; Cavalli, R.; Aime, S.; Terreno, E., Improved paramagnetic liposomes for MRI visualization of pH triggered release. *Journal of Controlled Release* **2011,** *154* (2), 196-202.
[111] Barbosa, M. V.; Monteiro, L. O. F.; Carneiro, G.; Malagutti, A. R.; Vilela, J. M. C.; Andrade, M. S.; Oliveira, M. C.; Carvalho-Junior, A. D.; Leite, E. A., Experimental design of a liposomal lipid system: A potential strategy for paclitaxel-based breast cancer treatment. *Colloids and Surfaces B: Biointerfaces* **2015,** *136*, 553-561.
[112] Shimanouchi, T.; Kawasaki, H.; Fuse, M.; Umakoshi, H.; Kuboi, R., Membrane fusion mediated by phospholipase C under endosomal pH conditions. *Colloids and Surfaces B: Biointerfaces* **2013,** *103*, 75-83.
[113] Shaheen, S. M.; Akita, H.; Nakamura, T.; Takayama, S.; Futaki, S.; Yamashita, A.; Katoono, R.; Yui, N.; Harashima, H., KALA-modified multi-layered nanoparticles as gene carriers for MHC class-I mediated antigen presentation for a DNA vaccine. *Biomaterials* **2011,** *32* (26), 6342-6350.
[114] Hersch, N.; Wolters, B.; Ungvari, Z.; Gautam, T.; Deshpande, D.; Merkel, R.; Csiszar, A.; Hoffmann, B.; Csiszár, A., Biotin-conjugated fusogenic liposomes for high-quality cell purification. *Journal of Biomaterials Applications* **2015,** *30* (6), 846-856.
[115] Thamphiwatana, S.; Fu, V.; Zhu, J.; Lu, D.; Gao, W.; Zhang, L., Nanoparticle-Stabilized Liposomes for pH-Responsive Gastric Drug Delivery. *Langmuir* **2013,** *29* (39), 12228-12233.
[116] Kube, S.; Hersch, N.; Naumovska, E.; Gensch, T.; Hendriks, J.; Franzen, A.; Landvogt, L.; Siebrasse, J.-P.; Kubitscheck, U.; Hoffmann, B.; Merkel, R.; Csiszár, A., Fusogenic

Liposomes as Nanocarriers for the Delivery of Intracellular Proteins. *Langmuir* **2017,** *33* (4), 1051-1059.
[117] Kim, B.; Pang, H.-B.; Kang, J.; Park, J.-H.; Ruoslahti, E.; Sailor, M. J., Immunogene therapy with fusogenic nanoparticles modulates macrophage response to Staphylococcus aureus. *Nature Communications* **2018,** *9* (1), 1969.
[118] Xu, Y.; Szoka, F. C., Mechanism of DNA Release from Cationic Liposome/DNA Complexes Used in Cell Transfection. *Biochemistry* **1996,** *35* (18), 5616-5623.
[119] Zelphati, O.; Szoka, F. C., Mechanism of oligonucleotide release from cationic liposomes. *Proceedings of the National Academy of Sciences* **1996,** *93* (21), 11493.
[120] Felgner, P. L.; Gadek, T. R.; Holm, M.; Roman, R.; Chan, H. W.; Wenz, M.; Northrop, J. P.; Ringold, G. M.; Danielsen, M., Lipofection: a highly efficient, lipid-mediated DNA-transfection procedure. *Proceedings of the National Academy of Sciences* **1987,** *84* (21), 7413-7417.
[121] Zuhorn, I. S.; Bakowsky, U.; Polushkin, E.; Visser, W. H.; Stuart, M. C. A.; Engberts, J. B. F. N.; Hoekstra, D., Nonbilayer phase of lipoplex–membrane mixture determines endosomal escape of genetic cargo and transfection efficiency. *Molecular Therapy* **2005,** *11* (5), 801-810.
[122] Bartomeu Garcia, C.; Shi, D.; Webster, T. J., Tat-functionalized liposomes for the treatment of meningitis: an in vitro study. *International journal of nanomedicine* **2017,** *12*, 3009-3021.
[123] Wang, T.; Yang, S.; Petrenko, V. A.; Torchilin, V. P., Cytoplasmic Delivery of Liposomes into MCF-7 Breast Cancer Cells Mediated by Cell-Specific Phage Fusion Coat Protein. *Molecular Pharmaceutics* **2010,** *7* (4), 1149-1158.
[124] Csiszár, A.; Hersch, N.; Dieluweit, S.; Biehl, R.; Merkel, R.; Hoffmann, B., Novel Fusogenic Liposomes for Fluorescent Cell Labeling and Membrane Modification. *Bioconjugate Chemistry* **2010,** *21* (3), 537-543.
[125] Andreev, O. A.; Engelman, D. M.; Reshetnyak, Y. K., Targeting acidic diseased tissue: New technology based on use of the pH (Low) Insertion Peptide (pHLIP). *Chim Oggi* **2009,** *27* (2), 34-37.
[126] Yao, L.; Daniels, J.; Wijesinghe, D.; Andreev, O. A.; Reshetnyak, Y. K., pHLIP®-mediated delivery of PEGylated liposomes to cancer cells. *Journal of Controlled Release* **2013,** *167* (3), 228-237.
[127] Sosunov, E. A.; Anyukhovsky, E. P.; Sosunov, A. A.; Moshnikova, A.; Wijesinghe, D.; Engelman, D. M.; Reshetnyak, Y. K.; Andreev, O. A., pH (low) insertion peptide (pHLIP) targets ischemic myocardium. *Proceedings of the National Academy of Sciences* **2013,** *110* (1), 82-86.
[128] Li, W.; Nicol, F.; Szoka, F. C., GALA: a designed synthetic pH-responsive amphipathic peptide with applications in drug and gene delivery. *Advanced Drug Delivery Reviews* **2004,** *56* (7), 967-985.
[129] Andreev, O. A.; Dupuy, A. D.; Segala, M.; Sandugu, S.; Serra, D. A.; Chichester, C. O.; Engelman, D. M.; Reshetnyak, Y. K., Mechanism and uses of a membrane peptide that targets tumors and other acidic tissues in vivo. *Proceedings of the National Academy of Sciences* **2007,** *104* (19), 7893-7898.
[130] El-Say, K. M.; El-Sawy, H. S., Polymeric nanoparticles: Promising platform for drug delivery. *International Journal of Pharmaceutics* **2017,** *528* (1), 675-691.

[131] Xu, Y.; Du, Y.; Huang, R.; Gao, L., Preparation and modification of N-(2-hydroxyl) propyl-3-trimethyl ammonium chitosan chloride nanoparticle as a protein carrier. *Biomaterials* **2003,** *24* (27), 5015-5022.
[132] McNeil, S. E., Nanotechnology for the biologist. *Journal of Leukocyte Biology* **2005,** *78* (3), 585-594.
[133] Zhang, H.; Zhai, Y.; Wang, J.; Zhai, G., New progress and prospects: The application of nanogel in drug delivery. *Materials Science and Engineering: C* **2016,** *60*, 560-568.
[134] Sasaki, Y.; Akiyoshi, K., Nanogel engineering for new nanobiomaterials: from chaperoning engineering to biomedical applications. *The Chemical Record* **2010,** *10* (6), 366-376.
[135] Steinhilber, D.; Witting, M.; Zhang, X.; Staegemann, M.; Paulus, F.; Friess, W.; Küchler, S.; Haag, R., Surfactant free preparation of biodegradable dendritic polyglycerol nanogels by inverse nanoprecipitation for encapsulation and release of pharmaceutical biomacromolecules. *Journal of Controlled Release* **2013,** *169* (3), 289-295.
[136] Fujioka-Kobayashi, M.; Ota, M. S.; Shimoda, A.; Nakahama, K.-i.; Akiyoshi, K.; Miyamoto, Y.; Iseki, S., Cholesteryl group- and acryloyl group-bearing pullulan nanogel to deliver BMP2 and FGF18 for bone tissue engineering. *Biomaterials* **2012,** *33* (30), 7613-7620.
[137] Soppimath, K. S.; Aminabhavi, T. M.; Kulkarni, A. R.; Rudzinski, W. E., Biodegradable polymeric nanoparticles as drug delivery devices. *Journal of Controlled Release* **2001,** *70* (1), 1-20.
[138] Banik, B. L.; Fattahi, P.; Brown, J. L., Polymeric nanoparticles: the future of nanomedicine. *WIREs Nanomedicine and Nanobiotechnology* **2016,** *8* (2), 271-299.
[139] Wang, Y.; Li, P.; Truong-Dinh Tran, T.; Zhang, J.; Kong, L., Manufacturing Techniques and Surface Engineering of Polymer Based Nanoparticles for Targeted Drug Delivery to Cancer. *Nanomaterials* **2016,** *6* (2), 26.
[140] Masood, F., Polymeric nanoparticles for targeted drug delivery system for cancer therapy. *Materials Science and Engineering: C* **2016,** *60*, 569-578.
[141] Ma, Y.; Ge, Y.; Li, L., Advancement of multifunctional hybrid nanogel systems: Construction and application in drug co-delivery and imaging technique. *Materials Science and Engineering: C* **2017,** *71*, 1281-1292.
[142] Uhrich, K. E.; Cannizzaro, S. M.; Langer, R. S.; Shakesheff, K. M., Polymeric Systems for Controlled Drug Release. *Chemical Reviews* **1999,** *99* (11), 3181-3198.
[143] Paramonov, S. E.; Bachelder, E. M.; Beaudette, T. T.; Standley, S. M.; Lee, C. C.; Dashe, J.; Fréchet, J. M. J., Fully Acid-Degradable Biocompatible Polyacetal Microparticles for Drug Delivery. *Bioconjugate Chemistry* **2008,** *19* (4), 911-919.
[144] Chen, W.; Hou, Y.; Tu, Z.; Gao, L.; Haag, R., pH-degradable PVA-based nanogels via photo-crosslinking of thermo-preinduced nanoaggregates for controlled drug delivery. *Journal of Controlled Release* **2017,** *259*, 160-167.
[145] Dong, L.; Xia, S.; Wu, K.; Huang, Z.; Chen, H.; Chen, J.; Zhang, J., A pH/Enzyme-responsive tumor-specific delivery system for doxorubicin. *Biomaterials* **2010,** *31* (24), 6309-6316.
[146] Wong, C.; Stylianopoulos, T.; Cui, J.; Martin, J.; Chauhan, V. P.; Jiang, W.; Popović, Z.; Jain, R. K.; Bawendi, M. G.; Fukumura, D., Multistage nanoparticle delivery system for deep penetration into tumor tissue. *Proceedings of the National Academy of Sciences* **2011,** *108* (6), 2426-2431.

[147] Gu, Z.; Yan, M.; Hu, B.; Joo, K.-I.; Biswas, A.; Huang, Y.; Lu, Y.; Wang, P.; Tang, Y., Protein Nanocapsule Weaved with Enzymatically Degradable Polymeric Network. *Nano Letters* **2009,** *9* (12), 4533-4538.
[148] Dorresteijn, R.; Billecke, N.; Schwendy, M.; Pütz, S.; Bonn, M.; Parekh, S. H.; Klapper, M.; Müllen, K., Polylactide-block-Polypeptide-block-Polylactide Copolymer Nanoparticles with Tunable Cleavage and Controlled Drug Release. *Advanced Functional Materials* **2014,** *24* (26), 4026-4033.
[149] Yang, C.; Wang, X.; Yao, X.; Zhang, Y.; Wu, W.; Jiang, X., Hyaluronic acid nanogels with enzyme-sensitive cross-linking group for drug delivery. *Journal of Controlled Release* **2015,** *205*, 206-217.
[150] Aguirre, G.; Ramos, J.; Forcada, J., Synthesis of new enzymatically degradable thermo-responsive nanogels. *Soft Matter* **2013,** *9* (1), 261-270.
[151] Thornton, P. D.; Mart, R. J.; Ulijn, R. V., Enzyme-Responsive Polymer Hydrogel Particles for Controlled Release. *Advanced Materials* **2007,** *19* (9), 1252-1256.
[152] Kozielski, K. L.; Tzeng, S. Y.; Hurtado De Mendoza, B. A.; Green, J. J., Bioreducible Cationic Polymer-Based Nanoparticles for Efficient and Environmentally Triggered Cytoplasmic siRNA Delivery to Primary Human Brain Cancer Cells. *ACS Nano* **2014,** *8* (4), 3232-3241.
[153] Wilson, D. S.; Dalmasso, G.; Wang, L.; Sitaraman, S. V.; Merlin, D.; Murthy, N., Orally delivered thioketal nanoparticles loaded with TNF-α–siRNA target inflammation and inhibit gene expression in the intestines. *Nature Materials* **2010,** *9* (11), 923-928.
[154] Li, Y.-L.; Zhu, L.; Liu, Z.; Cheng, R.; Meng, F.; Cui, J.-H.; Ji, S.-J.; Zhong, Z., Reversibly Stabilized Multifunctional Dextran Nanoparticles Efficiently Deliver Doxorubicin into the Nuclei of Cancer Cells. *Angewandte Chemie International Edition* **2009,** *48* (52), 9914-9918.
[155] Pei, M.; Jia, X.; Zhao, X.; Li, J.; Liu, P., Alginate-based cancer-associated, stimuli-driven and turn-on theranostic prodrug nanogel for cancer detection and treatment. *Carbohydrate Polymers* **2018,** *183*, 131-139.
[156] Tian, Y.; Zheng, J.; Tang, X.; Ren, Q.; Wang, Y.; Yang, W., Near-Infrared Light-Responsive Nanogels with Diselenide-Cross-Linkers for On-Demand Degradation and Triggered Drug Release. *Particle & Particle Systems Characterization* **2015,** *32* (5), 547-551.
[157] Ohya, Y.; Takahashi, A.; Kuzuya, A., Preparation of Biodegradable Oligo(lactide)s-Grafted Dextran Nanogels for Efficient Drug Delivery by Controlling Intracellular Traffic. *International Journal of Molecular Sciences* **2018,** *19* (6).
[158] de Gracia Lux, C.; McFearin, C. L.; Joshi-Barr, S.; Sankaranarayanan, J.; Fomina, N.; Almutairi, A., Single UV or Near IR Triggering Event Leads to Polymer Degradation into Small Molecules. *ACS Macro Letters* **2012,** *1* (7), 922-926.
[159] Fomina, N.; McFearin, C.; Sermsakdi, M.; Edigin, O.; Almutairi, A., UV and Near-IR Triggered Release from Polymeric Nanoparticles. *Journal of the American Chemical Society* **2010,** *132* (28), 9540-9542.
[160] Viger, M. L.; Grossman, M.; Fomina, N.; Almutairi, A., Low Power Upconverted Near-IR Light for Efficient Polymeric Nanoparticle Degradation and Cargo Release. *Advanced Materials* **2013,** *25* (27), 3733-3738.
[161] Huang, Q.; Bao, C.; Ji, W.; Wang, Q.; Zhu, L., Photocleavable coumarin crosslinkers based polystyrene microgels: phototriggered swelling and release. *Journal of Materials Chemistry* **2012,** *22* (35), 18275-18282.

[162] Lee, Y.; Miyata, K.; Oba, M.; Ishii, T.; Fukushima, S.; Han, M.; Koyama, H.; Nishiyama, N.; Kataoka, K., Charge-Conversion Ternary Polyplex with Endosome Disruption Moiety: A Technique for Efficient and Safe Gene Delivery. *Angewandte Chemie International Edition* **2008,** *47* (28), 5163-5166.
[163] Morton, S. W.; Poon, Z.; Hammond, P. T., The architecture and biological performance of drug-loaded LbL nanoparticles. *Biomaterials* **2013,** *34* (21), 5328-5335.
[164] Dreaden, E. C.; Morton, S. W.; Shopsowitz, K. E.; Choi, J.-H.; Deng, Z. J.; Cho, N.-J.; Hammond, P. T., Bimodal Tumor-Targeting from Microenvironment Responsive Hyaluronan Layer-by-Layer (LbL) Nanoparticles. *ACS Nano* **2014,** *8* (8), 8374-8382.
[165] Oishi, M.; Sumitani, S.; Nagasaki, Y., On−Off Regulation of 19F Magnetic Resonance Signals Based on pH-Sensitive PEGylated Nanogels for Potential Tumor-Specific Smart 19F MRI Probes. *Bioconjugate Chemistry* **2007,** *18* (5), 1379-1382.
[166] Kabanov, A. V.; Vinogradov, S. V., Nanogels as Pharmaceutical Carriers: Finite Networks of Infinite Capabilities. *Angewandte Chemie International Edition* **2009,** *48* (30), 5418-5429.
[167] Hirakura, T.; Nomura, Y.; Aoyama, Y.; Akiyoshi, K., Photoresponsive Nanogels Formed by the Self-Assembly of Spiropyrane-Bearing Pullulan That Act as Artificial Molecular Chaperones. *Biomacromolecules* **2004,** *5* (5), 1804-1809.
[168] Chang, R.; Tsai, W.-B., Fabrication of Photothermo-Responsive Drug-Loaded Nanogel for Synergetic Cancer Therapy. *Polymers (Basel)* **2018,** *10* (10), 1098.
[169] Liu, Q.; Chen, X.; Jia, J.; Zhang, W.; Yang, T.; Wang, L.; Ma, G., pH-Responsive Poly(d,l-lactic-co-glycolic acid) Nanoparticles with Rapid Antigen Release Behavior Promote Immune Response. *ACS Nano* **2015,** *9* (5), 4925-4938.
[170] Wang, X.-G.; Dong, Z.-Y.; Cheng, H.; Wan, S.-S.; Chen, W.-H.; Zou, M.-Z.; Huo, J.-W.; Deng, H.-X.; Zhang, X.-Z., A multifunctional metal–organic framework based tumor targeting drug delivery system for cancer therapy. *Nanoscale* **2015,** *7* (38), 16061-16070.
[171] Tan, L.-L.; Li, H.; Qiu, Y.-C.; Chen, D.-X.; Wang, X.; Pan, R.-Y.; Wang, Y.; Zhang, S. X.-A.; Wang, B.; Yang, Y.-W., Stimuli-responsive metal–organic frameworks gated by pillar[5]arene supramolecular switches. *Chemical Science* **2015,** *6* (3), 1640-1644.
[172] Park, C.; Kim, H.; Kim, S.; Kim, C., Enzyme Responsive Nanocontainers with Cyclodextrin Gatekeepers and Synergistic Effects in Release of Guests. *Journal of the American Chemical Society* **2009,** *131* (46), 16614-16615.
[173] Angelos, S.; Choi, E.; Vögtle, F.; De Cola, L.; Zink, J. I., Photo-Driven Expulsion of Molecules from Mesostructured Silica Nanoparticles. *The Journal of Physical Chemistry C* **2007,** *111* (18), 6589-6592.
[174] Kempen, P. J.; Greasley, S.; Parker, K. A.; Campbell, J. L.; Chang, H.-Y.; Jones, J. R.; Sinclair, R.; Gambhir, S. S.; Jokerst, J. V., Theranostic mesoporous silica nanoparticles biodegrade after pro-survival drug delivery and ultrasound/magnetic resonance imaging of stem cells. *Theranostics* **2015,** *5* (6), 631-642.
[175] Fu, C.; Liu, T.; Li, L.; Liu, H.; Chen, D.; Tang, F., The absorption, distribution, excretion and toxicity of mesoporous silica nanoparticles in mice following different exposure routes. *Biomaterials* **2013,** *34* (10), 2565-2575.
[176] Liu, T.; Li, L.; Teng, X.; Huang, X.; Liu, H.; Chen, D.; Ren, J.; He, J.; Tang, F., Single and repeated dose toxicity of mesoporous hollow silica nanoparticles in intravenously exposed mice. *Biomaterials* **2011,** *32* (6), 1657-1668.

[177] Shen, D.; Yang, J.; Li, X.; Zhou, L.; Zhang, R.; Li, W.; Chen, L.; Wang, R.; Zhang, F.; Zhao, D., Biphase Stratification Approach to Three-Dimensional Dendritic Biodegradable Mesoporous Silica Nanospheres. *Nano Letters* **2014,** *14* (2), 923-932.
[178] Steel, A.; Carr, S. W.; Anderson, M. W., 29Si solid-state NMR study of mesoporous M41S materials. *Chemistry of Materials* **1995,** *7* (10), 1829-1832.
[179] Hao, X.; Hu, X.; Zhang, C.; Chen, S.; Li, Z.; Yang, X.; Liu, H.; Jia, G.; Liu, D.; Ge, K.; Liang, X.-J.; Zhang, J., Hybrid Mesoporous Silica-Based Drug Carrier Nanostructures with Improved Degradability by Hydroxyapatite. *ACS Nano* **2015,** *9* (10), 9614-9625.
[180] Fatieiev, Y.; Croissant, J. G.; Julfakyan, K.; Deng, L.; Anjum, D. H.; Gurinov, A.; Khashab, N. M., Enzymatically degradable hybrid organic–inorganic bridged silsesquioxane nanoparticles for in vitro imaging. *Nanoscale* **2015,** *7* (37), 15046-15050.
[181] Zhang, Q.; Shen, C.; Zhao, N.; Xu, F.-J., Redox-Responsive and Drug-Embedded Silica Nanoparticles with Unique Self-Destruction Features for Efficient Gene/Drug Codelivery. *Advanced Functional Materials* **2017,** *27* (10), 1606229.
[182] Xu, Z.; Zhang, K.; Liu, X.; Zhang, H., A new strategy to prepare glutathione responsive silica nanoparticles. *RSC Advances* **2013,** *3* (39), 17700-17702.
[183] Vivero-Escoto, J. L.; Rieter, W. J.; Lau, H.; Huxford-Phillips, R. C.; Lin, W., Biodegradable Polysilsesquioxane Nanoparticles as Efficient Contrast Agents for Magnetic Resonance Imaging. *Small* **2013,** *9* (20), 3523-3531.
[184] Wang, D.; Xu, Z.; Chen, Z.; Liu, X.; Hou, C.; Zhang, X.; Zhang, H., Fabrication of Single-Hole Glutathione-Responsive Degradable Hollow Silica Nanoparticles for Drug Delivery. *ACS Applied Materials & Interfaces* **2014,** *6* (15), 12600-12608.
[185] Maggini, L.; Cabrera, I.; Ruiz-Carretero, A.; Prasetyanto, E. A.; Robinet, E.; De Cola, L., Breakable mesoporous silica nanoparticles for targeted drug delivery. *Nanoscale* **2016,** *8* (13), 7240-7247.
[186] Croissant, J.; Cattoën, X.; Man, M. W. C.; Gallud, A.; Raehm, L.; Trens, P.; Maynadier, M.; Durand, J.-O., Biodegradable Ethylene-Bis(Propyl)Disulfide-Based Periodic Mesoporous Organosilica Nanorods and Nanospheres for Efficient In-Vitro Drug Delivery. *Advanced Materials* **2014,** *26* (35), 6174-6180.
[187] Wu, J.; Williams, G. R.; Niu, S.; Gao, F.; Tang, R.; Zhu, L.-M., A Multifunctional Biodegradable Nanocomposite for Cancer Theranostics. *Advanced Science* **2019,** *6* (14), 1802001.
[188] Huang, P.; Chen, Y.; Lin, H.; Yu, L.; Zhang, L.; Wang, L.; Zhu, Y.; Shi, J., Molecularly organic/inorganic hybrid hollow mesoporous organosilica nanocapsules with tumor-specific biodegradability and enhanced chemotherapeutic functionality. *Biomaterials* **2017,** *125*, 23-37.
[189] Zhang, S.; Chu, Z.; Yin, C.; Zhang, C.; Lin, G.; Li, Q., Controllable Drug Release and Simultaneously Carrier Decomposition of SiO2-Drug Composite Nanoparticles. *Journal of the American Chemical Society* **2013,** *135* (15), 5709-5716.
[190] Lai, C.-Y.; Trewyn, B. G.; Jeftinija, D. M.; Jeftinija, K.; Xu, S.; Jeftinija, S.; Lin, V. S. Y., A Mesoporous Silica Nanosphere-Based Carrier System with Chemically Removable CdS Nanoparticle Caps for Stimuli-Responsive Controlled Release of Neurotransmitters and Drug Molecules. *Journal of the American Chemical Society* **2003,** *125* (15), 4451-4459.
[191] Giri, S.; Trewyn, B. G.; Stellmaker, M. P.; Lin, V. S.-Y., Stimuli-Responsive Controlled-Release Delivery System Based on Mesoporous Silica Nanorods Capped with Magnetic Nanoparticles. *Angewandte Chemie International Edition* **2005,** *44* (32), 5038-5044.

[192] Gan, Q.; Lu, X.; Yuan, Y.; Qian, J.; Zhou, H.; Lu, X.; Shi, J.; Liu, C., A magnetic, reversible pH-responsive nanogated ensemble based on Fe3O4 nanoparticles-capped mesoporous silica. *Biomaterials* **2011,** *32* (7), 1932-1942.
[193] Zeng, X.; Liu, G.; Tao, W.; Ma, Y.; Zhang, X.; He, F.; Pan, J.; Mei, L.; Pan, G., A drug-self-gated mesoporous antitumor nanoplatform based on pH-sensitive dynamic covalent bond. *Advanced Functional Materials* **2017,** *27* (11), 1605985.
[194] Zhou, Z.; Zhu, S.; Zhang, D., Grafting of thermo-responsive polymer inside mesoporous silica with large pore size using ATRP and investigation of its use in drug release. *Journal of Materials Chemistry* **2007,** *17* (23), 2428-2433.
[195] Bernardos, A.; Mondragón, L.; Aznar, E.; Marcos, M. D.; Martínez-Máñez, R.; Sancenón, F.; Soto, J.; Barat, J. M.; Pérez-Payá, E.; Guillem, C.; Amorós, P., Enzyme-Responsive Intracellular Controlled Release Using Nanometric Silica Mesoporous Supports Capped with "Saccharides". *ACS Nano* **2010,** *4* (11), 6353-6368.
[196] Meng, H.; Xue, M.; Xia, T.; Zhao, Y.-L.; Tamanoi, F.; Stoddart, J. F.; Zink, J. I.; Nel, A. E., Autonomous in Vitro Anticancer Drug Release from Mesoporous Silica Nanoparticles by pH-Sensitive Nanovalves. *Journal of the American Chemical Society* **2010,** *132* (36), 12690-12697.
[197] Guo, R.; Li, L.-L.; Zhao, W.-H.; Chen, Y.-X.; Wang, X.-Z.; Fang, C.-J.; Feng, W.; Zhang, T.-L.; Ma, X.; Lu, M.; Peng, S.-Q.; Yan, C.-H., The intracellular controlled release from bioresponsive mesoporous silica with folate as both targeting and capping agent. *Nanoscale* **2012,** *4* (11), 3577-3583.
[198] Zhang, J.; Yuan, Z.-F.; Wang, Y.; Chen, W.-H.; Luo, G.-F.; Cheng, S.-X.; Zhuo, R.-X.; Zhang, X.-Z., Multifunctional Envelope-Type Mesoporous Silica Nanoparticles for Tumor-Triggered Targeting Drug Delivery. *Journal of the American Chemical Society* **2013,** *135* (13), 5068-5073.
[199] Patel, K.; Angelos, S.; Dichtel, W. R.; Coskun, A.; Yang, Y.-W.; Zink, J. I.; Stoddart, J. F., Enzyme-Responsive Snap-Top Covered Silica Nanocontainers. *Journal of the American Chemical Society* **2008,** *130* (8), 2382-2383.
[200] Liu, R.; Zhao, X.; Wu, T.; Feng, P., Tunable Redox-Responsive Hybrid Nanogated Ensembles. *Journal of the American Chemical Society* **2008,** *130* (44), 14418-14419.
[201] He, D.; He, X.; Wang, K.; Cao, J.; Zhao, Y., A Light-Responsive Reversible Molecule-Gated System Using Thymine-Modified Mesoporous Silica Nanoparticles. *Langmuir* **2012,** *28* (8), 4003-4008.
[202] Chen, Z.; Li, Z.; Lin, Y.; Yin, M.; Ren, J.; Qu, X., Bioresponsive Hyaluronic Acid-Capped Mesoporous Silica Nanoparticles for Targeted Drug Delivery. *Chemistry – A European Journal* **2013,** *19* (5), 1778-1783.
[203] Hu, S. H.; Chen, S. Y.; Liu, D. M.; Hsiao, C. S., Core/Single-Crystal-Shell Nanospheres for Controlled Drug Release via a Magnetically Triggered Rupturing Mechanism. *Advanced Materials* **2008,** *20* (14), 2690-2695.
[204] Paris, J. L.; Cabañas, M. V.; Manzano, M.; Vallet-Regí, M., Polymer-Grafted Mesoporous Silica Nanoparticles as Ultrasound-Responsive Drug Carriers. *ACS Nano* **2015,** *9* (11), 11023-11033.
[205] Park, J.; Jiang, Q.; Feng, D.; Mao, L.; Zhou, H.-C., Size-Controlled Synthesis of Porphyrinic Metal–Organic Framework and Functionalization for Targeted Photodynamic Therapy. *Journal of the American Chemical Society* **2016,** *138* (10), 3518-3525.

[206] Wu, M.-X.; Yang, Y.-W., Metal–Organic Framework (MOF)-Based Drug/Cargo Delivery and Cancer Therapy. *Advanced Materials* **2017,** *29* (23), 1606134.
[207] Zhuang, J.; Kuo, C.-H.; Chou, L.-Y.; Liu, D.-Y.; Weerapana, E.; Tsung, C.-K., Optimized Metal–Organic-Framework Nanospheres for Drug Delivery: Evaluation of Small-Molecule Encapsulation. *ACS Nano* **2014,** *8* (3), 2812-2819.
[208] Lin, W.; Hu, Q.; Jiang, K.; Yang, Y.; Yang, Y.; Cui, Y.; Qian, G., A porphyrin-based metal–organic framework as a pH-responsive drug carrier. *Journal of Solid State Chemistry* **2016,** *237*, 307-312.
[209] Ke, F.; Yuan, Y.-P.; Qiu, L.-G.; Shen, Y.-H.; Xie, A.-J.; Zhu, J.-F.; Tian, X.-Y.; Zhang, L.-D., Facile fabrication of magnetic metal–organic framework nanocomposites for potential targeted drug delivery. *Journal of Materials Chemistry* **2011,** *21* (11), 3843-3848.
[210] Tan, L.-L.; Li, H.; Zhou, Y.; Zhang, Y.; Feng, X.; Wang, B.; Yang, Y.-W., Zn2+-Triggered Drug Release from Biocompatible Zirconium MOFs Equipped with Supramolecular Gates. *Small* **2015,** *11* (31), 3807-3813.
[211] Meng, X.; Gui, B.; Yuan, D.; Zeller, M.; Wang, C., Mechanized azobenzene-functionalized zirconium metal-organic framework for on-command cargo release. *Science Advances* **2016,** *2* (8), e1600480.
[212] Fang, J.; Yang, Y.; Xiao, W.; Zheng, B.; Lv, Y.-B.; Liu, X.-L.; Ding, J., Extremely low frequency alternating magnetic field–triggered and MRI–traced drug delivery by optimized magnetic zeolitic imidazolate framework-90 nanoparticles. *Nanoscale* **2016,** *8* (6), 3259-3263.
[213] Bian, R.; Wang, T.; Zhang, L.; Li, L.; Wang, C., A combination of tri-modal cancer imaging and in vivo drug delivery by metal–organic framework based composite nanoparticles. *Biomaterials Science* **2015,** *3* (9), 1270-1278.
[214] Adhikari, C.; Chakraborty, A., Smart Approach for In Situ One-Step Encapsulation and Controlled Delivery of a Chemotherapeutic Drug using Metal–Organic Framework–Drug Composites in Aqueous Media. *ChemPhysChem* **2016,** *17* (7), 1070-1077.
[215] Zheng, H.; Zhang, Y.; Liu, L.; Wan, W.; Guo, P.; Nyström, A. M.; Zou, X., One-pot Synthesis of Metal–Organic Frameworks with Encapsulated Target Molecules and Their Applications for Controlled Drug Delivery. *Journal of the American Chemical Society* **2016,** *138* (3), 962-968.
[216] Sun, C.-Y.; Qin, C.; Wang, X.-L.; Yang, G.-S.; Shao, K.-Z.; Lan, Y.-Q.; Su, Z.-M.; Huang, P.; Wang, C.-G.; Wang, E.-B., Zeolitic imidazolate framework-8 as efficient pH-sensitive drug delivery vehicle. *Dalton Transactions* **2012,** *41* (23), 6906-6909.
[217] Gong, M.; Yang, J.; Li, Y.; Gu, J., Glutathione-responsive nanoscale MOFs for effective intracellular delivery of the anticancer drug 6-mercaptopurine. *Chemical Communications* **2020**.
[218] Zhao, J.; Yang, Y.; Han, X.; Liang, C.; Liu, J.; Song, X.; Ge, Z.; Liu, Z., Redox-Sensitive Nanoscale Coordination Polymers for Drug Delivery and Cancer Theranostics. *ACS Applied Materials & Interfaces* **2017,** *9* (28), 23555-23563.
[219] Lei, B.; Wang, M.; Jiang, Z.; Qi, W.; Su, R.; He, Z., Constructing Redox-Responsive Metal–Organic Framework Nanocarriers for Anticancer Drug Delivery. *ACS Applied Materials & Interfaces* **2018,** *10* (19), 16698-16706.
[220] Epley, C. C.; Roth, K. L.; Lin, S.; Ahrenholtz, S. R.; Grove, T. Z.; Morris, A. J., Cargo delivery on demand from photodegradable MOF nano-cages. *Dalton Transactions* **2017,** *46* (15), 4917-4922.

[221] Paul, M.; Dastidar, P., Coordination Polymers Derived from Non-Steroidal Anti-Inflammatory Drugs for Cell Imaging and Drug Delivery. *Chemistry – A European Journal* **2016,** *22* (3), 988-998.
[222] Liu, J.; Chen, Q.; Zhu, W.; Yi, X.; Yang, Y.; Dong, Z.; Liu, Z., Nanoscale-Coordination-Polymer-Shelled Manganese Dioxide Composite Nanoparticles: A Multistage Redox/pH/H2O2-Responsive Cancer Theranostic Nanoplatform. *Advanced Functional Materials* **2017,** *27* (10), 1605926.
[223] Rieter, W. J.; Pott, K. M.; Taylor, K. M. L.; Lin, W., Nanoscale Coordination Polymers for Platinum-Based Anticancer Drug Delivery. *Journal of the American Chemical Society* **2008,** *130* (35), 11584-11585.
[224] Yang, Y.; Liu, J.; Liang, C.; Feng, L.; Fu, T.; Dong, Z.; Chao, Y.; Li, Y.; Lu, G.; Chen, M.; Liu, Z., Nanoscale Metal–Organic Particles with Rapid Clearance for Magnetic Resonance Imaging-Guided Photothermal Therapy. *ACS Nano* **2016,** *10* (2), 2774-2781.
[225] Wang, W.; Wang, L.; Li, Z.; Xie, Z., BODIPY-containing nanoscale metal–organic frameworks for photodynamic therapy. *Chemical Communications* **2016,** *52* (31), 5402-5405.
[226] Wang, D.; Zhou, J.; Chen, R.; Shi, R.; Xia, G.; Zhou, S.; Liu, Z.; Zhang, N.; Wang, H.; Guo, Z.; Chen, Q., Magnetically guided delivery of DHA and Fe ions for enhanced cancer therapy based on pH-responsive degradation of DHA-loaded Fe3O4@C@MIL-100(Fe) nanoparticles. *Biomaterials* **2016,** *107*, 88-101.
[227] Chen, W.; Ouyang, J.; Liu, H.; Chen, M.; Zeng, K.; Sheng, J.; Liu, Z.; Han, Y.; Wang, L.; Li, J.; Deng, L.; Liu, Y.-N.; Guo, S., Black Phosphorus Nanosheet-Based Drug Delivery System for Synergistic Photodynamic/Photothermal/Chemotherapy of Cancer. *Advanced Materials* **2017,** *29* (5), 1603864.
[228] Yu, Y.; Chen, C.-K.; Law, W.-C.; Weinheimer, E.; Sengupta, S.; Prasad, P. N.; Cheng, C., Polylactide-graft-doxorubicin Nanoparticles with Precisely Controlled Drug Loading for pH-Triggered Drug Delivery. *Biomacromolecules* **2014,** *15* (2), 524-532.
[229] Zhang, P.; Zhang, H.; He, W.; Zhao, D.; Song, A.; Luan, Y., Disulfide-Linked Amphiphilic Polymer-Docetaxel Conjugates Assembled Redox-Sensitive Micelles for Efficient Antitumor Drug Delivery. *Biomacromolecules* **2016,** *17* (5), 1621-1632.
[230] Lv, S.; Tang, Z.; Zhang, D.; Song, W.; Li, M.; Lin, J.; Liu, H.; Chen, X., Well-defined polymer-drug conjugate engineered with redox and pH-sensitive release mechanism for efficient delivery of paclitaxel. *Journal of Controlled Release* **2014,** *194*, 220-227.
[231] Vasey, P. A.; Kaye, S. B.; Morrison, R.; Twelves, C.; Wilson, P.; Duncan, R.; Thomson, A. H.; Murray, L. S.; Hilditch, T. E.; Murray, T.; Burtles, S.; Fraier, D.; Frigerio, E.; Cassidy, J., Phase I Clinical and Pharmacokinetic Study of PK1 [N-(2-Hydroxypropyl)methacrylamide Copolymer Doxorubicin]: First Member of a New Class of Chemotherapeutic Agents—Drug-Polymer Conjugates. *Clinical Cancer Research* **1999,** *5* (1), 83.
[232] Zhang, C.; Pan, D.; Luo, K.; She, W.; Guo, C.; Yang, Y.; Gu, Z., Peptide Dendrimer–Doxorubicin Conjugate-Based Nanoparticles as an Enzyme-Responsive Drug Delivery System for Cancer Therapy. *Advanced Healthcare Materials* **2014,** *3* (8), 1299-1308.
[233] Nani, R. R.; Gorka, A. P.; Nagaya, T.; Kobayashi, H.; Schnermann, M. J., Near-IR Light-Mediated Cleavage of Antibody–Drug Conjugates Using Cyanine Photocages. *Angewandte Chemie International Edition* **2015,** *54* (46), 13635-13638.

[234] Zhou, Z.; Ma, X.; Jin, E.; Tang, J.; Sui, M.; Shen, Y.; Van Kirk, E. A.; Murdoch, W. J.; Radosz, M., Linear-dendritic drug conjugates forming long-circulating nanorods for cancer-drug delivery. *Biomaterials* **2013,** *34* (22), 5722-5735.
[235] Azagarsamy, M. A.; Anseth, K. S., Wavelength-Controlled Photocleavage for the Orthogonal and Sequential Release of Multiple Proteins. *Angewandte Chemie International Edition* **2013,** *52* (51), 13803-13807.
[236] Dreaden, E. C.; Alkilany, A. M.; Huang, X.; Murphy, C. J.; El-Sayed, M. A., The golden age: gold nanoparticles for biomedicine. *Chemical Society Reviews* **2012,** *41* (7), 2740-2779.
[237] Kim, C. K.; Ghosh, P.; Pagliuca, C.; Zhu, Z.-J.; Menichetti, S.; Rotello, V. M., Entrapment of Hydrophobic Drugs in Nanoparticle Monolayers with Efficient Release into Cancer Cells. *Journal of the American Chemical Society* **2009,** *131* (4), 1360-1361.
[238] Alkilany, A. M.; Frey, R. L.; Ferry, J. L.; Murphy, C. J., Gold Nanorods as Nanoadmicelles: 1-Naphthol Partitioning into a Nanorod-Bound Surfactant Bilayer. *Langmuir* **2008,** *24* (18), 10235-10239.
[239] Zhang, Z.; Wang, L.; Wang, J.; Jiang, X.; Li, X.; Hu, Z.; Ji, Y.; Wu, X.; Chen, C., Mesoporous Silica-Coated Gold Nanorods as a Light-Mediated Multifunctional Theranostic Platform for Cancer Treatment. *Advanced Materials* **2012,** *24* (11), 1418-1423.
[240] Kaminskas, L. M.; McLeod, V. M.; Kelly, B. D.; Sberna, G.; Boyd, B. J.; Williamson, M.; Owen, D. J.; Porter, C. J. H., A comparison of changes to doxorubicin pharmacokinetics, antitumor activity, and toxicity mediated by PEGylated dendrimer and PEGylated liposome drug delivery systems. *Nanomedicine: Nanotechnology, Biology and Medicine* **2012,** *8* (1), 103-111.
[241] Tao, W.; Zhu, X.; Yu, X.; Zeng, X.; Xiao, Q.; Zhang, X.; Ji, X.; Wang, X.; Shi, J.; Zhang, H.; Mei, L., Black Phosphorus Nanosheets as a Robust Delivery Platform for Cancer Theranostics. *Advanced Materials* **2017,** *29* (1), 1603276.
[242] Ji, X.; Kong, N.; Wang, J.; Li, W.; Xiao, Y.; Gan, S. T.; Zhang, Y.; Li, Y.; Song, X.; Xiong, Q.; Shi, S.; Li, Z.; Tao, W.; Zhang, H.; Mei, L.; Shi, J., A Novel Top-Down Synthesis of Ultrathin 2D Boron Nanosheets for Multimodal Imaging-Guided Cancer Therapy. *Advanced Materials* **2018,** *30* (36), 1803031.
[243] Zhu, Z.; Su, M., Polydopamine nanoparticles for combined chemo-and photothermal cancer therapy. *Nanomaterials* **2017,** *7* (7), 160.
[244] Liu, F.; He, X.; Lei, Z.; Liu, L.; Zhang, J.; You, H.; Zhang, H.; Wang, Z., Facile Preparation of Doxorubicin-Loaded Upconversion@Polydopamine Nanoplatforms for Simultaneous In Vivo Multimodality Imaging and Chemophotothermal Synergistic Therapy. *Advanced Healthcare Materials* **2015,** *4* (4), 559-568.
[245] Pasut, G.; Scaramuzza, S.; Schiavon, O.; Mendichi, R.; Veronese, F. M., PEG-epirubicin Conjugates with High Drug Loading. *Journal of Bioactive and Compatible Polymers* **2005,** *20* (3), 213-230.
[246] Soto-Castro, D.; Cruz-Morales, J. A.; Apan, M. T. R.; Guadarrama, P., Solubilization and anticancer-activity enhancement of Methotrexate by novel dendrimeric nanodevices synthesized in one-step reaction. *Bioorganic Chemistry* **2012,** *41-42*, 13-21.
[247] Zhang, C.; Pan, D.; Luo, K.; Li, N.; Guo, C.; Zheng, X.; Gu, Z., Dendrimer–doxorubicin conjugate as enzyme-sensitive and polymeric nanoscale drug delivery vehicle for ovarian cancer therapy. *Polymer Chemistry* **2014,** *5* (18), 5227-5235.

[248] Cui, J.; Yan, Y.; Such, G. K.; Liang, K.; Ochs, C. J.; Postma, A.; Caruso, F., Immobilization and Intracellular Delivery of an Anticancer Drug Using Mussel-Inspired Polydopamine Capsules. *Biomacromolecules* **2012,** *13* (8), 2225-2228.
[249] Sun, I.-C.; Lee, S.; Koo, H.; Kwon, I. C.; Choi, K.; Ahn, C.-H.; Kim, K., Caspase Sensitive Gold Nanoparticle for Apoptosis Imaging in Live Cells. *Bioconjugate Chemistry* **2010,** *21* (11), 1939-1942.
[250] Yu, Y.; Chen, C.-K.; Law, W.-C.; Sun, H.; Prasad, P. N.; Cheng, C., A degradable brush polymer–drug conjugate for pH-responsive release of doxorubicin. *Polymer Chemistry* **2015,** *6* (6), 953-961.
[251] Gianasi, E.; Wasil, M.; Evagorou, E. G.; Keddle, A.; Wilson, G.; Duncan, R., HPMA copolymer platinates as novel antitumour agents: in vitro properties, pharmacokinetics and antitumour activity in vivo. *European Journal of Cancer* **1999,** *35* (6), 994-1002.
[252] Guidry, E. N.; Farand, J.; Soheili, A.; Parish, C. A.; Kevin, N. J.; Pipik, B.; Calati, K. B.; Ikemoto, N.; Waldman, J. H.; Latham, A. H.; Howell, B. J.; Leone, A.; Garbaccio, R. M.; Barrett, S. E.; Parmar, R. G.; Truong, Q. T.; Mao, B.; Davies, I. W.; Colletti, S. L.; Sepp-Lorenzino, L., Improving the In Vivo Therapeutic Index of siRNA Polymer Conjugates through Increasing pH Responsiveness. *Bioconjugate Chemistry* **2014,** *25* (2), 296-307.
[253] Lee, M. H.; Sessler, J. L.; Kim, J. S., Disulfide-Based Multifunctional Conjugates for Targeted Theranostic Drug Delivery. *Accounts of Chemical Research* **2015,** *48* (11), 2935-2946.
[254] Griffin, D. R.; Schlosser, J. L.; Lam, S. F.; Nguyen, T. H.; Maynard, H. D.; Kasko, A. M., Synthesis of Photodegradable Macromers for Conjugation and Release of Bioactive Molecules. *Biomacromolecules* **2013,** *14* (4), 1199-1207.
[255] Griffin, D. R.; Kasko, A. M., Photoselective Delivery of Model Therapeutics from Hydrogels. *ACS Macro Letters* **2012,** *1* (11), 1330-1334.
[256] Du, J.-Z.; Du, X.-J.; Mao, C.-Q.; Wang, J., Tailor-Made Dual pH-Sensitive Polymer–Doxorubicin Nanoparticles for Efficient Anticancer Drug Delivery. *Journal of the American Chemical Society* **2011,** *133* (44), 17560-17563.
[257] Ganivada, M. N.; Rao N, V.; Dinda, H.; Kumar, P.; Das Sarma, J.; Shunmugam, R., Biodegradable Magnetic Nanocarrier for Stimuli Responsive Drug Release. *Macromolecules* **2014,** *47* (8), 2703-2711.
[258] Aguirre-Chagala, Y. E.; Santos, J. L.; Huang, Y.; Herrera-Alonso, M., Phenylboronic Acid-Installed Polycarbonates for the pH-Dependent Release of Diol-Containing Molecules. *ACS Macro Letters* **2014,** *3* (12), 1249-1253.
[259] Carmeliet, P.; Jain, R. K., Angiogenesis in cancer and other diseases. *Nature* **2000,** *407* (6801), 249-257.
[260] Haley, B.; Frenkel, E., Nanoparticles for drug delivery in cancer treatment. *Urologic Oncology: Seminars and Original Investigations* **2008,** *26* (1), 57-64.
[261] Maeda, H.; Nakamura, H.; Fang, J., The EPR effect for macromolecular drug delivery to solid tumors: Improvement of tumor uptake, lowering of systemic toxicity, and distinct tumor imaging in vivo. *Advanced Drug Delivery Reviews* **2013,** *65* (1), 71-79.
[262] Bissery, M. C., Preclinical pharmacology of docetaxel. *European Journal of Cancer* **1995,** *31*, S1-S6.
[263] Zamboni, W. C.; Strychor, S.; Joseph, E.; Parise, R. A.; Egorin, M. J.; Eiseman, J. L., Tumor, tissue, and plasma pharmacokinetic studies and antitumor response studies of docetaxel in

combination with 9-nitrocamptothecin in mice bearing SKOV-3 human ovarian xenografts. *Cancer Chemotherapy and Pharmacology* **2008,** *62* (3), 417-426.
[264] Kamaly, N.; Xiao, Z.; Valencia, P. M.; Radovic-Moreno, A. F.; Farokhzad, O. C., Targeted polymeric therapeutic nanoparticles: design, development and clinical translation. *Chemical Society Reviews* **2012,** *41* (7), 2971-3010.
[265] Bae, Y. H.; Park, K., Targeted drug delivery to tumors: Myths, reality and possibility. *Journal of Controlled Release* **2011,** *153* (3), 198-205.
[266] Hobbs, S. K.; Monsky, W. L.; Yuan, F.; Roberts, W. G.; Griffith, L.; Torchilin, V. P.; Jain, R. K., Regulation of transport pathways in tumor vessels: Role of tumor type and microenvironment. *Proceedings of the National Academy of Sciences* **1998,** *95* (8), 4607-4612.
[267] Chrastina, A.; Massey, K. A.; Schnitzer, J. E., Overcoming in vivo barriers to targeted nanodelivery. *WIREs Nanomedicine and Nanobiotechnology* **2011,** *3* (4), 421-437.
[268] Lammers, T.; Kiessling, F.; Hennink, W. E.; Storm, G., Drug targeting to tumors: Principles, pitfalls and (pre-) clinical progress. *Journal of Controlled Release* **2012,** *161* (2), 175-187.
[269] Jiang, W.; Kim, B. Y. S.; Rutka, J. T.; Chan, W. C. W., Nanoparticle-mediated cellular response is size-dependent. *Nature Nanotechnology* **2008,** *3* (3), 145-150.
[270] Maeda, H., Toward a full understanding of the EPR effect in primary and metastatic tumors as well as issues related to its heterogeneity. *Advanced Drug Delivery Reviews* **2015,** *91*, 3-6.
[271] Zhao, L.; Yuan, W.; Li, J.; Yang, L.; Su, Y.; Peng, J.; Chen, R.; Tham, H. P.; Chen, H.; Lim, W. Q.; Xiang, H.; Xing, P.; Li, F.; Zhao, Y., Independent of EPR Effect: A Smart Delivery Nanosystem for Tracking and Treatment of Nonvascularized Intra-Abdominal Metastases. *Advanced Functional Materials* **2018,** *28* (50), 1806162.
[272] Singhana, B.; Slattery, P.; Melancon, M. P., 14 - Targeted gold nanoshells. In *Applications of Nanoscience in Photomedicine*, Hamblin, M. R.; Avci, P., Eds. Chandos Publishing: Oxford, 2015; pp 267-290.
[273] Maeda, H., Tumor-Selective Delivery of Macromolecular Drugs via the EPR Effect: Background and Future Prospects. *Bioconjugate Chemistry* **2010,** *21* (5), 797-802.
[274] Mulder, W. J. M.; Douma, K.; Koning, G. A.; van Zandvoort, M. A.; Lutgens, E.; Daemen, M. J.; Nicolay, K.; Strijkers, G. J., Liposome-enhanced MRI of neointimal lesions in the ApoE-KO mouse. *Magnetic Resonance in Medicine* **2006,** *55* (5), 1170-1174.
[275] Heldin, C.-H.; Rubin, K.; Pietras, K.; Östman, A., High interstitial fluid pressure — an obstacle in cancer therapy. *Nature Reviews Cancer* **2004,** *4* (10), 806-813.
[276] Jain, R. K.; Stylianopoulos, T., Delivering nanomedicine to solid tumors. *Nature Reviews Clinical Oncology* **2010,** *7* (11), 653-664.
[277] Mitchell, M. J.; Jain, R. K.; Langer, R., Engineering and physical sciences in oncology: challenges and opportunities. *Nature Reviews Cancer* **2017,** *17* (11), 659-675.
[278] Libutti, S. K.; Tamarkin, L.; Nilubol, N., Targeting the invincible barrier for drug delivery in solid cancers: interstitial fluid pressure. *Oncotarget* **2018,** *9* (87), 35723-35725.
[279] Fang, J.; Nakamura, H.; Maeda, H., The EPR effect: Unique features of tumor blood vessels for drug delivery, factors involved, and limitations and augmentation of the effect. *Advanced Drug Delivery Reviews* **2011,** *63* (3), 136-151.
[280] Eikenes, L.; Tari, M.; Tufto, I.; Bruland, Ø. S.; de Lange Davies, C., Hyaluronidase induces a transcapillary pressure gradient and improves the distribution and uptake of liposomal

doxorubicin (Caelyx™) in human osteosarcoma xenografts. *British Journal of Cancer* **2005,** *93* (1), 81-88.
[281] Seynhaeve, A. L. B.; Hoving, S.; Schipper, D.; Vermeulen, C. E.; aan de Wiel-Ambagtsheer, G.; van Tiel, S. T.; Eggermont, A. M. M.; ten Hagen, T. L. M., Tumor Necrosis Factor α Mediates Homogeneous Distribution of Liposomes in Murine Melanoma that Contributes to a Better Tumor Response. *Cancer Research* **2007,** *67* (19), 9455-9462.
[282] Kano, M. R.; Bae, Y.; Iwata, C.; Morishita, Y.; Yashiro, M.; Oka, M.; Fujii, T.; Komuro, A.; Kiyono, K.; Kaminishi, M.; Hirakawa, K.; Ouchi, Y.; Nishiyama, N.; Kataoka, K.; Miyazono, K., Improvement of cancer-targeting therapy, using nanocarriers for intractable solid tumors by inhibition of TGF-β signaling. *Proceedings of the National Academy of Sciences* **2007,** *104* (9), 3460-3465.
[283] McKee, T. D.; Grandi, P.; Mok, W.; Alexandrakis, G.; Insin, N.; Zimmer, J. P.; Bawendi, M. G.; Boucher, Y.; Breakefield, X. O.; Jain, R. K., Degradation of Fibrillar Collagen in a Human Melanoma Xenograft Improves the Efficacy of an Oncolytic Herpes Simplex Virus Vector. *Cancer Research* **2006,** *66* (5), 2509-2513.
[284] Perentes, J. Y.; McKee, T. D.; Ley, C. D.; Mathiew, H.; Dawson, M.; Padera, T. P.; Munn, L. L.; Jain, R. K.; Boucher, Y., In vivo imaging of extracellular matrix remodeling by tumor-associated fibroblasts. *Nature Methods* **2009,** *6* (2), 143-145.
[285] Attia, M. F.; Anton, N.; Wallyn, J.; Omran, Z.; Vandamme, T. F., An overview of active and passive targeting strategies to improve the nanocarriers efficiency to tumour sites. *Journal of Pharmacy and Pharmacology* **2019,** *71* (8), 1185-1198.
[286] Narum, S. M.; Le, T.; Le, D. P.; Lee, J. C.; Donahue, N. D.; Yang, W.; Wilhelm, S., Chapter 4 - Passive targeting in nanomedicine: fundamental concepts, body interactions, and clinical potential. In *Nanoparticles for Biomedical Applications*, Chung, E. J.; Leon, L.; Rinaldi, C., Eds. Elsevier: 2020; pp 37-53.
[287] Ghaffari, M.; Dehghan, G.; Abedi-Gaballu, F.; Kashanian, S.; Baradaran, B.; Ezzati Nazhad Dolatabadi, J.; Losic, D., Surface functionalized dendrimers as controlled-release delivery nanosystems for tumor targeting. *European Journal of Pharmaceutical Sciences* **2018,** *122*, 311-330.
[288] Sakurai, Y.; Akita, H.; Harashima, H., Targeting Tumor Endothelial Cells with Nanoparticles. *International Journal of Molecular Sciences* **2019,** *20* (23).
[289] Wang, Y.; Xu, J.; Xia, X.; Yang, M.; Vangveravong, S.; Chen, J.; Mach, R. H.; Xia, Y., SV119-gold nanocage conjugates: a new platform for targeting cancer cellsvia sigma-2 receptors. *Nanoscale* **2012,** *4* (2), 421-424.
[290] Zhao, B.; Dong, K.; Lin, M.; Dong, G.; Shan, S.; Lawson, T.; Yan, L.; Zhang, W.; Shi, B.; Chou, S.; Baker, M. S.; Liu, Y., A Transferrin Triggered Pathway for Highly Targeted Delivery of Graphene-Based Nanodrugs to Treat Choroidal Melanoma. *Advanced Healthcare Materials* **2018,** *7* (16), 1800377.
[291] Bagalkot, V.; Gao, X., siRNA-Aptamer Chimeras on Nanoparticles: Preserving Targeting Functionality for Effective Gene Silencing. *ACS Nano* **2011,** *5* (10), 8131-8139.
[292] Zhang, H.; Shang, Y.; Li, Y.-H.; Sun, S.-K.; Yin, X.-B., Smart Metal–Organic Framework-Based Nanoplatforms for Imaging-Guided Precise Chemotherapy. *ACS Applied Materials & Interfaces* **2019,** *11* (2), 1886-1895.
[293] Zhang, Q.; Liu, F.; Nguyen, K. T.; Ma, X.; Wang, X.; Xing, B.; Zhao, Y., Multifunctional Mesoporous Silica Nanoparticles for Cancer-Targeted and Controlled Drug Delivery. *Advanced Functional Materials* **2012,** *22* (24), 5144-5156.

[294] Palanikumar, L.; Choi, E. S.; Cheon, J. Y.; Joo, S. H.; Ryu, J.-H., Noncovalent Polymer-Gatekeeper in Mesoporous Silica Nanoparticles as a Targeted Drug Delivery Platform. *Advanced Functional Materials* **2015,** *25* (6), 957-965.
[295] Zhang, L.; Wang, Y.; Zhang, X.; Wei, X.; Xiong, X.; Zhou, S., Enzyme and Redox Dual-Triggered Intracellular Release from Actively Targeted Polymeric Micelles. *ACS Applied Materials & Interfaces* **2017,** *9* (4), 3388-3399.
[296] Ke, W.; Li, J.; Zhao, K.; Zha, Z.; Han, Y.; Wang, Y.; Yin, W.; Zhang, P.; Ge, Z., Modular Design and Facile Synthesis of Enzyme-Responsive Peptide-Linked Block Copolymers for Efficient Delivery of Doxorubicin. *Biomacromolecules* **2016,** *17* (10), 3268-3276.
[297] Cheng, Y.-J.; Luo, G.-F.; Zhu, J.-Y.; Xu, X.-D.; Zeng, X.; Cheng, D.-B.; Li, Y.-M.; Wu, Y.; Zhang, X.-Z.; Zhuo, R.-X.; He, F., Enzyme-Induced and Tumor-Targeted Drug Delivery System Based on Multifunctional Mesoporous Silica Nanoparticles. *ACS Applied Materials & Interfaces* **2015,** *7* (17), 9078-9087.
[298] Lei, Q.; Qiu, W.-X.; Hu, J.-J.; Cao, P.-X.; Zhu, C.-H.; Cheng, H.; Zhang, X.-Z., Multifunctional Mesoporous Silica Nanoparticles with Thermal-Responsive Gatekeeper for NIR Light-Triggered Chemo/Photothermal-Therapy. *Small* **2016,** *12* (31), 4286-4298.
[299] Xu, X.; Zhang, L.; Assanhou, A. G.; Wang, L.; Zhang, Y.; Li, W.; Xue, L.; Mo, R.; Zhang, C., Acid/redox dual-activated liposomes for tumor-targeted drug delivery and enhanced therapeutic efficacy. *RSC Advances* **2015,** *5* (83), 67803-67808.
[300] Kim, M. S.; Lee, D.-W.; Park, K.; Park, S.-J.; Choi, E.-J.; Park, E. S.; Kim, H. R., Temperature-triggered tumor-specific delivery of anticancer agents by cRGD-conjugated thermosensitive liposomes. *Colloids and Surfaces B: Biointerfaces* **2014,** *116*, 17-25.
[301] Bareford, L. M.; Swaan, P. W., Endocytic mechanisms for targeted drug delivery. *Advanced Drug Delivery Reviews* **2007,** *59* (8), 748-758.
[302] Farokhzad, O. C.; Cheng, J.; Teply, B. A.; Sherifi, I.; Jon, S.; Kantoff, P. W.; Richie, J. P.; Langer, R., Targeted nanoparticle-aptamer bioconjugates for cancer chemotherapy in vivo. *Proceedings of the National Academy of Sciences* **2006,** *103* (16), 6315-6320.
[303] Chase, D. M.; Chaplin, D. J.; Monk, B. J., The development and use of vascular targeted therapy in ovarian cancer. *Gynecologic Oncology* **2017,** *145* (2), 393-406.
[304] Nel, A. E.; Mädler, L.; Velegol, D.; Xia, T.; Hoek, E. M. V.; Somasundaran, P.; Klaessig, F.; Castranova, V.; Thompson, M., Understanding biophysicochemical interactions at the nano–bio interface. *Nature Materials* **2009,** *8* (7), 543-557.
[305] Wang, S.; Dormidontova, E. E., Nanoparticle Design Optimization for Enhanced Targeting: Monte Carlo Simulations. *Biomacromolecules* **2010,** *11* (7), 1785-1795.
[306] Stefanick, J. F.; Ashley, J. D.; Kiziltepe, T.; Bilgicer, B., A Systematic Analysis of Peptide Linker Length and Liposomal Polyethylene Glycol Coating on Cellular Uptake of Peptide-Targeted Liposomes. *ACS Nano* **2013,** *7* (4), 2935-2947.
[307] Hlavacek, W. S.; Posner, R. G.; Perelson, A. S., Steric Effects on Multivalent Ligand-Receptor Binding: Exclusion of Ligand Sites by Bound Cell Surface Receptors. *Biophysical Journal* **1999,** *76* (6), 3031-3043.
[308] Gu, F.; Zhang, L.; Teply, B. A.; Mann, N.; Wang, A.; Radovic-Moreno, A. F.; Langer, R.; Farokhzad, O. C., Precise engineering of targeted nanoparticles by using self-assembled biointegrated block copolymers. *Proceedings of the National Academy of Sciences* **2008,** *105* (7), 2586-2591.
[309] Hristov, D. R.; Rocks, L.; Kelly, P. M.; Thomas, S. S.; Pitek, A. S.; Verderio, P.; Mahon, E.; Dawson, K. A., Tuning of nanoparticle biological functionality through controlled surface

chemistry and characterisation at the bioconjugated nanoparticle surface. *Scientific Reports* **2015,** *5* (1), 17040.
[310] Elias, D. R.; Poloukhtine, A.; Popik, V.; Tsourkas, A., Effect of ligand density, receptor density, and nanoparticle size on cell targeting. *Nanomedicine: Nanotechnology, Biology and Medicine* **2013,** *9* (2), 194-201.
[311] Kaufmann, R.; MÜLler, P.; Hildenbrand, G.; Hausmann, M.; Cremer, C., Analysis of Her2/neu membrane protein clusters in different types of breast cancer cells using localization microscopy. *Journal of Microscopy* **2011,** *242* (1), 46-54.
[312] Smart, E. J.; Mineo, C.; Anderson, R. G., Clustered folate receptors deliver 5-methyltetrahydrofolate to cytoplasm of MA104 cells. *Journal of Cell Biology* **1996,** *134* (5), 1169-1177.
[313] Cluzel, C.; Saltel, F. d. r.; Lussi, J.; Paulhe, F. d. r.; Imhof, B. A.; Wehrle-Haller, B., The mechanisms and dynamics of αvβ3 integrin clustering in living cells. *Journal of Cell Biology* **2005,** *171* (2), 383-392.
[314] Liu, A. P.; Aguet, F.; Danuser, G.; Schmid, S. L., Local clustering of transferrin receptors promotes clathrin-coated pit initiation. *Journal of Cell Biology* **2010,** *191* (7), 1381-1393.
[315] Poon, Z.; Chen, S.; Engler, A. C.; Lee, H.-i.; Atas, E.; von Maltzahn, G.; Bhatia, S. N.; Hammond, P. T., Ligand-Clustered "Patchy" Nanoparticles for Modulated Cellular Uptake and In Vivo Tumor Targeting. *Angewandte Chemie International Edition* **2010,** *49* (40), 7266-7270.
[316] Pirollo, K. F.; Chang, E. H., Does a targeting ligand influence nanoparticle tumor localization or uptake? *Trends in Biotechnology* **2008,** *26* (10), 552-558.
[317] Farokhzad, O. C.; Langer, R., Impact of Nanotechnology on Drug Delivery. *ACS Nano* **2009,** *3* (1), 16-20.
[318] Kirpotin, D. B.; Drummond, D. C.; Shao, Y.; Shalaby, M. R.; Hong, K.; Nielsen, U. B.; Marks, J. D.; Benz, C. C.; Park, J. W., Antibody Targeting of Long-Circulating Lipidic Nanoparticles Does Not Increase Tumor Localization but Does Increase Internalization in Animal Models. *Cancer Research* **2006,** *66* (13), 6732-6740.
[319] Sun, Y.; Davis, E., Nanoplatforms for Targeted Stimuli-Responsive Drug Delivery: A Review of Platform Materials and Stimuli-Responsive Release and Targeting Mechanisms. *Nanomaterials* **2021,** *11* (3), 746.
[320] Longmire, M.; Choyke, P. L.; Kobayashi, H., Clearance properties of nano-sized particles and molecules as imaging agents: considerations and caveats. *Nanomedicine (Lond)* **2008,** *3* (5), 703-717.
[321] Moghimi, S. M.; Hunter, A. C.; Murray, J. C., Long-Circulating and Target-Specific Nanoparticles: Theory to Practice. *Pharmacological Reviews* **2001,** *53* (2), 283-318.
[322] Schädlich, A.; Caysa, H.; Mueller, T.; Tenambergen, F.; Rose, C.; Göpferich, A.; Kuntsche, J.; Mäder, K., Tumor Accumulation of NIR Fluorescent PEG–PLA Nanoparticles: Impact of Particle Size and Human Xenograft Tumor Model. *ACS Nano* **2011,** *5* (11), 8710-8720.
[323] Zhao, J.; Stenzel, M. H., Entry of nanoparticles into cells: the importance of nanoparticle properties. *Polymer Chemistry* **2018,** *9* (3), 259-272.
[324] Smith, S. A.; Selby, L. I.; Johnston, A. P. R.; Such, G. K., The Endosomal Escape of Nanoparticles: Toward More Efficient Cellular Delivery. *Bioconjugate Chemistry* **2019,** *30* (2), 263-272.
[325] Liang, W.; Lam, J. K., Endosomal escape pathways for non-viral nucleic acid delivery systems. *Molecular regulation of endocytosis* **2012**, 429-456.

[326] Zhang, S.; Gao, H.; Bao, G., Physical Principles of Nanoparticle Cellular Endocytosis. *ACS Nano* **2015,** *9* (9), 8655-8671.
[327] Yuan, H.; Zhang, S., Effects of particle size and ligand density on the kinetics of receptor-mediated endocytosis of nanoparticles. *Applied Physics Letters* **2010,** *96* (3), 033704.
[328] Chithrani, B. D.; Ghazani, A. A.; Chan, W. C. W., Determining the Size and Shape Dependence of Gold Nanoparticle Uptake into Mammalian Cells. *Nano Letters* **2006,** *6* (4), 662-668.
[329] Lu, F.; Wu, S.-H.; Hung, Y.; Mou, C.-Y., Size Effect on Cell Uptake in Well-Suspended, Uniform Mesoporous Silica Nanoparticles. *Small* **2009,** *5* (12), 1408-1413.
[330] Jin, H.; Heller, D. A.; Sharma, R.; Strano, M. S., Size-Dependent Cellular Uptake and Expulsion of Single-Walled Carbon Nanotubes: Single Particle Tracking and a Generic Uptake Model for Nanoparticles. *ACS Nano* **2009,** *3* (1), 149-158.
[331] Osaki, F.; Kanamori, T.; Sando, S.; Sera, T.; Aoyama, Y., A Quantum Dot Conjugated Sugar Ball and Its Cellular Uptake. On the Size Effects of Endocytosis in the Subviral Region. *Journal of the American Chemical Society* **2004,** *126* (21), 6520-6521.
[332] Zhao, J.; Babiuch, K.; Lu, H.; Dag, A.; Gottschaldt, M.; Stenzel, M. H., Fructose-coated nanoparticles: a promising drug nanocarrier for triple-negative breast cancer therapy. *Chemical Communications* **2014,** *50* (100), 15928-15931.
[333] Chaudhuri, A.; Battaglia, G.; Golestanian, R., The effect of interactions on the cellular uptake of nanoparticles. *Physical Biology* **2011,** *8* (4), 046002.
[334] Albanese, A.; Chan, W. C. W., Effect of Gold Nanoparticle Aggregation on Cell Uptake and Toxicity. *ACS Nano* **2011,** *5* (7), 5478-5489.
[335] Hamilton, S. K.; Harth, E., Molecular Dendritic Transporter Nanoparticle Vectors Provide Efficient Intracellular Delivery of Peptides. *ACS Nano* **2009,** *3* (2), 402-410.
[336] Khine, Y. Y.; Callari, M.; Lu, H.; Stenzel, M. H., Direct Correlation Between Zeta Potential and Cellular Uptake of Poly(methacrylic acid) Post-Modified with Guanidinium Functionalities. *Macromolecular Chemistry and Physics* **2016,** *217* (20), 2302-2309.
[337] Cho, E. C.; Xie, J.; Wurm, P. A.; Xia, Y., Understanding the Role of Surface Charges in Cellular Adsorption versus Internalization by Selectively Removing Gold Nanoparticles on the Cell Surface with a I2/KI Etchant. *Nano Letters* **2009,** *9* (3), 1080-1084.
[338] Slowing, I.; Trewyn, B. G.; Lin, V. S. Y., Effect of Surface Functionalization of MCM-41-Type Mesoporous Silica Nanoparticles on the Endocytosis by Human Cancer Cells. *Journal of the American Chemical Society* **2006,** *128* (46), 14792-14793.
[339] Roser, M.; Fischer, D.; Kissel, T., Surface-modified biodegradable albumin nano- and microspheres. II: effect of surface charges on in vitro phagocytosis and biodistribution in rats. *European Journal of Pharmaceutics and Biopharmaceutics* **1998,** *46* (3), 255-263.
[340] Cedervall, T.; Lynch, I.; Lindman, S.; Berggård, T.; Thulin, E.; Nilsson, H.; Dawson, K. A.; Linse, S., Understanding the nanoparticle–protein corona using methods to quantify exchange rates and affinities of proteins for nanoparticles. *Proceedings of the National Academy of Sciences* **2007,** *104* (7), 2050-2055.
[341] Liu, Y.; Yin, Y.; Wang, L.; Zhang, W.; Chen, X.; Yang, X.; Xu, J.; Ma, G., Surface hydrophobicity of microparticles modulates adjuvanticity. *Journal of Materials Chemistry B* **2013,** *1* (32), 3888-3896.
[342] Shahbazi, M.-A.; Fernández, T. D.; Mäkilä, E. M.; Le Guével, X.; Mayorga, C.; Kaasalainen, M. H.; Salonen, J. J.; Hirvonen, J. T.; Santos, H. A., Surface chemistry dependent

immunostimulative potential of porous silicon nanoplatforms. *Biomaterials* **2014,** *35* (33), 9224-9235.
[343] Knop, K.; Hoogenboom, R.; Fischer, D.; Schubert, U. S., Poly(ethylene glycol) in Drug Delivery: Pros and Cons as Well as Potential Alternatives. *Angewandte Chemie International Edition* **2010,** *49* (36), 6288-6308.
[344] Koide, H.; Asai, T.; Hatanaka, K.; Urakami, T.; Ishii, T.; Kenjo, E.; Nishihara, M.; Yokoyama, M.; Ishida, T.; Kiwada, H.; Oku, N., Particle size-dependent triggering of accelerated blood clearance phenomenon. *International Journal of Pharmaceutics* **2008,** *362* (1), 197-200.
[345] Ulbricht, J.; Jordan, R.; Luxenhofer, R., On the biodegradability of polyethylene glycol, polypeptoids and poly(2-oxazoline)s. *Biomaterials* **2014,** *35* (17), 4848-4861.
[346] Nugraha, B., Application of PEG in Drug Delivery System. In *Gels Handbook*, WORLD SCIENTIFIC: 2016; pp 137-147.
[347] Gulati, N. M.; Stewart, P. L.; Steinmetz, N. F., Bioinspired Shielding Strategies for Nanoparticle Drug Delivery Applications. *Molecular Pharmaceutics* **2018,** *15* (8), 2900-2909.
[348] Wei, W.; Luo, C.; Yang, J.; Sun, B.; Zhao, D.; Liu, Y.; Wang, Y.; Yang, W.; Kan, Q.; Sun, J.; He, Z., Precisely albumin-hitchhiking tumor cell-activated reduction/oxidation-responsive docetaxel prodrugs for the hyperselective treatment of breast cancer. *Journal of Controlled Release* **2018,** *285*, 187-199.
[349] Yan, J.; Yu, J.; Wang, C.; Gu, Z., Red Blood Cells for Drug Delivery. *Small Methods* **2017,** *1* (12), 1700270.
[350] Zhang, D.; Yang, J.; Guan, J.; Yang, B.; Zhang, S.; Sun, M.; Yang, R.; Zhang, T.; Zhang, R.; Kan, Q.; Zhang, H.; He, Z.; Shang, L.; Sun, J., In vivo tailor-made protein corona of a prodrug-based nanoassembly fabricated by redox dual-sensitive paclitaxel prodrug for the superselective treatment of breast cancer. *Biomaterials Science* **2018,** *6* (9), 2360-2374.
[351] Schrade, A.; Mailänder, V.; Ritz, S.; Landfester, K.; Ziener, U., Surface Roughness and Charge Influence the Uptake of Nanoparticles: Fluorescently Labeled Pickering-Type Versus Surfactant-Stabilized Nanoparticles. *Macromolecular Bioscience* **2012,** *12* (11), 1459-1471.
[352] Piloni, A.; Wong, C. K.; Chen, F.; Lord, M.; Walther, A.; Stenzel, M. H., Surface roughness influences the protein corona formation of glycosylated nanoparticles and alter their cellular uptake. *Nanoscale* **2019,** *11* (48), 23259-23267.
[353] Verma, A.; Uzun, O.; Hu, Y.; Hu, Y.; Han, H.-S.; Watson, N.; Chen, S.; Irvine, D. J.; Stellacci, F., Surface-structure-regulated cell-membrane penetration by monolayer-protected nanoparticles. *Nature Materials* **2008,** *7* (7), 588-595.
[354] Gratton, S. E. A.; Ropp, P. A.; Pohlhaus, P. D.; Luft, J. C.; Madden, V. J.; Napier, M. E.; DeSimone, J. M., The effect of particle design on cellular internalization pathways. *Proceedings of the National Academy of Sciences* **2008,** *105* (33), 11613.
[355] Arnida; Malugin, A.; Ghandehari, H., Cellular uptake and toxicity of gold nanoparticles in prostate cancer cells: a comparative study of rods and spheres. *Journal of Applied Toxicology* **2010,** *30* (3), 212-217.
[356] Arnida; Janát-Amsbury, M. M.; Ray, A.; Peterson, C. M.; Ghandehari, H., Geometry and surface characteristics of gold nanoparticles influence their biodistribution and uptake by macrophages. *Eur J Pharm Biopharm* **2011,** *77* (3), 417-423.

[357] Champion, J. A.; Mitragotri, S., Shape Induced Inhibition of Phagocytosis of Polymer Particles. *Pharmaceutical Research* **2009,** *26* (1), 244-249.
[358] Li, Y.; Kröger, M.; Liu, W. K., Shape effect in cellular uptake of PEGylated nanoparticles: comparison between sphere, rod, cube and disk. *Nanoscale* **2015,** *7* (40), 16631-16646.
[359] Muro, S.; Garnacho, C.; Champion, J. A.; Leferovich, J.; Gajewski, C.; Schuchman, E. H.; Mitragotri, S.; Muzykantov, V. R., Control of Endothelial Targeting and Intracellular Delivery of Therapeutic Enzymes by Modulating the Size and Shape of ICAM-1-targeted Carriers. *Molecular Therapy* **2008,** *16* (8), 1450-1458.
[360] Cho, E. C.; Au, L.; Zhang, Q.; Xia, Y., The Effects of Size, Shape, and Surface Functional Group of Gold Nanostructures on Their Adsorption and Internalization by Cells. *Small* **2010,** *6* (4), 517-522.
[361] Banerjee, A.; Qi, J.; Gogoi, R.; Wong, J.; Mitragotri, S., Role of nanoparticle size, shape and surface chemistry in oral drug delivery. *Journal of Controlled Release* **2016,** *238*, 176-185.
[362] Alexander, J. F.; Kozlovskaya, V.; Chen, J.; Kuncewicz, T.; Kharlampieva, E.; Godin, B., Cubical Shape Enhances the Interaction of Layer-by-Layer Polymeric Particles with Breast Cancer Cells. *Advanced Healthcare Materials* **2015,** *4* (17), 2657-2666.
[363] Champion, J. A.; Mitragotri, S., Role of target geometry in phagocytosis. *Proc Natl Acad Sci U S A* **2006,** *103* (13), 4930-4934.
[364] Champion, J. A.; Katare, Y. K.; Mitragotri, S., Particle shape: A new design parameter for micro- and nanoscale drug delivery carriers. *Journal of Controlled Release* **2007,** *121* (1), 3-9.
[365] Geng, Y.; Dalhaimer, P.; Cai, S.; Tsai, R.; Tewari, M.; Minko, T.; Discher, D. E., Shape effects of filaments versus spherical particles in flow and drug delivery. *Nature Nanotechnology* **2007,** *2* (4), 249-255.
[366] Shimoni, O.; Yan, Y.; Wang, Y.; Caruso, F., Shape-Dependent Cellular Processing of Polyelectrolyte Capsules. *ACS Nano* **2013,** *7* (1), 522-530.
[367] Florez, L.; Herrmann, C.; Cramer, J. M.; Hauser, C. P.; Koynov, K.; Landfester, K.; Crespy, D.; Mailänder, V., How Shape Influences Uptake: Interactions of Anisotropic Polymer Nanoparticles and Human Mesenchymal Stem Cells. *Small* **2012,** *8* (14), 2222-2230.
[368] Black, K. C. L.; Wang, Y.; Luehmann, H. P.; Cai, X.; Xing, W.; Pang, B.; Zhao, Y.; Cutler, C. S.; Wang, L. V.; Liu, Y.; Xia, Y., Radioactive 198Au-Doped Nanostructures with Different Shapes for In Vivo Analyses of Their Biodistribution, Tumor Uptake, and Intratumoral Distribution. *ACS Nano* **2014,** *8* (5), 4385-4394.
[369] Barua, S.; Yoo, J.-W.; Kolhar, P.; Wakankar, A.; Gokarn, Y. R.; Mitragotri, S., Particle shape enhances specificity of antibody-displaying nanoparticles. *Proceedings of the National Academy of Sciences* **2013,** *110* (9), 3270-3275.
[370] Zhang, K.; Rossin, R.; Hagooly, A.; Chen, Z.; Welch, M. J.; Wooley, K. L., Folate-mediated cell uptake of shell-crosslinked spheres and cylinders. *Journal of Polymer Science Part A: Polymer Chemistry* **2008,** *46* (22), 7578-7583.
[371] Li, D.; Tang, Z.; Gao, Y.; Sun, H.; Zhou, S., A Bio-Inspired Rod-Shaped Nanoplatform for Strongly Infecting Tumor Cells and Enhancing the Delivery Efficiency of Anticancer Drugs. *Advanced Functional Materials* **2016,** *26* (1), 66-79.
[372] Chauhan, V. P.; Popović, Z.; Chen, O.; Cui, J.; Fukumura, D.; Bawendi, M. G.; Jain, R. K., Fluorescent Nanorods and Nanospheres for Real-Time In Vivo Probing of Nanoparticle Shape-Dependent Tumor Penetration. *Angewandte Chemie International Edition* **2011,** *50* (48), 11417-11420.

[373] Huang, X.; Li, L.; Liu, T.; Hao, N.; Liu, H.; Chen, D.; Tang, F., The Shape Effect of Mesoporous Silica Nanoparticles on Biodistribution, Clearance, and Biocompatibility in Vivo. *ACS Nano* **2011,** *5* (7), 5390-5399.
[374] Yi, X.; Gao, H., Kinetics of receptor-mediated endocytosis of elastic nanoparticles. *Nanoscale* **2017,** *9* (1), 454-463.
[375] Yi, X.; Shi, X.; Gao, H., Cellular Uptake of Elastic Nanoparticles. *Physical Review Letters* **2011,** *107* (9), 098101.
[376] Shen, Z.; Ye, H.; Li, Y., Understanding receptor-mediated endocytosis of elastic nanoparticles through coarse grained molecular dynamic simulation. *Physical Chemistry Chemical Physics* **2018,** *20* (24), 16372-16385.
[377] Sun, H.; Wong, E. H. H.; Yan, Y.; Cui, J.; Dai, Q.; Guo, J.; Qiao, G. G.; Caruso, F., The role of capsule stiffness on cellular processing. *Chemical Science* **2015,** *6* (6), 3505-3514.
[378] Hartmann, R.; Weidenbach, M.; Neubauer, M.; Fery, A.; Parak, W. J., Stiffness-Dependent In Vitro Uptake and Lysosomal Acidification of Colloidal Particles. *Angewandte Chemie International Edition* **2015,** *54* (4), 1365-1368.
[379] Liu, W.; Zhou, X.; Mao, Z.; Yu, D.; Wang, B.; Gao, C., Uptake of hydrogel particles with different stiffness and its influence on HepG2 cell functions. *Soft Matter* **2012,** *8* (35), 9235-9245.
[380] Sun, J.; Zhang, L.; Wang, J.; Feng, Q.; Liu, D.; Yin, Q.; Xu, D.; Wei, Y.; Ding, B.; Shi, X.; Jiang, X., Tunable Rigidity of (Polymeric Core)–(Lipid Shell) Nanoparticles for Regulated Cellular Uptake. *Advanced Materials* **2015,** *27* (8), 1402-1407.
[381] Banquy, X.; Suarez, F.; Argaw, A.; Rabanel, J.-M.; Grutter, P.; Bouchard, J.-F.; Hildgen, P.; Giasson, S., Effect of mechanical properties of hydrogel nanoparticles on macrophage cell uptake. *Soft Matter* **2009,** *5* (20), 3984-3991.
[382] Sun, H.; Björnmalm, M.; Cui, J.; Wong, E. H. H.; Dai, Y.; Dai, Q.; Qiao, G. G.; Caruso, F., Structure Governs the Deformability of Polymer Particles in a Microfluidic Blood Capillary Model. *ACS Macro Letters* **2015,** *4* (11), 1205-1209.
[383] Alford, A.; Rich, M.; Kozlovskaya, V.; Chen, J.; Sherwood, J.; Bolding, M.; Warram, J.; Bao, Y.; Kharlampieva, E., Ultrasound-Triggered Delivery of Anticancer Therapeutics from MRI-Visible Multilayer Microcapsules. *Advanced Therapeutics* **2018,** *1* (5), 1800051.
[384] Merkel, T. J.; Jones, S. W.; Herlihy, K. P.; Kersey, F. R.; Shields, A. R.; Napier, M.; Luft, J. C.; Wu, H.; Zamboni, W. C.; Wang, A. Z.; Bear, J. E.; DeSimone, J. M., Using mechanobiological mimicry of red blood cells to extend circulation times of hydrogel microparticles. *Proceedings of the National Academy of Sciences* **2011,** *108* (2), 586-591.
[385] Guo, P.; Liu, D.; Subramanyam, K.; Wang, B.; Yang, J.; Huang, J.; Auguste, D. T.; Moses, M. A., Nanoparticle elasticity directs tumor uptake. *Nature Communications* **2018,** *9* (1), 130.
[386] Lee, H.; Dellatore, S. M.; Miller, W. M.; Messersmith, P. B., Mussel-Inspired Surface Chemistry for Multifunctional Coatings. *Science* **2007,** *318* (5849), 426.
[387] Liu, Y.; Ai, K.; Lu, L., Polydopamine and Its Derivative Materials: Synthesis and Promising Applications in Energy, Environmental, and Biomedical Fields. *Chemical Reviews* **2014,** *114* (9), 5057-5115.
[388] Meng, H.; Li, Y.; Faust, M.; Konst, S.; Lee, B. P., Hydrogen peroxide generation and biocompatibility of hydrogel-bound mussel adhesive moiety. *Acta Biomaterialia* **2015,** *17*, 160-169.

[389] Postma, A.; Yan, Y.; Wang, Y.; Zelikin, A. N.; Tjipto, E.; Caruso, F., Self-Polymerization of Dopamine as a Versatile and Robust Technique to Prepare Polymer Capsules. *Chemistry of Materials* **2009,** *21* (14), 3042-3044.
[390] Ku, S. H.; Ryu, J.; Hong, S. K.; Lee, H.; Park, C. B., General functionalization route for cell adhesion on non-wetting surfaces. *Biomaterials* **2010,** *31* (9), 2535-2541.
[391] Luo, R.; Tang, L.; Zhong, S.; Yang, Z.; Wang, J.; Weng, Y.; Tu, Q.; Jiang, C.; Huang, N., In Vitro Investigation of Enhanced Hemocompatibility and Endothelial Cell Proliferation Associated with Quinone-Rich Polydopamine Coating. *ACS Applied Materials & Interfaces* **2013,** *5* (5), 1704-1714.
[392] Abouelmagd, S. A.; Ku, Y. J.; Yeo, Y., Low molecular weight chitosan-coated polymeric nanoparticles for sustained and pH-sensitive delivery of paclitaxel. *Journal of Drug Targeting* **2015,** *23* (7-8), 725-735.
[393] Borovanský, J.; Elleder, M., Melanosome Degradation: Fact or Fiction. *Pigment Cell Research* **2003,** *16* (3), 280-286.
[394] Pezzella, A.; d'Ischia, M.; Napolitano, A.; Palumbo, A.; Prota, G., An integrated approach to the structure of Sepia melanin. Evidence for a high proportion of degraded 5,6-dihydroxyindole-2-carboxylic acid units in the pigment backbone. *Tetrahedron* **1997,** *53* (24), 8281-8286.
[395] Bettinger, C. J.; Bruggeman, J. P.; Misra, A.; Borenstein, J. T.; Langer, R., Biocompatibility of biodegradable semiconducting melanin films for nerve tissue engineering. *Biomaterials* **2009,** *30* (17), 3050-3057.
[396] Della Vecchia, N. F.; Avolio, R.; Alfè, M.; Errico, M. E.; Napolitano, A.; d'Ischia, M., Building-Block Diversity in Polydopamine Underpins a Multifunctional Eumelanin-Type Platform Tunable Through a Quinone Control Point. *Advanced Functional Materials* **2013,** *23* (10), 1331-1340.
[397] Cave, A. C.; Brewer, A. C.; Narayanapanicker, A.; Ray, R.; Grieve, D. J.; Walker, S.; Shah, A. M., NADPH Oxidases in Cardiovascular Health and Disease. *Antioxidants & Redox Signaling* **2006,** *8* (5-6), 691-728.
[398] Yu, B.; Wang, D. A.; Ye, Q.; Zhou, F.; Liu, W., Robust polydopamine nano/microcapsules and their loading and release behavior. *Chemical Communications* **2009,** (44), 6789-6791.
[399] Ding, W.; Chechetka, S. A.; Masuda, M.; Shimizu, T.; Aoyagi, M.; Minamikawa, H.; Miyako, E., Lipid Nanotube Tailored Fabrication of Uniquely Shaped Polydopamine Nanofibers as Photothermal Converters. *Chemistry – A European Journal* **2016,** *22* (13), 4345-4350.
[400] Gao, Y.; Wu, X.; Zhou, L.; Su, Y.; Dong, C.-M., A Sweet Polydopamine Nanoplatform for Synergistic Combination of Targeted Chemo-Photothermal Therapy. *Macromolecular Rapid Communications* **2015,** *36* (10), 916-922.
[401] Han, J.; Park, W.; Park, S.-j.; Na, K., Photosensitizer-Conjugated Hyaluronic Acid-Shielded Polydopamine Nanoparticles for Targeted Photomediated Tumor Therapy. *ACS Applied Materials & Interfaces* **2016,** *8* (12), 7739-7747.
[402] Liu, Q.; Yu, B.; Ye, W.; Zhou, F., Highly Selective Uptake and Release of Charged Molecules by pH-Responsive Polydopamine Microcapsules. *Macromolecular Bioscience* **2011,** *11* (9), 1227-1234.
[403] Xu, J.; Ma, A.; Liu, T.; Lu, C.; Wang, D.; Xu, H., Janus-like Pickering emulsions and their controllable coalescence. *Chemical Communications* **2013,** *49* (92), 10871-10873.

[404] Yu, B.; Liu, J.; Liu, S.; Zhou, F., Pdop layer exhibiting zwitterionicity: a simple electrochemical interface for governing ion permeability. *Chemical Communications* **2010,** *46* (32), 5900-5902.
[405] Feng, J.; Fan, H.; Zha, D.-a.; Wang, L.; Jin, Z., Characterizations of the Formation of Polydopamine-Coated Halloysite Nanotubes in Various pH Environments. *Langmuir* **2016,** *32* (40), 10377-10386.
[406] Wang, S.; Zhao, X.; Wang, S.; Qian, J.; He, S., Biologically Inspired Polydopamine Capped Gold Nanorods for Drug Delivery and Light-Mediated Cancer Therapy. *ACS Applied Materials & Interfaces* **2016,** *8* (37), 24368-24384.
[407] Kazunori, K.; Glenn S, K.; Masayuki, Y.; Teruo, O.; Yasuhisa, S., Block copolymer micelles as vehicles for drug delivery. *Journal of Controlled Release* **1993,** *24* (1), 119-132.
[408] Otsuka, H.; Nagasaki, Y.; Kataoka, K., PEGylated nanoparticles for biological and pharmaceutical applications. *Advanced Drug Delivery Reviews* **2003,** *55* (3), 403-419.
[409] Lee, H.; Rho, J.; Messersmith, P. B., Facile Conjugation of Biomolecules onto Surfaces via Mussel Adhesive Protein Inspired Coatings. *Advanced Materials* **2009,** *21* (4), 431-434.
[410] Zhu, D.; Tao, W.; Zhang, H.; Liu, G.; Wang, T.; Zhang, L.; Zeng, X.; Mei, L., Docetaxel (DTX)-loaded polydopamine-modified TPGS-PLA nanoparticles as a targeted drug delivery system for the treatment of liver cancer. *Acta Biomaterialia* **2016,** *30*, 144-154.
[411] Li, W.-Q.; Wang, Z.; Hao, S.; He, H.; Wan, Y.; Zhu, C.; Sun, L.-P.; Cheng, G.; Zheng, S.-Y., Mitochondria-Targeting Polydopamine Nanoparticles To Deliver Doxorubicin for Overcoming Drug Resistance. *ACS Applied Materials & Interfaces* **2017,** *9* (20), 16793-16802.
[412] Fan, X.; Lin, L.; Dalsin, J. L.; Messersmith, P. B., Biomimetic Anchor for Surface-Initiated Polymerization from Metal Substrates. *Journal of the American Chemical Society* **2005,** *127* (45), 15843-15847.
[413] Ma, Z.; Jia, X.; Hu, J.; Liu, Z.; Wang, H.; Zhou, F., Mussel-Inspired Thermosensitive Polydopamine-graft-Poly(N-isopropylacrylamide) Coating for Controlled-Release Fertilizer. *Journal of Agricultural and Food Chemistry* **2013,** *61* (50), 12232-12237.
[414] Waite, J. H., Mussel adhesion – essential footwork. *The Journal of Experimental Biology* **2017,** *220* (4), 517-530.
[415] Guo, L.; Liu, Q.; Li, G.; Shi, J.; Liu, J.; Wang, T.; Jiang, G., A mussel-inspired polydopamine coating as a versatile platform for the in situ synthesis of graphene-based nanocomposites. *Nanoscale* **2012,** *4* (19), 5864-5867.
[416] Chen, Y.; Ai, K.; Liu, J.; Ren, X.; Jiang, C.; Lu, L., Polydopamine-based coordination nanocomplex for T1/T2 dual mode magnetic resonance imaging-guided chemo-photothermal synergistic therapy. *Biomaterials* **2016,** *77*, 198-206.
[417] Horcajada, P.; Chalati, T.; Serre, C.; Gillet, B.; Sebrie, C.; Baati, T.; Eubank, J. F.; Heurtaux, D.; Clayette, P.; Kreuz, C.; Chang, J.-S.; Hwang, Y. K.; Marsaud, V.; Bories, P.-N.; Cynober, L.; Gil, S.; Férey, G.; Couvreur, P.; Gref, R., Porous metal–organic-framework nanoscale carriers as a potential platform for drug delivery and imaging. *Nature Materials* **2010,** *9* (2), 172-178.
[418] Hu, D.; Liu, C.; Song, L.; Cui, H.; Gao, G.; Liu, P.; Sheng, Z.; Cai, L., Indocyanine green–loaded polydopamine–iron ions coordination nanoparticles for photoacoustic/magnetic resonance dual-modal imaging-guided cancer photothermal therapy. *Nanoscale* **2016,** *8* (39), 17150-17158.

[419] Liu, F.; He, X.; Zhang, J.; Chen, H.; Zhang, H.; Wang, Z., Controllable synthesis of polydopamine nanoparticles in microemulsions with pH-activatable properties for cancer detection and treatment. *Journal of Materials Chemistry B* **2015,** *3* (33), 6731-6739.
[420] Zheng, X.; Zhang, J.; Wang, J.; Qi, X.; Rosenholm, J. M.; Cai, K., Polydopamine Coatings in Confined Nanopore Space: Toward Improved Retention and Release of Hydrophilic Cargo. *The Journal of Physical Chemistry C* **2015,** *119* (43), 24512-24521.
[421] Liu, R.; Guo, Y.; Odusote, G.; Qu, F.; Priestley, R. D., Core–shell Fe3O4 polydopamine nanoparticles serve multipurpose as drug carrier, catalyst support and carbon adsorbent. *ACS applied materials & interfaces* **2013,** *5* (18), 9167-9171.
[422] Xu, H.; Nishida, J.; Ma, W.; Wu, H.; Kobayashi, M.; Otsuka, H.; Takahara, A., Competition between Oxidation and Coordination in Cross-Linking of Polystyrene Copolymer Containing Catechol Groups. *ACS Macro Letters* **2012,** *1* (4), 457-460.
[423] Xiao, J.; Wang, C.; Lyu, S.; Liu, H.; Jiang, C.; Lei, Y., Enhancement of Fenton degradation by catechol in a wide initial pH range. *Separation and Purification Technology* **2016,** *169*, 202-209.
[424] Tang, L.; Shi, J.; Wang, X.; Zhang, S.; Wu, H.; Sun, H.; Jiang, Z., Coordination polymer nanocapsules prepared using metal–organic framework templates for pH-responsive drug delivery. *Nanotechnology* **2017,** *28* (27), 275601.
[425] Zeng, T.; Zhang, X.-l.; Niu, H.-y.; Ma, Y.-r.; Li, W.-h.; Cai, Y.-q., In situ growth of gold nanoparticles onto polydopamine-encapsulated magnetic microspheres for catalytic reduction of nitrobenzene. *Applied Catalysis B: Environmental* **2013,** *134-135*, 26-33.
[426] Ma, Z.; Jia, X.; Hu, J.; zhou, F.; Dai, B., Mussel-inspired chemistry for one-step synthesis of N-doped carbon–gold composites with morphology tailoring and their catalytic properties. *RSC Advances* **2014,** *4* (4), 1853-1856.
[427] Wu, M.; Huang, S., Magnetic nanoparticles in cancer diagnosis, drug delivery and treatment. *Mol Clin Oncol* **2017,** *7* (5), 738-746.
[428] Lee, J.-H.; Jang, J.-t.; Choi, J.-s.; Moon, S. H.; Noh, S.-h.; Kim, J.-w.; Kim, J.-G.; Kim, I.-S.; Park, K. I.; Cheon, J., Exchange-coupled magnetic nanoparticles for efficient heat induction. *Nature Nanotechnology* **2011,** *6* (7), 418-422.
[429] Hou, C.; Zhu, H.; Li, Y.; Li, Y.; Wang, X.; Zhu, W.; Zhou, R., Facile synthesis of oxidic PEG-modified magnetic polydopamine nanospheres for Candida rugosa lipase immobilization. *Applied Microbiology and Biotechnology* **2015,** *99* (3), 1249-1259.
[430] Martín, M.; Salazar, P.; Villalonga, R.; Campuzano, S.; Pingarrón, J. M.; González-Mora, J. L., Preparation of core–shell Fe3O4@poly(dopamine) magnetic nanoparticles for biosensor construction. *Journal of Materials Chemistry B* **2014,** *2* (6), 739-746.
[431] Ni, K.; Lu, H.; Wang, C.; Black, K. C. L.; Wei, D.; Ren, Y.; Messersmith, P. B., A novel technique for in situ aggregation of Gluconobacter oxydans using bio-adhesive magnetic nanoparticles. *Biotechnology and Bioengineering* **2012,** *109* (12), 2970-2977.
[432] Sureshkumar, M.; Lee, C.-K., Polydopamine coated magnetic-chitin (MCT) particles as a new matrix for enzyme immobilization. *Carbohydrate Polymers* **2011,** *84* (2), 775-780.
[433] Zhang, X.; Wang, S.; Xu, L.; Feng, L.; Ji, Y.; Tao, L.; Li, S.; Wei, Y., Biocompatible polydopamine fluorescent organic nanoparticles: facile preparation and cell imaging. *Nanoscale* **2012,** *4* (18), 5581-5584.
[434] Chen, X.; Yan, Y.; Müllner, M.; van Koeverden, M. P.; Noi, K. F.; Zhu, W.; Caruso, F., Engineering Fluorescent Poly(dopamine) Capsules. *Langmuir* **2014,** *30* (10), 2921-2925.

[435] Yildirim, A.; Bayindir, M., Turn-on Fluorescent Dopamine Sensing Based on in Situ Formation of Visible Light Emitting Polydopamine Nanoparticles. *Analytical Chemistry* **2014,** *86* (11), 5508-5512.
[436] Lin, J.-H.; Yu, C.-J.; Yang, Y.-C.; Tseng, W.-L., Formation of fluorescent polydopamine dots from hydroxyl radical-induced degradation of polydopamine nanoparticles. *Physical Chemistry Chemical Physics* **2015,** *17* (23), 15124-15130.
[437] Zhao, C.; Zuo, F.; Liao, Z.; Qin, Z.; Du, S.; Zhao, Z., Mussel-Inspired One-Pot Synthesis of a Fluorescent and Water-Soluble Polydopamine–Polyethyleneimine Copolymer. *Macromolecular Rapid Communications* **2015,** *36* (10), 909-915.
[438] Qiang, W.; Li, W.; Li, X.; Chen, X.; Xu, D., Bioinspired polydopamine nanospheres: a superquencher for fluorescence sensing of biomolecules. *Chemical Science* **2014,** *5* (8), 3018-3024.
[439] Xing, Y.; Zhang, J.; Chen, F.; Liu, J.; Cai, K., Mesoporous polydopamine nanoparticles with co-delivery function for overcoming multidrug resistance via synergistic chemo-photothermal therapy. *Nanoscale* **2017,** *9* (25), 8781-8790.
[440] Chen, F.; Xing, Y.; Wang, Z.; Zheng, X.; Zhang, J.; Cai, K., Nanoscale Polydopamine (PDA) Meets π–π Interactions: An Interface-Directed Coassembly Approach for Mesoporous Nanoparticles. *Langmuir* **2016,** *32* (46), 12119-12128.
[441] Hu, H.; Dyke, J. C.; Bowman, B. A.; Ko, C.-C.; You, W., Investigation of Dopamine Analogues: Synthesis, Mechanistic Understanding, and Structure–Property Relationship. *Langmuir* **2016,** *32* (38), 9873-9882.
[442] Hong, D.; Lee, H.; Kim, B. J.; Park, T.; Choi, J. Y.; Park, M.; Lee, J.; Cho, H.; Hong, S.-P.; Yang, S. H.; Jung, S. H.; Ko, S.-B.; Choi, I. S., A degradable polydopamine coating based on disulfide-exchange reaction. *Nanoscale* **2015,** *7* (47), 20149-20154.
[443] Repenko, T.; Fokong, S.; De Laporte, L.; Go, D.; Kiessling, F.; Lammers, T.; Kuehne, A. J. C., Water-soluble dopamine-based polymers for photoacoustic imaging. *Chemical Communications* **2015,** *51* (28), 6084-6087.
[444] Kiriy, A.; Senkovskyy, V.; Sommer, M., Kumada Catalyst-Transfer Polycondensation: Mechanism, Opportunities, and Challenges. *Macromolecular Rapid Communications* **2011,** *32* (19), 1503-1517.
[445] Kang, S. M.; Hwang, N. S.; Yeom, J.; Park, S. Y.; Messersmith, P. B.; Choi, I. S.; Langer, R.; Anderson, D. G.; Lee, H., One-Step Multipurpose Surface Functionalization by Adhesive Catecholamine. *Advanced Functional Materials* **2012,** *22* (14), 2949-2955.
[446] You, I.; Jeon, H.; Lee, K.; Do, M.; Seo, Y. C.; Lee, H. A.; Lee, H., Polydopamine coating in organic solvent for material-independent immobilization of water-insoluble molecules and avoidance of substrate hydrolysis. *Journal of Industrial and Engineering Chemistry* **2017,** *46*, 379-385.
[447] McNeil, S. E., Nanoparticle therapeutics: a personal perspective. *Wiley Interdisciplinary Reviews: Nanomedicine and Nanobiotechnology* **2009,** *1* (3), 264-271.
[448] Kobayashi, H.; Kawamoto, S.; Jo, S.-K.; Bryant, H. L.; Brechbiel, M. W.; Star, R. A., Macromolecular MRI Contrast Agents with Small Dendrimers: Pharmacokinetic Differences between Sizes and Cores. *Bioconjugate Chemistry* **2003,** *14* (2), 388-394.
[449] Malik, N.; Wiwattanapatapee, R.; Klopsch, R.; Lorenz, K.; Frey, H.; Weener, J. W.; Meijer, E. W.; Paulus, W.; Duncan, R., Dendrimers:: Relationship between structure and biocompatibility in vitro, and preliminary studies on the biodistribution of 125I-labelled polyamidoamine dendrimers in vivo. *Journal of Controlled Release* **2000,** *65* (1), 133-148.

[450] Nigavekar, S. S.; Sung, L. Y.; Llanes, M.; El-Jawahri, A.; Lawrence, T. S.; Becker, C. W.; Balogh, L.; Khan, M. K., 3H Dendrimer Nanoparticle Organ/Tumor Distribution. *Pharmaceutical Research* **2004,** *21* (3), 476-483.
[451] Champion, J. A.; Mitragotri, S., Role of target geometry in phagocytosis. *Proceedings of the National Academy of Sciences* **2006,** *103* (13), 4930-4934.
[452] Champion, J. A.; Katare, Y. K.; Mitragotri, S., Particle shape: a new design parameter for micro-and nanoscale drug delivery carriers. *Journal of controlled release* **2007,** *121* (1-2), 3-9.
[453] Malugin, A.; Ghandehari, H., Cellular uptake and toxicity of gold nanoparticles in prostate cancer cells: a comparative study of rods and spheres. *Journal of Applied Toxicology: An International Journal* **2010,** *30* (3), 212-217.
[454] Janát-Amsbury, M.; Ray, A.; Peterson, C.; Ghandehari, H., Geometry and surface characteristics of gold nanoparticles influence their biodistribution and uptake by macrophages. *European Journal of Pharmaceutics and Biopharmaceutics* **2011,** *77* (3), 417-423.
[455] Zhang, K.; Fang, H.; Chen, Z.; Taylor, J.-S. A.; Wooley, K. L., Shape Effects of Nanoparticles Conjugated with Cell-Penetrating Peptides (HIV Tat PTD) on CHO Cell Uptake. *Bioconjugate Chemistry* **2008,** *19* (9), 1880-1887.
[456]Niikura, K.; Matsunaga, T.; Suzuki, T.; Kobayashi, S.; Yamaguchi, H.; Orba, Y.; Kawaguchi, A.; Hasegawa, H.; Kajino, K.; Ninomiya, T.; Ijiro, K.; Sawa, H., Gold Nanoparticles as a Vaccine Platform: Influence of Size and Shape on Immunological Responses in Vitro and in Vivo. *ACS Nano* **2013,** *7* (5), 3926-3938.
[457] Doshi, N.; Mitragotri, S., Macrophages Recognize Size and Shape of Their Targets. *PLOS One* **2010,** *5* (4), e10051.
[458] Zhao, X.; Ng, S.; Heng, B. C.; Guo, J.; Ma, L.; Tan, T. T. Y.; Ng, K. W.; Loo, S. C. J., Cytotoxicity of hydroxyapatite nanoparticles is shape and cell dependent. *Archives of Toxicology* **2013,** *87* (6), 1037-1052.
[459] van de Ven, A. L.; Kim, P.; Haley, O. H.; Fakhoury, J. R.; Adriani, G.; Schmulen, J.; Moloney, P.; Hussain, F.; Ferrari, M.; Liu, X.; Yun, S.-H.; Decuzzi, P., Rapid tumoritropic accumulation of systemically injected plateloid particles and their biodistribution. *Journal of Controlled Release* **2012,** *158* (1), 148-155.
[460] Riahi, R.; Tamayol, A.; Shaegh, S. A. M.; Ghaemmaghami, A. M.; Dokmeci, M. R.; Khademhosseini, A., Microfluidics for advanced drug delivery systems. *Current Opinion in Chemical Engineering* **2015,** *7*, 101-112.
[461] Xu, S.; Nie, Z.; Seo, M.; Lewis, P.; Kumacheva, E.; Stone, H. A.; Garstecki, P.; Weibel, D. B.; Gitlin, I.; Whitesides, G. M., Generation of Monodisperse Particles by Using Microfluidics: Control over Size, Shape, and Composition. *Angewandte Chemie* **2005,** *117* (5), 734-738.
[462] Dendukuri, D.; Tsoi, K.; Hatton, T. A.; Doyle, P. S., Controlled Synthesis of Nonspherical Microparticles Using Microfluidics. *Langmuir* **2005,** *21* (6), 2113-2116.
[463] Dendukuri, D.; Pregibon, D. C.; Collins, J.; Hatton, T. A.; Doyle, P. S., Continuous-flow lithography for high-throughput microparticle synthesis. *Nature Materials* **2006,** *5*, 365.
[464] Canelas, D. A.; Herlihy, K. P.; DeSimone, J. M., Top-down particle fabrication: control of size and shape for diagnostic imaging and drug delivery. *Wiley Interdisciplinary Reviews: Nanomedicine and Nanobiotechnology* **2009,** *1* (4), 391-404.

[465] Doshi, N.; Mitragotri, S., Needle-shaped polymeric particles induce transient disruption of cell membranes. *Journal of The Royal Society Interface* **2010,** *7* (suppl_4), S403-S410.
[466] Geng, Y.; Dalhaimer, P.; Cai, S.; Tsai, R.; Tewari, M.; Minko, T.; Discher, D. E., Shape effects of filaments versus spherical particles in flow and drug delivery. *Nature Nanotechnology* **2007,** *2*, 249.
[467] Lohse, S. E.; Murphy, C. J., The Quest for Shape Control: A History of Gold Nanorod Synthesis. *Chemistry of Materials* **2013,** *25* (8), 1250-1261.
[468] Scarabelli, L.; Grzelczak, M.; Liz-Marzán, L. M., Tuning Gold Nanorod Synthesis through Prereduction with Salicylic Acid. *Chemistry of Materials* **2013,** *25* (21), 4232-4238.
[469] Ward, C. J.; Tronndorf, R.; Eustes, A. S.; Auad, M. L.; Davis, E. W., Seed-mediated growth of gold nanorods: limits of length to diameter ratio control. *Journal of Nanomaterials* **2014,** *2014*, 47.
[470] Zhang, M.; Zhang, L.; Chen, Y.; Li, L.; Su, Z.; Wang, C., Precise synthesis of unique polydopamine/mesoporous calcium phosphate hollow Janus nanoparticles for imaging-guided chemo-photothermal synergistic therapy. *Chemical Science* **2017,** *8* (12), 8067-8077.
[471] Yu, J.; Bai, X.; Suh, J.; Lee, S. B.; Son, S. J., Mechanical Capping of Silica Nanotubes for Encapsulation of Molecules. *Journal of the American Chemical Society* **2009,** *131* (43), 15574-15575.
[472] Newland, B.; Taplan, C.; Pette, D.; Friedrichs, J.; Steinhart, M.; Wang, W.; Voit, B.; Seib, F.; Werner, C., Soft and flexible poly (ethylene glycol) nanotubes for local drug delivery. *Nanoscale* **2018,** *10* (18), 8413-8421.
[473] Chen, G.; Chen, R.; Zou, C.; Yang, D.; Chen, Z.-S., Fragmented polymer nanotubes from sonication-induced scission with a thermo-responsive gating system for anti-cancer drug delivery. *Journal of Materials Chemistry B* **2014,** *2* (10), 1327-1334.
[474] Abidian, M. R.; Kim, D.-H.; Martin, D. C., Conducting-Polymer Nanotubes for Controlled Drug Release. *Advanced Materials* **2006,** *18* (4), 405-409.
[475] Huczko, A., Template-based synthesis of nanomaterials. *Applied Physics A* **2000,** *70* (4), 365-376.
[476] Ma, P.-C.; Siddiqui, N. A.; Marom, G.; Kim, J.-K., Dispersion and functionalization of carbon nanotubes for polymer-based nanocomposites: A review. *Composites Part A: Applied Science and Manufacturing* **2010,** *41* (10), 1345-1367.
[477] Daniel, S.; Rao, T. P.; Rao, K. S.; Rani, S. U.; Naidu, G. R. K.; Lee, H.-Y.; Kawai, T., A review of DNA functionalized/grafted carbon nanotubes and their characterization. *Sensors and Actuators B: Chemical* **2007,** *122* (2), 672-682.
[478] Sahoo, N. G.; Rana, S.; Cho, J. W.; Li, L.; Chan, S. H., Polymer nanocomposites based on functionalized carbon nanotubes. *Progress in Polymer Science* **2010,** *35* (7), 837-867.
[479] Wang, Y.; Su, X.; Ding, P.; Lu, S.; Yu, H., Shape-Controlled Synthesis of Hollow Silica Colloids. *Langmuir* **2013,** *29* (37), 11575-11581.
[480] Xue, J.; Zheng, W.; Wang, L.; Jin, Z., Scalable fabrication of polydopamine nanotubes based on curcumin crystals. *ACS Biomaterials Science & Engineering* **2016,** *2* (4), 489-493.
[481] Yan, D.; Xu, P.; Xiang, Q.; Mou, H.; Xu, J.; Wen, W.; Li, X.; Zhang, Y., Polydopamine nanotubes: bio-inspired synthesis, formaldehyde sensing properties and thermodynamic investigation. *Journal of Materials Chemistry A* **2016,** *4* (9), 3487-3493.
[482] Fan, D.; Zhu, X.; Zhai, Q.; Wang, E.; Dong, S., Polydopamine nanotubes as an effective fluorescent quencher for highly sensitive and selective detection of biomolecules assisted with exonuclease III amplification. *Analytical chemistry* **2016,** *88* (18), 9158-9165.

[483] Yuan, P.; Southon, P. D.; Liu, Z.; Green, M. E. R.; Hook, J. M.; Antill, S. J.; Kepert, C. J., Functionalization of Halloysite Clay Nanotubes by Grafting with γ-Aminopropyltriethoxysilane. *The Journal of Physical Chemistry C* **2008,** *112* (40), 15742-15751.
[484] Liu, M.; Jia, Z.; Jia, D.; Zhou, C., Recent advance in research on halloysite nanotubes-polymer nanocomposite. *Progress in Polymer Science* **2014,** *39* (8), 1498-1525.
[485] Vinokurov, V. A.; Stavitskaya, A. V.; Chudakov, Y. A.; Ivanov, E. V.; Shrestha, L. K.; Ariga, K.; Darrat, Y. A.; Lvov, Y. M., Formation of metal clusters in halloysite clay nanotubes. *Science and Technology of Advanced Materials* **2017,** *18* (1), 147-151.
[486] Singh, B., Why Does Halloysite Roll?--A New Model. *Clays and Clay Minerals* **1996,** *44* (2), 191-196.
[487] Lvov, Y. M.; Shchukin, D. G.; Möhwald, H.; Price, R. R., Halloysite Clay Nanotubes for Controlled Release of Protective Agents. *ACS Nano* **2008,** *2* (5), 814-820.
[488] Ward, C. J.; Song, S.; Davis, E. W., Controlled Release of Tetracycline-HCl from Halloysite-Polymer Composite Films. *Journal of Nanoscience and Nanotechnology* **2010,** *10* (10), 6641-6649.
[489] Ward, C. J.; DeWitt, M.; Davis, E. W., Halloysite Nanoclay for Controlled Release Applications. *Nanomaterials for Biomedicine* **2012,** *10*, 209-238.
[490] Abdullayev, E.; Lvov, Y., Halloysite clay nanotubes as a ceramic "skeleton" for functional biopolymer composites with sustained drug release. *Journal of Materials Chemistry B* **2013,** *1* (23), 2894-2903.
[491] Jain, R. K.; Stylianopoulos, T., Delivering nanomedicine to solid tumors. *Nature Reviews Clinical Oncology* **2010,** *7*, 653.
[492] Xie, A.; Dai, J.; Chen, X.; Zou, T.; He, J.; Chang, Z.; Li, C.; Yan, Y., Hollow imprinted polymer nanorods with a tunable shell using halloysite nanotubes as a sacrificial template for selective recognition and separation of chloramphenicol. *RSC Advances* **2016,** *6* (56), 51014-51023.
[493] Liu, Y.; Nan, H.; Cai, Q.; Li, H., Fabrication of halloysite@polypyrrole composite particles and polypyrrole nanotubes on halloysite templates. *Journal of Applied Polymer Science* **2012,** *125* (S1), E638-E643.
[494] Della Vecchia, N. F.; Luchini, A.; Napolitano, A.; D'Errico, G.; Vitiello, G.; Szekely, N.; d'Ischia, M.; Paduano, L., Tris buffer modulates polydopamine growth, aggregation, and paramagnetic properties. *Langmuir* **2014,** *30* (32), 9811-9818.
[495] Li, Y.; Jiang, C.; Zhang, D.; Wang, Y.; Ren, X.; Ai, K.; Chen, X.; Lu, L., Targeted polydopamine nanoparticles enable photoacoustic imaging guided chemo-photothermal synergistic therapy of tumor. *Acta Biomaterialia* **2017,** *47*, 124-134.
[496] Luo, R.; Tang, L.; Wang, J.; Zhao, Y.; Tu, Q.; Weng, Y.; Shen, R.; Huang, N., Improved immobilization of biomolecules to quinone-rich polydopamine for efficient surface functionalization. *Colloids and Surfaces B: Biointerfaces* **2013,** *106*, 66-73.
[497] Chen, Y.; Zhang, Y.; Liu, J.; Zhang, H.; Wang, K., Preparation and antibacterial property of polyethersulfone ultrafiltration hybrid membrane containing halloysite nanotubes loaded with copper ions. *Chemical Engineering Journal* **2012,** *210*, 298-308.
[498] Huang, X.; Neretina, S.; El-Sayed, M. A., Gold nanorods: from synthesis and properties to biological and biomedical applications. *Advanced materials* **2009,** *21* (48), 4880-4910.

[499] Razzano, G.; Rizzo, V.; Vigevani, A., Determination of phenolic ionization constants of anthracyclines with modified substitution pattern of anthraquinone chromophore. *Farmaco* **1990,** *45* (2), 215-222.
[500] Fülöp, Z.; Gref, R.; Loftsson, T., A permeation method for detection of self-aggregation of doxorubicin in aqueous environment. *International Journal of Pharmaceutics* **2013,** *454* (1), 559-561.
[501] Liu, Q.; Yu, B.; Ye, W.; Zhou, F., Highly selective uptake and release of charged molecules by pH-responsive polydopamine microcapsules. *Macromolecular Bioscience* **2011,** *11* (9), 1227-1234.
[502] Lee, E. S.; Oh, K. T.; Kim, D.; Youn, Y. S.; Bae, Y. H., Tumor pH-responsive flower-like micelles of poly(l-lactic acid)-b-poly(ethylene glycol)-b-poly(l-histidine). *Journal of Controlled Release* **2007,** *123* (1), 19-26.
[503] Liu, Q.; Chen, X.; Jia, J.; Zhang, W.; Yang, T.; Wang, L.; Ma, G., pH-responsive poly (d, l-lactic-co-glycolic acid) nanoparticles with rapid antigen release behavior promote immune response. *ACS Nano* **2015,** *9* (5), 4925-4938.
[504] Wang, S.; Lin, J.; Wang, Z.; Zhou, Z.; Bai, R.; Lu, N.; Liu, Y.; Fu, X.; Jacobson, O.; Fan, W., Core – Satellite Polydopamine – Gadolinium - Metallofullerene Nanotheranostics for Multimodal Imaging Guided Combination Cancer Therapy. *Advanced Materials* **2017,** *29* (35), 1701013.
[505] Anasori, B.; Lukatskaya, M. R.; Gogotsi, Y., 2D metal carbides and nitrides (MXenes) for energy storage. *Nature Reviews Materials* **2017,** *2* (2), 16098.
[506] Zhang, Y.; Ahn, J.; Liu, J.; Qin, D., Syntheses, Plasmonic Properties, and Catalytic Applications of Ag–Rh Core-Frame Nanocubes and Rh Nanoboxes with Highly Porous Walls. *Chemistry of Materials* **2018,** *30* (6), 2151-2159.
[507] Yao, Y.; McDowell, M. T.; Ryu, I.; Wu, H.; Liu, N.; Hu, L.; Nix, W. D.; Cui, Y., Interconnected Silicon Hollow Nanospheres for Lithium-Ion Battery Anodes with Long Cycle Life. *Nano Letters* **2011,** *11* (7), 2949-2954.
[508] Xie, C.; Li, P.; Han, L.; Wang, Z.; Zhou, T.; Deng, W.; Wang, K.; Lu, X., Electroresponsive and cell-affinitive polydopamine/polypyrrole composite microcapsules with a dual-function of on-demand drug delivery and cell stimulation for electrical therapy. *NPG Asia Materials* **2017,** *9* (3), e358-e358.
[509] Teranishi, T.; Inoue, Y.; Nakaya, M.; Oumi, Y.; Sano, T., Nanoacorns: Anisotropically Phase-Segregated CoPd Sulfide Nanoparticles. *Journal of the American Chemical Society* **2004,** *126* (32), 9914-9915.
[510] Lee, K. J.; Yoon, J.; Lahann, J., Recent advances with anisotropic particles. *Current Opinion in Colloid & Interface Science* **2011,** *16* (3), 195-202.
[511] Herrmann, C.; Bannwarth, M. B.; Landfester, K.; Crespy, D., Re-dispersible Anisotropic and Structured Nanoparticles: Formation and Their Subsequent Shape Change. *Macromolecular Chemistry and Physics* **2012,** *213* (8), 829-838.
[512] Cheong, S.; Watt, J. D.; Tilley, R. D., Shape control of platinum and palladium nanoparticles for catalysis. *Nanoscale* **2010,** *2* (10), 2045-2053.
[513] Lin, Z.; Tian, H.; Xu, F.; Yang, X.; Mai, Y.; Feng, X., Facile synthesis of bowl-shaped nitrogen-doped carbon hollow particles templated by block copolymer "kippah vesicles" for high performance supercapacitors. *Polymer Chemistry* **2016,** *7* (11), 2092-2098.
[514] Du, X.; Li, W.; Shi, B.; Su, L.; Li, X.; Huang, H.; Wen, Y.; Zhang, X., Facile synthesis of mesoporous organosilica nanobowls with bridged silsesquioxane framework by one-pot

growth and dissolution mechanism. *Journal of Colloid and Interface Science* **2018,** *528*, 379-388.
[515] Zhang, H.-M.; Zhao, Y.; Zhang, Y.; Zhang, M.; Cheng, M.; Yu, J.; Liu, H.; Ji, M.; Zhu, C.; Xu, J., Fe3O4 encapsulated in porous carbon nanobowls as efficient oxygen reduction reaction catalyst for Zn-air batteries. *Chemical Engineering Journal* **2019,** *375*, 122058.
[516] Fu, J.; Yang, W.; Hou, L.; Chen, Z.; Qiu, T.; Yang, H.; Li, Y., Enhanced Electromagnetic Microwave Absorption Performance of Lightweight Bowl-like Carbon Nanoparticles. *Industrial & Engineering Chemistry Research* **2017,** *56* (40), 11460-11466.
[517] Wang, X. D.; Graugnard, E.; King, J. S.; Wang, Z. L.; Summers, C. J., Large-scale fabrication of ordered nanobowl arrays. *Nano Letters* **2004,** *4* (11), 2223-2226.
[518] Yu, T.; Varghese, B.; Shen, Z.; Lim, C.-T.; Sow, C.-H., Large-scale metal oxide nanostructures on template-patterned microbowls: A simple method for growth of hierarchical structures. *Materials Letters* **2008,** *62* (3), 389-393.
[519] Ye, J.; Van Dorpe, P.; Van Roy, W.; Borghs, G.; Maes, G., Fabrication, characterization, and optical properties of gold nanobowl submonolayer structures. *Langmuir* **2009,** *25* (3), 1822-1827.
[520] Xu, M.; Lu, N.; Xu, H.; Qi, D.; Wang, Y.; Chi, L., Fabrication of Functional Silver Nanobowl Arrays via Sphere Lithography. *Langmuir* **2009,** *25* (19), 11216-11220.
[521] Ye, X.; Li, Y.; Dong, J.; Xiao, J.; Ma, Y.; Qi, L., Facile synthesis of ZnS nanobowl arrays and their applications as 2D photonic crystal sensors. *Journal of Materials Chemistry C* **2013,** *1* (38), 6112-6119.
[522] Zhu, A.; Gao, R.; Zhao, X.; Zhang, F.; Zhang, X.; Yang, J.; Zhang, Y.; Chen, L.; Wang, Y., Site-selective growth of Ag nanoparticles controlled by localized surface plasmon resonance of nanobowl arrays. *Nanoscale* **2019,** *11* (14), 6576-6583.
[523] Xiong, L.; Qiao, S.-Z., A mesoporous organosilica nano-bowl with high DNA loading capacity – a potential gene delivery carrier. *Nanoscale* **2016,** *8* (40), 17446-17450.
[524] Liu, X.; Song, P.; Hou, J.; Wang, B.; Xu, F.; Zhang, X., Revealing the Dynamic Formation Process and Mechanism of Hollow Carbon Spheres: From Bowl to Sphere. *ACS Sustainable Chemistry & Engineering* **2018,** *6* (2), 2797-2805.
[525] Guan, B. Y.; Yu, L.; Lou, X. W., Formation of Asymmetric Bowl-Like Mesoporous Particles via Emulsion-Induced Interface Anisotropic Assembly. *Journal of the American Chemical Society* **2016,** *138* (35), 11306-11311.
[526] Cao, J.; Zhu, Q.; Dou, J.; Li, C.; Chen, W.; Li, Z., Controlling sol–gel polymerization to create bowl-shaped polysilsesquioxane particles with a kippah structure. *Polymer* **2013,** *54* (10), 2493-2497.
[527] Huang, M.; Jiang, X.; Zhang, H.; Yin, H.; Li, X.; Ju, X., Bowl-like carbon sheet for high-rate electrochemical capacitor application. *Journal of Power Sources* **2014,** *272*, 1-7.
[528] Zhao, Z.; Feng, D.; Xie, G.; Ma, X., Functionalized hollow double-shelled polymeric nano-bowls as effective heterogeneous organocatalysts for enhanced catalytic activity in asymmetric Michael addition. *Journal of Catalysis* **2018,** *359*, 36-45.
[529] Liang, J.; Yu, X.-Y.; Zhou, H.; Wu, H. B.; Ding, S.; Lou, X. W., Bowl-like SnO2@Carbon Hollow Particles as an Advanced Anode Material for Lithium-Ion Batteries. *Angewandte Chemie International Edition* **2014,** *53* (47), 12803-12807.
[530] Riegel, I. C.; Eisenberg, A.; Petzhold, C. L.; Samios, D., Novel Bowl-Shaped Morphology of Crew-Cut Aggregates from Amphiphilic Block Copolymers of Styrene and 5-(N,N-Diethylamino)isoprene. *Langmuir* **2002,** *18* (8), 3358-3363.

[531] Liu, X.; Kim, J.-S.; Wu, J.; Eisenberg, A., Bowl-Shaped Aggregates from the Self-Assembly of an Amphiphilic Random Copolymer of Poly (styrene-co-methacrylic acid). *Macromolecules* **2005,** *38* (16), 6749-6751.
[532] Azzam, T.; Eisenberg, A., Fully collapsed (kippah) vesicles: preparation and characterization. *Langmuir* **2010,** *26* (13), 10513-23.
[533] Hyuk Im, S.; Jeong, U.; Xia, Y., Polymer hollow particles with controllable holes in their surfaces. *Nature Materials* **2005,** *4* (9), 671-675.
[534] Dong, Y.; Wang, E.; Yu, L.; Wang, R.; Zhu, Y.; Fu, Y.; Ni, Q., Self-templated route to synthesis bowl-like and deflated balloon-like hollow silica spheres. *Materials Letters* **2017,** *206*, 150-153.
[535] He, K.; Wen, Q.; Wang, C.; Wang, B.; Yu, S.; Hao, C.; Chen, K., The preparation and electrorheological behavior of bowl-like titanium oxide nanoparticles. *Soft Matter* **2017,** *13* (41), 7677-7688.
[536] Wang, Y.; Shang, B.; Liu, M.; Shi, F.; Peng, B.; Deng, Z., Hollow polydopamine colloidal composite particles: Structure tuning, functionalization and applications. *Journal of Colloid and Interface Science* **2018,** *513*, 43-52.
[537] Wang, N.; Cheng, X.; Li, N.; Wang, H.; Chen, H., Nanocarriers and Their Loading Strategies. *Advanced Healthcare Materials* **2019,** *8* (6), 1801002.
[538] Wu, M.; Wang, Q.; Zhang, D.; Liao, N.; Wu, L.; Huang, A.; Liu, X., Magnetite nanocluster@poly(dopamine)-PEG@ indocyanine green nanobead with magnetic field-targeting enhanced MR imaging and photothermal therapy in vivo. *Colloids and Surfaces B: Biointerfaces* **2016,** *141*, 467-475.
[539] Xu, L. Q.; Yang, W. J.; Neoh, K.-G.; Kang, E.-T.; Fu, G. D., Dopamine-induced reduction and functionalization of graphene oxide nanosheets. *Macromolecules* **2010,** *43* (20), 8336-8339.
[540] Wang, C.; Wang, D.; Dai, T.; Xu, P.; Wu, P.; Zou, Y.; Yang, P.; Hu, J.; Li, Y.; Cheng, Y., Skin Pigmentation - Inspired Polydopamine Sunscreens. *Advanced Functional Materials* **2018,** *28* (33), 1802127.
[541] Li, H.; Aulin, Y. V.; Frazer, L.; Borguet, E.; Kakodkar, R.; Feser, J.; Chen, Y.; An, K.; Dikin, D. A.; Ren, F., Structure Evolution and Thermoelectric Properties of Carbonized Polydopamine Thin Films. *ACS Applied Materials & Interfaces* **2017,** *9* (8), 6655-6660.
[542] Beyranvand, S.; Pourghobadi, Z.; Sattari, S.; Soleymani, K.; Donskyi, I.; Gharabaghi, M.; Unger, W. E.; Farjanikish, G.; Nayebzadeh, H.; Adeli, M., Boronic acid functionalized graphene platforms for diabetic wound healing. *Carbon* **2020,** *158*, 327-336.
[543] Beyranvand, S.; Gholami, M. F.; Tehrani, A. D.; Rabe, J. r. P.; Adeli, M., Construction and Evaluation of a Self-Calibrating Multiresponse and Multifunctional Graphene Biosensor. *Langmuir* **2019,** *35* (32), 10461-10474.
[544] Sun, Y.; Davis, E. W., Facile Fabrication of Polydopamine Nanotubes for Combined Chemo-Photothermal Therapy. *Journal of Materials Chemistry B* **2019**.
[545] Lei, C.; Li, Q.; Yang, L.; Deng, F.; Li, J.; Ye, Z.; Wang, Y.; Zhang, Z., Controlled reversible buckling of polydopamine spherical microcapsules: revealing the hidden rich phenomena of post-buckling of spherical polymeric shells. *Soft Matter* **2019,** *15* (32), 6504-6517.
[546] Zhu, W.; Yang, H.; Lan, Y.; Yin, X.; Wang, S.; Wang, C.; Gao, N.; Li, G., Photonic Janus Films with Highly Tunable Janus Balance. *Advanced Materials Interfaces* **2016,** *3* (17), 1600225.

[547] Lin, J.; Wang, H.; Ren, E.; Song, Q.; Lan, J.; Chen, S.; Yan, B., Stomatocyte-like hollow polydopamine nanoparticles for rapid removal of water-soluble dyes from water. *Chemical Communications* **2019,** *55* (56), 8162-8165.
[548] Shang, B.; Wang, Y.; Yang, P.; Peng, B.; Deng, Z., Synthesis of superhydrophobic polydopamine-Ag microbowl/nanoparticle array substrates for highly sensitive, durable and reproducible surface-enhanced Raman scattering detection. *Sensors and Actuators B: Chemical* **2018,** *255*, 995-1005.
[549] Zhang, M.; Chen, X.; Zhang, L.; Li, L.; Su, Z.-M.; Wang, C., Spadix-Bract Structured Nanobowls for Bimodal Imaging-Guided Multidrug Chemo-Photothermal Synergistic Therapy. *Chemistry of Materials* **2018,** *30* (11), 3722-3733.
[550] Li, S.; Zhang, L.; Liang, X.; Wang, T.; Chen, X.; Liu, C.; Li, L.; Wang, C., Tailored synthesis of hollow MOF/polydopamine Janus nanoparticles for synergistic multi-drug chemo-photothermal therapy. *Chemical Engineering Journal* **2019,** *378*, 122175.
[551] Ni, Y.-Z.; Jiang, W.-F.; Tong, G.-S.; Chen, J.-X.; Wang, J.; Li, H.-M.; Yu, C.-Y.; Huang, X.-h.; Zhou, Y.-F., Preparation of polydopamine nanocapsules in a miscible tetrahydrofuran–buffer mixture. *Organic & biomolecular chemistry* **2015,** *13* (3), 686-690.
[552] Yan, J.; Yang, L.; Lin, M. F.; Ma, J.; Lu, X.; Lee, P. S., Polydopamine spheres as active templates for convenient synthesis of various nanostructures. *Small* **2013,** *9* (4), 596-603.
[553] Ball, V.; Frari, D. D.; Toniazzo, V.; Ruch, D., Kinetics of polydopamine film deposition as a function of pH and dopamine concentration: Insights in the polydopamine deposition mechanism. *Journal of Colloid and Interface Science* **2012,** *386* (1), 366-372.
[554] Sun, Y.; Chen, H.; Liu, G.; Ma, L.; Wang, Z., The controllable growth of ultrathin MnO2 on polydopamine nanospheres as a single nanoplatform for the MRI-guided synergistic therapy of tumors. *Journal of Materials Chemistry B* **2019,** *7* (45), 7152-7161.
[555] Tian, Y.; Lei, M., Polydopamine-Based Composite Nanoparticles with Redox-Labile Polymer Shells for Controlled Drug Release and Enhanced Chemo-Photothermal Therapy. *Nanoscale Research Letters* **2019,** *14* (1), 186.
[556] Ho, C.-C.; Ding, S.-J., The pH-controlled nanoparticles size of polydopamine for anti-cancer drug delivery. *Journal of Materials Science: Materials in Medicine* **2013,** *24* (10), 2381-2390.
[557] Yue, Q.; Wang, M.; Sun, Z.; Wang, C.; Wang, C.; Deng, Y.; Zhao, D., A versatile ethanol-mediated polymerization of dopamine for efficient surface modification and the construction of functional core–shell nanostructures. *Journal of Materials Chemistry B* **2013,** *1* (44), 6085-6093.
[558] Souza, T. G.; Ciminelli, V. S.; Mohallem, N. D. S. In *A comparison of TEM and DLS methods to characterize size distribution of ceramic nanoparticles*, Journal of Physics: Conference Series, IOP Publishing: 2016; p 012039.
[559] Bernsmann, F.; Ponche, A.; Ringwald, C.; Hemmerlé, J.; Raya, J.; Bechinger, B.; Voegel, J.-C.; Schaaf, P.; Ball, V., Characterization of Dopamine−Melanin Growth on Silicon Oxide. *The Journal of Physical Chemistry C* **2009,** *113* (19), 8234-8242.
[560] Bernsmann, F.; Ball, V.; Addiego, F.; Ponche, A.; Michel, M.; Gracio, J. J. d. A.; Toniazzo, V.; Ruch, D., Dopamine−Melanin Film Deposition Depends on the Used Oxidant and Buffer Solution. *Langmuir* **2011,** *27* (6), 2819-2825.
[561] Ryu, J. H.; Messersmith, P. B.; Lee, H., Polydopamine Surface Chemistry: A Decade of Discovery. *ACS Applied Materials & Interfaces* **2018,** *10* (9), 7523-7540.

[562] Zhang, M.; Chen, X.; Zhang, L.; Li, L.; Su, Z.-M.; Wang, C., Spadix-Bract Structured Nanobowls for Bimodal Imaging-Guided Multidrug Chemo-Photothermal Synergistic Therapy. **2018**.
[563] Yang, C.; Li, W.; Wu, C., Laser light-scattering study of solution dynamics of water/cycloether mixtures. *The Journal of Physical Chemistry B* **2004,** *108* (31), 11866-11870.
[564] Jiang, X.; Wang, Y.; Li, M., Selecting water-alcohol mixed solvent for synthesis of polydopamine nano-spheres using solubility parameter. *Scientific Reports* **2014,** *4* (1), 6070.
[565] Kochanek, K. D.; Xu, J.; Arias, E. *Mortality in the United States, 2019*; National Center for Health, Statistics: Hyattsville, MD, 2020.
[566] Group, E. B. C. T. C., Polychemotherapy for early breast cancer: an overview of the randomised trials. *The Lancet* **1998,** *352* (9132), 930-942.
[567] Gajra, A.; Zemla, T. J.; Jatoi, A.; Feliciano, J. L.; Wong, M. L.; Chen, H.; Maggiore, R.; McMurray, R. P.; Hurria, A.; Muss, H. B.; Cohen, H. J.; Lafky, J.; Edelman, M. J.; Lilenbaum, R.; Le-Rademacher, J. G., Time-to-Treatment-Failure and Related Outcomes Among 1000+ Advanced Non–Small Cell Lung Cancer Patients: Comparisons Between Older Versus Younger Patients (Alliance A151711). *Journal of Thoracic Oncology* **2018,** *13* (7), 996-1003.
[568] Sun, Y.; Davis, E., Nanoplatforms for Targeted Stimuli-Responsive Drug Delivery: A Review of Platform Materials and Stimuli-Responsive Release and Targeting Mechanisms. *Nanomaterials* **2021,** *11* (3).
[569] Agrahari, V.; Agrahari, V.; Mitra, A. K., Nanocarrier fabrication and macromolecule drug delivery: challenges and opportunities. *Therapeutic delivery* **2016,** *7* (4), 257-278.
[570] Wang, Y.; Huang, X.; Tang, Y.; Zou, J.; Wang, P.; Zhang, Y.; Si, W.; Huang, W.; Dong, X., A light-induced nitric oxide controllable release nano-platform based on diketopyrrolopyrrole derivatives for pH-responsive photodynamic/photothermal synergistic cancer therapy. *Chemical Science* **2018,** *9* (42), 8103-8109.
[571] Vinciguerra, D.; Denis, S.; Mougin, J.; Jacobs, M.; Guillaneuf, Y.; Mura, S.; Couvreur, P.; Nicolas, J., A facile route to heterotelechelic polymer prodrug nanoparticles for imaging, drug delivery and combination therapy. *Journal of Controlled Release* **2018,** *286*, 425-438.
[572] Guo, X.; Shao, B.; Zhou, S.; Aprahamian, I.; Chen, Z., Visualizing intracellular particles and precise control of drug release using an emissive hydrazone photochrome. *Chemical Science* **2020,** *11* (11), 3016-3021.
[573] Lee, H.; Dellatore, S. M.; Miller, W. M.; Messersmith, P. B., Mussel-inspired surface chemistry for multifunctional coatings. *Science* **2007,** *318* (5849), 426-430.
[574] Battaglini, M.; Marino, A.; Carmignani, A.; Tapeinos, C.; Cauda, V.; Ancona, A.; Garino, N.; Vighetto, V.; La Rosa, G.; Sinibaldi, E.; Ciofani, G., Polydopamine Nanoparticles as an Organic and Biodegradable Multitasking Tool for Neuroprotection and Remote Neuronal Stimulation. *ACS Applied Materials & Interfaces* **2020,** *12* (32), 35782-35798.
[575] Xu, X.; Bai, B.; Wang, H.; Suo, Y., A Near-Infrared and Temperature-Responsive Pesticide Release Platform through Core–Shell Polydopamine@PNIPAm Nanocomposites. *ACS Applied Materials & Interfaces* **2017,** *9* (7), 6424-6432.
[576] Li, H.; Jia, Y.; Feng, X.; Li, J., Facile fabrication of robust polydopamine microcapsules for insulin delivery. *Journal of Colloid and Interface Science* **2017,** *487*, 12-19.

[577] Zhang, D.; Wu, M.; Zeng, Y.; Wu, L.; Wang, Q.; Han, X.; Liu, X.; Liu, J., Chlorin e6 Conjugated Poly(dopamine) Nanospheres as PDT/PTT Dual-Modal Therapeutic Agents for Enhanced Cancer Therapy. *ACS Applied Materials & Interfaces* **2015,** *7* (15), 8176-8187.
[578] Clodt, J. I.; Filiz, V.; Rangou, S.; Buhr, K.; Abetz, C.; Höche, D.; Hahn, J.; Jung, A.; Abetz, V., Double Stimuli-Responsive Isoporous Membranes via Post-Modification of pH-Sensitive Self-Assembled Diblock Copolymer Membranes. *Advanced Functional Materials* **2013,** *23* (6), 731-738.
[579] Cooley, M.; Sarode, A.; Hoore, M.; Fedosov, D. A.; Mitragotri, S.; Sen Gupta, A., Influence of particle size and shape on their margination and wall-adhesion: implications in drug delivery vehicle design across nano-to-micro scale. *Nanoscale* **2018,** *10* (32), 15350-15364.
[580] Li, L.; Liu, T.; Fu, C.; Tan, L.; Meng, X.; Liu, H., Biodistribution, excretion, and toxicity of mesoporous silica nanoparticles after oral administration depend on their shape. *Nanomedicine: Nanotechnology, Biology and Medicine* **2015,** *11* (8), 1915-1924.
[581] Kolhar, P.; Anselmo, A. C.; Gupta, V.; Pant, K.; Prabhakarpandian, B.; Ruoslahti, E.; Mitragotri, S., Using shape effects to target antibody-coated nanoparticles to lung and brain endothelium. *Proceedings of the National Academy of Sciences* **2013,** *110* (26), 10753.
[582] Dendukuri, D.; Pregibon, D. C.; Collins, J.; T, A. H.; Doyle, P. S., Continuous-flow lithography for high-throughput microparticle synthesis. *Nature Materials* **2006,** *5* (5), 365-369.
[583] Heslinga, M. J.; Mastria, E. M.; Eniola-Adefeso, O., Fabrication of biodegradable spheroidal microparticles for drug delivery applications. *Journal of Controlled Release* **2009,** *138* (3), 235-242.
[584] Jindal, A. B., The effect of particle shape on cellular interaction and drug delivery applications of micro- and nanoparticles. *International Journal of Pharmaceutics* **2017,** *532* (1), 450-465.
[585] Gao, C.; Lu, Z.; Yin, Y., Gram-Scale Synthesis of Silica Nanotubes with Controlled Aspect Ratios by Templating of Nickel-Hydrazine Complex Nanorods. *Langmuir* **2011,** *27* (19), 12201-12208.
[586] Sun, Y.; Davis, E. W., Facile fabrication of polydopamine nanotubes for combined chemo-photothermal therapy. *Journal of Materials Chemistry B* **2019,** *7* (43), 6828-6839.
[587] Wen, H.; Dong, C.; Dong, H.; Shen, A.; Xia, W.; Cai, X.; Song, Y.; Li, X.; Li, Y.; Shi, D., Engineered Redox-Responsive PEG Detachment Mechanism in PEGylated Nano-Graphene Oxide for Intracellular Drug Delivery. *Small* **2012,** *8* (5), 760-769.
[588] Rong, R.; Xu, X.; Zhu, S.; Li, B.; Wang, X.; Tang, K., Facile preparation of homogeneous and length controllable halloysite nanotubes by ultrasonic scission and uniform viscosity centrifugation. *Chemical Engineering Journal* **2016,** *291*, 20-29.
[589] Evanghelidis, A.; Beregoi, M.; Diculescu, V. C.; Galatanu, A.; Ganea, P.; Enculescu, I., Flexible Delivery Patch Systems based on Thermoresponsive Hydrogels and Submicronic Fiber Heaters. *Scientific Reports* **2018,** *8* (1), 17555.
[590] Pyne, A.; Kundu, S.; Banerjee, P.; Sarkar, N., Unveiling the Aggregation Behavior of Doxorubicin Hydrochloride in Aqueous Solution of 1-Octyl-3-methylimidazolium Chloride and the Effect of Bile Salt on These Aggregates: A Microscopic Study. *Langmuir* **2018,** *34* (10), 3296-3306.
[591] Siepmann, J.; Peppas, N. A., Higuchi equation: Derivation, applications, use and misuse. *International Journal of Pharmaceutics* **2011,** *418* (1), 6-12.

[592] Mircioiu, C.; Voicu, V.; Anuta, V.; Tudose, A.; Celia, C.; Paolino, D.; Fresta, M.; Sandulovici, R.; Mircioiu, I., Mathematical Modeling of Release Kinetics from Supramolecular Drug Delivery Systems. *Pharmaceutics* **2019,** *11* (3), 140.
[593] Gao, X.; Cao, Y.; Song, X.; Zhang, Z.; Xiao, C.; He, C.; Chen, X., pH- and thermo-responsive poly(N-isopropylacrylamide-co-acrylic acid derivative) copolymers and hydrogels with LCST dependent on pH and alkyl side groups. *Journal of Materials Chemistry B* **2013,** *1* (41), 5578-5587.

Appendices

Appendix A

SAS code for the reaction time effect on nanoparticle dimension change (at 3.3.2)

```
set anova_react_t;
if Type= "Wall Thi";
if Sample='Nanocaps';
run;

data NS_out;
set anova_react_t;
if Type="Outer  Di";
if Sample="Nanosphe";
run;

title 'NC_OUT';
proc glm data=NC_out;
class time;
model Dimension_nm = time;
means time / HOVTEST=levene welch;
run;

title 'NC_IN';
proc glm data=NC_in;
class time;
model Dimension_nm = time;
means time / HOVTEST=levene welch lines;
run;

title 'NC_WALL';
proc glm data=NC_wall;
class time;
model Dimension_nm = time;
means time / HOVTEST=levene welch;
run;

title 'NS_OUT';
proc glm data=ns_out;
class time;
model Dimension_nm = time;
means time / HOVTEST=levene welch;
run;

if 6<t<12;
```

```
run;

proc ttest h0=0 sides=l data=ns_out_8_10;
        class time;
        var dimension_nm;
run;

data ns_out_10_12;
set ns_out;
if 8<t<14;
run;

proc ttest h0=0 sides=l data=ns_out_10_12;
        class time;
        var dimension_nm;
run;

proc reg data = nc_out;
model dimension_nm = t;  run;
proc reg data = nc_in;
model dimension_nm = t;  run;
proc reg data = nc_wall;
model dimension_nm = t;  run;
proc reg data = ns_out;
model dimension_nm = t;  run;

proc corr data= nc_out;
var dimension_nm;
with t; run;
proc corr data= nc_in;
var dimension_nm;
with t; run;
proc corr data= nc_wall;
var dimension_nm;
with t; run;
proc corr data= ns_out;
var dimension_nm;
with t; run;
```

Appendix B

SAS code for the DA concentration and seal condition effect on wall thickness (at 3.3.4)

```
data thick;
infile '/home/u49813056/Grad/LongFormData.csv' delimiter = ',' dsd missover firstobs=2;
input Wallthick Conc $ Cap $;
run;

proc glm data=thick;
 class Conc Cap;
 model Wallthick = Conc Cap Conc*Cap/ ss3;
 means Conc*Cap;
run;
```

Appendix C

SAS code for the thickness increase on halloysite (at 4.3.1)

```
data thickness;
infile '/home/u49813056/Grad/thickness_sum.csv'  delimiter = ',' dsd missover firstobs=2;
input excel_label $ times ratio th_nm;
drop excel_label;
ratio4 = max(0, ratio-4);
rt = times*ratio;
r4t = times*ratio4;
run;

proc reg data=thickness;
model th_nm = times ratio rt;
run;

proc reg data=thickness ;
model th_nm = times ratio ratio4 rt r4t;
output out=weight_set predicted=pred residual=resid;
run;

proc reg data = weight_set;
model resid = pred;
output out=weight predicted=pred;
run;

data thickness_w;
set weight;
w = 1/pred**2;
run;

proc reg data=thickness_w;
model th_nm = times ratio ratio4 rt r4t / selection=cp rsquare adjrsq mse bic aic;
weight w;
run;

proc reg data = thickness_w;
model th_nm = ratio ratio4 rt;
weight w;
output out=result predicted=results;
run;
```

Appendix D

SAS code for the release model in response for three stimuli (at 4.3.4)

```
data release;
infile '/home/u49813056/Grad/linear_mix.csv' delimiter = ',' dsd missover firstobs=2;
input condition $ time percent laser pH5 mag ln_t ln_perc ID;
t=ln_t;
lasermag = laser*mag;
pH5mag = pH5*mag;
pH5laser= pH5*laser;
lasermagpH5 = laser*mag*pH5;
ln_tlaser = ln_t*laser;
ln_tmag = ln_t*mag;
ln_tpH5 = ln_t*pH5;
ln_tpH5mag = ln_t*pH5*mag;
ln_tpH5laser = ln_t*pH5*laser;
ln_tlasermag= ln_t*laser*mag;
ln_tlasermagpH5 = ln_t*laser*mag*pH5;
run;

proc glmselect data = release plots(stepaxis=normb)=all seed=1;
model ln_perc = ln_t laser mag pH5 lasermag pH5mag pH5laser lasermagpH5 ln_tlaser ln_tmag
ln_tpH5 ln_tpH5mag ln_tpH5laser ln_tlasermag ln_tlasermagpH5 / cvmethod=split(5)
selection=lasso(stop=none choose=sbc)
details=all;
partition fraction (validate = 0.3 test = 0.1);
run;

proc reg data=release;
model ln_perc = ln_t laser mag pH5 lasermag pH5mag pH5laser lasermagpH5 ln_tlaser ln_tmag
ln_tpH5 ln_tpH5mag ln_tpH5laser ln_tlasermag ln_tlasermagpH5 / selection=cp rsquare adjrsq
mse bic aic;
run;

title 'Full model';
proc reg data=release;
model ln_perc = ln_t laser mag pH5 lasermag pH5mag pH5laser lasermagpH5 ln_tlaser ln_tmag
ln_tpH5 ln_tpH5mag ln_tpH5laser ln_tlasermag ln_tlasermagpH5;
run;

title 'Reduced model';
proc reg data=release ;
```

```
model ln_perc = ln_t laser mag pH5 lasermag pH5mag ln_tlaser ln_tmag ln_tpH5 ln_tpH5laser
ln_tlasermagpH5/ r cli clm;
run;

title 'Linear mixed full model';
proc mixed data = release covtest method=reml;
class ID t;
model ln_perc = ln_t laser mag pH5 lasermag pH5mag pH5laser lasermagpH5 ln_tlaser ln_tmag
ln_tpH5
                                    ln_tpH5mag ln_tpH5laser ln_tlasermag ln_tlasermagpH5 / s;
random intercept ln_t/ type = un subject = ID g v vcorr;
run;

title 'Linear mixed model - reduced 1';
proc mixed data = release covtest method=reml;
class ID t;
model ln_perc = ln_t laser mag pH5 lasermag pH5mag ln_tlaser ln_tmag ln_tpH5 ln_tpH5laser
ln_tlasermagpH5/ s chisq outpm=predM;
random intercept ln_t/ type = un subject = ID g v vcorr;
run;

title 'Linear mixed model - reduced';
proc mixed data = release covtest method=reml;
class ID t;
model ln_perc = ln_t laser mag pH5 ln_tmag ln_tpH5 ln_tpH5laser ln_tlasermagpH5/ chisq
outpm=predM;
random intercept ln_t/ type = un subject = ID g v vcorr;
run;

proc print data=predM;run;
DATA pvalues; chsq = SDF('chisquare',810-805.4,12-9); RUN;
DATA pvalues; chsq = SDF('chisquare',814.3-805.4,16-9); RUN;
```